Influence of Functional Groups on Low-Temperature Combustion Chemistry of Biofuels

Brandon Rotavera[*, 1, 2] and Craig A. Taatjes[3]

[1]College of Engineering, *University of Georgia*, Athens, Georgia
[2]Department of Chemistry, *University of Georgia*, Athens, Georgia
[3]Combustion Research Facility, *Sandia National Laboratories*, Livermore, CA

[*]corresponding author

Abstract

Ongoing progress in synthetic biology, metabolic engineering, and catalysis continues to produce a diverse array of advanced biofuels with complex molecular structure and functional groups. In order to integrate biofuels into existing combustion systems, and to optimize the design of next-generation combustion systems, understanding connections between molecular structure and ignition at low-temperature conditions (< 1000 K) remains a priority that is addressed in part using chemical kinetics modeling. The development of predictive models relies on detailed information, derived from experimental and theoretical studies, on molecular structure and chemical reactivity, both of which influence the balance of chain reactions that occur during combustion – propagation, termination, and branching. In broad context, three main categories of reactions affect ignition behavior: (i) initiation reactions that generate a distribution of organic radicals, Ṙ; (ii) competing unimolecular decomposition of Ṙ and bimolecular reaction of Ṙ with O_2; (iii) decomposition mechanisms of peroxy radical adducts (RO$\dot{O}$), including isomerization via RO$\dot{O}$ ⇌ $\dot{Q}$OOH. All three categories are influenced by functional groups in different ways, which causes a shift in the balance of chain reactions that unfold over complex temperature- and pressure-dependent mechanisms.

The objective of the present review is three-fold: (1) to provide a historical account of research on low-temperature oxidation of biofuels, including initiation reactions, peroxy radical reactions, $\dot{Q}$OOH-mediated reaction mechanisms, and chain-branching chemistry; (2) to summarize the influence of functional groups on chemical kinetics relevant to chain-branching reactions, which are responsible for the accelerated production of radicals that leads to ignition; (3) to identify areas of research that are needed – experimentally and computationally – to address fundamental questions that remain.

Results from experimental, quantum chemical, and chemical kinetics modeling studies are reviewed for several classes of biofuels – alcohols, esters, ketones, acyclic ethers and cyclic ethers – and are compared against analogous results in alkane oxidation. The review is organized into separate sections for each biofuel class, which include studies on thermochemistry and bond dissociation energies, rate coefficients for initiation reactions via H-abstraction and related branching fractions, reaction mechanisms and product formation from reactive intermediates, ignition delay times, and chemical kinetics modeling. Each section is then summarized in order to identify areas for which additional functional group-specific work is required. The review concludes with an outline for research directions for improving the fundamental understanding of biofuel ignition chemistry and related chemical kinetics modeling.

1. Introduction

Growing needs for sustainable transportation energy provide substantial motivation for continued investment in fundamental chemical kinetics research [1-7], including on the combustion of hydrogen [8], methane [9], and ammonia [10]. Oxygenated hydrocarbon biofuels also provide a viable path to sustainable energy [11-18] and may contribute to increasing the efficiency of combustion systems even at low blending levels [19, 20]. In addition to being a lower-carbon-intensive energy source, biofuels offer the potential for mitigation of adverse climate impacts [12, 21-34]. Because of the importance to transportation energy needs, numerous organizations focus on combustion chemistry research and related impact on engine efficiency and pollutant formation, including the U.S. DOE Co-Optima program [35-38], the Fuel Science Center at Aachen University in Germany [39, 40], and the Computational Chemistry Consortium (C3) [41]. In parallel are several U.S. Department of Energy research consortia tasked with the development and realization of alternative biofuels: the Joint BioEnergy Institute (JBEI) [42], the Great Lakes Bioenergy Research Center [43] led by the University of Wisconsin-Madison, the BioEnergy Science Center [44] at Oak Ridge National Laboratory, and the Center for Advanced Bioenergy and Bioproducts Innovation (CABBI) led by the University of Illinois Urbana-Champaign [11, 45]. In addition, the Fuel Science Center at Aachen University [39, 40, 46] combines biofuel combustion research with synthetic biology research on the production of alternative biofuels. One continuing challenge of such organizations is to understand, among other topics, the interplay between fundamental combustion chemistry of new biofuels and ongoing design of advanced engine strategies.

Advanced compression-ignition (ACI) [47] is a category of technologies that are considered in the design of next-generation combustion engine strategies focused on high-efficiency, low-emissions operation. Some examples of ACI include kinetically controlled strategies such as homogeneous charge compression-ignition [48-50] (HCCI), dual-fuel strategies such as reactivity controlled compression-ignition (RCCI) [51], and hybrid concepts such as multi-mode engines [52, 53]. All of these approaches rely extensively on fundamental knowledge of oxidation chemistry at low temperatures (< 1000 K) [54-57]. As a result, the development of new technologies for sustainable transportation relies firmly on an understanding of reactions that govern ignition timing and heat-release rates, which depend on chain-branching chemistry. The degree to which this understanding is useful, however, depends on the ability to simulate combustion over practical conditions using chemical kinetics mechanisms. The efficacy of such mechanisms hinges on validation against measurements of rate coefficients, species profiles, and ignition delay times, and quantum chemical modeling of rate coefficients, branching fractions, and reaction mechanisms, all of which are strongly influenced by molecular structure.

Functional groups of biofuels, including alcohol (R–OH), ester (R–(C=O)–O–R), ketone (R–(C=O)–R), and ether (R–O–R), add complexity to reaching an understanding of chain-branching kinetics. Just as for features in hydrocarbon molecular structure, including C=C bonds [58-62] and branching [63, 64], functional groups of biofuels can lead to profound effects on combustion chemistry. For example, compared with hydrocarbon analogs, functional groups can lengthen or shorten ignition delay times owing to a combination of functional-group effects at each step involved in autoignition (branching of initial radical, changes in peroxy radical reaction mechanisms, etc.). As the development of advanced combustion strategies continues, fundamental understanding of biofuel chemical kinetics becomes increasingly important, particularly under low-temperature conditions, where ignition is governed by molecular structure due to the dependence on peroxy radical chemistry.

Ignition behavior is dictated by distinct chain-branching reactions, the nature of which depends on temperature. Three distinctive regimes of temperature are observed in combustion chemistry: high-temperature (> 1100 K), intermediate temperature (~800 – 1100 K), and low-temperature (< 800 K). In the high-temperature region, the main chain-branching reactions are $\dot{H} + O_2 \rightleftharpoons \dot{O}H + \dot{O}$ [65-68] and $\dot{O} + H_2 \rightleftharpoons \dot{O}H + \dot{H}$ [69, 70] while at intermediate temperatures $H_2O_2 \rightarrow \dot{O}H + \dot{O}H$ [71-74] is the governing reaction. Hydrogen peroxide is formed largely from H-abstraction reactions from RH by $H\dot{O}O$ [75-80] and by $H\dot{O}O$ self-reaction [81-85]. At high temperature, $H\dot{O}O$ dissociates to $\dot{H} + O_2$ while at lower temperatures it is relatively unreactive and populates from low-temperature oxidation reactions, e.g. $\dot{R} + O_2 \rightarrow H\dot{O}O$ + alkene. With decreasing temperature, H_2O_2 is too stable to provide a chain-branching pathway and a shift in the balance of reactions occurs, to chain branching by reactions of oxygenated hydrocarbon (alkylperoxy) radicals, as explained in the section below. This chain branching chemistry is species-specific and effective at lower temperatures. For some species, a gap may form between the temperature above which alkylperoxy chemistry can no longer sustain the chain reaction and the higher temperature at which $H_2O_2 \rightarrow \dot{O}H + \dot{O}H$ can take over. That gap is the negative temperature coefficient (NTC) region, within which reactivity decreases with increasing temperature. In the NTC region a plot of ignition delay against temperature takes on an S-shaped curve, the magnitude and location of which depend on the formation and fate of peroxy radicals that drive low-temperature combustion, which are strongly influenced by pressure and by molecular structure.

1.1. Low-temperature combustion chemistry

Hydrocarbon and biofuel oxidation follows a degenerate chain-branching mechanism [86-89] (**Figure 1**), which is governed by the formation and reaction of carbon-centered hydroperoxy-substituted radicals, $\dot{Q}OOH$ [90]. The sequence is initiated by the production of an organic radical $\dot{R}$ formed via H-abstraction from a parent molecule (RH) by $\dot{O}H$ or other radicals, including $H\dot{O}O$ and $\dot{C}H_3$. Subsequent formation of organic peroxy radicals, $RO\dot{O}$, from the addition reaction $\dot{R} + O_2 \rightleftharpoons RO\dot{O}$, gives rise to two reaction pathways in the forward direction: isomerization, $RO\dot{O} \rightleftharpoons \dot{Q}OOH$, and concerted decomposition to a conjugate alkene and hydroperoxyl, $RO\dot{O} \longrightarrow$ alkene + $H\dot{O}O$. Reactions of the latter type are chain-inhibiting since hydroperoxyl radicals primarily form hydrogen peroxide (H_2O_2), via $RH + H\dot{O}O \longrightarrow \dot{R} + H_2O_2$ and via $H\dot{O}O + H\dot{O}O \longrightarrow O_2 + H_2O_2$, which is stable up to ~1000 K. Unimolecular reactions of $\dot{Q}OOH$ can also produce $H\dot{O}O$ or undergo chain-propagation reactions, yielding one $\dot{O}H$ radical, which lead either to the formation of cyclic ether species or to other products such as carbonyls and alkenes via β-scission reactions.

The isomerization reaction $RO\dot{O} \rightleftharpoons \dot{Q}OOH$ is required for chain-branching, the multiplication of radicals that accelerates overall oxidation rates of RH. In competition with chain-propagation and chain-inhibiting reactions, because $\dot{Q}OOH$ are carbon-centered radicals, bimolecular reaction with O_2 (termed second O_2-addition) can occur: $\dot{Q}OOH + O_2 \rightleftharpoons \dot{O}OQOOH$. The hydroperoxyalkylperoxy radical, $\dot{O}OQOOH$, can again isomerize by an internal hydrogen shift to form a carbon-centered radical with two –OOH groups, denoted $HOO\dot{P}OOH$. This isomerization often tends to favor transfer of a hydrogen on the same carbon that holds the first –OOH, because the C–H bond is weakened by the hydroperoxyl group. That transfer gives a $HOO\dot{P}OOH$ that is an unstable α-hydroperoxy radical and that rapidly sheds an $\dot{O}H$ radical to give a closed-shell molecule with a carbonyl (ketone) functional group and a hydroperoxyl group – a ketohydroperoxide. As the linchpin for autoignition, ketohydroperoxides dissociate at moderate temperatures into a second $\dot{O}H$ and another oxy radical, providing the necessary chain-branching step.

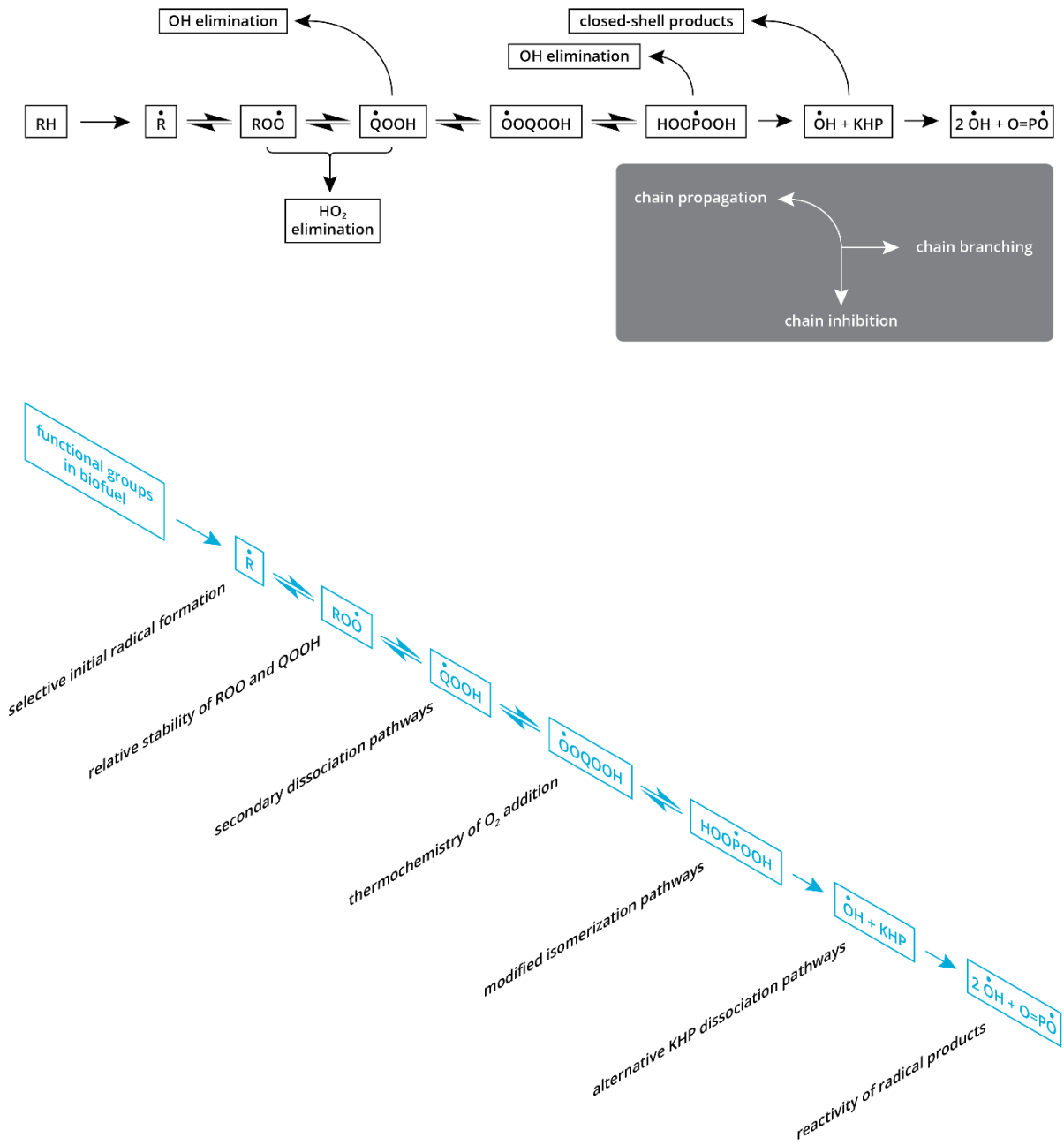

Figure 1. (a) Conventional chain-branching mechanism for alkane oxidation. Reactions along the main path proceed towards chain branching. The side reactions either form reactive radicals, such as ȮH, and are chain-propagating (depicted as curved arrows returning towards the start of the sequence) or produce less reactive species such as HOȮ and are chain-inhibiting at low temperature (depicted as downward-directed arrows). For example, reactions of ȮOOH proceed either via unimolecular ȮH elimination to form cyclic ethers, shown as the curved arrow, or bimolecular reaction with O_2 leading to the adduct ȮOQOOH. The balance of the two pathways governs reactivity characteristics of hydrocarbons and biofuels. (b) Oxygenated functional groups can impact each step in the sequence; examples of functional group effects are listed at each point.

The paradigm for alkane oxidation in **Figure 1** is dependent on molecular structure, e.g. such as the presence of C=C bonds [60, 90] or oxygenated functional groups [91]. One key objective of fundamental ignition chemistry research is to understand what diverts progress from the path to chain-branching causing differences in chain-branching and ignition chemistry due to molecular structure. For example, dissociation of a ketohydroperoxide into two stable species, as occurs in Korcek decomposition [92-95], prevents chain branching and makes ȮH + KHP a chain-propagating channel (because only one ȮH radical is formed from the initial Ṙ). Each step in the degenerate chain-branching mechanism in **Figure 1** (radical initiation, O_2-addition, Ṙ + O_2 ⇌ ROȮ, ROȮ isomerization, Q̇OOH reactions, etc.) is affected by functional groups in fundamentally different ways that depend on fuel structure. Specific types of interactions are depicted in **Figure 1b** for each step in the mechanism. For example, the selectivity of initial radical formation by hydrogen abstraction from the fuel is affected by changes in C-H bond energy near the oxygenated group and (as will be clear in the subsequent sections) the presence of hydrogen bonding in the entrance channel and transition state of the abstraction. The availability of hydrogen bonding is an important consequence of oxygenation whose effects are most pronounced at lower temperature, but which can influence branching fractions well into the low-temperature ignition regime. The reaction of the initially formed radical with O_2 produces an ROȮ radical, whose stabilization and isomerization will be changed by the differences in relative stability created by the effects of the oxygenated functional group (e.g., through vinoxylic resonance stabilization), and so on for each step in the chain. An example of the layers of fundamental chemical research necessary to identify and characterize functional group influence on low-temperature autoignition is schematically illustrated in **Figure 2**.

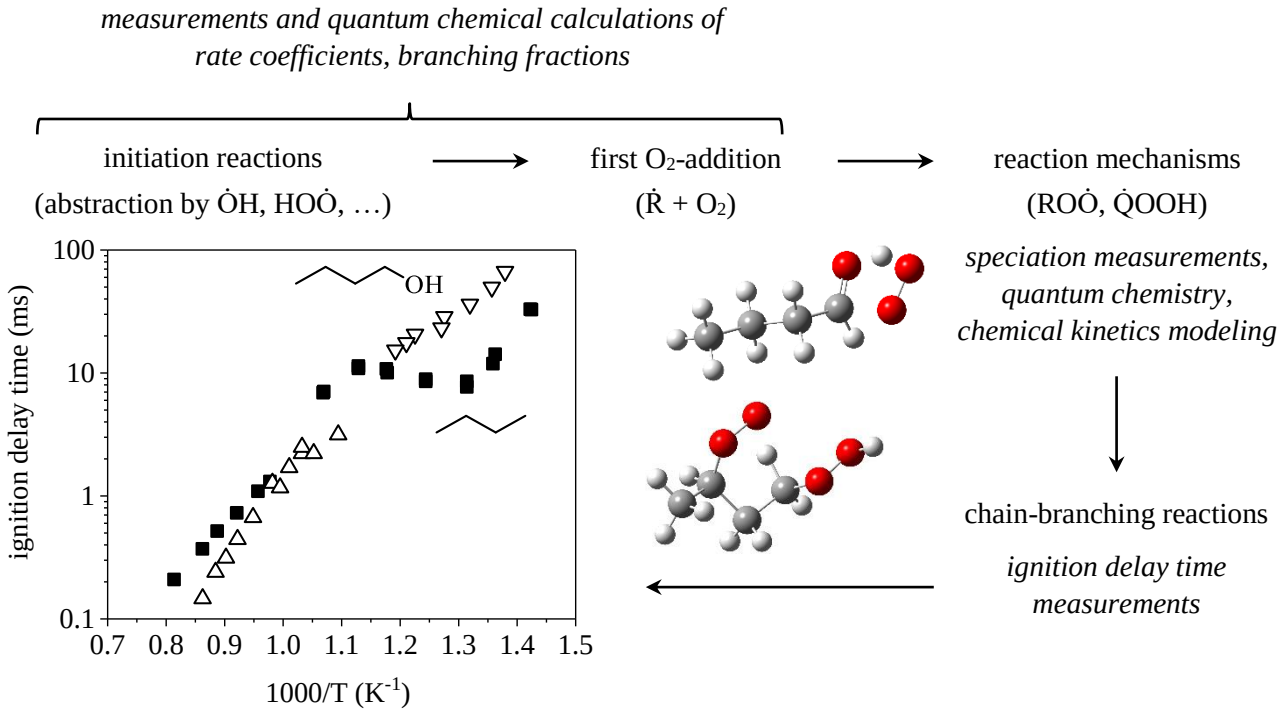

Figure 2. Schematic depiction of the set of functional group effects that enter into consideration of low-temperature combustion chemistry of a biofuel. Stoichiometric ignition delay time measurements of *n*-butane (20 atm) from Healy et al. [96] compared with 1-butanol (15 atm) from Weber et al. [97] and Heufer et al. [98]. Ignition delay times of *n*-butane exhibit NTC behavior from ~775 – 900 K. The alcohol functional group alters the balance of reactions involving ROȮ and Q̇OOH, which is the cause for longer ignition delay times below 900 K.

Ignition delay times are global observables that are important for understanding the potential impact of a biofuel on combustion systems and provide critical validation targets for chemical kinetics mechanism development and combustion modeling. Leading up to the observed ignition event are the chemical mechanisms delineated in **Figure 1** and **Figure 2**. As fundamental targets for mechanism development, and in support of enabling predictive capabilities for modeling ignition, quantitative speciation measurements, particularly of ȮOOH-mediated products, are central for validating branching fractions of initial radicals and for $\dot{R} + O_2$ rates determined via experimental measurements or via quantum chemical and theoretical kinetics calculations. Assuming that the balance of reactions producing and consuming ȮOOH are well-prescribed (both chemical kinetics and thermochemistry), chain-branching chemistry becomes predictable and mechanisms become reliable in simulations of ignition delay times with high fidelity.

The chemistry of low-temperature autoignition has been extensively reviewed. Battin-Leclerc [99] described the development and use of detailed chemical mechanisms in predicting low-temperature hydrocarbon combustion, Tran et al. [91] specifically reviewed mechanisms for biofuels, and Sarathy et al. [100] reviewed alcohol combustion. Zádor et al. [54] reviewed the elementary reaction kinetics that such mechanisms incorporate. Recently, Wang et al. [101] highlighted the role of hydroperoxides, including the key ketohydroperoxide species, in low-temperature combustion chemistry. The distinctive chemistry of biofuel combustion was highlighted by Kohse-Höinghaus [102], with emphasis on the insights given by flame chemistry measurements. The present review focuses on elementary reaction kinetics and describes the current understanding of the role of oxygenated functional groups in biofuels on alterations to reaction pathways that occur in the low-temperature combustion of hydrocarbons.

1.2. Molecular structures of biofuels

Progress in synthetic biology [103-109], catalysis [110-116], and metabolic engineering [117-122] is diversifying the types of biofuels suitable for transportation applications, which at present is largely comprised of ethanol and biodiesel. **Table 1** lists structures and molecular formulae of current and proposed next-generation biofuels and references for corresponding synthesis techniques. The biofuels listed in **Table 1** are in various stages of practical utility, from laboratory scale results to scaled-up production, similar to 2,6,10-trimethyldodecane (farnesane) [123]. It is also emphasized that a particular biofuel need not be a complete replacement for diesel or gasoline, as even small amounts can enable operation at significantly improved engine efficiency [19]. Methanol is not listed in **Table 1**, yet is a potential biofuel additive [124] or can be used to produce other biofuels [125-128].

Some hydrocarbon biofuel molecules may be structurally complex compared with hydrocarbons that constitute gasoline [129, 130] or diesel [131-133], e.g., with cyclic moieties bonded to branched side-chains (bisabolane, limonane). However, the low-temperature chemistry of such fuels is largely captured by the framework developed for traditional distillate fuels. The subject of this review is the chemistry of the large set of emerging oxygenated biofuels, types of which include ethers, furans and furan derivatives, ketones, and hybrid species. In addition to altering physical properties, the different molecular bonding structure brought about by oxygenation affects fundamental chemical properties that govern low-temperature autoignition chemistry.

Table 1. Structures and molecular formulae of oxygenated biofuels with references for synthesis techniques. Biofuels within a given class are in order of increasing carbon number.

alcohols	
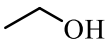	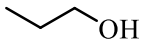
ethanol (C_2H_5OH) [120, 134-147]	1-propanol (C_3H_7OH) [109, 120, 137, 139, 147-154]
	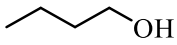
iso-propanol (C_3H_7OH) [137, 147, 150, 155-158]	1-butanol (C_4H_9OH) [109, 120, 137, 147-150, 154, 159-180]
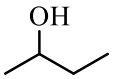	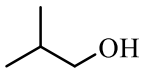
2-butanol (C_4H_9OH) [181-184]	*iso*-butanol (C_4H_9OH) [109, 120, 137, 148-150, 162, 169, 176, 185-189]
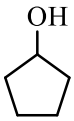	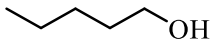
cyclopentanol (C_5H_9OH) [190-193]	1-pentanol ($C_5H_{11}OH$) [109, 148, 150, 154, 194, 195]
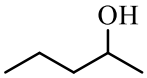	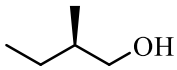
2-pentanol ($C_5H_{11}OH$) [154]	2-methyl-1-butanol ($C_5H_{11}OH$) [109, 120, 137, 147-149, 162, 169, 194]
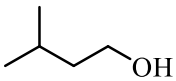	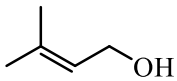
iso-pentanol ($C_5H_{11}OH$) [109, 118, 120, 137, 147-150, 158, 169, 185, 186, 194, 196-203]	prenol (C_5H_9OH) [147, 150, 194, 197, 204]
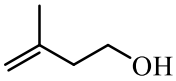	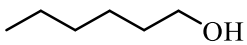
iso-prenol (*iso*-C_5H_9OH) [147, 150, 194, 197, 204, 205]	1-hexanol ($C_6H_{13}OH$) [109, 148, 150, 162, 177, 195]
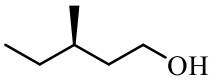	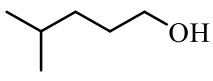
3-methyl-1-pentanol ($C_6H_{13}OH$) [109, 120, 147, 148, 150, 169]	4-methyl-1-pentanol ($C_6H_{13}OH$) [109, 150, 169]

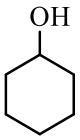

cyclohexanol ($C_6H_{11}OH$) [206-211]

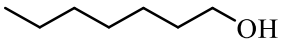

1-heptanol ($C_7H_{15}OH$) [195]

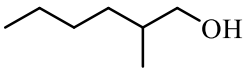

2-methyl-1-hexanol ($C_7H_{15}OH$) [162]

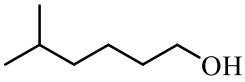

5-methyl-1-hexanol ($C_7H_{15}OH$) [169]

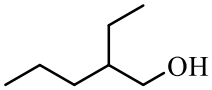

2-ethyl-1-pentanol ($C_7H_{15}OH$) [162]

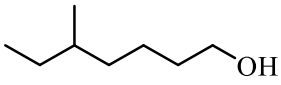

5-methyl-1-heptanol ($C_8H_{17}OH$) [150]

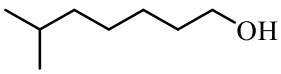

6-methyl-1-heptanol ($C_8H_{17}OH$) [109]

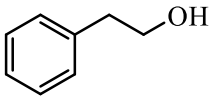

2-phenylethanol (C_8H_9OH) [109, 149, 185]

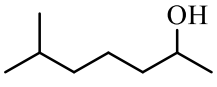

6-methyl-2-heptanol ($C_8H_{17}OH$) [212]

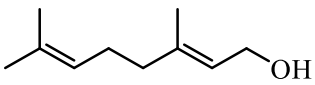

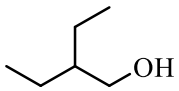

2-ethyl-1-butanol ($C_6H_{13}OH$) [162]

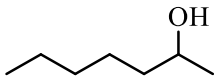

2-heptanol ($C_7H_{15}OH$) [162]

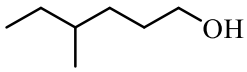

4-methyl-1-hexanol ($C_7H_{15}OH$) [109, 150, 169]

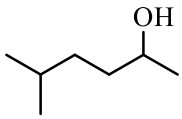

5-methyl-2-hexanol ($C_7H_{15}OH$) [162, 212]

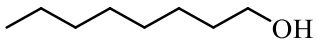

1-octanol ($C_8H_{17}OH$) [162, 195, 213]

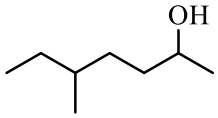

5-methyl-2-heptanol ($C_8H_{17}OH$) [162]

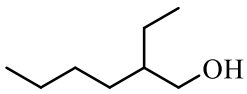

2-ethyl-1-hexanol ($C_8H_{17}OH$) [162]

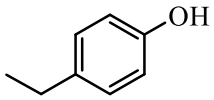

4-ethylphenol (C_8H_9OH) [214, 215]

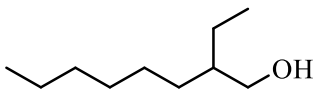

2-ethyl-1-octanol ($C_{10}H_{21}OH$) [162]

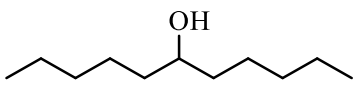

geraniol ($C_{10}H_{17}OH$) [216]

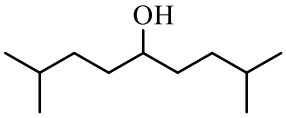

6-undecanol ($C_{11}H_{23}OH$) [162]

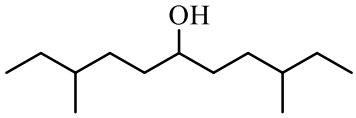

2,8-dimethyl-5-nonanol ($C_{11}H_{23}OH$) [162, 212]

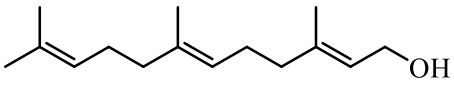

3,9-dimethyl-6-undecanol ($C_{13}H_{27}OH$) [162]

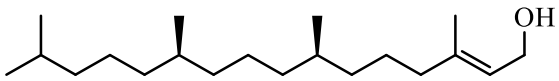

farnesol ($C_{15}H_{25}OH$) [216]

phytol ($C_{20}H_{39}OH$) [217]

esters

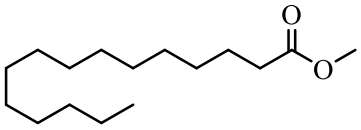

saturated (methyl/ethyl) esters [115, 120, 134, 147, 150, 218-221]

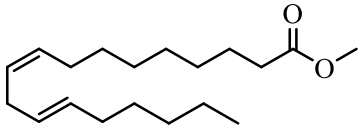

unsaturated (methyl/ethyl) esters [115, 134, 150, 218-221]

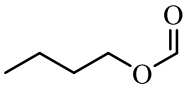

n-butyl formate ($C_5H_{10}O_2$) [222]

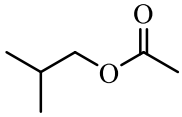

2-methylpropyl acetate ($C_6H_{12}O_2$) [185, 223]

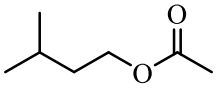

iso-amyl acetate ($C_7H_{14}O_2$) [223]

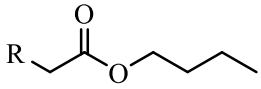

butyl esters [147]

ketones

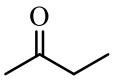

butanone (C_4H_8O) [118, 185, 224-228]

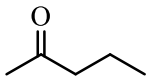

2-pentanone ($C_5H_{10}O$) [118, 177, 227, 229]

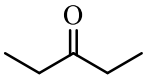

3-pentanone ($C_5H_{10}O$) [230]

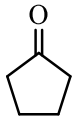

cyclopentanone (C_5H_8O) [190, 231-239]

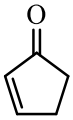

2-cyclopenten-1-one (C_5H_6O) [240]

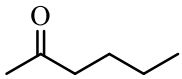

2-hexanone ($C_6H_{12}O$) [227]

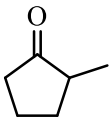

2-methylcyclopentanone ($C_6H_{10}O$) [241, 242]

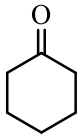

cyclohexanone ($C_6H_{10}O$) [207, 209-211, 243]

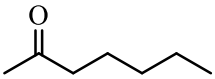

2-heptanone ($C_7H_{14}O$) [227, 229]

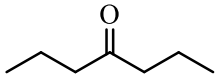

4-heptanone ($C_7H_{14}O$) [229]

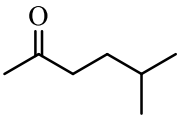

5-methyl-2-hexanone ($C_7H_{14}O$) [162, 212]

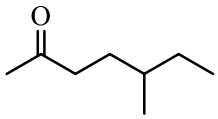

5-methyl-2-heptanone ($C_8H_{16}O$) [162]

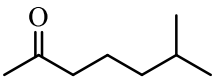

6-methyl-2-heptanone ($C_8H_{16}O$) [212]

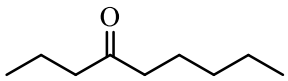

4-nonanone ($C_9H_{18}O$) [162, 229]

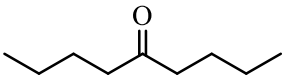

5-nonanone ($C_9H_{18}O$) [244]

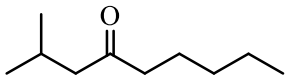

2-methyl-4-nonanone ($C_{10}H_{20}O$) [229]

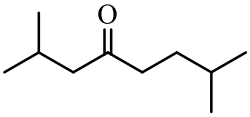

2,7-dimethyl-4-octanone ($C_{10}H_{20}O$) [212]

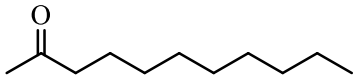

2-undecanone ($C_{11}H_{22}O$) [245]

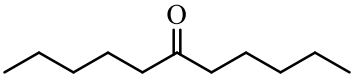

6-undecanone ($C_{11}H_{22}O$) [162, 229]

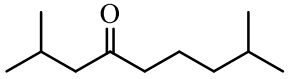

2,8-dimethyl-4-nonanone ($C_{11}H_{22}O$) [212]

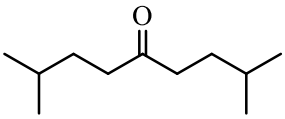

2,8-dimethyl-5-nonanone ($C_{11}H_{22}O$) [162, 212]

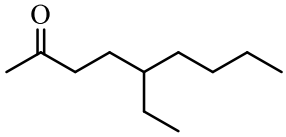

5-ethyl-2-nonanone ($C_{11}H_{22}O$) [162]

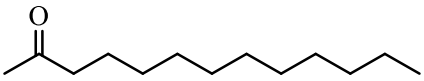

2-tridecanone ($C_{13}H_{26}O$) [245]

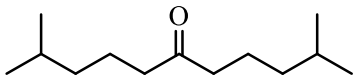

2,10-dimethyl-6-undecanone ($C_{13}H_{26}O$) [212]

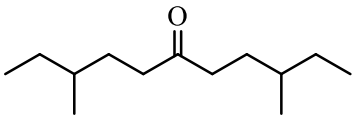

3,9-dimethyl-6-undecanone ($C_{13}H_{26}O$) [162]

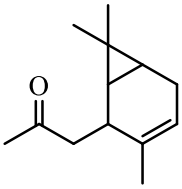

2-(acetylmethyl)-3-carene ($C_{13}H_{20}O$) [185]

acyclic ethers

dimethyl ether (C_2H_6O) [126, 127, 164, 246-252]

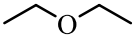

diethyl ether ($C_4H_{12}O$) [253, 254]

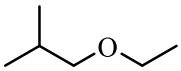

ethyl-*tert*-butyl ether ($C_6H_{14}O$) [150, 255-257]

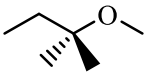

2-methoxy-2-methylbutane ($C_6H_{14}O$) [150, 255, 258]

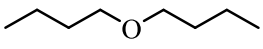

di-*n*-butyl ether ($C_8H_{18}O$) [39, 164, 213]

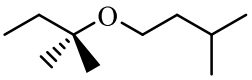

3-methyl-1-(tert-pentyloxy)butane ($C_{10}H_{22}O$) [259]

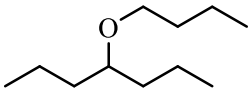

4-butoxyheptane ($C_{11}H_{24}O$) [260]

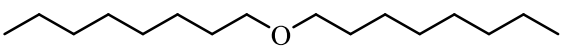

di-*n*-octyl ether ($C_{16}H_{34}O$) [213]

cyclic ethers

furan (C_4H_4O) [261, 262]

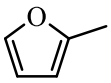

2-methylfuran (C_5H_6O) [243, 261-268]

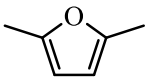

2,5-dimethylfuran (C_6H_8O) [115, 209, 232, 261, 262, 266, 269-279]

tetrahydrofuran (C_4H_8O) [154, 209, 244, 262, 267, 280]

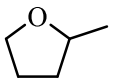

2-methyltetrahydrofuran ($C_5H_{10}O$) [115, 154, 209, 244, 261, 262, 267, 280-285]

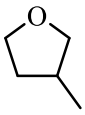

3-methyltetrahydrofuran ($C_5H_{10}O$) [209, 261, 282]

tetrahydropyran ($C_5H_{10}O$) [286, 287]

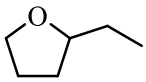

ethyltetrahydrofuran ($C_6H_{12}O$) [209]

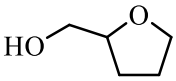

(tetrahydrofuran-2-yl)methanol ($C_5H_{10}O_2$) [275]

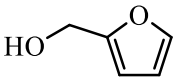

furan-2-ylmethanol ($C_5H_6O_2$) [275]

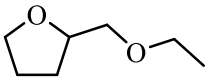

2-(ethoxymethyl)tetrahydrofuran ($C_7H_{14}O_2$) [280, 291]

1,8-cineole ($C_{10}H_{18}O$) [293]

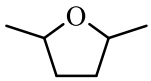

2,5-dimethyltetrahydrofuran ($C_6H_{12}O$) [209, 262, 277, 278, 281]

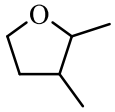

2,3-dimethyltetrahydrofuran ($C_6H_{12}O$) [288, 289]

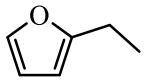

2-ethylfuran (C_6H_8O) [277]

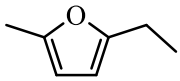

2-ethyl-5-methylfuran ($C_7H_{10}O$) [290]

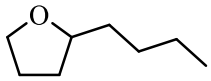

n-butyl-tetrahydrofuran ($C_8H_{16}O$) [213, 292]

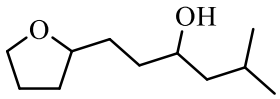

5-methyl-1-(tetrahydrofuran-2-yl)hexan-3-ol ($C_{11}H_{22}O_2$) [294]

2. Methods of studying low-temperature combustion chemistry

Autoignition reflects a balance of competing chemical reaction pathways and chain-reactions that consume the fuel and contribute to heat release rates and subsequent pressure rise in engines that in turn affect the time at which ignition occurs. In-cylinder fluid dynamics, including fuel injection and fuel-air charge-compression, inherently create temperature and concentration gradients in the reactive fuel-air mixture, which alters the balance of chemical reactions. Because molecular structure governs the sensitivity of fuel oxidation to both temperature and pressure, an important target remains the development of well-constrained computational models to predict the effects of temperature and pressure on autoignition in order to aid in the design of next-generation engine strategies. The trajectory of fundamental understanding of autoignition, from chemical reactions to mechanism development, involves multi-faceted experimental, computational, and theoretical research efforts that target the influence of fuel structure. Because functional groups are differentiating molecular features of oxygenated biofuels from conventional fuels, autoignition studies routinely center on the influence of biofuel structure on fundamental chemical pathways and the global ignition behavior.

A full-spectrum approach to studying low-temperature biofuel autoignition requires a broad range of measurements, obtained from numerous experimental techniques, coupled with insight from computational and theoretical chemistry to describe functional-group effects on autoignition. The following sections outline the principal experimental, computational, and theoretical approaches currently utilized to study autoignition chemistry. The experimental apparatus are separated in terms of focus: transient speciation, steady-state speciation, and ignition delay times from shock tube and rapid compression machines. Computational and theoretical approaches are separated according to scope, from *ab initio* calculations of rate coefficients to detailed chemical kinetics modeling. In general, experimental results on autoignition kinetics are intended to serve as modeling targets. However, modeling efforts also contribute to defining new experimental targets. The broader objective of the combined experimental and computational efforts is a fundamental description of biofuel autoignition chemistry that can be utilized in modeling combustion phenomena in complex reactive flows in engines.

2.1. Time-dependent speciation experiments

Rate coefficient measurements of fundamental reactions are vital for modeling autoignition chemistry. To define and verify the chemical understanding of low-temperature combustion, it is most important to obtain direct measurements of species in the ROȮ decomposition mechanism in Figure 1 [295-299], fundamental hydrocarbon chemistry [300], and unique decomposition pathways not included in the paradigm of Figure 1 [301, 302]. Measurements that use photolysis to initiate controlled oxidation can be coupled with spectroscopic probes that target key intermediates like the hydroxyl radical [303]. The multi-pass near-infrared (NIR) absorption approach of Taatjes [304] has led to rate coefficient measurements of $\dot{R} + O_2$ reactions [305-308] and $\dot{Q}OOH + O_2 \rightleftharpoons OO\dot{Q}OOH$ [297], where $\dot{Q}OOH$ was derived from *tert*-butylhydroperoxide. The NIR experiments also provide measurements for constraining chemical kinetics mechanisms by measuring ȮH and HOȮ time histories below 800 K [304, 307, 309]. The multiplexed photoionization mass spectrometry (MPIMS) approach [90, 310-312] has extended such measurements to allow simultaneous detection and characterization of a wide range of products and intermediates, increasing the detail of information that can be obtained on fundamental reaction mechanisms important to low-temperature combustion chemistry. The quiescent reflected-shock region and optical access afforded by shock tubes permits the application of laser-based diagnostics to measurements of rate coefficients [313]

using highly diluted systems (i.e. RH ~ 0.1% vol. [314]), and the multi-species time history measurements of Hanson and Davidson et al. (e.g. [315-319]) provide critical information for refining chemical kinetics mechanisms. More extensive speciation in single-pulse shock tubes [320] has been obtained using GC by Lifshitz [321, 322] and Brezinsky et al. [323-325], the conventional shock tube approach by Ferris et al. [326, 327], and by VUV photoionization by Tranter and Lynch [328, 329]. Speciation from RCM have also yielded kinetics insight at engine-relevant conditions [330, 331].

2.2. Steady state speciation experiments

Flow reactors provide a means of quantifying species formed as intermediates from oxidation and enable speciation measurements related to autoignition from ~500 < T (K) < 1200, mostly over the pressure range 1 – 10 atm. Speciation of stable intermediates in flow reactor experiments is typically performed by direct sampling using a tandem of gas chromatography/mass spectrometry (GC/MS), flame ionization detection (FID), and thermal conductivity detection (TCD). Flow reactor designs most commonly utilized to investigate low-temperature chemistry include plug-flow reactors [332-337], micro reactors [338-340], and jet-stirred reactors (JSR) [341-343], all of which provide homogeneous mixing of reactants under controlled conditions of temperature, pressure, and residence time. Jet-stirred reactors coupled with molecular beam mass spectrometry (MBMS) have led to new insight into low-temperature chemistry [344]. The reviews by Dryer et al. [345] on plug-flow reactors, and by Herbinet and Battin-Leclerc [346] and Dayma and Herbinet [347] on jet-stirred reactors, provide thorough insight into the underlying physics and related measurements. Mole fractions measured are obtained over a range of temperature, pressure, and equivalence ratio, and dilute conditions are employed to minimize heat release in the reactor and to minimize the rates of bimolecular reactions during the gas-sampling process.

2.3. Ignition delay times

Two apparatus are most commonly used to measure ignition delay time trends: shock tubes and rapid-compression machines (RCM). Both experiments operate using well-characterized initial conditions and are near-ideal reactors with minimal or no influence from gas dynamics. For conditions where non-idealities exist, facility-specific effects are accounted for in the interpretation of the ignition delay time measurements. Necessary conditions for shock tube measurements to be void of interference from gas dynamic effects are outlined in Petersen and Hanson [348, 349], Davidson and Hanson [314], and in Chaos and Dryer [350], and the conditions for rapid-compression machines are discussed in detail in Goldsborough et al. [331], Griffiths [351, 352], Sung and Curran [330], Kéromnès [353], and Ihme [354].

Shock tubes provide a method of measuring ignition delay times under both dilute (>98% inert gas) and non-dilute conditions [355], differing from RCM experiments in the mechanism of gas compression. In shock-tube ignition experiments, reflected shock waves generate temperatures and pressures relevant to autoignition on μs-timescales [356, 357]. Ignition delay times are measured in shock tubes from chemical reactions occurring in the quiescent reflected-shock region, using either pressure histories [358], laser absorption [359], or emission-based definitions [360, 361], where the latter measurements involve broadband emission, such as OH* ($X^2\Pi \leftarrow A^2\Sigma^+$) or CH* ($X^2\Pi \leftarrow A^2\Delta$) chemiluminescence. The main point of contrast with RCM experiments is the available timeframe within which measurements are conducted and the need to include a model for facility-specific heat-loss rates. Shock-heated gas temperatures overlap the middle of the temperature range in RCM experiments (~800 K) and extend to 1500 K or higher. Low-temperature capabilities in conventional shock tubes are limited by

expansion/compression wave interactions that cause a change in the near-isothermal/isobaric conditions within the reflected-shock region and ultimately define the test time (typically 2 – 3 ms). Test times are extendable by delaying the arrival of the expansion wave at the test section using driver-gas tailoring, a method which effectively reduces the acoustic speed of the expansion waves, as discussed by Petersen et al. [362], or by the use of driver-section inserts as designed by Hanson et al. [363]. Combined with driver-gas tailoring, advances in experimental design by Hanson et al., including the aerosol shock tube [364], which allows for gas-phase experiments on low-vapor-pressure hydrocarbons and biofuels, and the constrained-reaction-volume (CRV) shock tube [365], which provides more-ideal shock tube conditions, permits low-temperature ignition measurements of relevant biofuels, including 1-butanol [366] and methyl esters related to biodiesel [367]. The ideal conditions of the CRV approach avoids errors associated with modeling reflected-shock gas dynamics using either constant internal energy (U) and volume (V), or constant pressure (P) and enthalpy (H) [314].

Rapid-compression machines use controlled, piston-driven gas-compression to measure ignition delay time trends under practical conditions of temperature, pressure, and fuel concentration [98, 330, 331, 351, 368, 369]. The RCM apparatus is designed to closely replicate a single compression stroke in an engine, yet under near-adiabatic conditions. Pressure is measured over the course of the compression stroke, and peak pressure is recorded as the compressed-gas pressure and defines time-zero for monitoring ignition delay times. Using pressure time-histories and adiabatic approximations, a compressed-gas temperature is then calculated which serves as the initial temperature of the reaction. Typical operating ranges are ~500 < T (K) < 1100 and 10 < P (atm) < 100. Modeling and analysis of pressure time-histories is also employed in RCM experiments to closely reproduce the temporal variation in temperature and accurately determine gas-dynamic-induced temperature changes as a function of time, including for multi-stage ignition [370]. The primary advantage of RCM measurements is operation over the entire negative-temperature-coefficient (NTC) region of hydrocarbon autoignition at engine-relevant conditions: high-pressure, low-temperature, non-dilute conditions (N_2 ~76% vol.). Commonly, ignition is defined using measurements of pressure, where a sharp increase occurs relative to P_c, indicating primary fuel ignition. Two-stage fuel-ignition, similar to the phenomenon in engine measurements, is also detectable. Other diagnostics applied to RCM experiments include speciation and chemiluminescence imaging [371, 372].

2.4. Detailed chemical kinetics mechanisms

Chemical kinetics mechanisms focusing on low-temperature autoignition chemistry of biofuels are ubiquitous in the literature [99, 373-389], and continue to increase in size (i.e. number of species and reactions) to accommodate interest in engine-relevant fuels [390, 391]. Pioneering efforts of Dixon-Lewis [392, 393], Miller et al. [394], Kee et al. [395, 396], Warnatz [397], Troe [398], Westbrook and Dryer [375, 399], and countless others over the past several decades led to the development of efficient computational methods that enable detailed analysis of complex combustion reactions using chemical kinetics mechanisms. Owing to computational advances in matrix preconditioning [391], the use of larger chemical kinetics mechanisms is becoming more feasible in combustion simulations of practical systems, which is particularly important for low-temperature autoignition, where ROȮ adducts can decompose along numerous pathways involving thousands of species and reactions. Detailed chemical kinetics mechanisms and related derivatives (e.g. semi-empirical, skeletal) offer some insight into experimental ignition delay times, species profiles, and can indicate which of the underlying pathways are more favored. Over the past decade, automated methods for developing reaction networks, such as Reaction Mechanism Generator

(RMG) [400] and Genesys [401, 402], are increasingly applied to producing detailed kinetic mechanisms for low-temperature combustion. Reviews by Dagaut [373], Westbrook and Dryer [375], Ranzi et al. [403], Pitz [132], Battin-Leclerc et al. [404], Wang et al. [405, 406], and Curran [88] provide extensive details on chemical kinetics mechanism development.

2.5. Theoretical chemical kinetics

The rate coefficients that are required for detailed chemical mechanisms are far too extensive in number and in pressure and temperature range for explicit experimental characterization ever to be complete. Rate expressions are therefore commonly generated via rate rules and structure-activity relationships [407-411] that couple experimental data with theory. As theory becomes more powerful and accurate calculation of reaction rate parameters can be extended to larger molecular systems, quantum chemistry and direct kinetics calculations [54, 412-415] are increasingly displacing the methods of experimental interpolation and analogy that had been used to develop such rate rules. Klippenstein [416] recently highlighted the state of the art in predictive theoretical kinetics, emphasizing the need to combine advanced theory in electronic structure calculations, reaction rate theory, energy transfer, and master equation kinetics methods. Accuracy in all of these areas can be critical to a theoretical description of the pressure dependent reactions governing autoignition. These reactions often take place on highly complex potential energy surfaces with multiple wells and many possible reaction channels. Miller et al. [417] provide an extensive review of theoretical chemical kinetics contributions and challenges in the context of combustion modeling. Similar to the implementation of automated methods for chemical network generation, new techniques are being introduced for automatically searching complex surfaces and characterizing the stationary points that determine the reaction kinetics [416, 418-422]. Such methods dramatically increase the throughput for calculation of reaction kinetics, and can locate transition states that manual methods have missed, as has been demonstrated for ketohydroperoxide decomposition [423], one of the most crucial low-temperature combustion reactions.

The present review provides a comprehensive comparison of rate coefficients for different types of reactions (initiation, addition, and isomerization), which are often calculated using different electronic structure methods and different kinetics modeling approaches. Zádor et al. [54] summarized the ideal strategy leading to accurate rate coefficient calculations (**Figure 3**): balance the level of electron correlation and basis set to increase the accuracy of the electronic structure calculations; balance the levels of the microcanonical rate coefficient model and the collision model to increase the accuracy of theoretical kinetics. Density functional methods lack the clear systematic path of improvement that is depicted in **Figure 3** for wave-function based electronic structure calculations, although a hierarchy of functional types has been proposed [424]. Detailed assessments of functionals (e.g., [425, 426]) can provide guidance on expected accuracy and appropriate areas of applicability within the density functional ‘zoo’ [427].

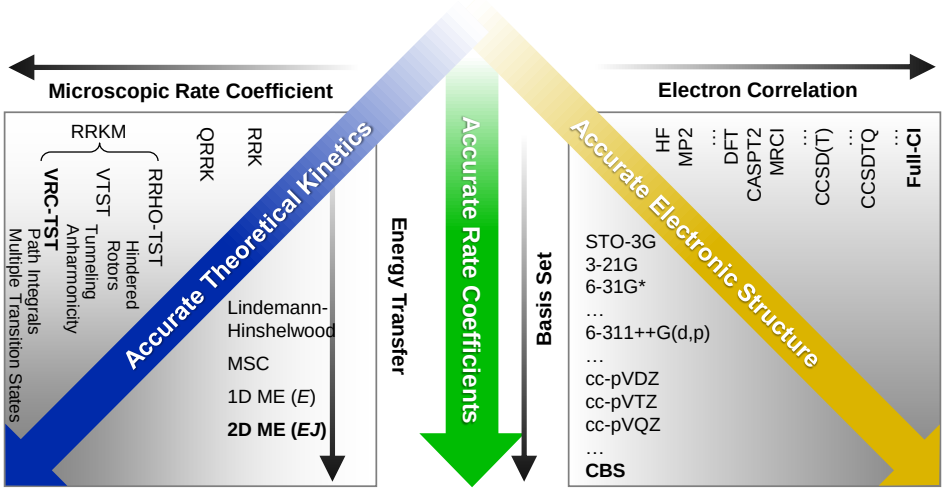

Figure 3. Methods for theoretical chemical kinetics and electronic structure calculations of rate coefficients [54].

3. *Functional group-specific oxidation chemistry*

The sections below describe the effects on low-temperature chain-branching mechanisms of several functional groups common to biofuels, drawing on inference from both experimental and computational studies in the literature. The discussion treats, in turn, the chemistry of alcohols, esters, ketones, and acyclic ethers, with an additional section describing the chemistry of cyclic ethers, which are also intermediate products of low-temperature alkane oxidation [428-430]. Emphasis is placed on the effects of functional groups on (i) initiation reactions leading to the formation of carbon-centered radicals, Ṙ, (ii) reactions of Ṙ with O_2, (iii) subsequent reaction pathways and product formation from ROȮ reactions, (iv) ȮOOH reactions, (v) speciation measurements, (vi) ignition delay times, and (vii) chemical kinetics modeling. While a large number of radicals are relevant to low-temperature combustion, including $CH_3\dot{O}$, $CH_3O\dot{O}$, and others, because the review concentrates on major initiation (abstraction) reactions, only with the most important radicals below 1000 K are considered: ȮH, HOȮ, and $\dot{C}H_3$. Other radicals that are more important at high temperature (Ḣ, Ö, CH_2, etc.) are not considered.

The molecular structure characteristics and related oxidation chemistry of functional groups that represent the majority of oxygenated biofuels are described: alcohols (*Section 3.1*), esters (*Section 3.2*), ketones (*Section 3.3*), acyclic ethers (*Section 3.4*), and cyclic ethers (*Section 3.5*). Each section is concluded with a summary of the literature and an augmented oxidation scheme that shows radical-specific reaction pathways impacted by the functional group. When feasible, the chemical kinetics are described relative to the non-functionalized hydrocarbon analog of the biofuel (e.g., for alcohols, –OH functionality is contextualized using 1-butanol in reference to *n*-butane).

3.1. alcohols

Alcohol biofuels include species where the hydroxy group (–OH) is bound to a primary carbon (e.g. ethanol, 1-pentanol, *iso*-pentanol) or to a secondary carbon (e.g. 2-butanol, cyclohexanol). The bond energy of hydroxylic hydrogen is ~105 kcal/mol [431, 432], which is higher by ~5 kcal/mol and ~7 kcal/mol compared to primary and secondary C–H bonds in alkanes, respectively. As a result, abstraction of hydrogen from the –OH group is disfavored at temperatures below ca. 1000 K [76, 433-436]. Initiation reactions involving ȮH or HOȮ are influenced by the presence of the –OH group, however, in part because of an alteration of C–H bond dissociation energies on α, β, and γ carbon sites (depicted in **Figure 4** for 1-pentanol) and because of hydrogen-bonding interactions that create pre-reaction complexes. Relative to analogous C–H bonds in *n*-alkanes, *ab initio* calculations conducted on linear alcohols indicate a reduction in bond dissociation energy of 5-6 kcal/mol on the carbon α to the functional group, an increase of 1-2 kcal/mol on β carbon, and ~1 kcal/mol reduction on γ carbon [431, 432, 437-439]. C–H bond dissociation energies beyond the γ position are relatively uninfluenced by the –OH group yet, despite the separation distance, hydrogen bonding with the abstracting radical is important [440]. Heufer et al. [437] ascribe the slight increase in C–H bond energy at the β site in linear alcohols, as opposed to a decrease similar to the adjacent C–H bonds, to steric interactions between the –OH group and the sp^2-hybridized radical site. For alcohols larger than ethanol, lower C–H bond energies coupled with electrostatic interaction with the –OH functional group skews branching fractions of initiation reactions (via H-abstraction by ȮH and HOȮ) in favor of α, β, and γ radicals. Bond dissociation energy trends differ somewhat for branched alcohols [441], however α radicals remain favored.

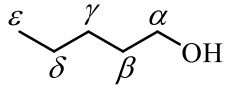

Figure 4. Structure of 1-pentanol with H-abstraction sites labeled. The influence of the –OH group extends from α to δ sites and affects the distribution of initial radicals formed via abstraction by ȮH, HOȮ, or other radicals. The formation of α radicals via H-abstraction is dominant at temperatures relevant to ROȮ chemistry.

3.1.1. initiation reactions and branching fractions

The distribution of initial radicals that react with O_2 at temperatures below 1000 K influences the balance of chain reaction pathways, which makes branching fractions critical to modeling alcohol oxidation mechanisms. Measurements of site-specific and total rate coefficients for H-abstraction at combustion-relevant temperatures are reported for several alcohols, including reactions of ȮH with ethanol [316, 436, 442-446] and with isomers of butanol [433, 434, 440, 447-451], which provide some constraint to theoretical predictions of branching fractions. Rate coefficients for hydrogen abstraction by HOȮ are also reported for alcohols [76, 435, 439, 452-454] and are shown to impact ignition delay time predictions [454]. Unlike reactions with ȮH, are all endothermic [453]. Abstraction reactions involving $\dot{C}H_3$ [455-458] are also reported in the literature and in some cases compare favorably with experiments [316, 443, 446].

The presence of hydrogen-bonding in the transition state, between the abstracting radical and the –OH functional group, leads to differences in rate coefficients and branching fractions of the initiation step, e.g. X + ROH → XH + ṘOH. Selected results for abstraction by ȮH, HOȮ, and $\dot{C}H_3$ in the high-pressure limit

are discussed below for ethanol, 1-butanol, and branched alcohols. In all cases, abstraction from α carbon remains the most favored site, and for abstraction by HOȮ is the exclusive site [76, 459-462].

3.1.1.1. linear alcohols + ȮH

Despite several studies on H-abstraction by ȮH from linear alcohols, discrepancies remain [443, 460, 463] [464]. Glarborg et al. [464] noted, that despite the consistency among the literature [316, 436, 443, 445, 446] on the total rate coefficient for ȮH + ethanol → Ṙ + H_2O, branching fraction predictions are in substantial disagreement. **Figure 5a** compares *ab initio* calculations in the high-pressure limit from Sivaramakrishnan et al. [436], Xu and Lin [445], and Zheng and Truhlar [446], all of which are consistent with the experimental results of Carr et al. [443], Stranic et al. [316], Sivaramakrishnan et al. [436], and others [444, 465-467]. **Figure 5b – 5d** show branching fractions from 500 – 1000 K from Sivaramakrishnan et al. [436], Xu and Lin [445], and Zheng and Truhlar [446]. Sivaramakrishnan et al. [436] used transition state theory with stationary points calculated at the QCISD(T)/CBS level of theory. Xu and Lin [445] computed potential energy surfaces at the CCSD(T)/6-311+G(3*df*,2*p*)//MP2/6-311+G(3*df*,2*p*) level of theory and used variational transition state theory and RRKM theory with VariFlex [468]. Zheng and Truhlar [446] employed MP-VTST level of theory with transmission coefficients of all reaction paths calculated explicitly from M08-HX/6-31+G(*d*,*p*) potential energy surfaces. The branching fractions in **Figure 5b – 5d** show consistency in that α radicals (1-hydroxyethyl) are significantly favored. However, predictions of the formation of β radicals varies from <5% in [436], to 10 – 15% in [445], to 20 – 25% in [446].

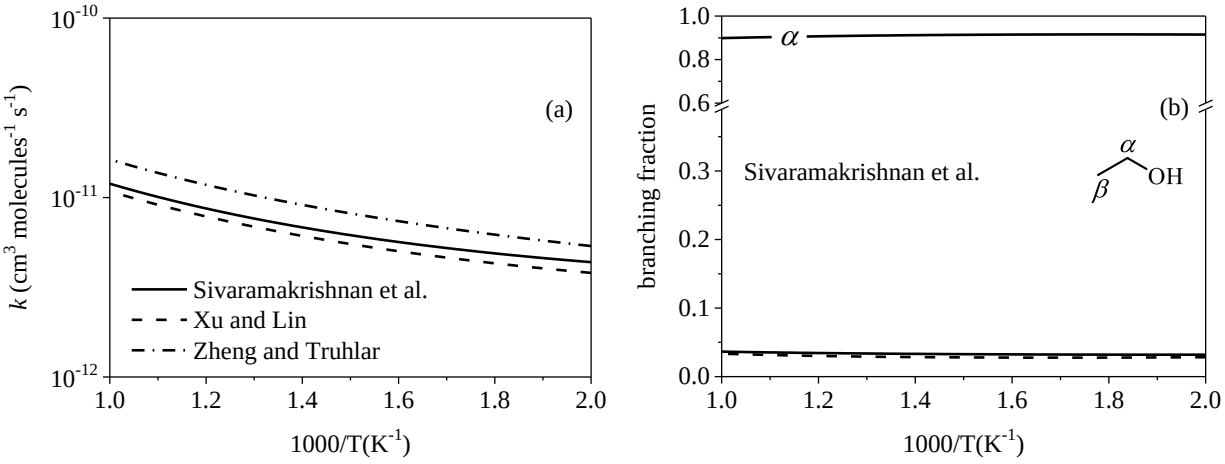

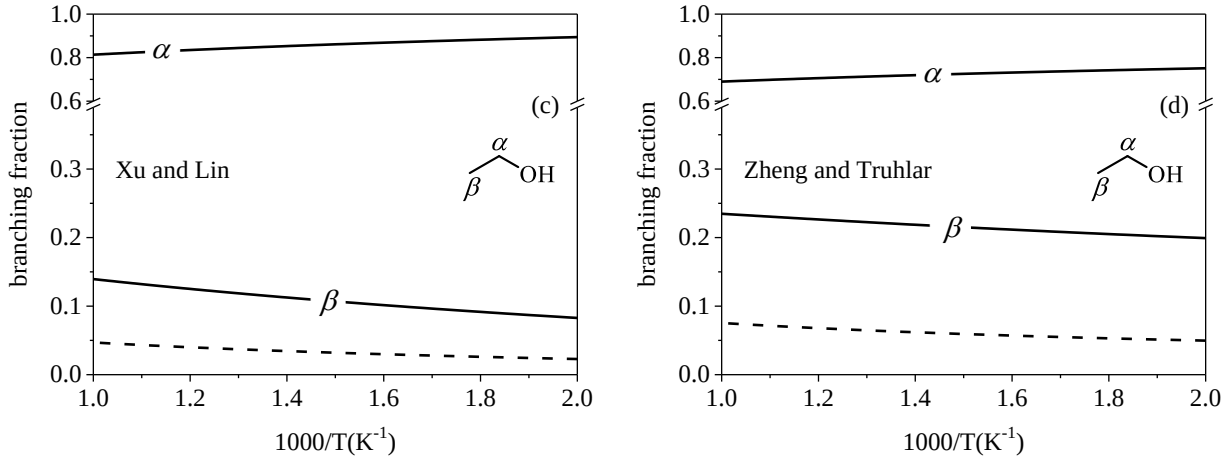

Figure 5. Total rate coefficients (a) and branching fractions (b – d) for ȮH + ethanol from Sivaramakrishnan et al. [436] Xu and Lin [445], and Zheng and Truhlar [446]. The dashed line in (b) – (d) represents branching fractions for abstraction from the –OH group.

The formation of α radicals dominates branching fractions in reactions with ȮH at temperatures below 1000 K [76, 433-435, 443, 449, 460] and, in several studies [76, 433-435], γ radicals are favored second. The consistency in the trend among alcohols, from ethanol to 1-butanol, to preferentially form α radicals upon reaction with ȮH stems primarily from the C–H bond energy of the α site being the lowest. Although β and γ sites differ from one another only marginally in bond dissociation energy (~1 kcal/mol), for 1-propanol and higher-order alcohols the formation of a stabilizing hydrogen bond in the transition state between the H atom of the abstracting ȮH and the O atom of the –OH group facilitates H-abstraction at the γ site up to ~350 K [469], above which α dominates. In the reaction ethanol + ȮH → $\dot{C}H_2CH_2OH$ + H_2O, similar hydrogen-bonding exists in the transition state for abstraction from β carbon. However, for higher-order alcohols such bonding is stronger in transition states involving γ carbon [469].

Expanding on the site-specific rate coefficient calculations for ȮH + 1-butanol in Galano et al. [469], Moc and Simmie [440] used second-order Møller-Plesset perturbation theory (MP2) with multiple coupled-cluster and correlation-consistent basis sets to calculate energies of transition states and related intermediates on the potential energy surface of ȮH reactions with the TGt conformer of 1-butanol [470], which is the lowest-energy structure. TGt nomenclature in [470] refers to the CC–CC bond in *trans*- conformation, CC–CO in *gauche*- conformation, and CC–OH in *trans*- conformation (**Figure 6a**). Moc and Simmie [440] report hydrogen-bonded transition states in ȮH + 1-butanol, including for abstraction from δ carbon (**Figure 6b**). Galano et al. [469] utilized a single basis set – CCSD(T)/6-311G(*d*,*p*) – and identified hydrogen bonding in all transition states for ȮH + 1-butanol, including for abstraction from the –OH group, yet neglected abstraction from the δ carbon.

(a) 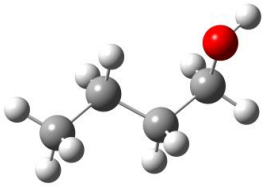 (b) 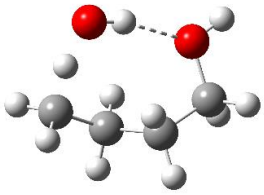

Figure 6. (a) *trans-gauche-trans* (TGt) conformer of 1-butanol from Moc et al. [470]. (b) Transition state for abstraction of δ hydrogen from 1-butanol by ȮH in Moc and Simmie [440] where the hydrogen bonding distance between the H atom of the hydroxyl radical and the O atom of the alcohol group is 1.996 Å.

Barrier heights for ȮH + 1-butanol in Moc and Simmie [440] followed $\alpha < \gamma < \beta < \delta <$ –OH ordering as reported in [76, 433-435]. The order of the barrier heights is different in Galano et al. [469], $\gamma < \beta < \alpha <$ –OH, which may reflect the use of a different basis set considering the range in energy in [440] varied up to 2.3 kcal/mol for the same transition state depending on the use of double-, triple-, or quadruple-ζ basis sets. Since Moc et al. [470] identified fourteen distinct conformers of 1-butanol within a range of 1.86 kcal/mol relative to the TGt conformer adopted in [440], comparison of the results of Galano et al. [469] and Moc and Simmie [440] indicates that the relevance of hydrogen-bonded transition states in H-abstraction reactions from 1-butanol is conformer dependent.

Subsequent to Moc and Simmie [440], Zhou et al. [433] utilized CCSD(T)/cc-PVQZ//MP2/6-311G(*d*,*p*) and G3 methods with variational transition state theory to determine site-specific rate coefficients for ȮH + 1-butanol. The calculations were conducted to differentiate between hydrogen atoms attached to the same carbon and the mechanism of abstraction, which is important due to the asymmetry of 1-butanol. Two types of mechanisms were included: indirect abstraction, which is characterized by a stepwise process involving the formation of a reactant complex in the entrance channel, and direct abstraction, which occurs without the formation of a complex. The differences between the H-atom-specific rates were substantial, particularly for α and γ sites, which are also the most consequential due to large branching fractions (**Figure 7c**).

Figure 7 plots total rate coefficients for ȮH + 1-butanol (**Figure 7a**) and branching fractions in the high-pressure limit. The results from Zhou et al. [433] (**Figure 7b**) were calculated at the G3 level of theory. Seal et al. [434] (**Figure 7c**) utilized M08-HX/MG3S with multi-structural variational transition state theory (MS-VTST) and noted the importance of torsional anharmonicity. McGillen et al. [450] produced Arrhenius parameters for the total *k*(T) of ȮH + 1-butanol from a fit of OH-LIF measurements from 221 – 381 K to shock tube experiments of Pang et al. [471]. Branching fractions in [450] (**Figure 7d**) were determined analytically by iterative parameterization using total rate coefficients and species yields from Cavalli et al. [472] and Hurley et al. [473]. While the temperature dependence of the three *k*(T) trends differ, the computational results from Zhou et al. [433] and Seal et al. [434] are within 50% of the analytical expression of McGillen et al. [450] at 500 K and are within 10% at 1000 K. However, similar to ethanol + ȮH, branching fraction predictions for ȮH + 1-butanol are not consistent. In all cases, α radical formation is favored up to 1000 K and abstraction of the hydroxylic hydrogen is relatively marginal. However, selectivity towards γ and β radicals differs significantly. Zhou et al. [433] predict 35% γ radicals and 5% β

radicals at 500 K and, at 1000 K, 30% and 6%, respectively. The calculations of Seal et al. [434] show negligible temperature dependence: 13% γ radicals and 15% β radicals at 500 K, and both are ~16% at 1000 K. McGillen et al. [450] ~20% of γ radicals and ~18% of β radicals at both 500 K and 1000 K.

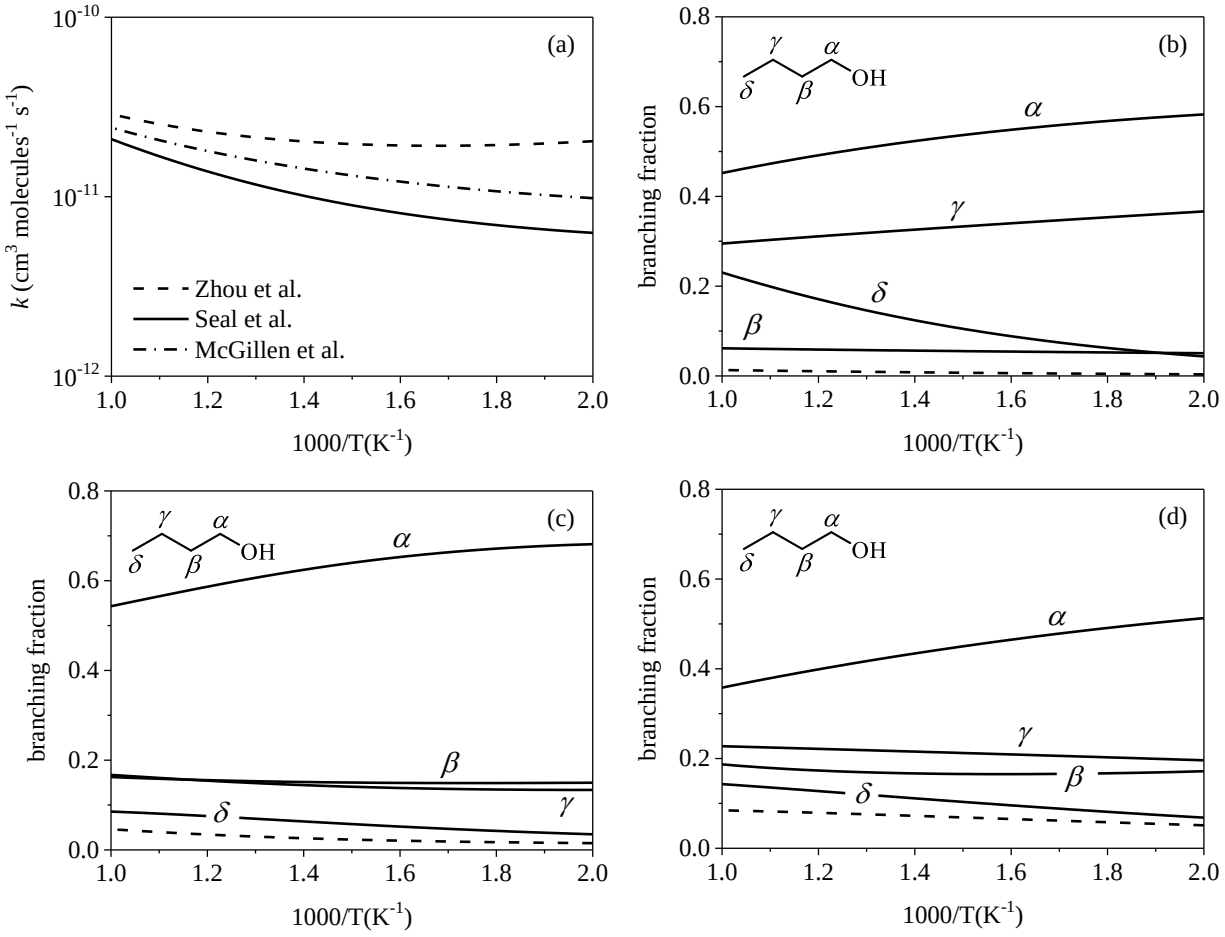

Figure 7. Total rate coefficients (a) and branching fractions for ȮH + 1-butanol from computations of Zhou et al. [433] (b) and Seal et al. [434] (c), and the semi-empirical fit of McGillen et al. [450] (d). The dashed line in (b) – (d) represents branching fractions for abstraction from the –OH group.

Compared to linear alcohols with a terminal –OH functional group, e.g. 1-butanol, few studies relevant to low-temperature oxidation exist for alcohols with non-terminal –OH, e.g. 2-propanol [469] and 2-butanol [451, 474]. Zheng et al. [474] employed canonical variational transition-state theory with small-curvature tunneling to calculate rate coefficients and branching fractions for H-abstraction via ȮH + 2-butanol → Ṙ + H_2O. While some dependence in the branching fractions on computational method was noted, specifically the selection of single or multiple paths in calculation of transmission coefficients, abstraction from (tertiary) α carbon and (secondary) β carbon accounted for 80 – 90% of the radical distribution below 1000 K and primary radicals were negligible. Sime et al. [451] measured total rate coefficients for ȮH + 2-butanol up to ~690 K, as well as for other isomers of butanol.

3.1.1.2. branched alcohols + ȮH

Mellouki et al. [475] measured rate coefficients for reaction of ȮH with *iso*-butanol, *iso*-pentanol, and 3-methyl-2-butanol from 241 – 373 K, which displayed negative temperature dependence similar to reactions of ȮH with linear alcohols [449]. Branching fractions were measured at ~1 atm in McGillen et al. [450, 476] for ȮH + *iso*-butanol from 251 – 340 K [476], where abstraction from α carbon increased with temperature to a branching fraction of nearly 50% at 340 K for all four butanol isomers [450] – 1-butanol, 2-butanol, *iso*-butanol, and *tert*-butanol. In McGillen et al. [450], site-specific rate coefficients were fit analytically over the temperature range 220 – 1800 K by combining pulsed-photolysis measurements of k(T) with prior measurements [447, 448, 471, 477]. The trends for all isomers followed non-Arrhenius behavior ($E_a < 0$), suggesting the formation of a pre-reaction complex. Transition of the total reaction rate coefficient to positive temperature dependence occurred above 600 K and to negative temperature dependence below ~250 K.

Figure 8a compares branching fractions from McGillen et al. [450] for H-abstraction from *tert*-butanol by ȮH via two different mechanisms: β_{direct} and $\beta_{complex}$, which involves a pre-reaction complex. The latter mechanism is relatively insignificant and, in contrast to other alcohols, abstraction of hydroxylic hydrogen contributes to 15 – 20% of the initial radical population of *tert*-butanol. **Figure 8b** compares rate coefficients from McGillen et al. [450], for *iso*-butanol and *tert*-butanol, and from Zheng et al. [478] for *iso*-butanol over the range 500 – 1000 K. The larger k(T) for *iso*-butanol is consistent with the availability of weakly bound hydrogen on both α carbon and on tertiary carbon, as opposed to *tert*-butanol in which only primary C–H bonds exist.

The analytical rate expression from McGillen et al. [450] for the total rate coefficient of ȮH + *iso*-butanol is consistent with the quantum chemical calculations of Zheng et al. [478]. Employing multi-path variational transition-state theory with small-curvature tunneling, Zheng et al. [478] included torsional anharmonicity in the partition function calculations for reactants and transition states using multi-structural methods. The inclusion of anharmonicity along the reaction path significantly affected k(T) and branching fractions compared to the standard approach of scaling harmonic vibrational frequencies. **Figure 8c** plots branching fractions for *iso*-butanol from McGillen et al. [450], which were derived analytically via iterative solution of Arrhenius rate parameters, to total rate coefficients and species yields from Andersen et al. [479], Baxley and Wells [480], and Chew and Atkinson [481]. Similar to ethanol, α radicals are favored, although β and γ radicals combine for ~60% of the branching fraction. Despite agreement on the total rate coefficient in the range 500 – 1000 K, branching fractions computed in Zheng et al. [478] (**Figure 8d**) differ with McGillen et al. [450], mainly in the temperature dependence for α and γ sites. From Zheng et al. [478], α radicals account for ~65%, compared to 50% (500 K) to 40% (1000 K), while γ radicals account for ~10% compared to 15 – 30% from McGillen et al. [450].

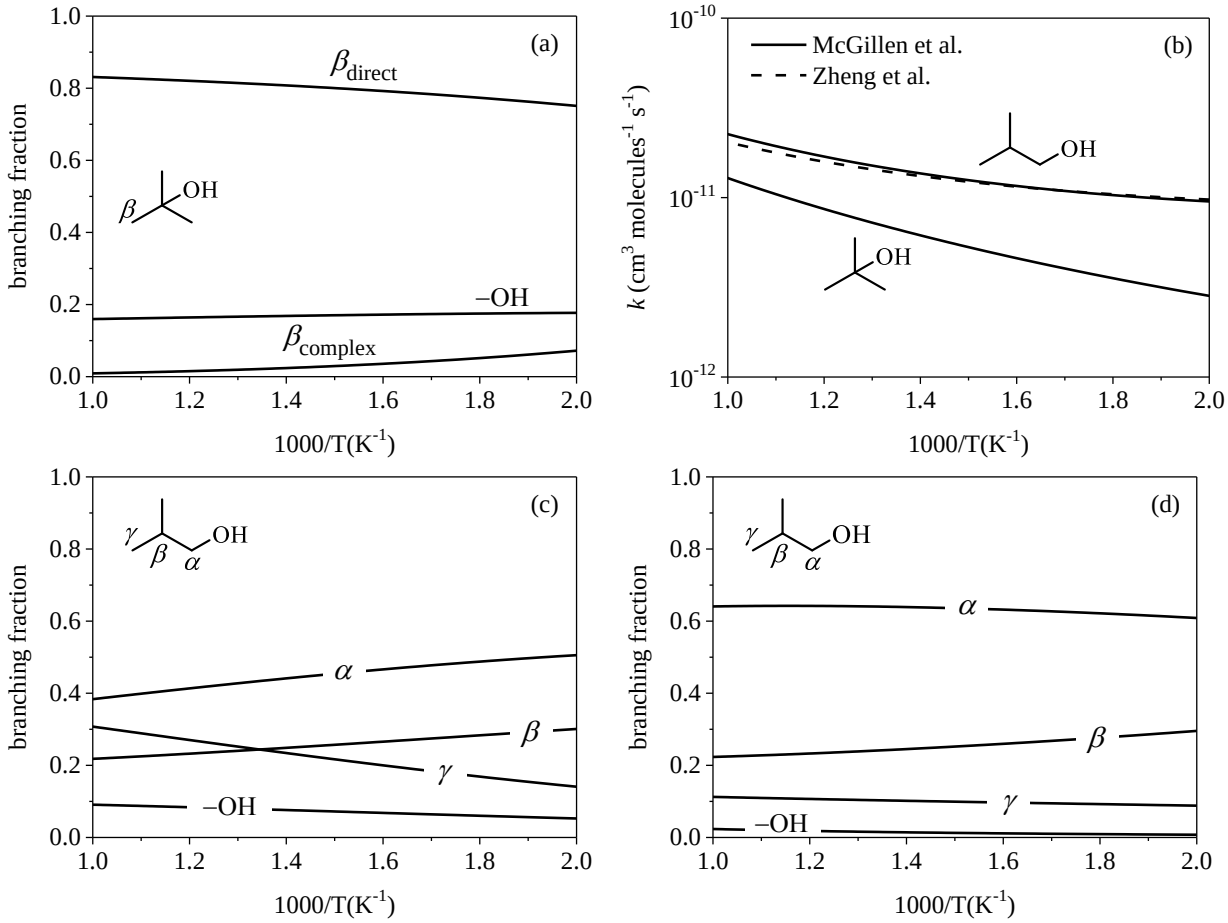

Figure 8. Total rate coefficients (a) and branching fractions for H-abstraction by ȮH from (b) *tert*-butanol (McGillen et al. [450]), (c) *iso*-butanol (McGillen et al. [450]), and (d) *iso*-butanol (Zheng et al. [478]).

Xing et al. [482] utilized multi-path variational transition state theory with small-curvature tunneling (MP-CVT/SCT) to calculate site-specific rate coefficients and branching fractions for ȮH + *iso*-pentanol → H_2O + Ṙ. The effects of several corrections were examined, including re-crossing, tunneling, and multiple structure anharmonicity, the latter of which being most significant. The branching fraction calculations were compared to results from conventional transition state theory, which produced different temperature dependence among the five abstraction channels, with the main impact being the balance between primary (δ) carbon and tertiary (γ) carbon. Branching fractions from α, β, and –OH sites were relatively unaffected. Using the variational method, at 750 K, the branching fractions for δ and γ were ~20% and ~15%, respectively, while conventional transition state theory yielded ~5% and ~30%. Additional comparisons in Xing et al. [482] to branching fractions predicted from chemical kinetics mechanisms of Sarathy et al. [483] and Tsujimura et al. [484], both of which utilized rate rules for prescribing rate parameters, reveal appreciable differences, yet abstraction from α carbon remains favored above 600 K.

3.1.1.3. linear alcohols + HOȮ

Abstraction by HOȮ is significantly less facile than abstraction by ȮH and is dominated by reaction at the α site. Zhao et al. [394] employed conventional and canonical variational transition state theory to calculate

rate coefficients for H-abstraction from ethanol by HOȮ. Potential energy surfaces were calculated using both CCSD(T)/cc-pVTZ//M06-2x/def-TZVP and CCSD(T)/CBS//M06-2x/def-TZVP levels of theory, and rate calculations below 750 K included zero-curvature tunneling corrections. The results using both methods were consistent with one another over the range of temperatures covered (200 – 2000 K). Two motivations for Zhao et al. [75] were (i) to provide rate coefficient calculations for HOȮ + ethanol → Ṙ + H_2O_2 and (ii) to determine the reliability of the using Arrhenius parameters extrapolated from HOȮ + 1-butanol calculated in Zhou et al. [76] in chemical kinetics mechanisms for ethanol. For the latter of the two, ignition delay times were simulated (*vide infra*) with chemical kinetics mechanisms of Curran et al. [485] and Jin et al. [486] using unmodified versions and other versions modified with the coupled cluster calculations.

Pre-reaction complexes were formed in all three abstraction channels in Zhao et al. [75], α, β, and –OH (**Figure 9**), with well-depths of –9.2 kcal/mol, –1.0 kcal/mol, and –9.0 kcal/mol, respectively; the well-depth for the α site is consistent with Zhou et al. [76] for abstraction from α carbon in 1-butanol (–9.3 kcal/mol). The deeper wells for both α and –OH were explained in [75] using independent gradient modeling [487], which revealed hydrogen bonding between the H atom in HOȮ and the O atom in the hydroxyl group with interaction distances of ~1.70 Å (**Figure 9a** and **9c**). For abstraction from β carbon, weaker van der Waals interaction exists between the terminal O atom in HOȮ and an H atom on α carbon (HOO···H ~2.61 Å).

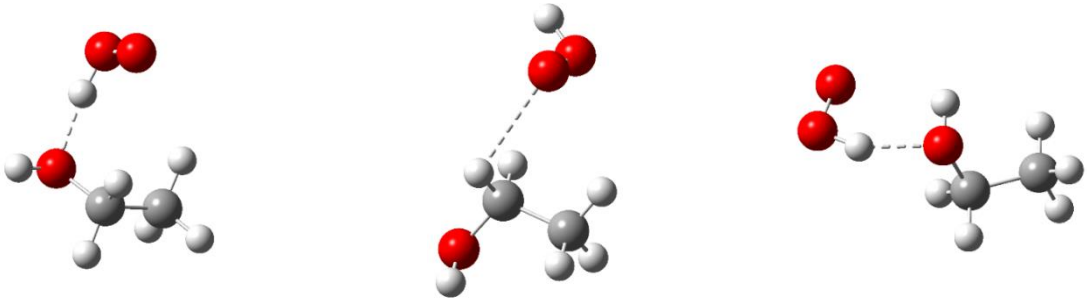

(a) (b) (c)

Figure 9. Pre-reaction complex structures for H-abstraction by HOȮ from (a) α carbon, (b) β carbon, and (c) hydroxy group of ethanol (Zhao et al. [75]).

Total rate coefficients and site-specific Arrhenius parameters were calculated in the high-pressure limit from 200 – 2000 K for each of the three abstraction channels. **Figure 10a** plots $k(T)$ from 500 – 1000 K. As indicated in the branching fractions from Zhao et al. [75] in **Figure 10b**, abstraction from α carbon dominates, whereas from β carbon and from the –OH group abstraction is negligible below 1000 K. At 1500 K, the branching fraction towards α radicals is ~94% and for β radicals is ~5%. The overwhelming selectivity by HOȮ towards α radicals ($CH_3\dot{C}HOH$) is a result of the barrier height being the lowest lying channel on the HOȮ + ethanol surface (by 5.5 kcal/mol). The barrier height to H-abstraction from the –OH group forming the ethoxy radical $CH_3CH_2\dot{O}$ is lower by 3.0 kcal/mol than from β carbon, despite higher bond energy. Distortion/interaction modeling [488], which calculates transition state energy as the sum of strain energy and interaction energy, revealed that while the former is higher for H-abstraction at the hydroxyl group, the interaction energy is significantly higher (~28 kcal/mol) than for abstraction from β

carbon [75]. However, because of hydrogen bonding stabilizing the pre-reaction complex, the overall barrier height for abstraction from the –OH group is higher by 5.0 kcal/mol, which results in abstraction remaining negligible (~1%). Similar to ȮH, Glarborg et al. [464] noted discrepancies among chemical kinetics mechanisms for abstraction reactions of ethanol with HOȮ.

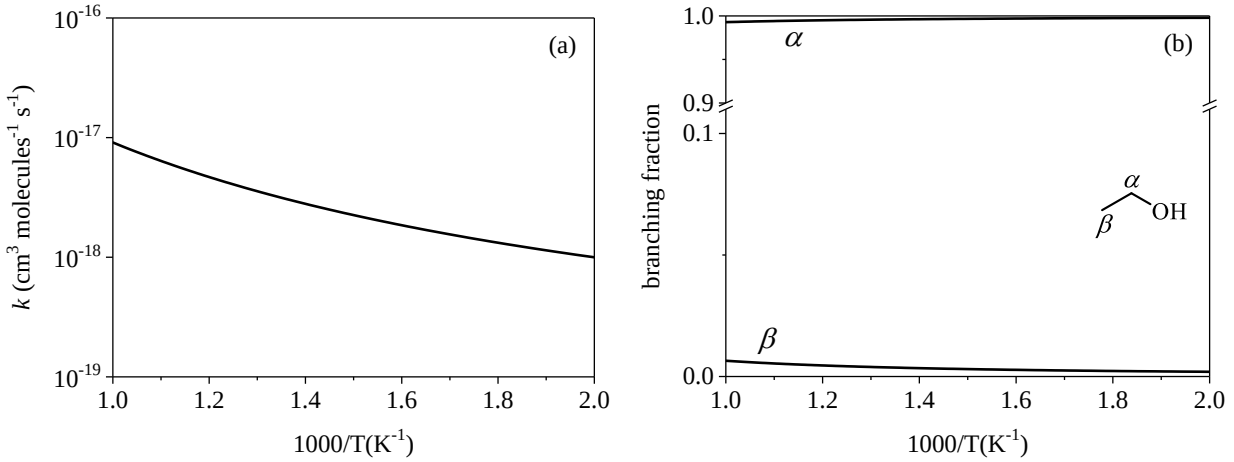

Figure 10. (a) Total rate coefficients and (b) branching fractions of HOȮ + ethanol from Zhao et al. [75] calculated at the CCSD(T)/CBS level of theory. Branching fractions from hydroxy group are <1% and are excluded in (b).

The calculated rate coefficients calculated in Zhao et al. [75] for abstraction from α, β, and –OH sites were compared to analogous rates from Zhou et al. [76] calculated for 1-butanol and to several chemical kinetics mechanisms for ethanol. For abstraction from α carbon, rate coefficients were within uncertainty estimations, which is important given the dominance of the branching fraction indicated in **Figure 10b**. For abstraction from β carbon, the Zhou et al. [76] calculations were also within the uncertainty bands of the coupled cluster calculations for HOȮ + ethanol, while rates from the chemical kinetics mechanisms were higher by up to ~10^2. However, because calculations for ethanol predict consistently that H-abstraction by HOȮ occurs almost exclusively at the α carbon below 1000 K [459, 460, 462, 489, 490], the uncertainties in branching to $\dot{C}H_2CH_2OH$ is likely unimportant for modeling ignition.

Black and Simmie [453] conducted an extensive series of barrier height calculations on the HOȮ + 1-butanol surface, accounting for conformer-specific transition states (10 in total) and the influence of computational method by using a range of DFT functionals and basis sets. Pre- and post-reaction complexes were identified for all cases except for abstraction from δ carbon. Only abstraction from β carbon exhibited H-atom-specific barrier heights, with the lowest in energy (by approximately 2 kcal/mol) being when the H atom being abstracted is in the plane of the –OH group leading to hydrogen-bonding between HOȮ and the –OH group. Such a stabilizing interaction is not present for H atoms that extend away from the –OH group. For all pathways, barrier heights followed the same order as in reactions with ȮH and in the direction of increasing endothermicity: $\alpha < \gamma < \beta < \delta <$ –OH. The lower barrier height of the γ carbon compared to β carbon is ascribed to rotation of the –OH group about the C–O bond in the transition state, which creates a stabilizing effect that facilitates hydrogen bonding with incoming HOȮ and contributes to the difference of 1 kcal/mol. The barrier height to abstraction from δ carbon was nearly identical to that in alkanes.

Abstraction from α carbon by HOȮ occurs with the lowest barrier, by 2.3 kcal/mol, similar to reactions with ȮH [440].

Zhou et al. [76] utilized conventional transition state theory to calculate site-specific rate coefficients and branching fractions for H-abstraction from 1-butanol by HOȮ from 500 – 2000 K. Formation of the α radical, (butan-1-ol-1-yl, $H_3CCH_2CH_2\dot{C}HOH$), remained the dominant pathway over the entire range of temperature and branching fractions remained >0.75 below 1000 K. From 500 – 700 K, branching to γ radicals was favored over β radicals and branching towards α radicals remained above 0.90. Zhou et al. [76] noted differences in branching fractions produced from the rate calculations of Vranckx et al. [435] and suggested torsional anharmonicity treatment and tunneling as potential sources of error.

Site-specific rate coefficients for the α radical were calculated by Alecu et al. [439] and for the γ radical (butan-1-ol-3-yl, $H_3C\dot{C}HCH_2CH_2OH$) by Seal et al. [452] using multi-structural canonical variational transition-state theory with multidimensional small-curvature tunneling (MS-CVT/SCT). Rate coefficients calculated in Zhou et al. [76] overlap remarkably with the results of Alecu et al. [439] for HOȮ + 1-butanol → H_2O_2 + $H_3CCH_2CH_2\dot{C}H$–OH (α radical), yet differ from Seal et al. [452] for HOȮ + 1-butanol → H_2O_2 + $H_3C\dot{C}HCH_2CH_2$–OH (γ radical) by ~10^1 below 1000 K. **Figure 11** plots the total rate coefficient and branching fractions for HOȮ + 1-butanol → H_2O_2 + Ṙ from Zhou et al. [76], which show that abstraction from α carbon is >75% from 500 – 1000 K.

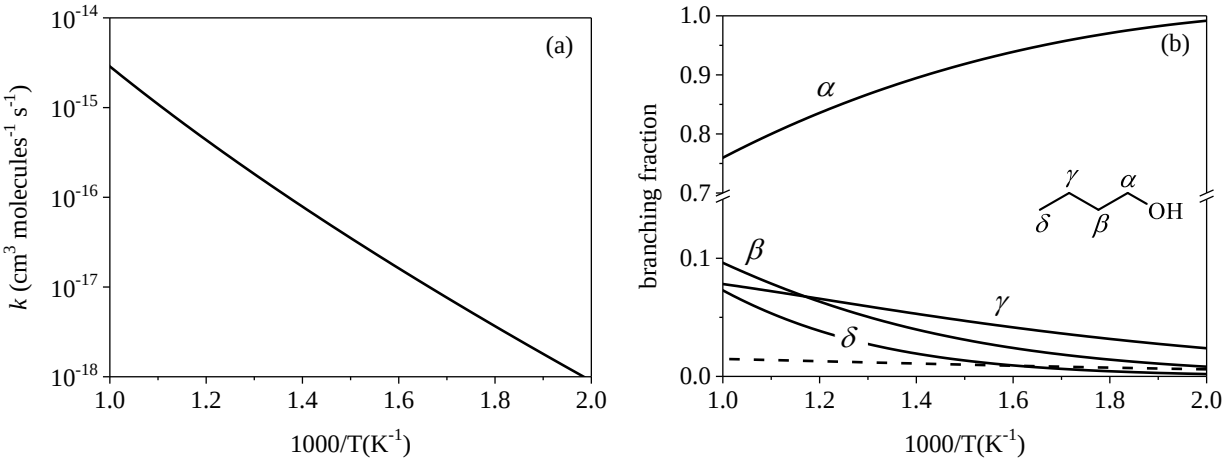

Figure 11. (a) Total and (b) site-specific rate coefficients for H-abstraction from 1-butanol by HOȮ from Zhou et al. [76]. The dashed line in (b) represents branching fractions for abstraction from the –OH group.

Bao et al. [491] calculated rate coefficients in the high-pressure limit for HOȮ + 2-butanol → H_2O_2 + Ṙ using multi-path variational transition state theory (MP-VTST) with small-curvature tunneling approximations for anharmonicity factors. Branching fractions were calculated and were qualitatively similar to 1-butanol in that, below 1000 K, abstraction of α hydrogen accounted for the majority (>80%) of the radical distribution, which creates tertiary radicals in the case of 2-butanol. Abstraction of secondary β hydrogen is the only other significant abstraction site below 1000 K – the other three sites (primary β, primary δ, and –OH) combined for <10%. Bao et al. [491] also conducted comprehensive analysis on the connection between hydrogen bonding in transition states and activation energy for abstraction. Relative

potential energies were calculated for three types of transition states – non-hydrogen bonded, bent hydrogen bonding, and non-bent hydrogen bonding between the H of the HOȮ radical and the O of the –OH group. From Chen et al. [492], a normal hydrogen bond occurs for O–H···O interactions ≤ 2.4 Å and an O–H–O angle ≥150° and a strongly bent hydrogen bond occurs when 90° < θ < 150°. Hydrogen bonding occurred in three of the five transition states – α (tertiary), β (secondary), and γ (primary). One conclusion drawn from the results is that hydrogen bonding lowers activation energies for abstraction by 2 – 3 kcal/mol. However, because of the coupling between stabilization and the reduction in entropy of the transition state, $\Delta S^{\neq}$, and despite lower barrier heights, hydrogen bonding can lead to a decrease in k(T) for cases where entropy is decreased significantly. No significant dependence of potential energy on the O–H–O angle in the transition state was noted.

3.1.1.4. branched alcohols + HOȮ

Parab et al. [493] calculated site-specific high-pressure-limit rate coefficients and branching fractions from 500 – 2000 K using the CBS-QB3 composite method for HOȮ + *iso*-pentanol → H_2O_2 + Ṙ (**Figure 12**). Hydrogen bonding was evident in transition states for H-abstraction from all four sites: α, β, γ, and δ carbon. Similar to reactions with other alcohols, abstraction from α carbon remained the dominant channel [76, 459, 460, 462]. However, in contrast to reactions with other alcohols, rate coefficients on a per-H-atom basis for abstraction from δ carbon, which make up the two methyl groups, are competitive near 750 K. In addition, total rate coefficients for abstraction from δ carbon exceed that for α carbon by nearly 10^1 at 1000 K despite C–H bond dissociation energies at that site being unaffected by the alcohol group. The difference is in part due to stabilization energy in the transition state from hydrogen bonding. Rate coefficients below 1000 K for abstraction from (tertiary) γ carbon were higher than from (secondary) γ carbon in 1-butanol [76]. Stabilization energy in the transition state also impacted abstraction from β carbon, leading to rate coefficients nearly 10^1 higher than for direct abstraction.

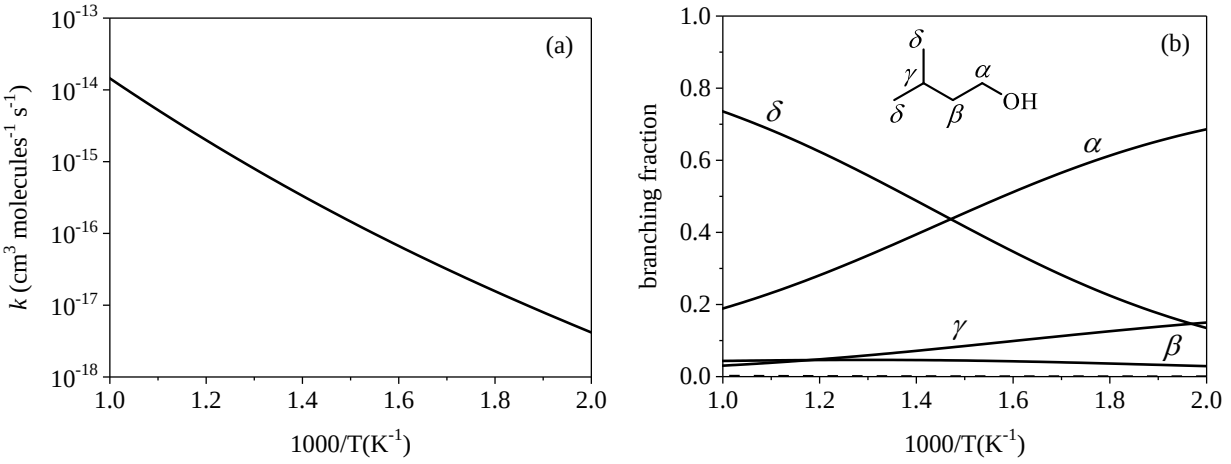

Figure 12. (a) Total and (b) site-specific rate coefficients for H-abstraction from *iso*-pentanol by HOȮ from Parab et al. [493]. The dashed line in (b) represents branching fractions for abstraction from the –OH group.

3.1.1.5. linear alcohols + $\dot{C}H_3$

Abstraction of H atoms from alcohols via reaction with $\dot{C}H_3$ are reported in a relatively limited number of studies: $\dot{C}H_3$ + ethanol [455, 456] and $\dot{C}H_3$ + 1-butanol [457, 458]. **Figure 13a** shows the total rate coefficient for $\dot{C}H_3$ + 1-butanol from 500 – 1000 K, which is similar in magnitude to abstraction by HOȮ shown in **Figure 11a**. Results from conventional and canonical variational transition state theory (CVTST) calculations applied to $\dot{C}H_3 + C_2H_5OH \rightarrow CH_4 + \dot{R}$ indicate that α radicals are favored (45% at 700 K) and abstraction of alcoholic H atoms (i.e. branching towards alkoxy radicals) is less competitive, with a branching fraction of approximately 20% at 700 K [455]. Similar results were reported in rate coefficient measurements of $\dot{C}H_3$ with CH_3CH_2OH, CH_3CD_2OH, and CH_3CH_2OD in Gray and Herod [456]. Transition states in Xu et al. [455] were optimized at the B3LYP/6-311+G(*d*,*p*) level of theory and shared the usual trait that linearity in the reaction coordinate, i.e. the bond angle $X\cdots H\cdots\dot{C}H_3$, is nearly 180° regardless of the abstraction site (X denotes $–CH_3$, $–CH_2–$, or –OH).

Katsikadakos et al. [457] expanded on the work of Xu et al. [455] by conducting a series of barrier height calculations on $\dot{C}H_3$ + 1-butanol at the ROCBS-QB3 level of theory and included conformational effects. Similar to the result of Xu et al. [455] for $\dot{C}H_3$ + ethanol, linearity in the reaction coordinate of $\dot{C}H_3$ + 1-butanol was observed in all of the optimized transition state geometries [457]. Additional calculations confirmed that the barrier height to H-abstraction by $\dot{C}H_3$ follows the order α > OH > γ > β > δ, with conformational differences within 1.5 kcal/mol, which differs from the order of abstraction reactions involving ȮH or HOȮ. Similar selectivity towards α and γ radicals were reported in *ab initio* calculations on H-abstraction reactions from 1-butanol by $\dot{C}H_3$ using conventional transition state theory [458]. Despite, however, the lower barrier height for abstraction from the –OH group, as compared to abstraction from γ, β, or δ sites [457], branching fractions below 1000 K for $\dot{C}H_3$ + 1-butanol $\rightarrow CH_4 + \dot{R}$ favor α and γ radicals (> 70%), β radicals ca. 15%. Abstraction from the δ carbon and from the –OH group are both below 10% (**Figure 13b**).

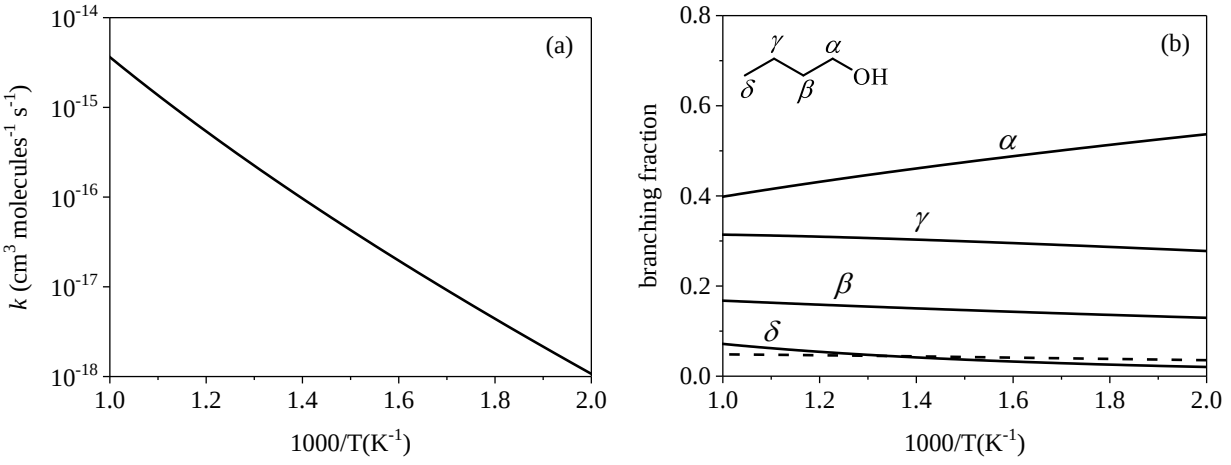

Figure 13. (a) Total rate coefficients for $\dot{C}H_3$ + 1-butanol $\rightarrow CH_4 + \dot{R}$ calculated by Katsikadakos et al. [458] calculated using VariFlex. The dashed line in (b) represents branching fractions for abstraction from the –OH group.

3.1.2. reactions of initial radicals with O_2

The –OH functional group in alcohols favors reaction pathways with O_2 that inhibit chain-branching compared to *n*-alkane oxidation (cf. **Figure 1**). Three pathways in particular are depicted in **Figure 14** using radicals derived from 1-butanol: direct aldehyde + HOȮ formation from α-ṘOH + O_2 (chain-inhibiting, weakly exothermic), **Figure 14a**, a Waddington-type mechanism (chain-propagating, moderately exothermic), **Figure 14b**, and water-elimination from γ-ȮOOH radicals (chain-propagating, strongly exothermic), **Figure 14c** [301]. Subsequent reactions of oxy radicals from the latter species include reaction with O_2 to form dicarbonyl species coincident with HOȮ.

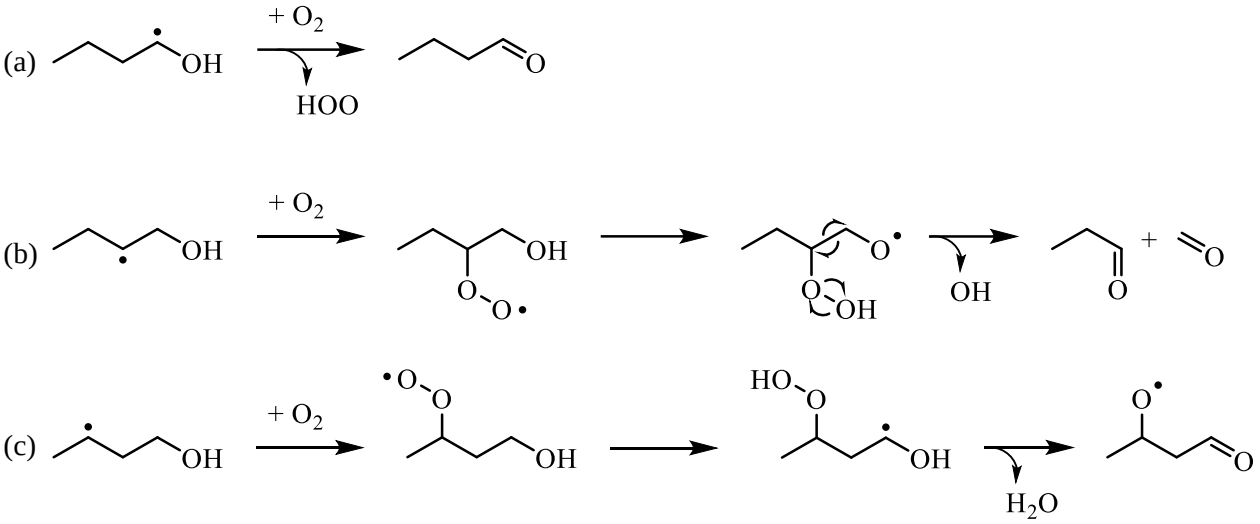

Figure 14. Reaction pathways relevant to low-temperature oxidation of alcohols: (a) direct aldehyde formation from α-ṘOH + O_2; (b) Waddington-type mechanism from β-ṘOH + O_2; (c) water-elimination from γ-ȮOOH [301]. All three reaction pathways disfavor low-temperature chain-branching by inhibiting second-O_2-addition. With increasing alkyl chain length, additional reaction pathways become available that favor ȮOOH formation, which enables chain-branching analogous to alkane oxidation that make long-chain alcohols more prone to autoignition.

The importance of the first pathway (**Figure 14a**) stems from the fact that branching fractions favor α radicals in the initiation step of alcohols, which are responsible for the high yield of aldehydes. Facile H-abstraction from α carbon and subsequent reaction of α-hydroxy radicals with O_2 leads preferentially to aldehyde + HOȮ [295, 296, 494-496] and is weakly dependent on both pressure [497-501] and temperature [500] due to the lack of stabilization of chemically activated α-ROȮ. Although at similar conditions the rate coefficient for H-abstraction at the α carbon by ȮH is ~10^4 higher than abstraction by HOȮ [434, 439], reactions of the latter type are important for predicting alcohol ignition delay times [97, 502-504] because of the tendency of α radicals towards aldehyde + HOȮ as opposed to undergoing chain-branching. Higher concentration of HOȮ therefore compounds aldehyde formation, the pathways of which proceed over lower barriers compared to the analogous reaction in alkanes due to the higher thermodynamic stability of C=O bonds compared to C=C bonds.

Duan et al. [505] calculated rate coefficients for unimolecular reactions of stabilized 1-hydroxy-1-peroxypentyl, the α-ROȮ radical of 1-petnanol, at the CCSD(T)/aug-cc-pVTZ//M06-2X/cc-pVTZ level of theory. Pressure-dependent rate coefficients were calculated using QRRK theory. In total, rate coefficients were calculated for seven reactions to determine the competition between ROȮ → ȮOOH isomerization and HOO-elimination, which yields either pent-1-en-1-ol + HOȮ or pentanal + HOȮ. Rates for the latter reaction were several orders of magnitude higher to the point where isomerization reactions and the enol-forming channels were deemed unimportant.

The second pathway important in low-temperature alcohol oxidation is a Waddington-type mechanism (**Figure 14b**), which is chain-propagating and leads to the formation of two carbonyl intermediates and an ȮH radical [295, 296, 494, 506]. The pathway differs from the conventional Waddington mechanism [507, 508] in that the hydroxyl-peroxy radical is not the result of OH-addition to unsaturated carbon. Instead, O_2-addition to an initial alcohol radical forms the hydroxy-peroxy radical, which then abstracts the hydroxylic H-atom and subsequently decomposes. Li et al. [509] conducted systematic *ab initio* and rate coefficient calculations for isomerization reactions (via 6-membered transition states) of hydroxy-peroxy radicals derived from isomers of butene and of butanol, and subsequent decomposition reactions via the Waddington mechanism. In total, potential energy surfaces were calculated for five unique pathways. All of the isomerization steps, where an oxy radical is produced by abstraction of H from the –OH group by the –OȮ group, were ~25 kcal/mol. Barrier heights for decomposition of the oxy radicals varied depending on molecular structure and were higher for radicals derived from 1-butanol and 2-butanol (~6-7 kcal/mol) than for radicals derived from butene isomers (~3-4 kcal/mol).

The third pathway, water-elimination (**Figure 14c**), arises due to the presence of labile hydrogen on the α carbon, which facilitates ROȮ → ȮOOH isomerization. Using *ab initio* calculations on *iso*-pentanol + O_2 potential energy surfaces, Welz et al. [301] identified a low-lying exothermic water-elimination channel evident in alcohol oxidation, which explained a prior discrepancy in acetone yield in *iso*-pentanol oxidation [295]. The mechanism involves concerted abstraction of the hydroxylic hydrogen by the OH moiety of the hydroperoxy group in ȮOOH and O–O bond-scission and leads to an oxy radical with a carbonyl group and H_2O. The water-elimination channel is potentially specific to alcohols – CBS-QB3 calculations for a similar channel in ketone oxidation (3-pentanone) revealed a barrier height >20 kcal/mol higher in energy [299].

The sections below review MPIMS experiments and *ab initio* calculations on alcohol oxidation, namely 1-butanol [296], *iso*-butanol [494], *iso*-pentanol [295], prenol and *iso*-prenol [506]. No MPIMS studies exist for 2-butanol oxidation despite other experimental and modeling studies [441, 447, 474, 491, 510-515]. Similarly for 1-pentanol [437, 495, 516].

3.1.2.1. reactions of initial radicals from primary alcohols with O_2

Welz et al. [296] conducted chlorine atom-initiated oxidation experiments of 1-butanol up to 700 K using MPIMS and calculated stationary point energies on the four Ṙ + O_2 potential energy surfaces using CBS-QB3. Deuterated isotopologues 1-butanol-1,1-d_2 and 1-butanol-4,4,4-d_3 were also employed to confirm reaction mechanisms postulated from the undeuterated 1-butanol experiments. The main emphasis in [296] was the determination of initial radical-specific oxidation pathways inferred from isomer-resolved photoionization spectra. Several species were quantified, including HOO-elimination products (butanal and

2-buten-1-ol) and carbonyls formed via C–C and/or C–O β-scission (e.g. propanal, acetaldehyde, and formaldehyde).

Despite energetically competitive pathways on the surfaces of β-, γ-, and δ-ROȮ radicals, none of the six possible cyclic ethers (**Figure 15**) were detected due either to low ionization efficiency or substantial dissociative ionization. In some cases, fragment ions provided indirect evidence. For example, appearance energy calculations in [296] for the ionization of 2-hydroxy-4-methyloxetane indicated that the cation undergoes facile ring-opening to yield (neutral) formic acid and propene cation $[C_3H_6]^+$, the latter of which was quantified in the experiments.

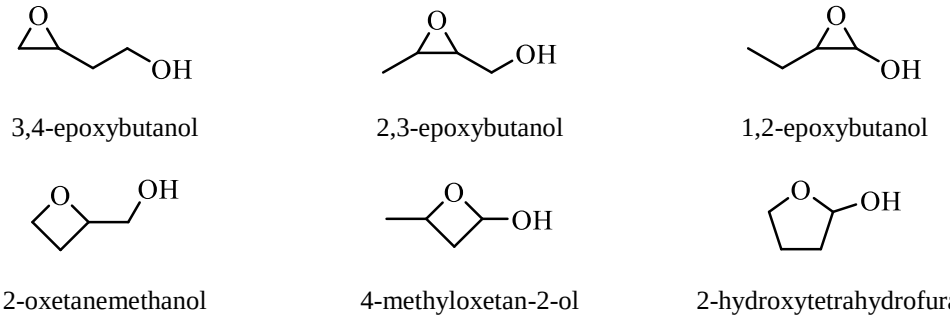

Figure 15. Molecular structure of cyclic ethers possible via ȮOOH-mediated reactions of 1-butanol.

To complement the ionization calculations in Welz et al. [296] and examine the propensity for poor Franck-Condon overlap and dissociative ionization, geometry optimization calculations were conducted at the CBS-QB3 level for the present review on two representative cyclic ethers: 2-hydroxy-4-methyloxetane and 2-oxetanemethanol (**Figure 16**). In both cases, significant geometry changes in the cation are evident. For 2-hydroxy-4-methyloxetane, the C–O bond distance of the ether group increases from 1.439 to 2.122 Å (**Figure 16a**). The cationic state is bound, yet the Franck-Condon overlap likely diminishes significantly due to the large geometry change. Ionization of 2-oxetanemethanol (**Figure 16b**) increases the length of the C–C bond adjacent to the ether group from 1.516 to 1.750 Å, which causes dissociation into a fragment ion and a neutral fragment. Transient ion signal in the experiments of Welz et al. [296] was not detected at the mass of the smaller fragment in **Figure 16b**, CH_2OH (*m/z* 31). However, signal at *m/z* 57 (C_3H_5O) was detected, which may indicate evidence of 2-oxetanemethanol formation.

neutral (a) neutral (b)

Figure 16. Molecular structure of neutral and cations of cyclic ethers from 1-butanol oxidation. For certain species, photoionization leads to (a) poor Franck-Condon overlap or (b) dissociative ionization, which inhibits or in some cases precludes experimental detection. (a) 2-hydroxy-4-methyloxetane. (b) 2-oxetanemethanol.

Because of the direct connection to ȮOOH radicals, closed-shell intermediates, and cyclic ethers in particular, often provide the most direct means of inferring reaction pathways. **Figure 17** shows the potential energy surface for δ-ROȮ in 1-butanol from which four pathways are possible: direct HOO-elimination and three ȮOOH-mediated pathways. The formation of but-3-en-1-ol is a minor channel, with yields ~1% [296]. Because the barrier heights between the ȮH-forming pathways calculated in Welz et al. [296] differ by only 3 kcal/mol, and are within the uncertainty of the theoretical method [517, 518], direct speciation measurements of 4-hydroxybutanal and 2-hydroxytetrahydrofuran are necessary – as are measurements for similar closed-shell intermediates for other ROȮ radicals of 1-butanol – to validating theoretical calculations of ȮOOH decomposition rates.

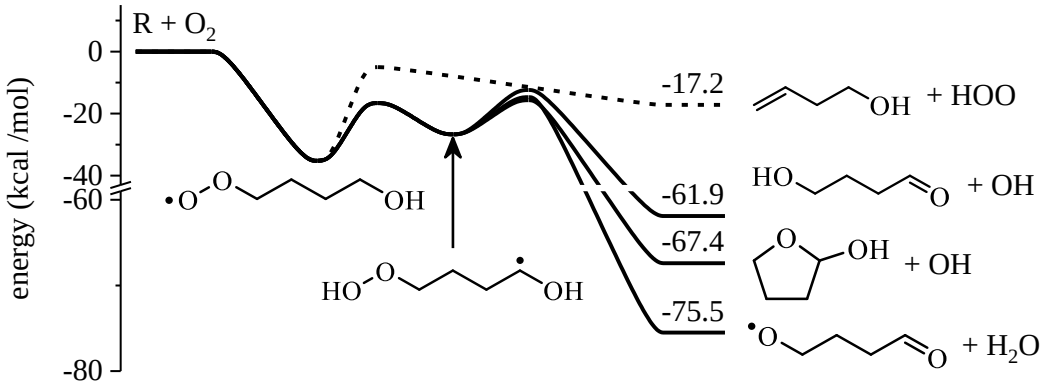

Figure 17. Zero-point-corrected electronic energies for δ-ȮOOH formation and decomposition in 1-butanol oxidation calculated at the CBS-QB3 level of theory [296]. Barrier heights: 4-hydroxybutanal + ȮH (E_a = 14.3 kcal/mol), 2-hydroxytetrahydrofuran + ȮH (E_a = 11.0 kcal/mol), 4-oxybutanal via water-elimination (E_a = 12.0 kcal/mol).

Employing partially deuterated isotopologues of 1-butanol confirmed that propanal is formed with the carbonyl group on the β carbon in 1-butanol, as expected both from the Waddington and water-elimination mechanisms (**Figure 18**). Although no direct evidence of water-elimination was reported, the formation of

$[CH_3]^+$ cation via photoionization of vinoxy radical, a co-product of 3-oxybutanal [296], provided indirect evidence.

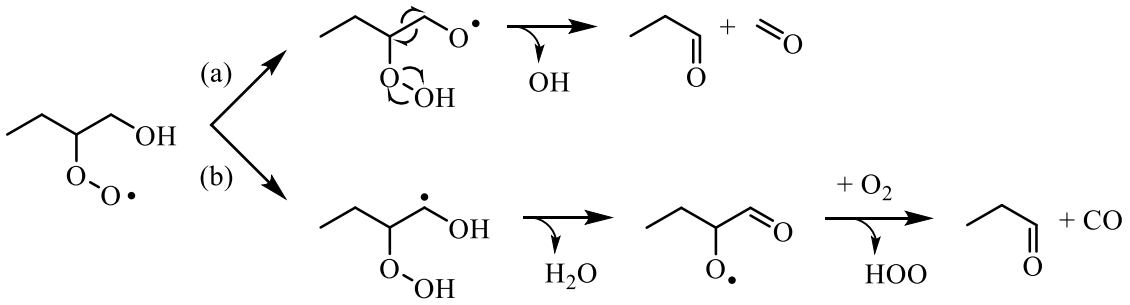

Figure 18. Formation of propanal from 1-butanol oxidation in Welz et al. [296] via (a) Waddington mechanism and (b) water-elimination mechanism.

The complexity of 1-butanol oxidation is evident from the PES calculations in Welz et al. [296]. The water-elimination channel, which requires peroxy radical formation, is available in three of the four initial radicals (*β*, *γ*, and *δ*). ROȮ formation is not possible for *α* radicals because of the inability to form a stabilized adduct. In each of the three water-elimination pathways, ȮOOH intermediates may traverse several decomposition pathways and barrier heights for the various channels are within 2 kcal/mol, with the exception of *γ*-ȮOOH for which the water-elimination channel is the lowest (by 6.8 kcal/mol), followed by 3-hydroxybutanal + ȮH and 4-methyloxetan-2-ol + ȮH, then *β*-scission into acetaldehyde + vinyl alcohol + ȮH (**Figure 19**). Because direct detection of water-elimination products is difficult, since the quantification of oxy radicals is required, direct measurements of the other ȮOOH decomposition products are necessary.

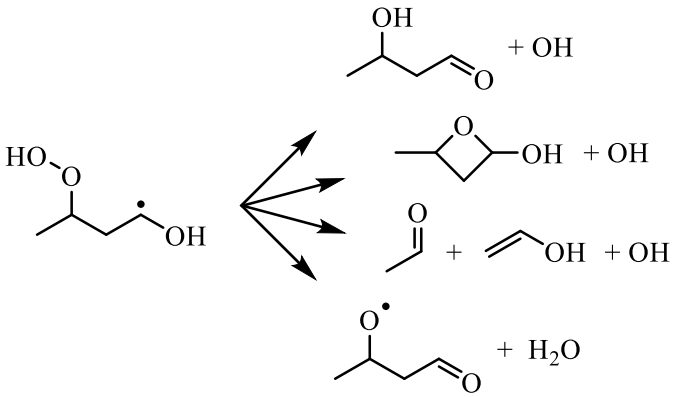

Figure 19. Decomposition pathways of a *γ*-ȮOOH isomer derived from 1-butanol.

3.1.2.2. reactions of initial radicals from branched alcohols with O_2

Welz et al. [494] conducted photoionization mass spectrometry experiments from 550 – 700 K to measure products from Ṙ + O_2 reactions of *iso*-butanol. Of the three HOO-elimination products – methylpropanal, 2-methyl-2-propen-1-ol, and 2-methyl-1-propen-1-ol – the latter two were minor, accounting for ~5% and ~1%, respectively; methylpropanal + HOȮ forms exclusively via reactions of *α* radicals $(CH_3)_2$CHĊHOH

with O_2. Other reactions that consume ȮOOH and inhibit second-O_2-addition were confirmed, including acetone + formaldehyde + ȮH (from β-ROȮ via the Waddington mechanism) and C–C β-scission of γ-ROȮ into propene + hydroxymethyl. Two Waddington channels are possible in *iso*-butanol oxidation, one from β-ROȮ and the other from γ-ROȮ. Based on the higher acetone yield relative to the two HOO-elimination products from β-ROȮ radicals (2-methyl-2-propen-1-ol and 2-methyl-1-propen-1-ol), Welz et al. [494] concluded that the Waddington mechanism (**Figure 20**) is the dominant pathway for *iso*-butanol, which is consistent with the predictions of Sun et al. [519]. Similar rationale, based on formaldehyde yield, led to the conclusion that γ-ROȮ radicals from *iso*-butanol favor reaction via the Waddington mechanism over HOO-elimination. Analogous conclusions were drawn for *iso*-pentanol oxidation in Welz et al. [295], where Waddington channels produced species such as *iso*-butyraldehyde + formaldehyde (from β-ROȮ) as well as 2,2,-dimethyloxirane + formaldehyde and acetone + ethenol (from γ-ROȮ). In contrast, as noted in [494], the results highlight an important difference between oxidation of alcohols and alkanes, noting that the corresponding alkane reaction, *tert*-butyl + O_2, undergoes HOO-elimination almost exclusively [520]. The main difference is that the alcohol functional group promotes chain-propagating pathways via Waddington pathways during low-temperature oxidation, whereas alkanes favor chain-inhibiting, HOȮ-yielding pathways.

Goldman et al. [501] computed stationary points on potential energy surfaces for O_2-addition to *iso*-butanol radicals using coupled cluster methods. Pressure-dependent rate coefficients were calculated using microcanonical master equation analysis. Reaction flux of products from chemically activated Ṙ + O_2 and collisionally stabilized ROȮ radicals were modeled up to 100 atm and up to 1200 K. High-pressure limit rate coefficients for reactions of the β peroxy isomer (2-peroxy-2-methylpropan-1-ol) were within an order of magnitude of Lizardo-Huerta et al. [521], in which an extensive series of rate calculations were conducted on unimolecular reactions of β-ROȮ and β-ȮOOH radicals of branched and linear alcohols. Discrepancies with Sun et al. [519] were noted and ascribed in Goldman et al. [501] to differences in barrier heights and partition function calculations.

All three radical isomers of *iso*-butanol – α, β, and γ (cf. **Figure 8b**) – were included in Goldman et al. [501]. Reactions of the α radical with O_2 led exclusively to *iso*-butanal + HOȮ through both chemical activation and stabilized ROȮ routes. Collisional stabilization for O_2-addition to the α carbon occurred only above ~50 atm and only below 500 K, indicating that at combustion conditions only the chain-inhibiting pathway is relevant. Reaction of O_2 with the β radical, at pressures above 1 atm, led mainly to collisionally stabilized β-ROȮ from 500 – 1000 K, above which HOO-elimination became competitive (forming propen-2-ol as a co-product). Dissociation back into Ṙ + O_2 dominated the flux of stabilized β-ROȮ, which indicated that partial equilibrium may exist and that secondary products govern the net flux of oxidation of the β radical. In particular, two product pairs were identified: 3,3-dimethyloxiran-2-ol + ȮH and acetone + CH_2O + ȮH via the Waddington mechanism. Reactions of O_2 with the γ radical were more complex. Collisional stabilization of γ-ROȮ is favored up to ~900 K at pressures higher than 1 atm. Above 900 K, and up to ~25 atm, approximately 40% of the reaction flux proceeded via a well-skipping mechanism through water-elimination forming 2-methoxypropanal + H_2O. Two competing channels dominate unimolecular reaction of collisionally stabilized γ-ROȮ above 500 K: back dissociation and water-elimination. For all three radicals, the lack of significant ȮOOH formation inhibits the second-O_2-addition step that is required for low-temperature chain-branching.

In *iso*-pentanol oxidation [295], Waddington mechanisms occurred via 6-, 7-, and 8-membered transition states. The latter two were confirmed by detection of 2,2-dimethyloxirane, which forms from both γ-ROȮ and δ-ROȮ. β-ROȮ radicals yield *iso*-butanal + HOȮ via the Waddington mechanism through a 6-membered transition state. Cyclic ethers were not detected in *iso*-butanol or in *iso*-pentanol oxidation because of low ionization efficiency [295, 296, 494, 497], which may result from poor Franck-Condon overlap, dissociative ionization, or from facile cation isomerization and subsequent fragmentation into other species [522]. Oxidation experiments were also conducted on *tert*-butanol in Welz et al. [494]. The Waddington mechanism from β-ROȮ led to acetone + CH_2O + ȮH, which were the most abundant products detected. Unimolecular decomposition of initial radicals of *tert*-butanol, forming acetone + $\dot{C}H_3$, became competitive with O_2-addition reactions above 550 K, consistent with Fittschen et al. [523].

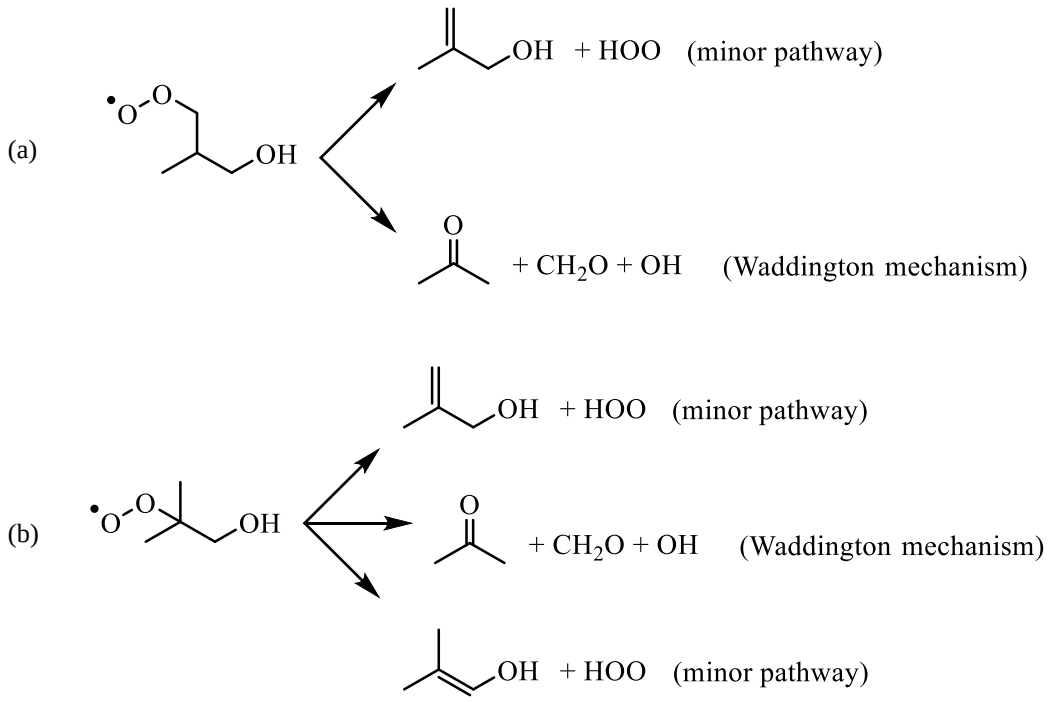

Figure 20. Product formation from branched alcohols via the Waddington mechanism is favored over HOO-elimination. (a) γ-ROȮ and (b) β-ROȮ pathways in *iso*-butanol oxidation [494].

3.1.2.3. reactions of initial radicals from unsaturated alcohols with O_2

In contrast to saturated linear and branched alcohols, experimental and modeling studies focusing on low-temperature oxidation mechanisms of unsaturated alcohols are practically nonexistent. Two exceptions are the studies on prenol and *iso*-prenol of Welz et al. [506], in which Cl-initiated oxidation experiments were conducted using photoionization mass spectrometry (MPIMS). The results were compared with previous MPIMS results on *iso*-pentanol [295]. Principal differences in unsaturated alcohol oxidation were the Waddington-type mechanism becoming a minor channel, the dominance of HOȮ-formation channels, and an increased importance of radical-radical reactions due to resonance-stabilization of the initial radicals. Primary products detected in Welz et al. [506] were aldehydes formed via HOȮ-elimination involving α

carbon: prenal (3-methyl-2-butenal) formed in prenol oxidation and *iso*-prenal (3-methyl-3-butenal) formed in *iso*-prenol oxidation. Similar to low-temperature oxidation chemistry of saturated alcohols, the two unsaturated alcohols also disfavor chain-branching pathways and no cyclic ethers were detected.

3.1.3. speciation from thermally initiated experiments

Speciation measurements from steady state flow reactors conducted on alcohol biofuels include ethanol [461, 464, 524], 1-butanol [525, 526], 2-butanol [512], *iso*-butanol [512], 1-pentanol [495, 526], 3-pentanol [527], 2-methyl-1-butanol [528], *iso*-pentanol [483, 529], 1-hexanol [526], and unsaturated alcohols prenol and *iso*-prenol [530].

Haas et al. [524] measured stable species from ethanol oxidation under lean conditions (ϕ = 0.43 and 0.91) at 12.5 atm and temperatures ranging from 523 – 903 K. Product formation began at ~650 K and exhibited no two-stage reactivity under the conditions examined. Formaldehyde, acetaldehyde, and ethene were major intermediates. Leplat et al. [461] employed a jet-stirred reactor to measure products from ethanol oxidation at 1 atm from 890 – 1250 K over a range of equivalence ratios. Decomposition of methoxy, formed via $\dot{C}H_3 + HO\dot{O} \rightarrow CH_3\dot{O} + \dot{O}H$, was postulated as a primary source of formaldehyde, accounting for ~60%. Glarborg et al. [464] measured species profiles from high-pressure oxidation of ethanol in a laminar flow reactor at 50 atm from 600 – 900 K and reported similar species as Haas et al. [524] and Leplat et al. [461], namely carbonyls, CO, CO_2, and H_2O.

Togbé et al. [512] conducted JSR experiments on 2-butanol and *iso*-butanol at 10 atm and compared mole fraction measurements of intermediates to 1-butanol measurements from Dagaut et al. [525]. Despite the similarity in depletion profiles of the three alcohols (**Figure 21a**), isomer-dependent selectivity in the types and amounts of aldehydes formed during oxidation was reported. **Figure 21b** and **Figure 21c** compare formaldehyde and acetaldehyde mole fractions, respectively. The differences between the production of both carbonyls are primarily below 1000 K, indicating that the details of ȮOOH-mediated chemistry and Waddington mechanisms vary appreciably depending on the location of the –OH group on the alcohol.

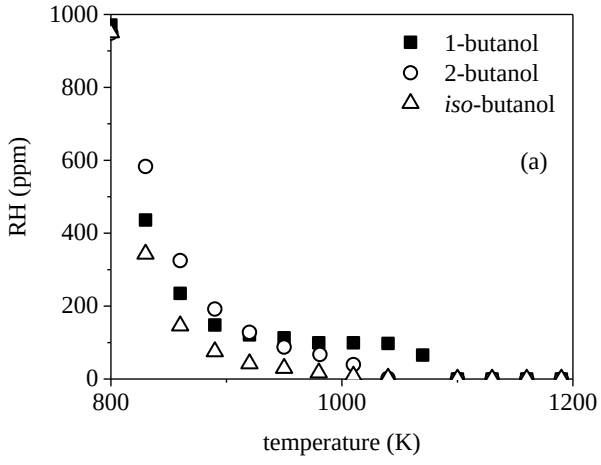

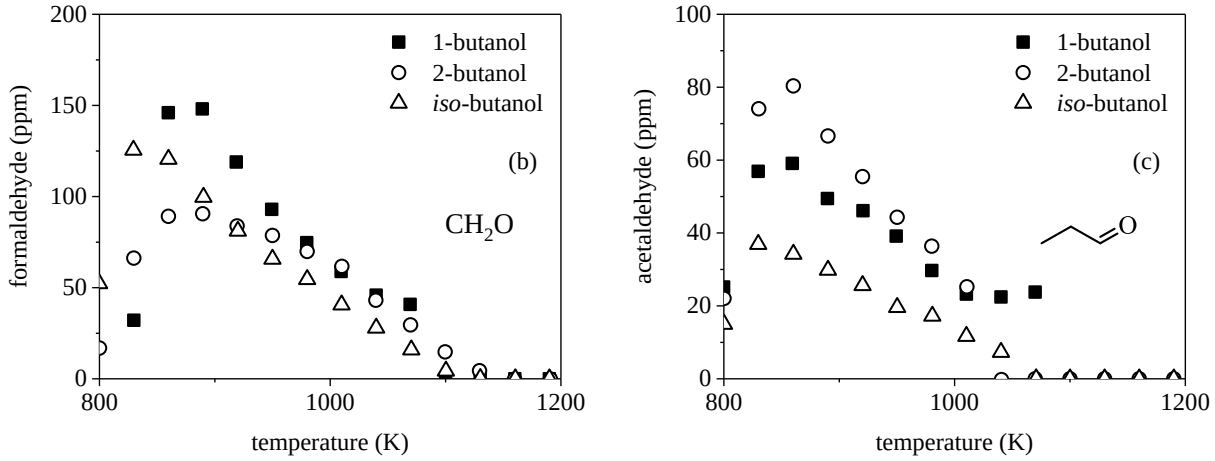

Figure 21. Species profile measurements of stoichiometric oxidation of butanol isomers in a JSR at 10 atm and a residence time of 700 ms (Togbé et al. [512]). Despite similar consumption rates in (a), intermediates are dependent on molecular structure of the parent alcohol (b and c).

Togbé [495] measured species profiles at 10 atm from 1-pentanol oxidation using a JSR. Other than pentanal, formed via oxidation of pentan-1-ol-1-yl radicals, no other low-temperature species were reported. Mole fractions were quantified for 1-pentene, which may arise from C–O β-scission of pentan-1-ol-2-yl radicals. Carbonnier et al. [527] measured species profiles from 3-pentanol oxidation at 10 atm in a JSR. Similar to 1-pentanol, the species profiles in [527] did not exhibit two-stage chemistry; both [495] and [527] utilized the same JSR and residence time of 700 ms. Common species such as water, ethene, CO, and CO_2, and were measured along with typical aldehydes (CH_2O, acetaldehyde, and propanal). With the exception of pentanal, formed via HOO-elimination from α radicals, no other species directly related to peroxy radicals, such as pent-1-en-3-ol from HOO-elimination in γ radicals of cyclic ethers, were measured.

Jet-stirred reactor experiments were conducted on *iso*-pentanol in Dayma et al. [529] and in Sarathy et al. [483]. Dayma et al. [529] measured species profiles at 10 atm and from 530 – 1220 K. Intermediate species predominantly from β-scission reactions, including propene, acetaldehyde, *iso*-butene, and *iso*-pentene, and *iso*-pentanal were quantified. However, cyclic ethers species were not. Similar species profiles were measured in Sarathy et al. [483] at 5 atm over the same range of temperature as [529]. Both studies are consistent with the low-pressure MPIMS experiments of Welz et al. [295, 494] on the selectivity of branched alcohols towards forming aldehydes via concerted HOȮ-elimination from ROȮ and via the Waddington mechanism.

Similar to *iso*-pentanol [483, 529], species profiles measured for 2-methylbutanol oxidation in the jet-stirred reactor experiments of Serinyel et al. [528] at 10 atm and from 700 – 1200 K did not exhibit two-stage chemistry. Product formation was largely ascribed to β-scission reactions and aldehyde + HOȮ formation via concerted reaction of α radicals with O_2. Mole fractions of several species measured in 2-methylbutanol oxidation were compared to *iso*-pentanol (i.e. 3-methylbutanol) to assess the influence of the methyl branch location on reaction pathways. The comparison revealed that the depletion profiles of both alcohols are similar except from 800 – 900 K where 2-methylbutanol consumption is slightly higher (**Figure 22a**). Mole fraction profiles from intermediate species differed substantially between the two $C_5H_{11}OH$ isomers, which

is akin to the comparison for 2-butanol and *iso*-butanol at 10 atm in Togbé et al. [512]. **Figure 22b** compares the mole fractions of methacrolein as an example. The main pathway to methacrolein from 2-methylbutanol is H-abstraction from 2-methylbutanal forming 2-methyl-butan-1-al-2-yl, which decomposes via C–C β-scission [528]; 2-methylbutanal is produced by HOO-elimination from the initial α radical of 2-methylbutanol. In contrast, pathways to methacrolein in *iso*-pentanol are indirectly related to initial peroxy radicals.

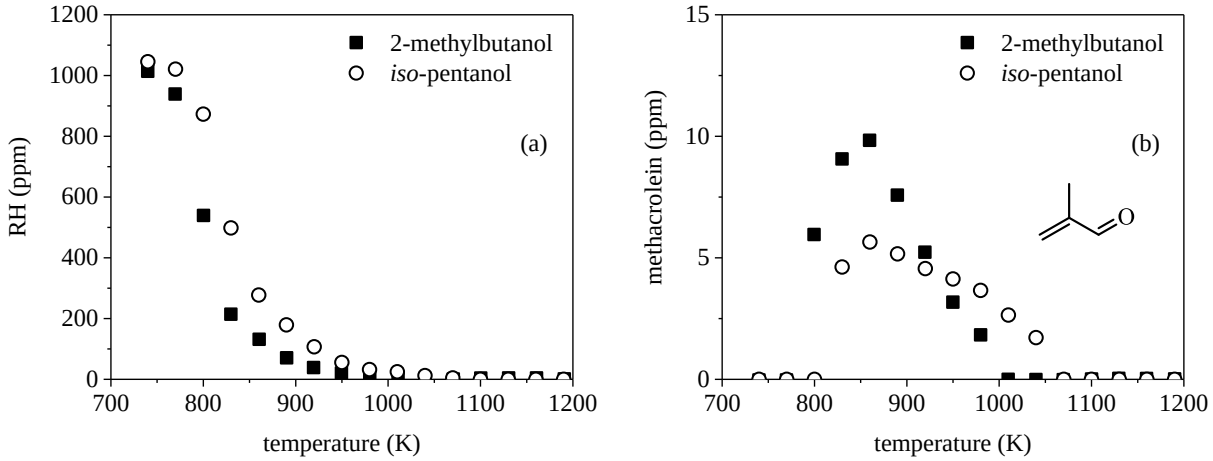

Figure 22. Comparison of (a) depletion profiles at a residence time of 700 ms from stoichiometric oxidation of 2-methylbutanol [528] and *iso*-pentanol [529] at 10 atm and (b) methacrolein species profiles.

Speciation measurements conducted on prenol and *iso*-prenol oxidation from 500 – 1100 K in a jet-stirred reactor at 1 atm revealed no two-stage chemistry in either species [530], consistent with conclusions in Welz et al. [506] in that the dominant oxidation pathways lead to prenal/*iso*-prenal + HOȮ. Oxidation products of *iso*-prenol measured in De Bruycker et al. [530] were largely ascribed to secondary reactions of *iso*-butene and formaldehyde formed directly via unimolecular decomposition of *iso*-prenol; no products from O_2-addition to initial radicals of *iso*-prenol (e.g. 3-methyl-1,3-butadienol formed coincident with HOȮ via a chain-inhibiting step) were reported. In prenol oxidation, however, 3-methyl-2-butenal (formed via HOȮ-elimination involving α carbon) was a major product and displayed maxima at 675 K and 800 K despite no evident two-stage depletion [530], indicating that the location of the C=C bond in the branched alcohol influenced product formation via $\dot{R} + O_2$.

3.1.4. influence of alcohol oxidation pathways on autoignition chemistry

The tendency of alcohol oxidation at low temperatures to primarily follow chain-inhibiting pathways, namely α-$\dot{R} + O_2 \rightarrow$ aldehyde + HOȮ, and chain-propagation pathways including the Waddington mechanism, effectively reduces the role of second-O_2-addition reactions and subsequent chain-branching. The net effect on autoignition chemistry is a diminishing of NTC behavior relative to the analogous *n*-alkane, which is evident in alcohols up to 1-butanol. NTC behavior is not observed in experimental ignition delay times of ethanol [372, 504, 531, 532] and is weak in 1-butanol [366], in contrast to *n*-alkane behavior where two-stage ignition chemistry is exhibited in propane oxidation [533-537]. Ignition measurements below 1000 K are not available for propanol isomers, while 1-pentanol exhibits clear NTC behavior [98]. Yang et al. [538] reported shock tube ignition delay time measurements from 1050 – 1800 K of propanol

isomers and propane. Over the range of temperatures covered, 1-propanol ignition delay times were shorter than those of propane by a factor of ~3. The sections below review ignition delay times measurements and chemical kinetics modeling of alcohol biofuels from ethanol up to 1-octanol.

3.1.4.1. ignition delay time measurements

Ignition delay time measurements of alcohols using both shock tubes and rapid compression machines are reported for methanol [539, 540], ethanol [372, 485, 489, 490, 504, 526, 531, 541, 542], propanol isomers [526, 543], butanol isomers [366, 435, 503, 526, 544-546], pentanol isomers [98, 526, 527], prenol isomers [547], 1-hexanol [98], 1-octanol [548], and cyclopentanol [549]. Experiments measuring ignition delay times of ethanol below 1000 K include Heufer et al. [531], Lee et al. [490], Mittal et al. [504], Wooldridge et al. [372], Cancino et al. [489], and Toulson et al. [550]. In all cases, ethanol exhibits single-stage ignition chemistry. Weber et al. [97] measured ignition delay times for 1-butanol using RCM experiments at 15 atm and 30 atm from 675 – 925 K. In subsequent experiments, Weber and Sung [545] conducted ignition measurements of 2-butanol, *iso*-butanol, and *tert*-butanol using an RCM at 15 atm and 30 atm over the temperature range 715 – 910 K. Within experimental uncertainty, ignition delay times of the three butanol isomers were nearly identical at 15 atm while ignition times for 1-butanol were shorter by more than a factor of 10 below 775 K. The results were similar at 30 atm, in that 1-butanol times were significantly shorter, yet 2-butanol and *tert*-butanol were distinct from *iso*-butanol and the latter species exhibited the longest ignition delay times. For either pressure, none of the butanol isomers exhibited NTC behavior. To compare with the corresponding *n*-alkane, **Figure 23a** plots ignition delay times of *n*-butane from Healy et al. [96] to 1-butanol from Vranckx et al. [435] and butanol isomers from Weber and Sung [545], and **Figure 23b** plots stoichiometric *iso*-butanol ignition delay times at 15 atm from Weber and Sung [545] to *iso*-butane from Gersen et al. [551]. In both comparisons, ignition delay times at lower temperature are significantly shorter for alkane species than the analogous alcohol.

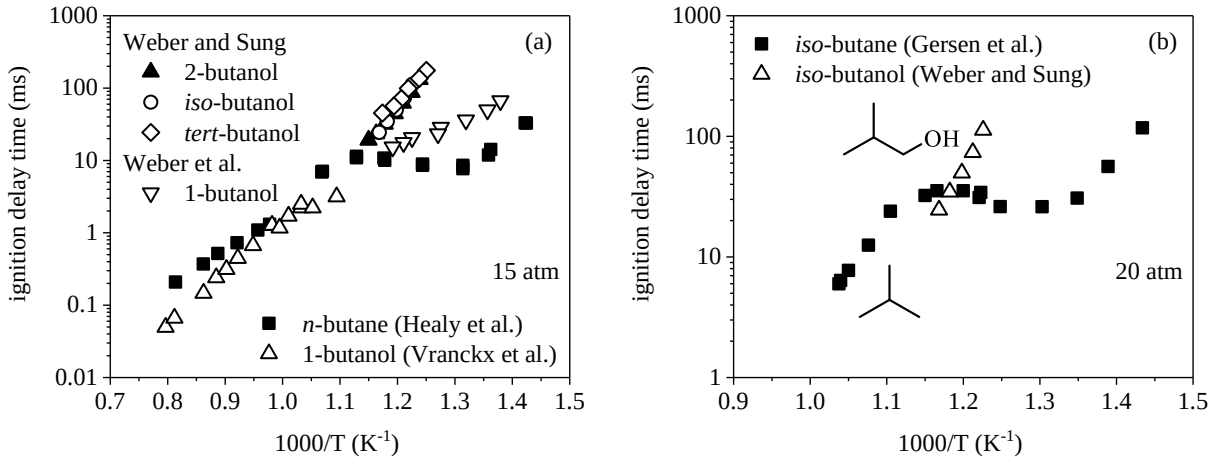

Figure 23. Stoichiometric ignition delay times. (a) isomers of butanol (15 atm) [97, 435, 545] compared with *n*-butane (20 atm) [96]. (b) *iso*-butanol [545] and *iso*-butane [551] at 15 atm.

Heufer et al. [98] measured 30-atm non-dilute ignition delay time trends of 1-butanol, 1-pentanol, and 1-hexanol and compared the results to *n*-alkanes with the same carbon number. Ignition delay times of the alcohols were shorter in the high-temperature region (> 950 K), likely due to more-facile C–C bond

scission. However, below 750 K, ignition times were significantly longer compared to the respective *n*-alkane. For example, near 650 K, 1-pentanol ~60 ms, compared to *n*-pentane ~20 ms. The dominance of initial α-Ṙ radicals in alcohols, coupled with the lack of α-ROȮ stabilization, disfavors isomerization to ȮOOH and results in longer ignition delay times compared to *n*-alkanes. However, the effects of the hydroxy group diminish with increasing size of the aliphatic component of the molecule, bringing linear alcohols and *n*-alkanes in close similarity, which is evidenced in comparison of the ignition delay time trends and NTC behavior of 1-butanol and 1-hexanol in Heufer et al. [98]. Comparing *n*-octanol with *n*-octane reveals a similar trend [548].

Ignition delay times of cyclic alcohols are largely unexplored, with the exception of the cyclopentanol experiments of Cai et al. [549, 552] at 20 atm and 40 atm, over the temperature range 690 – 1175 K, and for several equivalence ratios. NTC behavior is not exhibited in cyclopentanol oxidation. **Figure 24a** compares stoichiometric ignition delay times for cyclopentanol measured in [549] at 20 atm against cyclopentane measurements from Al Rashidi et al. [553] at the same conditions. In contrast to linear alcohols of the same carbon number (**Figure 24b**), as noted in [549], ignition delay times of cyclopentanol are similar to cyclopentane. The two trends are within the stated experimental uncertainty of ±20% above ~900 K. Below ~825 K, cyclopentanol ignition delay times are slightly shorter, perhaps due to facile abstraction of tertiary hydrogen and due to 1-hydroxycyclopentan-2-yl → cyclopentene + ȮH, which occurs via C–O β-scission. No analogous reaction yielding ȮH is possible from cyclopentyl.

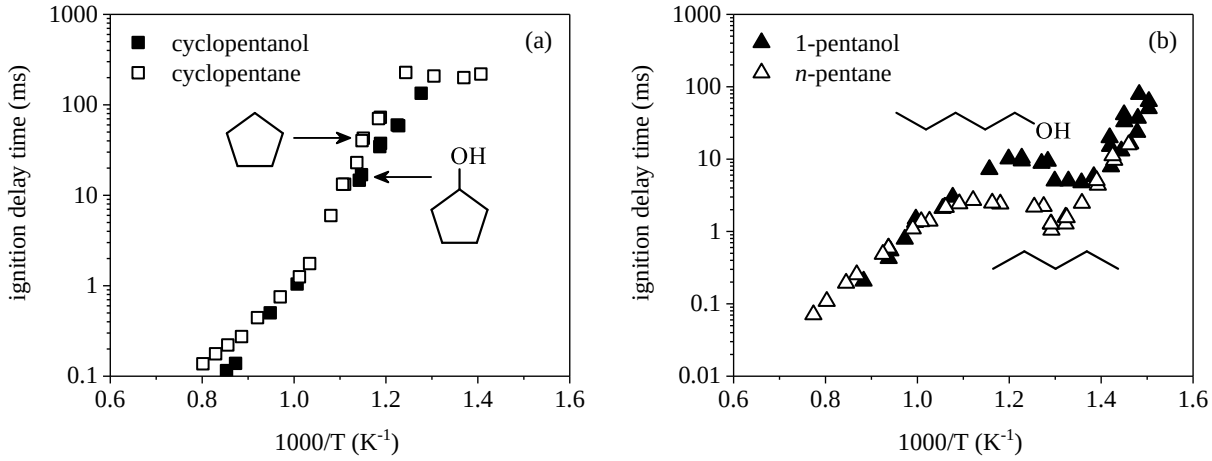

Figure 24. Comparison of stoichiometric ignition delay times at 20 atm of (a) cyclopentanol [552] and cyclopentane [553] and (b) 1-pentanol [552] and *n*-pentane [554]. Ignition delay times were scaled in Cai et al. [552] from measurements in Heufer et al. [98].

Ignition delay time measurements of 1-butanol in Vranckx et al. [435] highlighted an important result related to modeling low-temperature autoignition chemistry of alcohols, namely the role of peroxy radicals at high pressure. The Black et al. mechanism [432] most closely reproduced the shock tube measurements in [435], yet differed by more than an order of magnitude below 900 K. Two modifications were implemented by Vranckx et al. [435] into [432]: transition-state-theory-based *ab initio* calculations of the rate for HOȮ + 1-butanol → H_2O_2 + α-Ṙ and a replacement of the rate coefficient for H_2O_2 → ȮH + ȮH with a higher value based on experimental and theoretical studies, and the inclusion of fall-off parameters, which led to low-temperature ignition delay times being reconciled. The work of Vranckx et al. [435]

underscores the connection between global autoignition properties of biofuels and fundamental low-temperature oxidation chemistry.

As with linear alcohols ethanol [372, 504, 531, 532] and 1-butanol [97, 98], branched alcohols including *iso*-butanol, 2-methyl-1-butanol, and *iso*-pentanol exhibit no significant NTC behavior [483, 484] because of facilitation of HOȮ forming channels relative to second-O_2-addition to ȮOOH radicals and subsequent ketohydroperoxide formation [295, 483, 484, 512, 528, 529, 555]. Ignition delay times for *iso*-pentanol were measured from 1 – 60 atm in Sarathy et al. [483] and the measurements at 7 atm are plotted in **Figure 25** with the trend for 1-pentanol from Heufer et al. [98]. Although the region of overlap below 1000 K is limited, the effect of the methyl substituent appears significant: at ~875 K, a factor of ~7. The absence of NTC behavior in *iso*-pentanol oxidation is likely due to favorable HOO-elimination reactions of the α radical, forming 3-methylbutanal, which is similar to saturated linear alcohols [295, 296, 494-496]. Other factors may include selectivity towards prenol and *iso*-prenol formation [295], which are also coincident with HOȮ, and reactions via the Waddington mechanism.

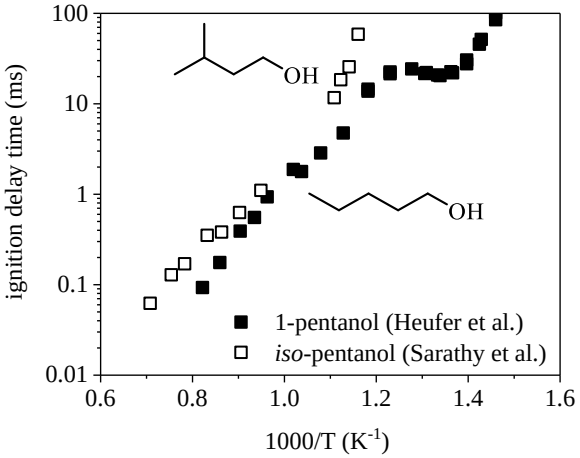

Figure 25. Ignition of 1-pentanol [98] and *iso*-pentanol [483]. Pressures in Heufer et al. [98] ranged from 8.7 – 11.4 atm and are scaled to 7 atm in Sarathy et al. [483].

Consistent with Serinyel et al. [528], ignition delay time measurements at 20 and 40 atm for 2-methyl-1-butanol showed no significant NTC behavior and, at temperatures below 950 K [555], were similar to ignition times of *iso*-pentanol [483]. Low-temperature chain-branching is inhibited in 2-methyl-1-butanol oxidation due to the majority of initiation reactions involving abstraction from α carbon, which creates initial radicals that react with O_2 to form 2-methylbutan-1-al + HOȮ, and because the most favorable isomerization of β-ROȮ and γ-ROȮ radicals is to transfer hydrogen from the α carbon to produce α-β-ȮOOH and α-γ-ȮOOH radicals, respectively. The first prefix, α, refers to the position of the carbon atom with the unpaired electron and the second, β/γ, designates the position of the hydroperoxy group relative to the –OH group. Subsequent reactions of such radicals led predominantly to hydroperoxy-substituted aldehyde + HOȮ, similar to linear alcohols, with second O_2-addition being of secondary importance. Based on reaction pathway analysis, the mechanism of Park et al. [555] indicated that ~10% of α-γ-ȮOOH undergoes water-elimination via the pathway discovered by Welz et al. [301]. **Figure 26** plots ignition delay times of Park et al. [555] for 2-methyl-1-butanol with 1-pentanol results from Heufer et al. [98] and

iso-pentanol from Sarathy et al. [483]. The limited range of temperature over which the measurements overlap precludes a detailed comparison.

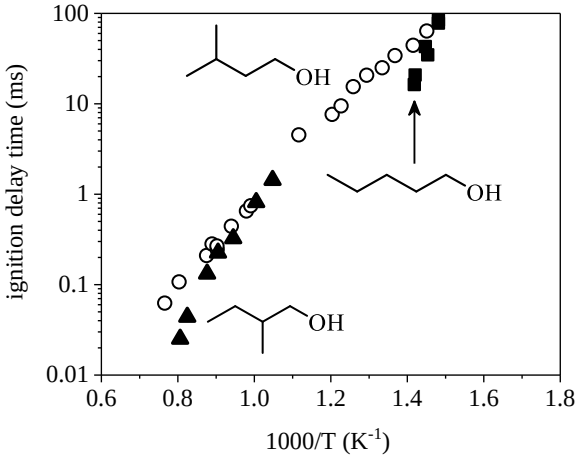

Figure 26. Stoichiometric ignition delay times at 20 atm of pentanol isomers.

3.1.4.2. detailed chemical kinetics mechanisms

Chemical kinetics mechanisms for several alcohols are abundant in the literature, particularly for methanol [459, 556-562], ethanol [459-464, 485, 504, 563-565], isomers of propanol [543, 566-568], isomers of butanol [432, 435, 509, 511, 514, 515, 525, 569-576], isomers of pentanol [437, 483, 484, 495, 505, 516, 528, 529, 555], and to a lesser extent for 1-hexanol [577], prenol/*iso*-prenol [530], 1-octanol [548], and cyclopentanol [549]. The comprehensive review of Sarathy et al. [100] summarized the status of chemical kinetics mechanisms for predicting alcohol oxidation and autoignition, and provided an overview of rate rules and other details related to mechanism development. Chemical kinetics mechanisms were developed for several alcohols since the review of Sarathy et al. [100], including for methanol [562], ethanol [460, 464], 2-methylbutanol [528, 555], prenol/*iso*-prenol [530], 1-octanol [548], and cyclopentanol [549]. Pelucchi et al. [576] developed an extensive chemical kinetics mechanism using rate rules and lumping procedures that combines linear alcohols from 1-propanol up to 1-hexanol. The mechanism includes alternative reactions, such as HOO-elimination from ȮOOH yielding carbonyl-hydroperoxides, ȮOOH dehydration reactions, chain-propagation of HOOĖOOH radicals derived from second-O_2-addition pathways and yielding carbonyl alkyl hydroperoxides, and Korcek reactions of ketohydroperoxides were also included.

Burke et al. [562] constructed a revised mechanism for methanol using Metcalfe et al. [459] as a base mechanism. The revision contained updated thermochemistry [578] and sub-mechanisms for H_2-O_2 [579] and for propene [580]. Several rate parameters were updated as well, including pressure-dependent unimolecular decomposition rates from Jasper et al. [581] and abstraction by ȮH [445], HOȮ [582], ĊH_3 [583], and other radicals.

Olm et al. [460] employed a hierarchical optimization approach to develop a mechanism for ethanol using the methodology of Turányi et al. [65, 584]. The mechanism of Saxena and Williams [585] was used as the starting point for the optimization, which involved optimization of all three Arrhenius parameters instead

of only the pre-exponential factor *A*, which is the typical approach. Temperature-dependent uncertainties of optimized rate coefficients were estimated. Glarborg et al. [464] developed a mechanism for ethanol using rate parameters and thermochemistry from the literature for hydrogen [586] and C1/C2 hydrocarbons [561, 587-590], and thermal decomposition rates from Sivaramakrishnan et al. [436]. Because of discrepancies in rate coefficients for H-abstraction by ȮH and HOȮ, ignition delay time predictions below 1000 K differed by an order of magnitude with experiments [489, 490, 531]. Independent of Glarborg et al. [464], Zhang et al. [485] produced a mechanism for ethanol using base chemistry from Metcalfe et al. [459] and Kéromnès et al. [579] and the sub-mechanism for ethanol from Mittal et al. [504]. Rate parameters for H-atom abstraction, ethanol radical decomposition and reaction with O_2 were adjusted in the mechanism with guidance from sensitivity analysis.

Subsequent to comparing site-specific rate coefficients for HOȮ + ethanol → Ṙ + H_2O_2, and in order to examine the influence of integrating the calculated rate coefficients into previous chemical kinetics mechanisms [485, 486], Zhao et al. [75] conducted ignition delay time simulations. For all cases, ignition delay times were longer than predictions using the unmodified models. Using a modified version of the Curran et al. [485] mechanism, the temperature and pressure conditions of shock tube measurements from Noorani et al. [542] at 2 atm and from Cancino et al. [489] at 50 atm were utilized. In both cases, discrepancies were noted towards lower temperature where the dominant reaction path for ethanol is the formation of acetaldehyde + HOȮ. Because of the similarity to rates from coupled cluster calculations, Zhao et al. [75] concluded that the commonly used analogies for rate parameters derived from 1-butanol are suitable and that existing discrepancies in chemical kinetics model predictions of ethanol ignition delay times are more likely due to deficient sub-mechanisms for primary intermediates such as acetaldehyde and vinyl alcohol.

Serinyel et al. [528] developed a chemical kinetics mechanism for 2-methyl-1-butanol using existing mechanisms for alcohols. Subsequently, Park et al. [555] utilized rate rules for reaction classes and expanded the Sarathy et al. [483] mechanism for *iso*-pentanol by adding ~100 species and approximately 400 reactions specific to 2-methyl-1-butanol. Rate parameters for several reactions were adjusted within uncertainty bounds to improve predictions of ignition delay times and species profiles.

De Bruycker et al. [530] employed automatic mechanism generation using Genesys [401] to produce a detailed chemical kinetics mechanism for prenol and *iso*-prenol oxidation. Optimized geometries and thermochemistry were calculated for initial radicals and peroxy radicals using CBS-QB3. Rate parameters were calculated from transition state theory using the CBS-QB3-optimized structures for several types of reactions involving the unsaturated alcohols, including H-abstraction by ĊH$_3$, ȮH-addition to C=C bonds, and HOO-elimination from ȮOOH, among others.

Cai et al. [548] used conventional hierarchical approaches of mechanisms for 1-butanol [511] and 1-pentanol [437, 483] to develop a mechanism for 1-octanol oxidation, incorporating a total of 30 reaction classes. To properly account for the chemistry of the larger alkyl substituent group, the C6-C8 alkane/alkene sub-mechanism from Westbrook and Dryer [375] was adopted. Similar to other alcohols, Waddington reaction and water-elimination pathways were included based on the results from Welz et al. [296, 301].

Duan et al. [505] revised the 1-pentanol mechanism of Heufer et al. [437] by replacing rate-rules-based Arrhenius parameters for reactions of collisionally stabilized α-ROȮ with rate parameters from coupled cluster calculations. Rates for seven reactions were calculated – five α-ROȮ → ȮOOH isomerization

reactions and two HOO-elimination reactions. Three of the reactions were excluded in the initial mechanism, including α-ROȮ → pentanal + HOȮ. Ignition delay times were calculated with the revised mechanism and were higher by ~50 – 70% below 775 K. Because of the significance of pentanal in the oxidation of the α radical (pentan-1-ol-1-yl), yields were quantified to determine the fraction formed from stabilized ROȮ versus from Ṙ + O_2 via chemical activation (well-skipping mechanism). Using ChemKin simulations under PSR conditions at 1 atm and 10 atm, the well-skipping mechanism accounted for the majority of pentanal. However, the revised mechanism showed sensitivity to the rate coefficient for Ṙ + O_2 → ROȮ, which in the initial mechanism [437] is that of butyl + O_2 measured in Lenhardt et al. [591].

Cai et al. [549] developed the first chemical kinetics mechanism for cyclopentanol. The approach involved a detailed sub-mechanism for cyclopentanol-related species, produced using a series of quantum chemical calculations of thermochemistry, potential energy surfaces for reactions of O_2 with all three initial carbon-centered radicals (α, β, γ), and rate coefficients relevant to low-temperature chemistry. Sub-mechanisms for intermediates such as cyclopentenol isomers were also developed.

To compare chemical kinetics mechanism predictions of alkane and alcohol oxidation, simulations of mole fractions were conducted for the present review using the PSR module in ChemKin for stoichiometric *n*-butane and 1-butanol at 10 atm under isothermal conditions at a residence time of 2000 ms using the mechanisms of Healy et al. [96] and Sarathy et al. [511], respectively. Initial concentrations of both species were 1000 ppm. **Figure 27a** compares the temperature dependence of *n*-butane and 1-butanol consumption. Low-temperature chain-branching and NTC behavior is evident for *n*-butane, starting around 600 K, which is due to a shift away from second-O_2-addition reactions (ȮOOH + O_2) forming ketohydroperoxides. Because of the pathways specific to alcohols (cf. **Figure 14**) such reactions are suppressed, which inhibits chain-branching and subsequent two-stage ignition for 1-butanol. **Figure 27b** compares species profiles of cyclic ether species, 2-methyloxetane and 2-oxetanylmethanol, and alkene species, 2-butene and but-2-en-1-ol, which are formed from *n*-butane and 1-butanol, respectively. Cyclic ether speciation measurements from alkanes, such as *n*-butane [592-595], are relatively common. However, while some ȮOOH decomposition products are reported in alcohol oxidation, namely alkenes and β-scission products [296], cyclic ethers are not. Because concentrations are similar to HOO-elimination products, such as the alkenes in **Figure 27c**, and because of the unique connection to ephemeral ȮOOH radicals, speciation of cyclic ethers is critical to improving the understanding of low-temperature oxidation of alcohols.

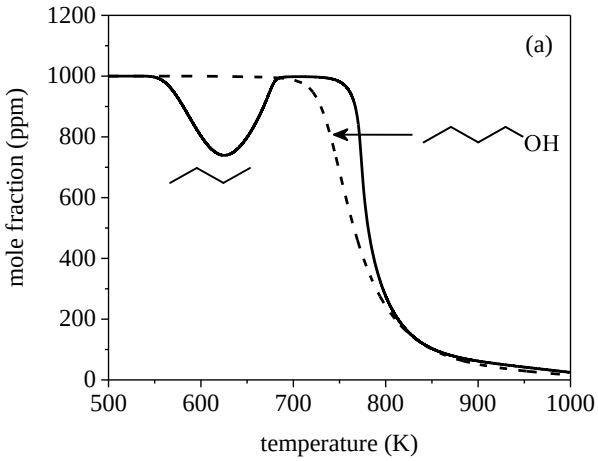

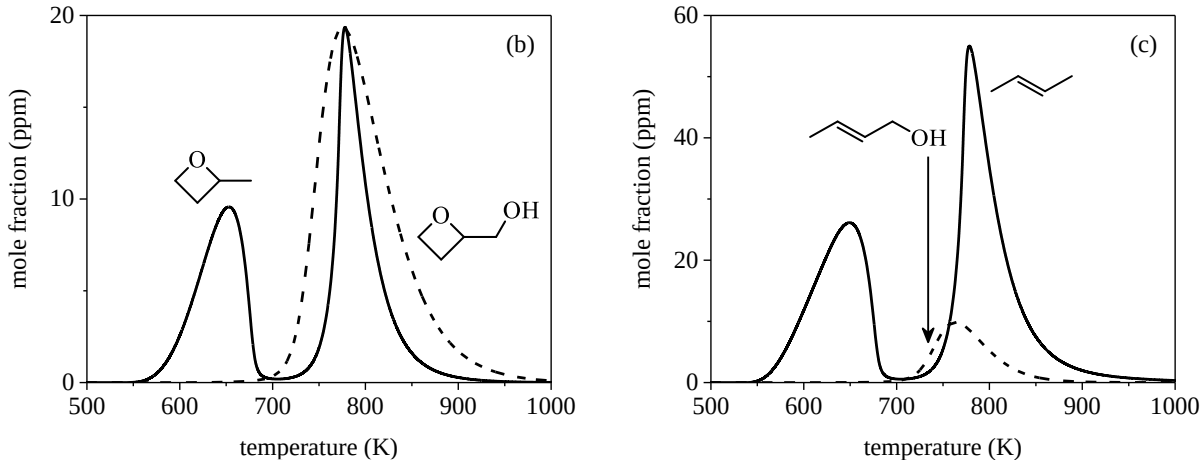

Figure 27. Model simulations of (a) consumption of *n*-butane and 1-butanol and concentrations of (b) cyclic ethers and (c) alkenes using the Healy et al. [96] mechanism (*n*-butane) and the Sarathy et al. [511] mechanism (1-butanol). 10 atm, $\phi = 1.0$, residence time = 2000 ms. Consistent with the consumption profiles for *n*-butane and 1-butanol, the formation of cyclic ether and alkene species occurs in distinct regions of temperature.

3.1.5. summary of –OH functional group effects

The –OH functional group affects branching fractions of initial alcohol radicals due to the 5 – 6 kcal/mol lower C–H bond energy on α carbon and to the formation of pre-reaction complexes for both ȮH- and HOȮ-initiated abstraction. Due to a lack of hydrogen bonding with the –OH group, no pre-reaction complexes form in abstraction reactions by $\dot{C}H_3$. For all alcohols, linear and branched, measurements of rate coefficients for H-abstraction are absent in the 400 – 900 K range. **Figure 28** shows the low-temperature chain-branching scheme augmented to emphasize pathways that diminish chain-branching and that are enhanced by the presence of the –OH functional group in linear and branched alcohols.

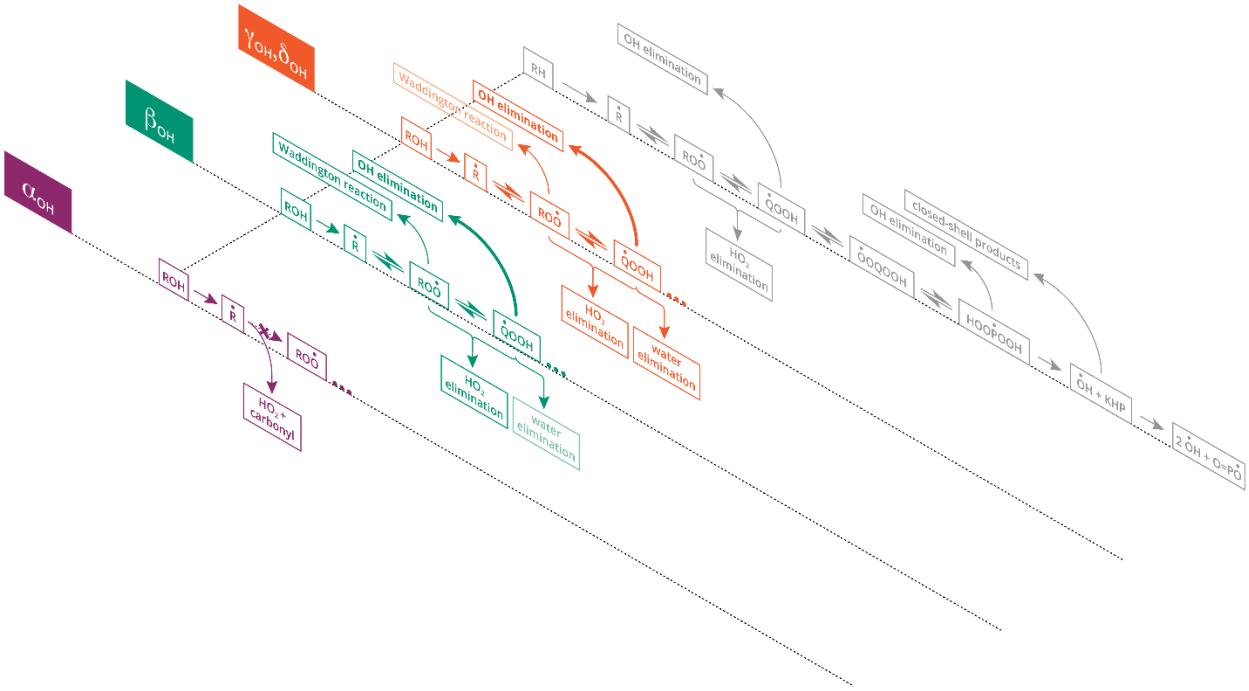

Figure 28. Summary of alcohol functional group effects on low-temperature chain-branching. Each type of initial radical is depicted in a separate plane, with different colors used to guide the eye. The alkane oxidation mechanism is depicted in the back plane for reference. Pathways that are enhanced by the effects of the functional group are emphasized with bold arrows and labels, and those that are diminished are made lighter or omitted. The leftward-pointing and downward-pointing arrows indicate a shift in flux away from chain-branching pathways responsible for ignition. The initial radical production in alcohols tends to favor α-hydroxyalkyl radicals, which react with O_2 to form HOȮ, inhibiting chain reaction. Reactions of other (β, γ, δ-hydroxy) radicals with O_2 show increased or new chain-propagation channels that can reduce the flux towards chain branching

For abstraction by ȮH, ethanol and 1-butanol are the only two for which multiple rate coefficients studies are available. Total k(T) for ethanol + ȮH is consistent among the calculations [436, 445, 446]. However, while branching fractions all favor α radical formation from 500 – 1000 K in the high-pressure limit, and negligible abstraction of hydroxylic H, predictions of branching towards β radicals are in disagreement. Similarly, rate coefficients calculations [433, 434, 450] for ȮH-initiated abstraction from 1-butanol are largely consistent with one another – overlapping within 20% at 1000 K and within a factor of ~3 at 500 K. Although branching fractions from the three quantum chemical studies for 1-butanol show disparities, consistent trends emerge. Branching towards α radicals is favored (~50 – 70% at 500 K and 35 – 55% at 1000 K) and γ radicals are favored second. From the calculations of Seal et al. [434] and the analytical equations of McGillen et al. [450], branching fractions towards β and γ radicals were similar, while Zhou et al. [433] predict larger branching towards γ over β radicals. In addition, δ radicals were favored over β radicals in [433] due to the inclusion of a pre-reaction complex not considered in other studies.

Abstraction by HOȮ also favors the formation of α radicals, which account for >95% of the branching fraction for ethanol over the range of temperatures relevant to low-temperature combustion. In 1-butanol, α radicals account for 99% of the radical pool at 500 K and ~75% at 1000 K. β, γ, and δ radicals of 1-butanol are competitive with one another starting near 900 K. HOȮ-initiated H-abstraction from *iso*-

pentanol also favors α radicals, although δ radical formation is significant owing to the six hydrogen atoms on the two methyl groups. Combined, α and δ account for ~90% of initial radical pool in *iso*-pentanol, with α favored below 700 K.

The propensity of alcohols – from ethanol to butanol isomers – to form a majority of α radicals in the initiation step is one of the primary reasons for the lack of low-temperature chain-branching, which is reflected in both experiments and chemical kinetics modeling [483, 484, 529]. The lack of stabilization of chemically activated α-ROȮ radicals, as shown in hydroxyethyl + O_2 [497], which is weakly dependent on both pressure [497-500] and temperature [500], and relatively low barrier heights for aldehyde + HOȮ channels, both inhibit the production of ȮOOH required for ketohydroperoxide formation. Reactions of radicals other than α, such as β, γ, and δ radicals, including the Waddington mechanism and the water-elimination mechanism proposed by Welz et al. [301], deplete ȮOOH radicals that are formed and prevents second-O_2-addition reactions as a result.

Li et al. [509] conducted quantum chemical calculations to produce pressure-dependent rate coefficients for Waddington pathways and thermochemical properties for the species involved, which were derived from isomers of butene (1-butene, *trans*-2-butene, and *iso*-butene) and of butanol (1-butanol and 2-butanol). The revised parameters were incorporated into a chemical kinetics mechanism and showed, consistent with inhibited second-O_2-addition, that ignition delay times increased by a factor of ~2 for *trans*-2-butene and *iso*-butene. The effects on 1-butene ignition times were marginal. Water-elimination pathways follow either chain-propagating or chain-inhibiting pathways. For example, 2-oxybutanal formed via water-elimination from 1-hydroxybutyl-2-peroxy (i.e. β-ROȮ), decomposes in a chain-propagating step to propanal + HĊO [296]. Alternatively, upon reaction with O_2, 2-oxybutanal yields 1,2-butadione + HOȮ. Water-elimination pathways involving δ-ROȮ – in which the peroxy group is on the terminal carbon and separated form –OH group by four carbon units – are possible [296]. The extent to which such pathways are relevant beyond δ carbon, however, remains unclear although are likely to diminish with larger alkyl substituents. Reactions of the analogous oxy radical in 1-pentanol oxidation – derived from ε-ROȮ – may yield 1,5-pentadione + HOȮ from reaction with O_2 or butan-1-al-4-yl + CH_2O via β-scission. In the latter case, 3-butenal is the likely oxidation product of the radical.

Increased flux of cyclic ether formation channels, ȮOOH → cyclic ether + ȮH, also contribute to diminished second-O_2-addition reactions given that the barrier heights to both ROȮ isomerization and ȮOOH decomposition are lowered when involving α carbon (where the –OH is bound). As an example, **Figure 29** compares analogous pathways yielding 5-membered cyclic ether species: 2-hydroxytetrahydrofuran and tetrahydrofuran. The barrier height for the 7-membered transition state from δ-ROȮ to 1-hydroperoxy-butanol-1-yl is 18.6 kcal/mol [296]. The analogous channel in *n*-butane via 1-hydroperoxy-butan-4-yl is 23.5 kcal/mol [595]. The alcohol channel is lower by ~5 kcal/mol. Similarly, unimolecular decomposition of ȮOOH into cyclic ether is lower in the alcohol case by 3 kcal/mol. Other cyclic ether channels involving α carbon reflect similar behavior. However, because no isomer-resolved speciation measurements of key species from unimolecular ȮOOH decomposition are reported for 1-butanol, chemical kinetics modeling is unable to determine the quantitative impact, i.e. the flux of ȮOOH radicals from 1-butanol proceeding via unimolecular decomposition versus second-O_2-addition.

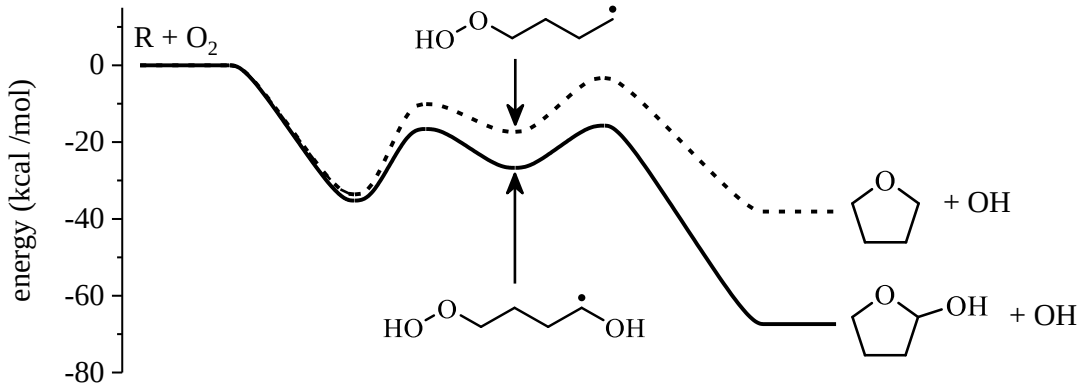

Figure 29. Comparison of barrier heights for the formation of 5-membered cyclic ethers in *n*-butane and 1-butanol. Similar effects occur in other cyclic ether pathways. The formation of cyclic ethers is facilitated in alcohol oxidation when α carbon is involved due to lower barriers to ROȮ → ȮOOH isomerization and ȮOOH decomposition. Stationary point energies for the *n*-butane system are from Eskola et al. [595] and for 1-butanol from Welz et al. [296].

Ignition delay time measurements below 1000 K are reported for several alcohols (*Section 3.1.4.1*): ethanol, 1-butanol, 2-butanol, *iso*-butanol, *tert*-butanol, as well as pentanol isomers (1-pentanol, 2-pentanol, *iso*-pentanol, and cyclopentanol). In contrast to *n*-alkanes, for which propane is the smallest species to exhibit two-stage ignition [533, 537], the smallest alcohol that undergoes low-temperature chain-branching is 1-pentanol [98]. Others include 1-hexanol [98] and 1-octanol [548]. In general, as alkyl substituents become longer, the influence of the –OH group is diminished – i.e. ignition delay times of 1-octanol are more similar to *n*-octane than 1-butanol to *n*-butane. However, because temperatures and pressures overlap in only a limited number of cases, between alcohols and alkanes and among alcohols, comparison of the influence of molecular structure on ignition is difficult. Accordingly, additional experiments are needed at identical conditions for both linear, branched, and cyclic alcohols to directly examine the effect of the –OH functional group relative to similar-sized alkane analogs, similar to the approach of Heufer et al. [98].

3.2. esters

Ester functional groups define the molecular structure of conventional biodiesel, which is a mixture of long-chain methyl or ethyl esters, the composition of which depends on the type of biomass-derived oil used in transesterification [596-598], e.g. soy [599], rapeseed [599], or algae [600]. While the specific amounts vary depending on the type of oil [601], three esters are most abundant: methyl hexadecanoate (methyl palmitate, $C_{17}H_{34}O_2$), methyl oleate (methyl 9-(*Z*)-octadecenoate, $C_{19}H_{36}O_2$), and methyl linoleate (methyl (9*Z*,12*Z*)-octadeca-9,12-dienoate, $C_{19}H_{34}O_2$) [600]. Two less abundant methyl esters are methyl stearate (methyl octadecanoate, $C_{19}H_{38}O_2$) and methyl linolenate (methyl (9*Z*,12*Z*,15*Z*)-octadeca-9,12,15-trienoate, $C_{19}H_{32}O_2$) [598]. Nomenclature of the type (x:y) is used for methyl esters to designate the size of the alkyl chain (x) and the degree of unsaturation (y). Examples include (16:0), which represents methyl palmitate, (18:1) for methyl oleate, and (18:2) for methyl linoleate.

In a similar vein to the hierarchical approach adopted for chemical kinetics mechanisms of hydrocarbons [375, 385], in which the $H_2/O_2/CO$ system serves as base chemistry and elementary reactions for larger species are added subsequently, the oxidation chemistry of small esters contributes to the foundation of mechanisms for larger esters relevant to practical biodiesel. Because of variation in both the size of the alkyl substituent and in the degree of unsaturation, smaller esters are employed in studies as surrogates to understand the role of the functional group on combustion. As a result, numerous studies exist on methyl esters up to methyl decanoate. Methyl butanoate oxidation is the most studied [602-617] and a smaller collection of work has examined the role of unsaturated carbon on reaction mechanisms below 1000 K [618, 619].

Figure 30 shows the molecular structure of several esters: methyl butanoate, methyl-*trans*-3-hexenoate, and methyl linoleate. The ester function group creates distinct abstraction sites along the alkyl chain (e.g. α', β', γ') and on the methoxy group (α), where the prime notation indicates carbon sites on the alkyl side of the ester consistent with Mendes et al. [620, 621]. While analogies with *n*-alkane chemistry are drawn for larger alkyl chains in esters [622-624], understanding the role of resonance stabilized radicals produced from abstraction at the α' site [377, 619, 625] and the role of C=C bonds on low-temperature oxidation [609, 619, 626, 627] are critical to understanding methyl ester oxidation.

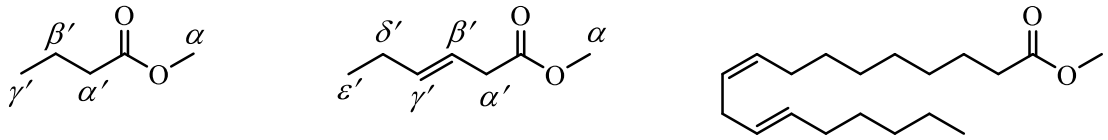

Figure 30. Molecular structure of methyl esters (a) methyl butanoate, (b) methyl *trans*-3-hexenoate, and (c) methyl linoleate. Smaller methyl esters are used as surrogates for larger biodiesel-relevant molecules.

Quantum chemical calculations of thermochemical properties of esters include bond energies, entropy, enthalpies of formation, and specific heats [603, 628-639]. Osmont et al. [628] developed a protocol for determining gas-phase thermochemical properties of methyl and ethyl esters at the B3LYP/6-31G(*d*,*p*) level and conducted an extensive series of calculations on standard enthalpies of formation, specific heats, and entropies for dozens of esters and radicals of esters [635]. The protocol employed atomic corrections, which were determined via least-squares fitting of experimental standard enthalpies of formation, to augment electronic and zero-point energies and thermal corrections. Subsequently, the approach was extended to calculations of C–O, (C=O)–O, and (C=O)–C bond energies in methyl esters [629] and to thermochemical properties of oxygenated radicals from methyl esters [630].

The ester functional group and unsaturated carbon in the alkyl side chain creates changes in C–C and C–H bond energies, including allylic and *bis*-allylic, which are lower in energy than alkylic sites and vinylic sites [635]. Because of the large molecular size of esters in practical biodiesel and related surrogates, high-level *ab initio* calculations are expensive. In addition to group additivity estimates [640], several studies on bond energy calculations of esters exist [222, 602, 631-634, 641].

To mitigate the computational expense for biodiesel-relevant esters, Oyeyemi et al. [632] calculated bond energies for C1 – C4 species, including methyl butanoate and methyl-*trans*-2-butenoate, using a composite, multireference-averaged coupled-pair functional (MRACPF2)-based scheme developed previously for hydrocarbons [642], and used structure-activity considerations to extend the results to larger esters that could not be calculated at that level. Accounting for differences in multireference character, several complete active space (CAS) methods were applied depending on the molecular structure and the type of bond-scission step. As an example, CAS(4e, 4o) was utilized for C–H bond-scission of allylic hydrogen on α' carbon (cf. **Figure 30**) to account for electrons in π/π^* orbitals in the C=O bond and electrons in σ/σ^* orbitals of the dissociating C–H bond. Bond energies for C–H, C–O, and C–C were computed using MRACPF2 for C1 – C4 methyl and ethyl esters, several alkanes, alkenes, and a representative diene (1,4-pentadiene), which act as surrogates for the molecular structure motifs in biodiesel-relevant esters. Results from the smaller, representative molecules were mapped onto methyl stearate (16:0), methyl oleate (18:1), methyl linoleate (18:2), and methyl linolenate (18:3) by assuming that the bond energies in sections of the esters were similar to bond energies in the surrogate species. Subsequently, Oyeyemi et al. [633] modified the multireference approach using a reduced scaling method to directly calculate bond energies of large esters, from methyl decanoate to methyl octadecanoate, and including saturated and unsaturated species. The results were largely similar to the sectional approach in [632] with the most substantial difference occurring at the *bis*-allylic site. The reduced-scaling method produced a C–H bond energy of 78.9 kcal/mol – higher by 2.8 kcal/mol than the earlier estimate using 1,4-pentadiene as a surrogate.

Li et al. [634] utilized Kohn-Sham exchange-correlation functionals [643] and coupled cluster theory with extrapolation to the complete basis set (CBS) limit to conduct a series of direct calculations on methyl linolenate. Using the M08-HX density functional and a minimally augmented basis set with valence triple-zeta polarization (M08-HX/ma-TZVP), C–H bond energies on the α' carbon (91.9 kcal/mol) were similar to calculations using MRACPF2 [632] and several kcal/mol lower than CBS-QB3 [614, 631]. **Figure 31** shows C–H bond energies calculated using M08-HX/ma-TZVP [634]. The lowest bond energy, due to the higher number of electrons involved in resonance-stabilization compared to allylic radicals, is on the two *bis*-allylic sites, followed by allylic C–H (82.4 kcal/mol and 83.1 kcal/mol). Both allylic sites are similar to analogous bond energies in alkenes [60]. Notably, however, the bond energies of the two *bis*-allylic sites differ by several kcal/mol. On the site closest to the terminal carbon on the alkyl chain, the C–H bond energy is 78.2 kcal/mol, while on the *bis*-allylic site closer to the ester group, the bond energy is 6 kcal/mol lower (72.1 kcal/mol). The substantial difference indicates that the nearby bonding environment, as well as structural relaxation in the radicals produced, affects bond strengths. Conformer-dependent calculations were not conducted in Li et al. [634]. However, Oyeyemi et al. [632] calculated the sensitivity of bond energies to conformational changes in methyl butanoate and reported no significant dependence.

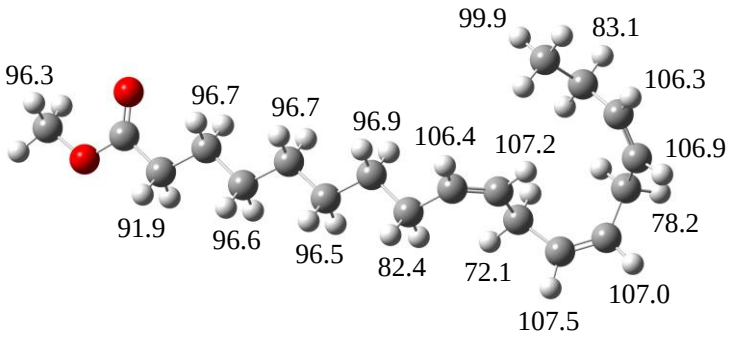

Figure 31. Optimized geometry of methyl linolenate and C–H bond dissociation energies (kcal/mol) calculated at the M08-HX/ma-TZVP level of theory [634].

The sections below discuss initiation reactions with ȮH and HOȮ and resulting branching fractions, mechanistic studies of methyl ester radicals with O_2, reactions of initial ester radicals with O_2, speciation from thermally initiated experiments, detailed kinetics modeling, and autoignition measurements using shock tubes and rapid compression machines. Due to broad coverage of a disparate number of esters, the sections are organized around a particular aspect of low-temperature oxidation, such as peroxy radical reactions, within which ester-specific chemistry is discussed. A summary on the impact of the ester moiety on low-temperature oxidation is then provided.

3.2.1.initiation reactions and branching fractions

Rate coefficients were reported for reactions of esters with ȮH [620, 627, 644-654], HOȮ [621, 645, 646, 655-657], and $\dot{C}H_3$ radicals [645, 646, 658, 659]. Studies are also reported for abstraction reactions by other radicals relevant at high-temperature, including Ḣ [645, 646, 648, 660, 661] and Ö [645, 646, 648]. Experiments at temperatures near 300 K suggest that hydrogen-bonded complexes could be important in ȮH reactions with esters. Wallington et al. [644] conducted flash photolysis/resonance fluorescence measurements of rate coefficient for a series for ȮH + esters at 296 K to independently examine the effects of size and structure of both the alkyl chain and the alkoxy group (up to four carbon atoms in both cases). An unusual increase in the rate coefficient when the size of either chain increased from three to four carbon atoms was ascribed to the formation of a hydrogen-bonded pre-reaction complex, similar to prior work by Wallington and Kurylo [662] on ketones. Wallington et al. [644] found a weak positive temperature dependence for the reactions of ȮH with methyl acetate and ethyl acetate from 296 – 440 K. The experiments by El Boudali et al. [649] and Le Calvé et al. [650, 652] from 233 – 372 K expanded rate coefficient measurements of ȮH + esters to include methyl pentanoate and methyl hexanoate and found negative temperature dependence in the rate coefficents for esters larger than methyl butanoate and for acetates larger than methyl acetate [652] up to ~400 K [649].

The sections below provide a review of ester reactions with ȮH and HOȮ, which involve the formation of pre-reaction complexes in both cases, and are separated according to molecular size, i.e. methyl formate up to C6 methyl esters.

Tan et al. [645] conducted *ab initio* quantum calculations of H-abstraction from methyl formate by ȮH using a multireference correlated wave function method (CBS-MRSDCI), which included size-extensivity corrections to calculate barrier heights and reaction enthalpies. High-pressure-limit rate coefficients were

calculated from 300 – 1500 K using canonical transition state theory with separable-hindered-rotor approximation for torsions and the harmonic oscillator approximation for other vibrational modes.

Jørgensen et al. [651] studied the reaction mechanism of ȮH + methyl acetate computationally using CCSD(T)/ccpVTZ//BH&HLYP/aVTZ and CBS-QB3 levels of theory. For abstraction from the methoxy group, optimized reactant geometries and transition states revealed in-plane and out-of-plane abstractions, the latter involving a strong hydrogen-bonding interaction between the H atom in the ȮH radical and the O atom in the carbonyl group. Similar, stabilizing pre-reaction bonding occurred in the transition state for abstraction from the methyl group. Rate coefficients and branching fractions were calculated up to 500 K by canonical TST; under these conditions out-of-plane abstraction from the methoxy group dominates (96% at ~ 298 K, in agreement with Wallington et al. [644].

Using coupled cluster (CCSD(T)) and multireference-averaged coupled pair functional theory (MRACPF2), Tan et al. [648] calculated abstraction reactions for methyl acetate with several co-reactants, which revealed pre-reaction complex formation for ȮH and HOȮ. Nearly identical rate coefficients were predicted using both conventional TST over a single transition state and a complex-mediated mechanism that used VRC-TST for the barrierless entrance channel. Mendes et al. [620] carried out a systematic study of hydrogen atom abstraction by ȮH radicals on esters (methyl acetate, methyl propanoate, methyl butanoate, methyl isobutyrate, ethyl ethanoate, propyl ethanoate, and isopropyl ethanoate), using conventional transition state theory with asymmetric Eckart tunneling corrections, using structures optimized at the MP2/6-311G(*d*,*p*) level and G3 energy calculations. For methyl acetate they also computed higher-level CCSD(T)/CBS energies. The high-pressure limit rate coefficients in Mendes et al. [620] for temperatures between 500 K and 2200 K are in reasonable agreement with those in Tan et al. [648], and both agree with Jørgensen et al. [651] that abstraction at the methoxy site dominates at low temperature. Mendes et al. [620] predict that methyl and methoxy abstractions become equal at about 1000 K, but Tan et al. [648] show a preference for methoxy abstraction across their temperature range.

Site-specific rate coefficients for H-abstraction from methyl propanoate by ȮH were calculated using VariFlex [468] in Mendes et al. [620] and Tan et al. [646]. Mendes et al. [620] employed conventional transition state theory with asymmetric Eckart tunneling corrections, using energies computed at the MP2/6-311G(*d*,*p*) level. Tan et al. [646] utilized several variations of transition state theory and the multi-structure all-structure (MS-AS) approach, with both multi-reference methods (MRSDCI) and coupled cluster methods, CCSD(T). Energies of reactant complexes, transition states, and products in Tan et al. [646] were consistent with Mendes et al. [620], and the total rate coefficients produced from the two methods were within 20% at 500 K and within 10% at 1000 K (**Figure 32a**). As in the case of methyl acetate, the branching ratio predictions differ somewhat (**Figure 32b, 32c**). The site-specific rate coefficients from Mendes et al. [620] are weakly dependent on temperature from 500 – 1000 K and α' radicals are dominant. Tan et al. [646] show a moderate temperature dependence and a different ordering for the β' and α' channels. Based on results from Georgievskii et al. [663] for C_2H_6 + ĊN, Mendes et al. [620] employed a single-transition-state model – neglecting the outer transition state involved in the pre-reaction complex. In contrast, Tan et al. [646] applied a two-transition-state model using variable reaction coordinate transition state theory (VRC-TST) for the barrierless complex formation. The effect of the reaction complex is larger at lower temperatures.

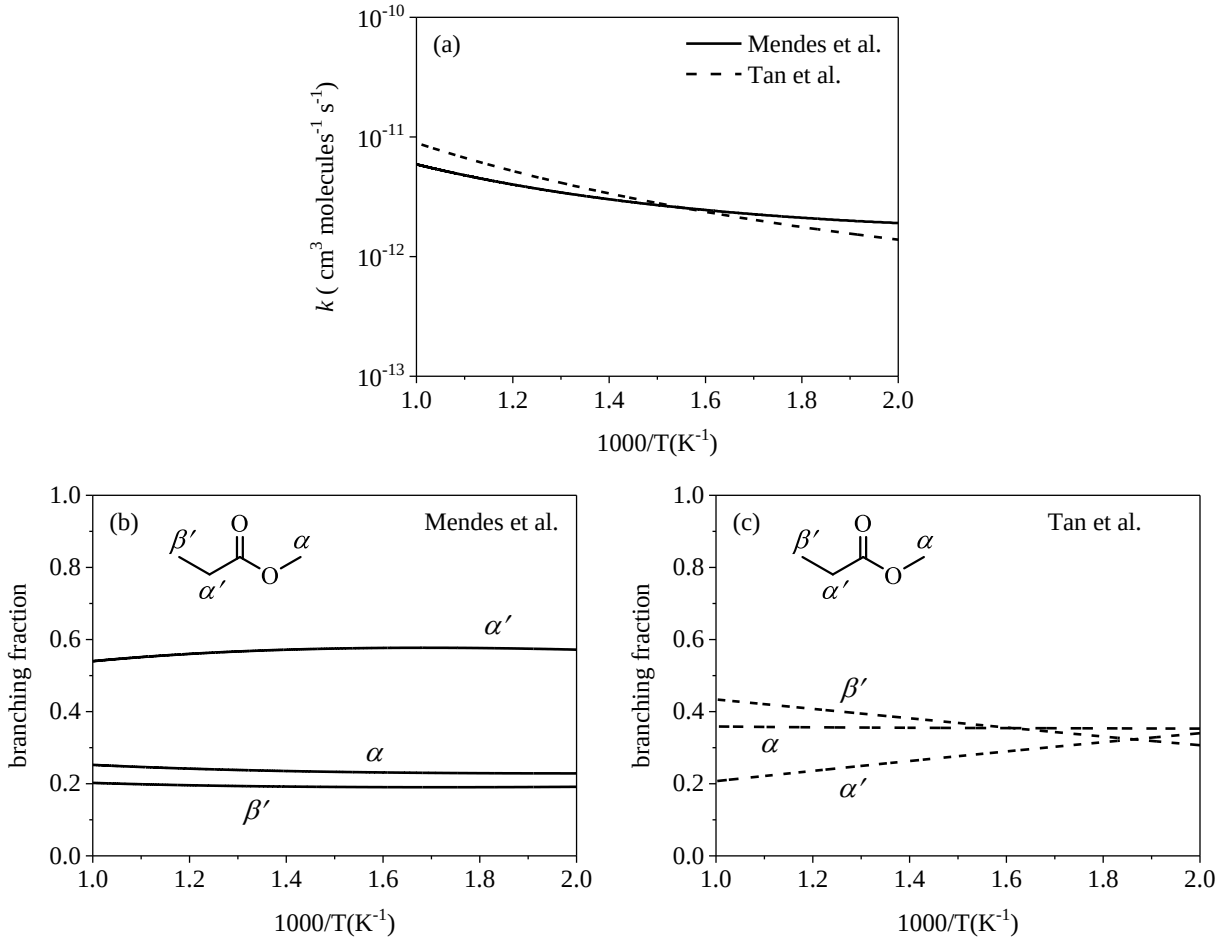

Figure 32. Comparison of (a) total rate coefficients and (b, c) branching fractions for abstraction reactions from methyl propanoate by ȮH from α, α', and β' sites calculated in Mendes et al. [620] and Tan et al. [646] obtained with MS-AS using CCSD(T)/CBS(D-T) energies.

Mendes et al. [620] also calculated rate coefficients and branching for reactions with methyl butanoate, methyl *iso*-propanoate, ethyl acetate, *n*-propyl acetate, and *iso*-propyl acetate to systematically examine the role of alkyl substituent size and structure in the formation of a pre-reaction complex (**Figure 33**). In the comparison of branching fractions calculated for the esters, *k*(T) primarily depended on the ability of ȮH to form a pre-reaction complex and secondarily on the type of C–H bond. For example, in methyl butanoate, the C–H bond energy on α' is ~4 – 5 kcal/mol lower than on β' [634], yet up to ~800 K branching towards β' radicals dominates due to interaction of ȮH with with carbonyl group (**Figure 34**).

Pre-reaction complexes were formed in abstraction reactions from four sites among the seven esters studied, α, α', β, and β', which were stabilized by 3.6 – 5.6 kcal/mol depending on the type of C–H bond and the spatial orientation of the abstraction site relative to the ester functional group. Product complexes were also formed in all four cases. The impact of excluding both pre-reaction and product complexes on rate coefficients was examined for a representative case: abstraction from α' carbon in ȮH + methyl acetate reactions. At 500 K, neglecting complex-mediated steps lowered the total rate coefficient by 70% and to a

lesser extent at 1000 K, changing only by ~10% [620]. However, while the impact on total rate coefficient is within typical uncertainty bounds, inclusion of the transition state for pre-reaction complexes may affect branching fractions as suggested in **Figure 32**.

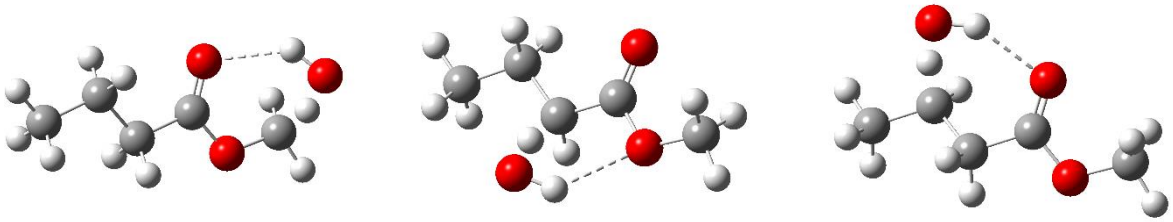

Figure 33. Transition states from Mendes et al. [620] showing pre-reaction complex-mediated H-abstraction from methyl butanoate at (a) α, (b) α', and (c) β' sites.

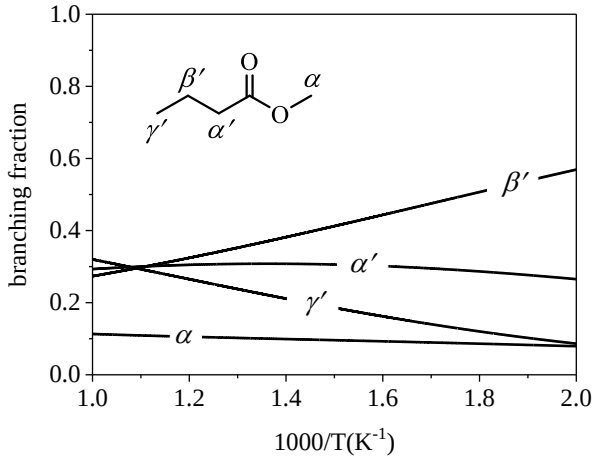

Figure 34. Branching fractions for H-abstraction from methyl butanoate by ȮH from Mendes et al. [620].

Rate coefficients for reactions of ȮH with four esters (methyl formate, methyl acetate, methyl propanoate, and methyl butanoate) were measured in Lam et al. [647] using absorption spectroscopy behind reflected shock waves. The rates were measured via exponential decay fitting of ȮH radical time profiles at ~1.5 atm and from ~875 – 1370 K and were compared to simulations using detailed chemical kinetics mechanisms of Dooley et al. for methyl formate/methyl acetate [641] and methyl butanoate [614]. For methyl propanoate, rate coefficients were adopted from the ethyl propanoate mechanism of Metcalfe et al. [613] and incorporated into the Dooley et al. [614] mechanism for methyl butanoate.

Figure 35 compares the Lam et al. [647] measurements with others obtained above 300 K [644, 649, 650, 652], and with *ab initio* calculations of Mendes et al. [620] and Tan et al. [646]. Discrepancies with the calculations for methyl formate + ȮH from Tan et al. [645] were noted, differing by a factor of ~5 at 850 K (**Figure 35a**). However the calculations for methyl acetate and methyl butanoate from Tan et al. [646, 648] are within experimental uncertainty over the entire range of temperature (**Figure 35b and 35c**). Similarly, the rate calculations are consistent with Mendes et al. [620] to within a factor of ~2.3 at 2000 K and ~1.5 at 500 K. Note that 500 K was the lower limit of temperature in [620], whereas Tan et al. [646,

648] extended calculations to 250 K. Similar overlap between the shock tube measurements of ȮH + methyl butanoate and the calculations in Mendes et al. [620] is exhibited (**Figure 35d**).

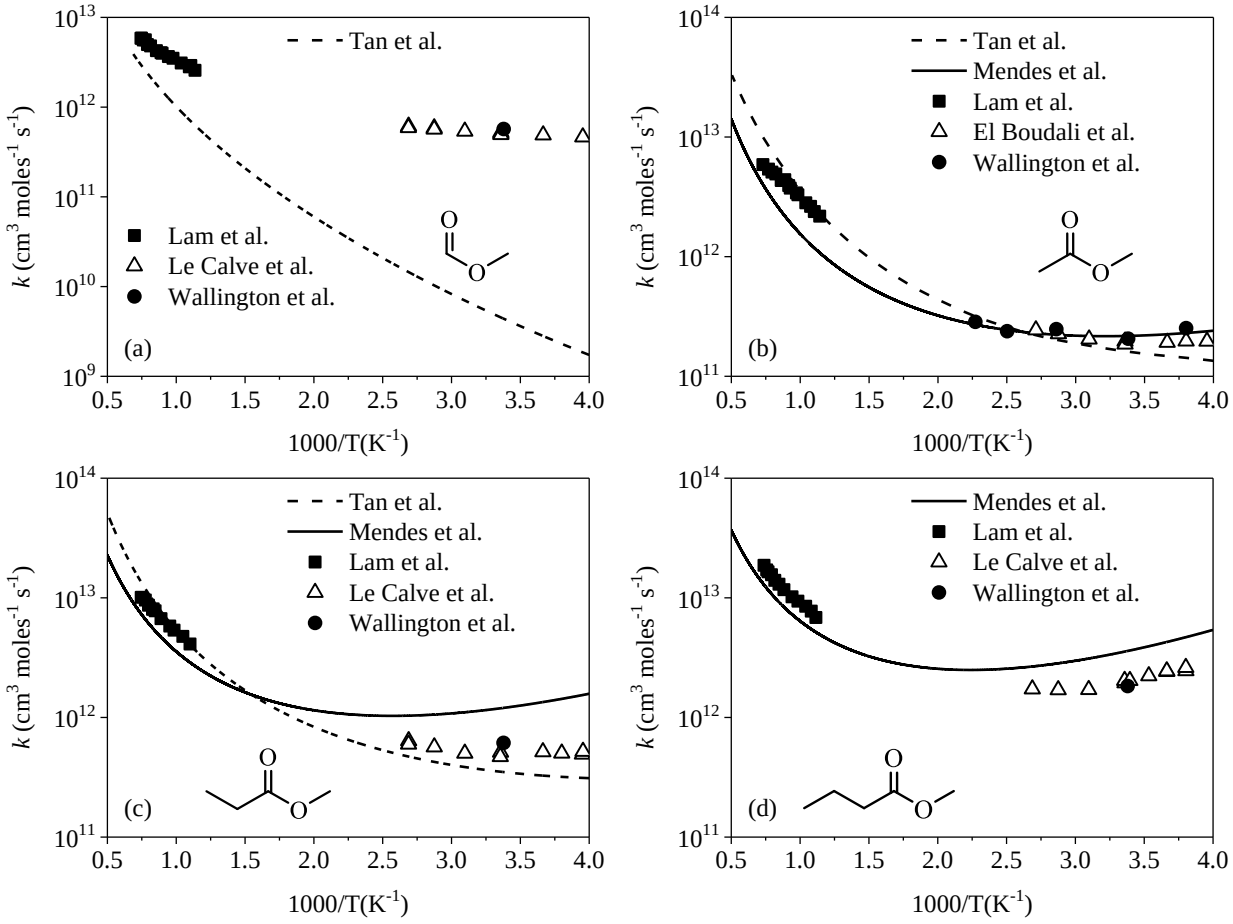

Figure 35. Rate coefficient measurements for H-abstraction by ȮH from methyl esters from Lam et al. [647], El Boudali et al. [649], Le Calve et al. [650, 652], and Wallington et al. [644] compared to *ab initio* calculations of Mendes et al. [620] and Tan et al. [646]. (a) methyl formate; (b) methyl acetate; (c) methyl propanoate; (d) methyl butanoate.

Shang et al. [654] utilized CCSD(T) methods to calculate rate coefficients and branching ratios for ȮH + methyl pentanoate → H_2O + Ṙ in the high-pressure limit from 200 – 2000 K. Geometry optimizations and frequency calculations were conducted using M06-2X/cc-pVTZ. Pre-reaction complex formation occurred in abstraction reactions with all carbon atoms on alkyl change. Branching fractions from 500 – 1000 K are competitive among α, γ, and β sites, accounting for 75 – 85%. Abstraction from δ carbon accounted for ~10% at 1000 K and ~5% at 500 K and was negligible from the methoxy site.

Wang and Ni [627] used CBS-QB3 methods and calculated high-pressure limit rate coefficients for ȮH-initiated H-abstraction from methyl pentanoate and five additional C6 methyl esters using conventional TST over a single transition state. The effect of the C=C bond position relative to the ester moiety was examined using methyl pentenoate isomers and two branched species were studied: methyl 2-methylbutanaote and methyl 2-methylbut-3-enoate. Similar to previous studies on H-abstraction, pre-

reaction complexes were identified between ȮH and the ester moiety at all sites except the terminal (δ) carbon due to weaker interactions at longer distance. Branching ratios in Wang and Ni [627] reveal that, in four of the six cases and regardless of C–H bond type (secondary, allylic, or vinylic), abstraction from β' is a major channel. Similar results are reflected in the calculations of Mendes et al. [620] for saturated methyl esters. Two exceptions in [627] were reactions with unsaturated esters: ȮH + methyl-4-pentenoate and ȮH + methyl 2-methylbut-3-enoate. In the former reaction, despite stronger C–H bond energy, abstraction at the two vinylic sites accounted for ~50% at 600 K and ~65% at 1000 K. In the latter, ȮH + methyl 2-methylbut-3-enoate, abstraction of primary hydrogen from the methyl group adjacent to the ester moiety and the lone tertiary hydrogen were the dominant abstraction sites. In both cases, abstraction of vinylic hydrogen from γ' and δ' carbon become the dominant channels towards 1000 K. Collectively, the site-specific abstraction comparisons of the C6 methyl esters in Wang and Ni [627] indicate that bond energies are not sufficient to predict branching fractions in reactions with ȮH.

Rate coefficients for H-abstraction by HOȮ are reported for methyl formate [645], methyl acetate [621, 648], methyl propanoate [621, 646], and methyl butanoate [621, 657]. In addition, Mendes et al. [621] computed *k*(T) for C5 methyl esters (methyl pentanoate and methyl iso-butanoate) and several acetate species (ethyl acetate, *n*-propyl acetate, and *iso*-propyl acetate). Kopp et al. [655] calculated rate coefficients for *n*-butyl formate, where, similar to reactions with OH, pre-reaction and product complexes were formed. **Figure 36** shows two examples from Mendes et al. [621] for HOȮ + methyl acetate.

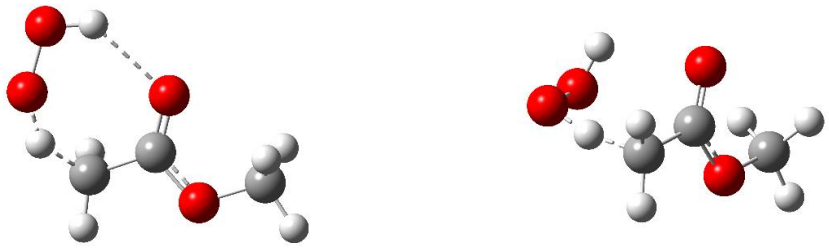

Figure 36. Transition states for in-plane hydrogen abstraction (left) and out-of-plane hydrogen abstraction (right) in reactions of hydroperoxyl with methyl acetate in Mendes et al. [621].

CCSD(T) and multireference-averaged coupled pair functional theory (MRACPF2) were utilized in Tan et al. [648] to calculate high-pressure limit rate coefficients for HOȮ + methyl acetate. Transition states for abstraction at both α and α' sites involved pre-reaction complex formation due to interactions with the oxygen atom in carbonyl group. Branching ratios for the two abstraction channels involving HOȮ were only moderately dependent on temperature. At 500 K, ~85% of abstraction occurred at the alkoxy group (i.e. α carbon) and ~15% from the methyl group (i.e. α' carbon). At 1000 K, abstraction from α carbon was ~78% and ~22% from α' carbon. Using CCSD(T) without MRACPF2, Mendes et al. [621] calculated similar total rate coefficients, yet sharply different branching ratios: ~63% from the methyl group and ~37% from the alkoxy group at 500 K, while at 1000 K branching ratios for the two channels were approximately equal. One notable difference between the two studies is the choice of either a single- or two-transition-state model (to account for complex-mediated steps). Tan et al. [648] used a single transition state in view of the large barrier (~17 kcal/mol above reactants). Similar energies were calculated on the potential energy

surfaces in Mendes et al. [621], however, a two-transition-state model was used. For the reactant complex, based on hindrance potential calculations, a ~2.5 kcal/mol barrier separated the two optimized transition states for in-plane and out-of-plane abstraction (cf. **Figure 36**). The lower of the two, in-plane abstraction where a hydrogen bond is formed between the hydrogen of the HOȮ radical and the oxygen atom of the carbonyl, was used as the abstraction transition state for the rate coefficient calculations.

Tan et al. [646] calculated high-pressure limit rate coefficients for abstraction reactions of HOȮ with methyl propanoate using several methods, including canonical- and variable reaction coordinate-transition state theory (VRC-TST) and multi-structure methods. Stationary point energies were calculated at the CCSD(T) and MRSDCI levels of theory. In contrast to prior calculations by Tan et al. [648] on methyl acetate + HOȮ, a two-transition state model was utilized to account for the role of complex formation during abstraction, which is important to note given the similarity of the rate coefficents (cf. **Figure 35c**) and branching ratios (**Figure 37**) with Mendes et al. [621], in which a two-transition-state model was also utilized. In both studies, abstraction of hydrogen by HOȮ occured primarily from α' carbon. Similar temperature dependence is predicted by both sets of calculations, and the major difference is a favoring of abstraction from α carbon over β carbon using the rate coefficents from Mendes et al. [621] (**Figure 37a**). The site-specific rate coefficients calculated in [621] were compared to analogous reactions in *n*-alkanes. For all types of abstraction, rate coefficients for HOȮ + methyl propanoate were lower than for the same type of H-abstraction in *n*-alkanes.

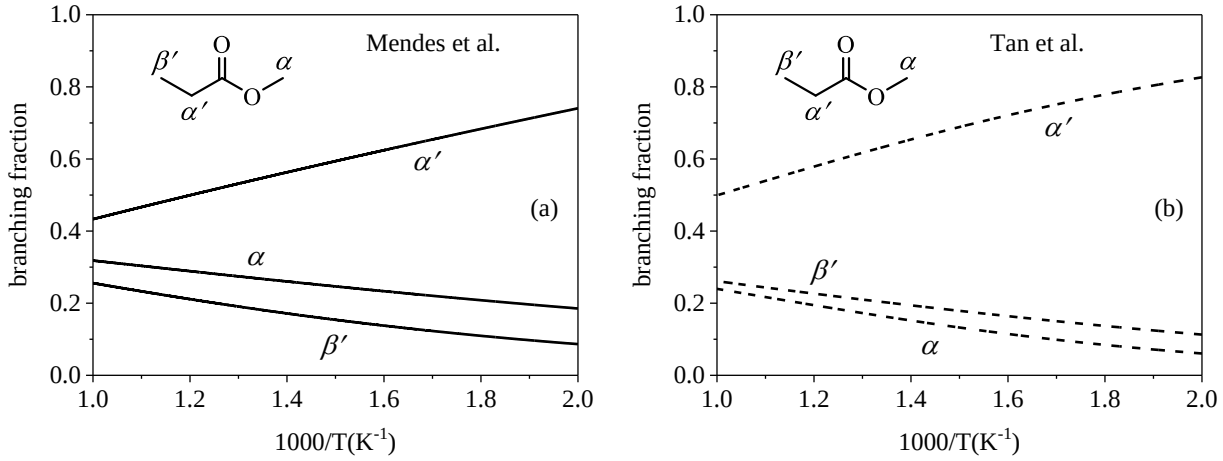

Figure 37. Comparison of branching fractions of abstraction reactions of methyl propanoate with HOȮ from α, α', and β' sites calculated in Mendes et al. [621] and Tan et al. [646].

The branching ratios in **Figure 37** are correlated approximately with C–H bond dissociation energy. However, similar to reactions with ȮH radicals, abstraction from the β' carbon by HOȮ is the major branching channel in reactions with larger esters. **Figure 38a** plots branching fractions calculated for HOȮ + methyl butanoate from the rate parameters in Mendes et al. [620]. The same trend is also reflected in the branching ratio calculations of Wang and Ni [627] on ȮH + esters. For example, in reactions of ȮH with methyl pentanoate, abstraction from β' site on the alkyl chain is the main channel below 800 K. While C–H bond energies near the ester moiety are lower than on the alkyl chain due to hyperconjugation, the stabilizing hydrogen bonding interaction facilitates abstraction from β' carbon. **Figure 38b** plots branching fractions from Meng et al. [657], which were calculated using transition state theory and accounted for

anharmonicity in low-frequency torsional modes using multistructural methods of Truhlar et al. [664, 665]. Stationary points were computed at the QCISD(T)/CBS//B3LYP/6-311++G(*d*,*p*) level of theory. Compared with Mendes et al. [620], barrier heights in Meng et al. [657] for abstraction from α' and β' are lower by ~1 kcal/mol and ~2 kcal/mol lower for abstraciton from γ', while the barrier for abstraction from α is higher by ~1 kcal/mol.

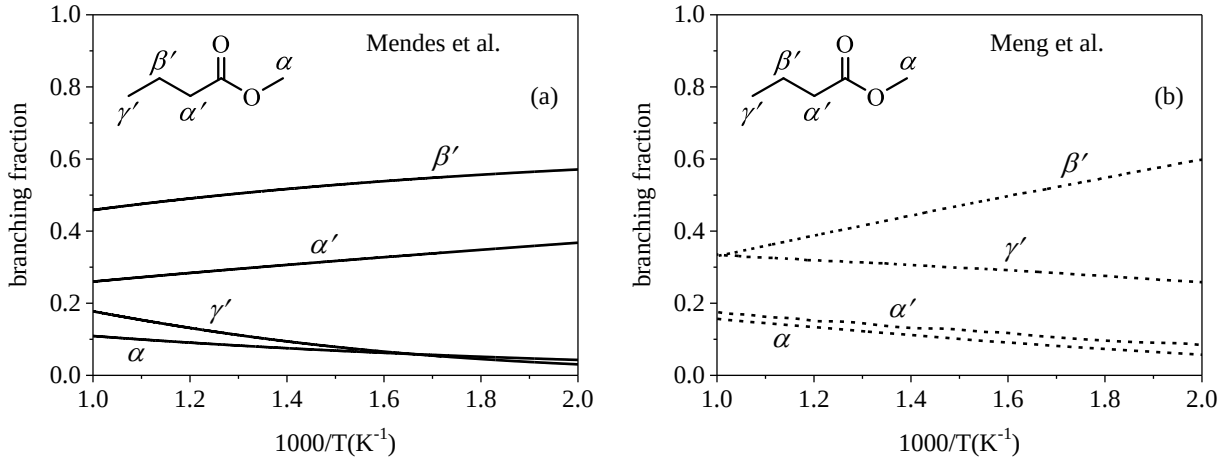

Figure 38. Branching fractions for H-abstraction from methyl butanoate by HOȮ from (a) Mendes et al. [621] and (b) Meng et al. [657].

Kopp et al. [655] calculated rate coefficients for HOȮ + *n*-butyl formate at the B2KPLYP/aug-cc-pVTZ level of theory. Extensive conformational analysis of the transition states revealed several distinct features on the potential energy surface. The lowest energy *n*-butyl formate conformer involves all carbon atoms lying in approximately the same plane, with an out-of-plane ester moiety (**Figure 39**) that enables hydrogen bonding interaction of either of the ester oxygens with abstracting HOȮ at the γ and δ positions. The latter position is notable because for abstractions more than three carbon atoms away, the functional group is often considered irrelevant. The transition state in **Figure 39** is the lowest energy pathway for abstraction from the δ carbon; the barrier to hydrogen abstraction from δ carbon was higher by 1.9 kcal/mol when involving hydrogen pointing away from the ester group. Barrier heights for abstraction depended on the type of hydrogen bonding. For example, a ~2 kcal/mol difference was noted for δ carbon when HOȮ interacts with the carbonyl group compared to hydrogen bonding with the oxygen atom in the alkoxy group. Abstraction of hydrogen in the formate position is dominant (~45%) and, as in abstraction reactions with larger esters [620, 627], branching towards β radicals is a major channel (~30%) due to the formation of stabilizing pre-reaction complex [655].

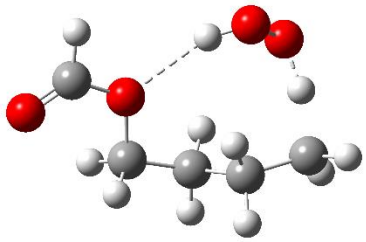

Figure 39. Transition state for H-abstraction from δ' carbon in *n*-butyl formate from Kopp et al. [655], optimized at the B2KPLYP/cc-pVTZ level of theory. The alkyl chain is approximately planar, which enables hydrogen-bonding between HOȮ and the oxygen atom in the alkoxy group.

3.2.2. reactions of initial ester radicals with O_2

Studies focusing on rate coefficients and reaction mechanisms of ester radicals with O_2 include methyl acetate [639], methyl propanoate [605, 666], methyl butanoate [602-606], methyl but-2-enoate [667], methyl pentanoate [602, 605], methyl octanoate [668], and ethyl butanoate [606]. With the exception of MPIMS experiments [605, 606], the majority are quantum chemical studies [602-604, 639, 666, 668] for which CBS-QB3 is the most common level of theory used for electronic structure calculations.

Mai et al. [639] calculated potential energy surfaces for methyl acetate radicals with O_2 at the CBS-QB3 level of theory. Several ȮOOH decomposition channels were considered, including cyclic ether + ȮH, intramolecular ȮH-transfer (producing an ȮH-substituted alkoxy radical), and carbonyl + ȮH. Pressure-dependent rate coefficients were calculated using QRRK theory. For the initial vinoxylic radical $\dot{C}H_2C(=O)OCH_3$ the isomerization to ȮOOH lies above the R + O_2 entrance channel and does not effectively compete with redissociation to reactants; only for the initial radical on the methoxy side is there significant isomerization to ȮOOH.

Reaction mechanisms and rate coefficients were computed in Le et al. [666] for methyl propanoate radicals with O_2. Potential energy calculations were conducted using CBS-QB3 for 36 reaction pathways across the three Ṙ + O_2 surfaces. In addition to cyclic ether, conjugate alkene, intramolecular ȮH-transfer in ȮOOH, and carbonyl product channels, barrier heights for C–C β-scission and keto-enol tautomerization of ȮOOH were calculated. Arrhenius rate parameters for rate coefficients in the high-pressure limit were calculated using canonical transition state theory. Using a similar approach to Mai et al. [639], pressure-dependent rate coefficients were calculated using QRRK theory. Le et al. [666] compared rate coefficients of methyl propanoate radical reactions with analogous reactions in alkyl + O_2 systems [408, 409], calculated at the same level of theory (CBS-QB3). Two notable differences were revealed (**Figure 40**). First, rates of ȮOOH reverse-isomerization to ROȮ via a 5-membered transition state were ~10^1 higher at 500 K for ester-derived ȮOOH than for analogous alkyl-derived radicals, particularly when the peroxy group is bound to secondary carbon in the β position (**Figure 40a**). Second, concerted elimination of HOȮ from both primary and secondary peroxy radicals of methyl propanoate were higher by 10^1 at 500 K than for alkylperoxy radicals (**Figure 40b**). In both cases, at 1000 K, the difference between the two rate coefficients decreases to approximately a factor of 2, with the rate coefficients for the ester-related reactions remaining higher.

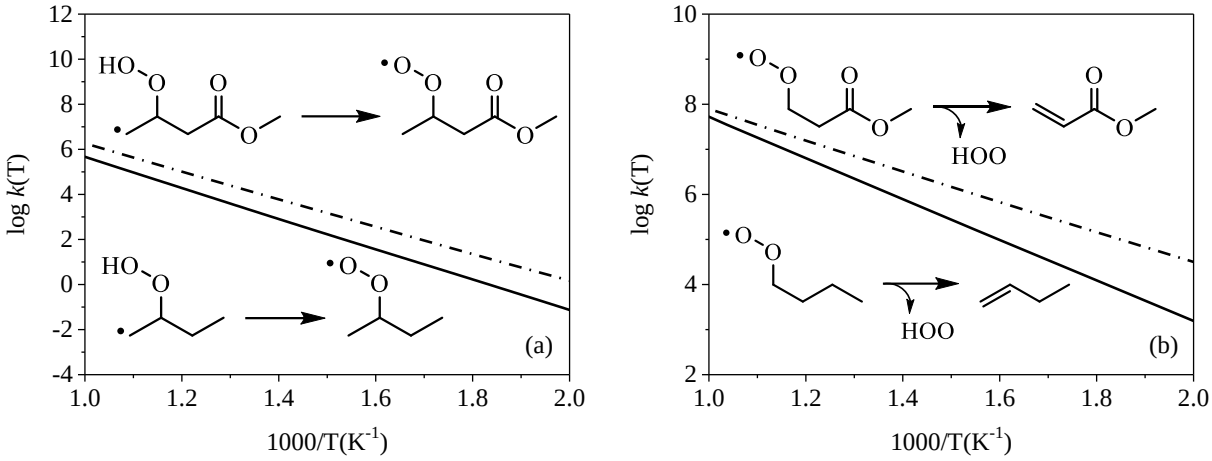

Figure 40. Comparison of rate reaction rates for (a) ȮOOH → ROȮ and (b) ROȮ → alkene + HOȮ between ester-peroxy radicals derived from methyl propanoate and reactions in alkylperoxy radicals [666].

Tao and Lin [603] used the G3MP2B3 composite method to calculate potential energy surfaces for methyl butanoate radicals reactions with O_2 and for reactions of the four ester-peroxy radicals with HOȮ. The latter type, initially proposed in Fisher et al. [669], form hydroperoxy-substituted methyl butanoates that promote chain reaction via barrierless dissociation into ȮH + alkoxy radicals. In total, high-pressure limit rate coefficients and Arrhenius parameters were calculated for 125 reactions related to Ṙ, ROȮ, and ROȮ + HOȮ chemistry of methyl butanoate. Rate coefficients were compared for ROȮ → ȮOOH and ROȮ → alkene + HOȮ in methyl butanoate to analogous reactions in alkanes. For isomerization on the alkyl chain, in exclusion of the ester moiety, rate coefficients were within a factor of 2. However, when incorporated in the transition state, isomerization rates were lower by ~10^2 at 500 K and by ~10^1 at 750 K.

Barrier heights for isomeration of methyl butanoate peroxy radicals in Tao and Lin [603] were similar to the calculations in Hayes and Burgess [602]. However, for reactions involving 6- and 7-membered transition states, isomerization rates below 1000 K differed by several orders of magnitude and were ascribed to differences in pre-exponential factors. Smaller discrepancies with rates from the detailed chemical kinetics mechanism of Herbinet et al. [670] were also noted. For ROȮ + HOȮ rate coefficients, which exhibit only moderate temperature dependence, disparities with the detailed mechanisms of Fisher et al. [669] and Herbinet et al. [670] were approximately an order of magnitude.

Jiao et al. [604] calculated potential energy surfaces for ȮOOH + O_2 reactions in methyl butanoate at the CBS-QB3 level of theory and included cyclic ether formation, in addition to conventional ȮOQOOH pathways leading to alkoxy + 2 ȮH (i.e. chain-branching). From calculations of high-pressure limit rate coefficients for 27 methyl butanoate ȮOQOOH isomerization reactions, Jiao et al. [604] suggested that peroxy radical interconversion rates (**Figure 41**) could be considerable, even those requiring 8-membered transition states and larger.

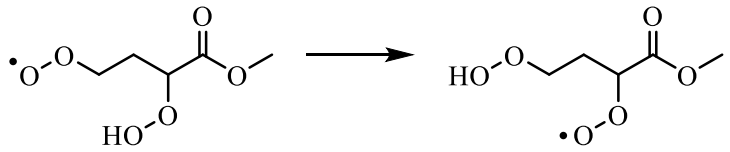

Figure 41. Peroxy radical interconversion reaction in methyl butanoate.

Muller et al. [605] employed MPIMS with chlorine-initiated oxidation of three methyl esters – propanoate, butanoate, and pentanoate – at 550 K and 650 K to examine product formation and quantify isomer ratios of the various alkenoate isomers produced via HOȮ-formation channels. For both methyl butanoate and methyl pentanoate, C=C bond formation from HOȮ-elimination is strongly favored on the carbon closest to the ester moiety, which is consistent with Tao and Lin [603]. In the former, methyl-2-butenoate was the only conjugate alkenoate produced at either temperature, while for methyl pentanoate the analogous species (methyl-2-pentenoate) was the only isomer at 550 K. At 650 K, the other two isomers also contributed, yet methyl-2-pentenoate remained the dominant pathway (isomer ratio of ~60%). Potential energy surfaces of peroxy radical decomposition were calculated at the CBS-QB3 level of theory and included select cyclic ether + ȮH channels in addition to conjugate alkene + HOȮ channels. Resonance-stabilized Q̇OOH were proposed as the most likely cyclic ether formation pathways. Ion signals were detected at the mass-to-charge ratio (m/z) corresponding to the cyclic ether co-product of chain-propagating OH-elimination from Q̇OOH. The isomeric composition was not determined, although the observed fragment ion pattern in methyl pentanoate oxidation was consistent with a contribution from methyl-tetrahydrofuran-2-carboxylate, which would be formed via a resonance-stabilized Q̇OOH.

In another low-pressure MPIMS study, Czekner et al. [606] studied product formation from chlorine-initiated oxidation of methyl butanoate and ethyl butanoate at 550 K. Potential energy surface calculations of HOȮ-elimination pathways from peroxy radicals and several types of β-scission channels were conducted on the two esters using CBS-QB3. Similar to Muller et al. [605], ion signal was detected at the m/z corresponding to cyclic ethers, but the isomer was not identified. Two additional types of pathways were postulated to explain the observed production of aldehydes from methyl butanoate and ethyl butanoate oxidation: (1) elimination of aldehyde from ROȮ derived from α radicals (where the radical site resides on the alkoxy portion of the ester), and (2) a bimolecular reaction between ROȮ and HOȮ radicals leading to a hydroperoxy-substituted ester that decomposes to aldehyde + resonance-stabilized ester radical. **Figure 42** depicts the pathway leading to acetaldehyde + ester radical. An analogous pathway to formaldehyde was also considered, where the peroxy group is located on the terminal carbon of the alkyl group [606].

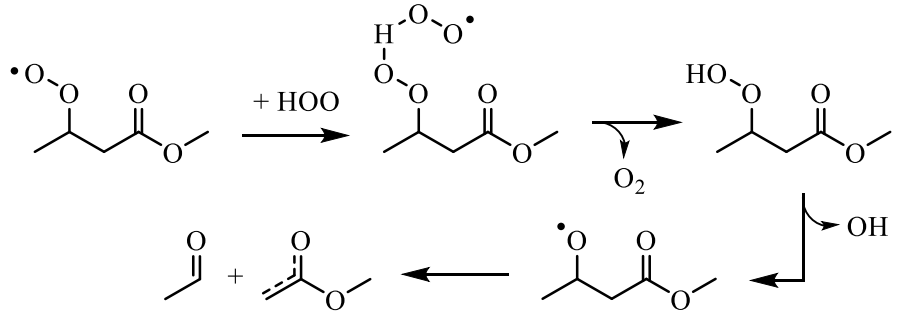

Figure 42. Bimolecular reaction pathway to aldehyde formation in methyl ester oxidation [606].

Tao and Lin [668] calculated unimolecular reaction rates of three pathways for methyl octanoate peroxy radicals: dissociation ($ROO \rightarrow R + O_2$), isomerization to QOOH, and concerted elimination of HOO. Rates were caculated in the high-pressure limit using canonical transition state theory with Eckart tunneling corrections and in the fall-off region using RRKM theory. Branching ratio analysis revealed that ROO → QOOH, primarily via 6-membered transition states, were the dominant reactions below ~800 K, above which dissociation reactions became competitive. One exception involved the radical in which the peroxy group is bound to the alkoxy site (α), which undergoes a 9-membered transition state and abstracts hydrogen from carbon in the γ' position relative to the ester group (cf. **Figure 30**). Branching ratios predicted in the high-pressure limit showed significant differences with the balance between dissociation and isomerization employed in chemical kinetics mechanisms [670, 671], which had been derived using rate-rules and structure-activity relationships. Tao and Lin [668] incorporated their high-pressure-limit rate parameters into the detailed mechanism of Togbé et al. [671], and found improved predictions, particularly in the NTC region, for methyl octanoate consumption profiles from JSR experiments, suggesting that direct *ab initio* calculations can improve on analogy-based approaches for functionalized molecules.

For resonance stabilized radicals, the lower stability of the peroxy radical product may limit the significance of their reaction with O_2 under combustion conditions. Joshi et al. [667] measured an upper limit rate coefficient of $7.5 \cdot 10^{-17}$ cm^3 $molec.^{-1}$ s^{-1} for reaction of the allylic radical ($\dot{C}H_2CHCHC(=O)OCH_3$) of methyl but-2-enoate with O_2 at 600 K. Because of the inefficient reaction with O_2, unimolecular reactions were considered as a primary consumption channel. They calculated a favorable isomerization step via ring-closure over a barrier of ~35 kcal/mol, which led subsequently to furan-2(5*H*)-one + $\dot{C}H_3$ over a barrier of 21.2 kcal/mol; master equation modeling using MESMER [672] could match their experiments only with a substantial lowering of the barriers to reaction.

3.2.3.speciation from thermally initiated experiments

Speciation measurements below 1000 K include flow reactor experiments on numerous methyl esters: methyl formate [641], methyl acetate [673], methyl butanoate [602-606], methyl *trans*-2-butenoate [609], methyl hexanoate [612, 674], methyl *trans*-3-hexenoate [619, 675], methyl heptanoate [623], methyl octanoate [676, 677], methyl *trans*-2-octenoate [676, 677], methyl decanoate [624], methyl palmitate [678], methyl stearate [618], methyl oleate [618, 678], and methyl linoleate [618, 678]. In contrast, only two low-temperature speciation studies exist for ethyl esters: laminar flow reactor experiments of Bennadji et al. [679] on ethyl butanoate, and JSR experiments on ethyl pentanoate in Dayma et al. [622]. Similarly, Dayma et al. [680] conducted the only speciation study on a propyl ester, propyl acetate. Several ester-based blended studies are also reported [625, 671, 681-683].

Dooley et al. [641] studied the oxidation of methyl formate using a variable-pressure flow reactor at 3 atm and 900 K and developed a detailed chemical kinetics mechanism, which included O_2-addition reactions with initial ester radicals $H_2\dot{C}OCHO$ and $H_3COC\dot{O}$. Two major products were methanol and formaldehyde, the latter of which was produced via two primary mechanisms: (1) hydroxymethyl ($H_2\dot{C}OH$) + O_2 yielding $HO\dot{O}$ + CH_2O and (2) $H_2\dot{C}OCHO$ + $HO\dot{O}$. Concerted elimination of CO was a minor consumption channel of methyl formate at 900 K (< 5%), yet was responsible for the majority of CH_3OH formation, which was the source for $H_2\dot{C}OH$, and accounted for ~50% of formaldehyde production.

Modeling the chemical kinetics of methyl formate oxidation and other small esters, including methyl acetate [673], is important to understanding the role of the ester moiety. Because of the initial perception [669],

based on chemical kinetics models that predicted similar ignition behavior to practical biodiesel, several studies examined the low-temperature oxidation chemistry of methyl butanoate using JSR experiments [607-611]. As evidenced in species profile measurements [608, 609], NTC behavior was not observed. As a result, methyl butanoate is no longer considered a biodiesel surrogate and subsequent studies examined larger saturated esters [612, 618, 623, 624, 674, 676, 677].

With increasing length of the alkyl chain in esters, low-temperature oxidation pathways become similar to those of the analogous hydrocarbon, and the impact of the functional group becomes diminished [683]. Isomerization reactions and decomposition of ester radicals becomes important with increasing alkyl chain length, as noted in the JSR studies on methyl pentanoate and methyl hexanoate oxidation in Dayma et al. [622, 623], on methyl decanoate oxidation in Glaude et al. [624], and in quantum chemical calculations [684, 685]. Methyl esters with an alkyl chain larger than five carbon atoms (i.e. methyl pentanoate and larger) exhibit clear NTC behavior, and because of the propensity of larger alkyl chains to undergo C–C β-scission reactions, alkane chemistry is an integral part of methyl ester oxidation [622-624].

The alkyl chain of practical methyl esters in biodiesel, such as methyl linoleate, contains unsaturated carbon, which impacts low-temperature chain-branching due to lower O_2-addition rates to allylic radical sites and radical-addition reactions, similar to alkenes [60, 686-689]. Zhang et al. [619] studied low-temperature oxidation of methyl trans-3-hexenoate using a jet-stirred reactor at 10 atm and compared to measurements of the saturated ester, methyl hexanoate, at the same conditions as Dayma et al. [674] (**Figure 43**). The presence of the single C=C bond completely inhibits chain-branching below 650 K and the diminished peroxy radical chemistry prevents NTC behavior typically associated with saturated species, suggesting that the C=C bond inhibits either the formation of stabilized peroxy radical adducts or subsequent isomerization reactions ($RO\dot{O} \rightleftharpoons \dot{Q}OOH$).

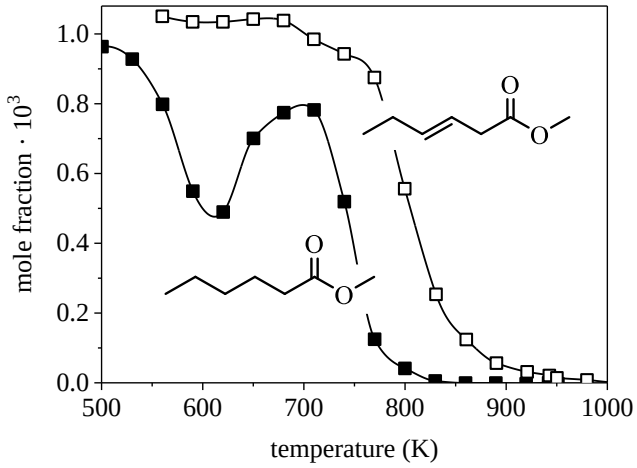

Figure 43. Consumption profiles from JSR experiments: methyl hexanoate (ϕ = 0.5, residence time = 1000 ms), Dayma et al. [674], and methyl *trans*-3-hexenoate (ϕ = 0.6, residence time = 700 ms), Zhang et al. [619]. Solid lines are Akima spline interpolations added for visual aid.

Rodriguez et al. [618] also examined the effect of unsaturated carbon in JSR experiments conducted at 1 atm from 500 – 1050 K on three species found in practical biodiesel (**Figure 44**). Consumption profiles of methyl stearate (18:0), methyl oleate (18:1), and methyl linoleate (18:2) exhibited NTC behavior (**Figure 45**) that confirms prior predictions in Westbrook et al. [626] and Dagaut et al. [619] that the presence of

unsaturated carbon diminishes the role of peroxy radical chemistry in ester oxidation, i.e. decreased NTC behavior with increasing unsaturation. As observed in the oxidation of unsaturated alcohols [506], product pairs from Waddington-type reactions were formed in the two unsaturated esters, e.g. nonanal and methyl 10-oxodecanoate in the case of methyl oleate, which indicates that ȮH-addition reactions play a role in ester oxidation.

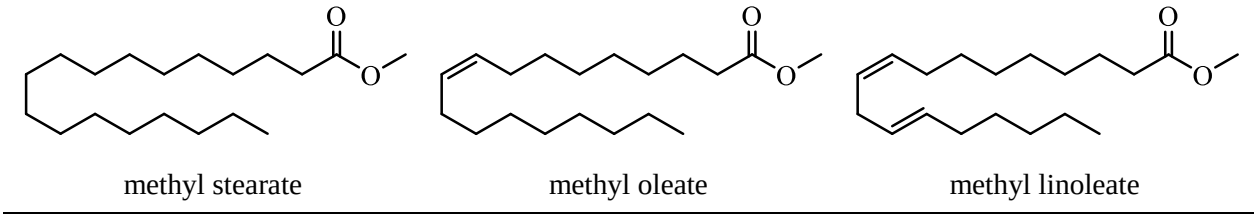

Figure 44. Molecular structure of C18 methyl esters.

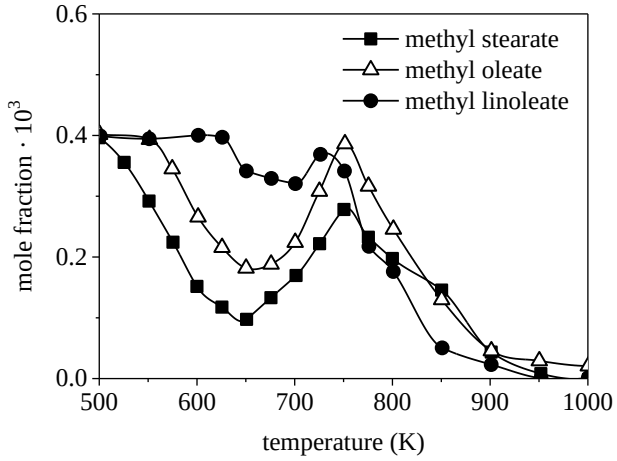

Figure 45. Mole fractions from stoichiometric oxidation of C18 methyl esters at 1 atm and a residence time of 2000 ms measured in JSR experiments of Rodriguez et al. [618].

Speciation measurements on methyl oleate oxidation in a JSR at 1 atm by Bax et al. [625] quantified products from radical-addition reactions to the single C=C bond in methyl oleate, namely methyl 10-oxooctadecanoate and methyl 8-(3-octyloxiran-2-yl)octanoate. The oxirane was proposed to arise from an epoxidation reaction that consumes HOȮ and produces cyclic ether + ȮH (**Figure 46**). Cagnina et al. [656] calculated stationary points for epoxidation of methyl *trans*-3-hexenoate by HOȮ at the CCSD(T)-F12//M06-2X level and applied RRKM master equation to derive rate coefficients. The results were consistent with rate rules for HOȮ + alkene in Villano et al. [407] and with measurements from Walker et al. [690] on *trans*-2-hexene oxidation. Cagnina et al. [656] incorporated their rate coefficients into the mechanism of Wagnon et al. [675] and predicted oxirane species that were qualitatively consistent with the experiments of Bax et al. [625]. Epoxidation rates are similar to H-abstraction reactions by HOȮ at the same temperature [621]. For example, at 100 atm, the rate coefficient for epoxidation at 800 K is $4.0 \cdot 10^{-17}$ cm^3 s^{-1} and for H-abstraction from methyl butanoate in the high-pressure limit, $k(800\ K) = 3.4 \cdot 10^{-17}$ cm^3 s^{-1}. Noting that methyl oleate contains only one C=C bond, the importance of epoxidation reactions may become more significant with polyunsaturated esters, such as methyl linoleate or methyl linolenate.

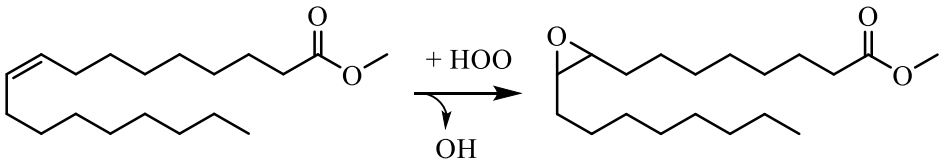

Figure 46. Epoxidation reaction in methyl oleate oxidation proposed in Bax et al. [625].

Because of the incremental degree of unsaturation among the three species, the experiments of Rodriguez et al. [618] revealed several details related to the effect of C=C bonds in the alkyl chain on oxidation pathways in esters. First, low-temperature formaldehyde production was evident only in the saturated ester, methyl stearate, and in the range 600 – 650 K. From prior JSR experiments on methyl butanoate [608] and methyl heptanoate [623], formaldehyde produced below 1000 K is ascribed primarily to the decomposition of ester radicals via C–O bond-scission, wherein the unpaired electron is localized on the alkoxy group. Dayma et al. [674], in experiments on methyl hexanoate at 10 atm, proposed a ȮOOH-mediated pathway involving the formation of 5-butyl-1,3-dioxolan-4-one as a precursor to formaldehyde. Both types of reactions imply that formaldehyde is derived primarily from reactions involving the ester moiety. Second, an increase in the number of C=C bonds from methyl stearate (C18:0) to methyl linoleate (C18:2) correlated with a reduction in the number of 1-alkene species. In methyl stearate oxidation, 1-butene up to 1-hexadecene were produced, which is likely due to the length of the alkyl chain and increased number of pathways to different alkene species via C–C β-scission reactions. Methyl linoleate oxidation, in contrast, produced only 1-butene. Third, diene formation near ~850 K was more abundant in Rodriguez et al. [618] for methyl linoleate than for methyl stearate. To explain the observed increase in the context of unsaturated carbon, a six-center decomposition reaction starting was postulated (**Figure 47**) wherein concerted C–C bond-scission reactions involving the C=C bond lead to saturated ester + diene. A similar, four-center reaction was postulated as a mechanism for the production of 1-alkene and unsaturated esters.

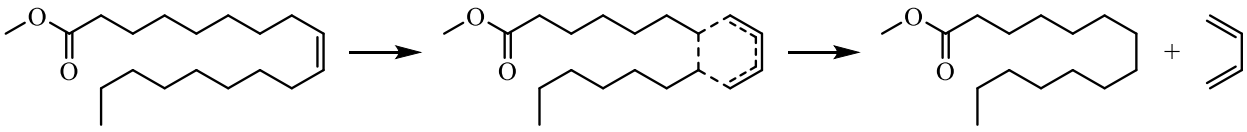

Figure 47. Six-membered molecular dissociation reaction of methyl oleate yielding 1,3-butadiene [618].

Other dissociation reactions are facilitated specifically by the ester functional group, including the formation of carboxylic acids by ethene elimination in ethyl esters [631], as observed in JSR experiments by Bennadji et al. [679] on ethyl butanoate (**Figure 48**) and by Dayma et al. [622] on ethyl pentanoate. Metcalfe et al. [691] characterized the role of ethene elimination in ethyl propanoate oxidation and proposed that the greater reactivity of ethyl propanoate over the isomeric methyl butanoate reflected the reactivity of the acid and ethene products of this molecular elimination [613].

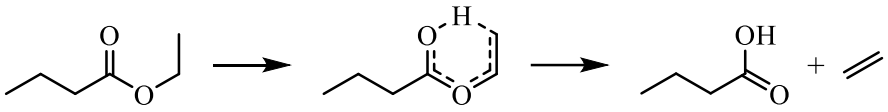

Figure 48. Six-membered molecular dissociation of ethyl butanoate to butanoic acid and ethene proposed in Bennadji et al. [679].

3.2.4. influence of ester oxidation pathways on autoignition chemistry

Early studies on the temperature dependence of ester oxidation by Parsons et al. [692-694] and Hoare et al. [695] showed NTC behavior in ethyl formate, n-propyl formate, and methyl butanoate, although more recent JSR experiments [607-611] show only single-stage oxidation for methyl butanoate. More recent studies on low-temperature autoignition of esters involve ignition delay time measurements from either shock-tube or rapid-compression machine experiments. The chemical mechanisms differentiating one ester from another are inferred from analysis via detailed chemical kinetics mechanisms. The two sections below review ignition delay times and chemical kinetics modeling of esters, focusing primarily on reactions below 1000 K. Because several extensive reviews on the combustion of esters from Coniglio et al. [696], Westbrook et al. [697], and Lai et al. [698] provide in-depth analysis of chemical kinetics mechanism development, only the mechanisms published subsequent to those reviews are discussed in *Section 3.2.4.2*.

3.2.4.1. ignition delay time measurements

Ignition delay time measurements are reported for a large number of esters (**Table 2**), only a limited number of which are below 1000 K. For ethyl esters, only four ignition studies exist and three are restricted to high-temperature shock tube measurements. One exception, the RCM experiments of Walton et al. [615], measured ethyl propanoate ignition at 10 atm from 988 – 1117 K to compare with methyl butanoate. The RCM measurements of Dooley et al. [614] from 640 – 950 K and from 10 – 40 atm confirmed that low-temperature chain-branching is not significant in methyl butanoate, as evident from the absence of an NTC region, and suggested that larger methyl esters are more appropriate for use as a biodiesel surrogate, as noted previously in the JSR experiments of Gäil et al. [608]. In the RCM experiments of Minetti et al. [612] near 15 atm, no ignition was observed below 800 K, above which autoignition occurred in a single stage. Other ignition delay time experiments on methyl butanoate provided additional confirmation [610, 615, 617].

Figure 49a compares ignition delay times of methyl butanoate from Dooley et al. [614] to *n*-butane at 10 atm. Above ~875 K the ignition delay times of methyl butanoate are shorter by a factor of ~10 than for *n*-butane, which may arise from higher rates of formation of HOȮ radicals from oxidation reactions of the ester. The impact of HOȮ on ignition is related to hydrogen peroxide chemistry – at higher [HOȮ], abstraction reactions become increasingly important and contribute to higher concentrations of hydrogen peroxide. With increasing temperature, the chain-branching step via $H_2O_2 \rightarrow \dot{O}H + \dot{O}H$ may cause the difference in **Figure 49a**.

Figure 49b compares *n*-butane ignition delay times at 20 atm from Healy et al. [96] to measurements of *n*-butyl formate ignition from Vranckx et al. [222]. NTC behavior is weaker for *n*-butyl formate for the conditions in **Figure 49b**. In comparison with methyl butanoate, one potential explanation for the shorter

ignition times below 750 K for *n*-butyl formate concerns ȮOOH formation pathways. In contrast to methyl butanoate, seven-membered transition states for ROȮ → ȮOOH are possible on the alkyl chain for *n*-butyl formate. The additional pathway, which is favorable entropically and energetically, may divert a portion of the flux of ROȮ radicals to chain-propagation pathways via cyclic ether + ȮH or to second-O_2-addition reactions over the chain-inhibiting step $\dot{R} + O_2 \rightarrow$ conjugate alkene + HOȮ. As a result, lower concentration of hydroperoxyl radicals and higher concentration of ȮH produced from *n*-butyl formate compared to methyl butanoate increases the rate of oxidation.

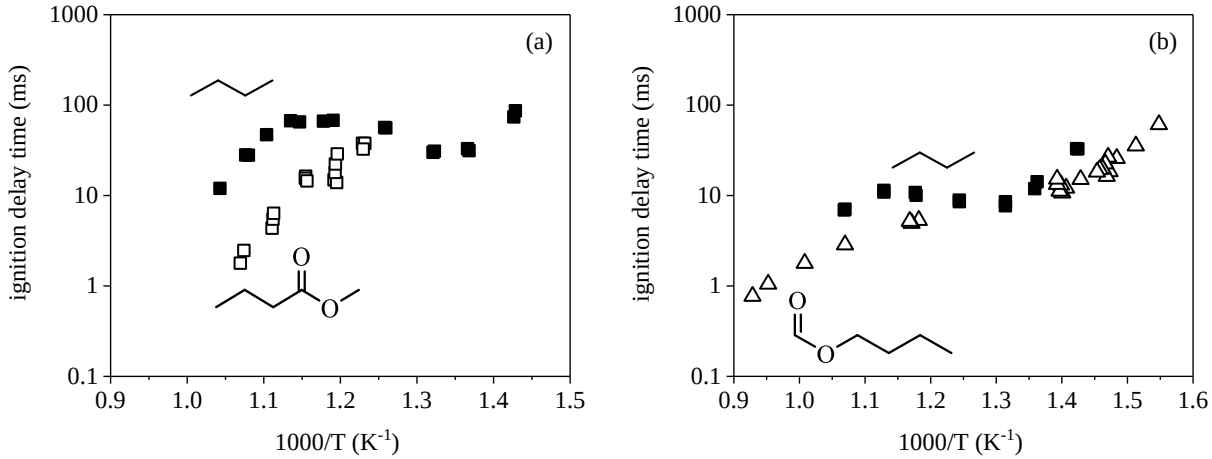

Figure 49. Comparison of stoichiometric ignition delay times at (a) 10 atm and (b) 20 atm for *n*-butane (Healy et al. [96]) and two $C_5H_{10}O_2$ esters: methyl butanoate (Dooley et al. [614]) and *n*-butyl formate (Vranckx et al. [222]).

Table 2. Ignition delay times studies of single-component esters.

species	*reference*
methyl esters	
methyl formate	[616, 641]
methyl acetate	[616]
methyl propanoate	[616, 699, 700]
methyl 2-propenoate	[701]
methyl butanoate	[610-617]
methyl (*E*)-2-butenoate	[701]
methyl pentanoate	[612, 702]
methyl hexanoate	[612]
methyl *trans*-3-hexenoate	[675, 703]
methyl heptanoate	[612]
methyl octanoate	[704]
methyl decanoate	[364, 705-707]
methyl 9-decenoate	[708]
methyl dodecanoate	[705]
methyl tetradecanoate	[705]
methyl hexadecanoate	[705]
ethyl esters	
ethyl ethanoate	[709]
ethyl propanoate	[613, 615, 709]

methyl (*E*)-2-butenoate [701]
ethyl (*E*)-2-butenoate [701]
butyl esters
n-butyl formate [222]

Methyl pentanoate is the smallest methyl ester that exhibits NTC behavior [612, 702]. RCM measurements of Weber et al. [702] conducted at 15 atm and 30 atm and from 680 – 1050 K revealed significant NTC behavior and from a comparison of ignition trends with *n*-pentane [710, 711] and with 1-pentanol [98], the authors concluded that the ester functional group shifts the NTC region towards lower temperatures. Similar conclusions were drawn in Minetti et al. [612], who measured ignition delay from 4 – 20 atm and 650 – 850 K for a series of saturated methyl esters (methyl butanoate, methyl pentanoate, methyl hexanoate, and methyl heptanoate) using a rapid compression machine. Second-stage ignition delay times correlated with alkyl chain length – methyl heptanoate producing the shortest ignition delay times at a given pressure. First-stage and second-stage ignition times of methyl hexanoate and *n*-alkanes (*n*-butane, *n*-pentane, and *n*-heptane) were measured at an average pressure of 8 atm (**Figure 50**), which revealed several implications of the ester group. First-stage ignition for *n*-pentane was longer than methyl hexanoate by a factor of ~3 indicating that, for the same alkyl chain length, the ester group promotes first-stage ignition. Moreover, the start of NTC behavior begins near 700 K for methyl hexanoate and ~775 K for *n*-pentane. Low-temperature ignition of methyl hexanoate was more closely approximated by *n*-heptane, both species exhibiting a nearly identical lower limit of temperature for ignition (~620 K) [612] and similar first-stage ignition delay times were similar. Second-stage ignition times diverge with increasing temperature, however. At 750 K, the upper limit for comparison, ignition times for methyl hexanoate are nearly a factor of 10 longer than for *n*-heptane.

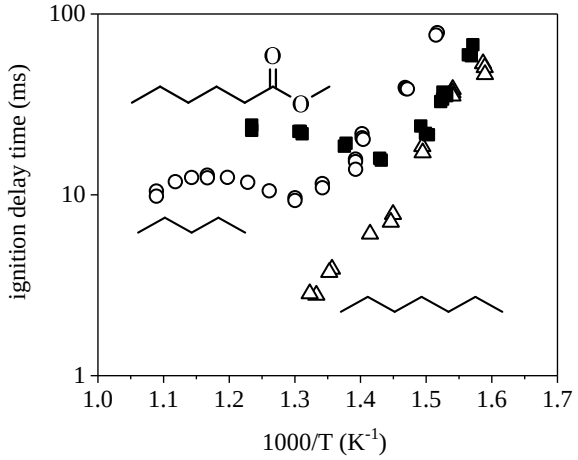

Figure 50. Stoichiometric ignition delay times from Minetti et al. [612] for methyl hexanoate, *n*-pentane, and *n*-heptane at an average pressure of 8 atm.

From the JSR experiments of Dagaut et al. [619] on trans-methyl-3-hexenoate, in which species profiles did not exhibit two-stage oxidation, the presence of a single C=C bond likely inhibits NTC behavior. In larger esters, the effects of a single C=C bond on ignition is less pronounced (**Figure 51**). Oehlschlaeger et al. [708] measured ignition delay times of methyl decanoate, methyl *trans*-9-decenoate, and a 50/50 blend of methyl *trans*-5-decenoate and methyl *trans*-6-decenoate at an average pressure of 20 atm and from 700

– 1300 K. Ignition delays for the saturated ester and methyl 9-decenoate overlap one another within experimental uncertainty and share the same NTC range: ~700 – 870 K. The methyl 5-/6-decenoate blend displayed weak NTC behavior and is within a factor of 2 of methyl decanoate ignition times [707] in the NTC region. The ignition trends indicate that the proximity of C=C bonds to the ester moiety weakly affects ignition, due perhaps to a restricted number of reaction pathways for peroxy radicals.

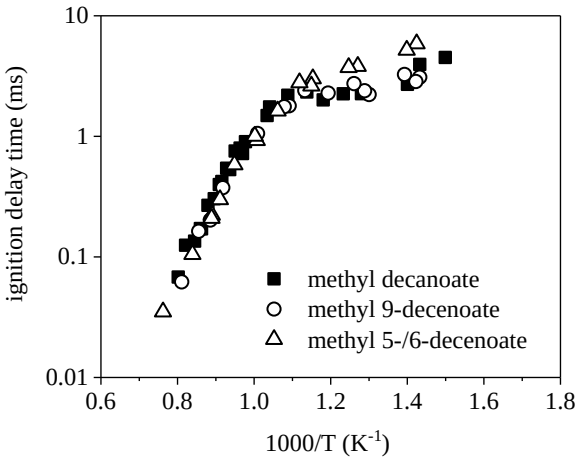

Figure 51. Stoichiometric ignition delay times for methyl decanoate and methyl decenoate isomers from shock tube measurements of Oehlschlaeger et al. [706-708].

3.2.4.2. detailed chemical kinetics mechanisms

Since the mechanism development in Fisher et al. [669] for methyl formate and methyl butanoate, many mechanisms were developed for numerous esters (**Table 3**). Two extensive reviews by Lai et al. [698] and by Coniglio et al. [696] summarized the progress on methyl ester combustion and several mechanisms developed since include: methyl propanoate (Felsmann et al. [712]), methyl pentanoate (Weber et al. [702]), methyl trans-3-hexenoate (Wagnon et al. [675] and Dagaut et al. [619]), and n-butyl formate (Vranckx et al. [222]).

Table 3. Chemical kinetics mechanisms of single-component methyl esters that include peroxy radical chemistry.

species	*reference*
methyl esters	
methyl formate	[641, 669]
methyl acetate	[673, 713, 714]
methyl propanoate	[699, 712]
methyl butanoate	[389, 608, 609, 611, 613-615, 669, 715]
methyl *trans*-2-butenoate	[609]
methyl pentanoate	[702]
methyl hexanoate	[624, 674]
methyl *trans*-3-hexenoate	[619, 675, 703]
methyl heptanoate	[623, 624]
methyl octanoate	[671, 676, 677, 716]
methyl *trans*-2-octenoate	[676, 677]

methyl decanoate	[381, 388, 624, 670, 717, 718]
methyl dodecanoate	[381]
methyl tetradecanoate	[381]
methyl palmitate	[377, 381]
methyl stearate	[377, 381, 618, 719]
methyl oleate	[377, 618, 719]
methyl linoleate	[377, 618]
methyl linolenate	[377]
ethyl esters	
ethyl acetate	[714]
ethyl propanoate	[613, 615]
ethyl butanoate	[611]
ethyl pentanoate	[622]
propyl esters	
propyl acetate	[680]
butyl esters	
n-butyl formate	[222]

Felsmann et al. [712] produced a detailed mechanism for methyl propanoate built on a prior mechanism for methyl acetate [713]. RRKM master equation calculations were conducted using VariFlex [468] utilizing high-pressure limit rate coefficients calculated in Tan et al. [646, 684] for H-abstraction reactions and for ester radical decomposition. Kumar et al. [700] conducted ignition delay time experiments from 15 – 45 atm and 899 – 1103 K using a rapid compression machine and modeled the results using several chemical kinetics mechanisms. Despite the shorter alkyl chain, ignition delay times below 950 K were shorter for methyl acetate than for methyl propanoate – a trend also reflected in all of the chemical kinetics mechanisms [712, 720, 721]. Sensitivity analysis using the Felsmann et al. [712] mechanism indicated HOO-related reactions, including $HO\dot{O} + CH_2O \rightarrow H\dot{C}O + H_2O_2$ and H-abstraction reactions at vinoxylic carbon (α') were common amongst the mechanisms. Similar reactions involving HOȮ radicals were also identified in Kumar and Sung [617] using local and global uncertainty analysis of ignition delay times for methyl butanoate, as well as H-abstraction from the α' carbon and subsequent reaction of the vinoxylic radical with O_2 to form methyl *trans*-2-butenoate + HOȮ.

Weber et al. [702] utilized RMG to develop a chemical kinetics mechanism for methyl pentanoate oxidation and compared with ignition delay times from rapid compression machine experiments along with predictions using the mechanism from Diévart et al. [720]. For both mechanisms, the predictions of temperature dependence were sharply inconsistent with experimental trends: ignition delay times for (ϕ = 2) were a factor of ~10 shorter at 775 K and a factor of ~10 longer near 700 K. In addition, neither mechanism predicted the clear NTC behavior observed in the measurements. Differences between the two were noted in the predictions of initial radical distributions.

Two detailed chemical kinetics mechanisms exist for methyl trans-3-hexenoate and were developed to model the effect of a C=C bond on methyl ester oxidation. Wagnon et al. [675] developed a mechanism on the basis of the sub-mechanism for methyl trans-5-decenoate within the methyl decanoate mechanism of

Herbinet et al. [722]. Dagaut et al. [619] expanded a prior mechanism developed for methyl hexanoate utilizing rate coefficient analogies to 1-alkenes [688] and unsaturated esters [722]. Both mechanisms included rate parameters for Waddington-type oxidation reactions for radicals derived from ȮH-addition to unsaturated carbon.

Consistent with the ignition delay time measurements of Oehlschlaeger et al. [706-708] (cf. **Figure 51**), predictions using the PSR module in ChemKin and the reaction mechanism of Westbrook et al. [626] indicate that an increase in the amount of unsaturated carbon results in the suppression of peroxy radical chemistry. **Figure 52** compares predictions of consumption profiles for stoichiometric oxidation of several methyl esters using an initial concentration of 2000 ppm, He as the diluent, and a residence time of 1500 ms. Five methyl esters are compared: two saturated species (methyl stearate and methyl palmitate) and three unsaturated species, methyl oleate (18:1), methyl linoleate (18:2), and methyl linolenate (18:3). The consumption profiles of the two saturated species are nearly identical. Comparing methyl stearate with methyl oleate, however, the influence of a single C=C bond position is apparent from 500 – 600 K where the consumption rate is lower for the unsaturated species. For an increasing number of C=C bonds, the effect is increased to the point where consumption of methyl linoleate and methyl linolenate begins near 675 K. Above 800 K, the ignition trends of the esters converge. Similar effects during the oxidation of hexene isomers is reported in Bounaceur et al. [687].

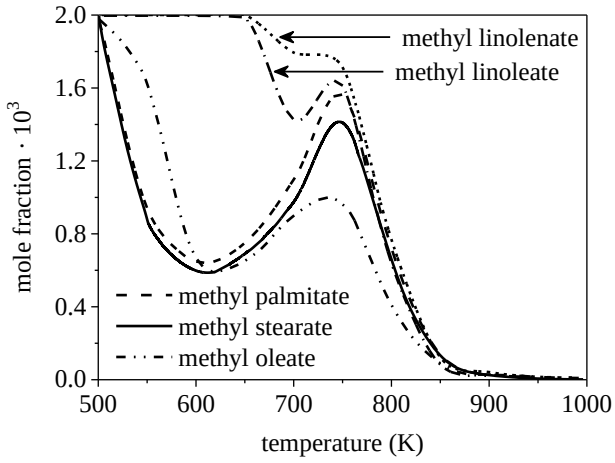

Figure 52. Chemical kinetics modeling of mole fractions from stoichiometric oxidation of methyl esters using the mechanism of Westbrook et al. [377]. Initial conditions: 2000 ppm of methyl ester with He as diluent, 10 atm and a residence time of 1500 ms.

3.2.5. Summary of ester functional group effects

The degree to which the ester functional group affects low-temperature chain-branching depends on the size of the alkyl substituent, which is a general trait of both hydrocarbons and biofuels. Two-stage oxidation chemistry is evident in methyl esters larger than methyl butanoate. In addition to alkyl substituent size, the degree of unsaturation significantly impacts the initiation step, $\dot{R} + O_2$ reaction rates, and subsequent ȮOOH reactions thereafter. Because conventional biodiesel is comprised of methyl esters with substituents of tetradecyl and larger, and contain up to three C=C bonds, additional experimental and theoretical studies on moderate-sized species may provide a closer understanding as to the influence of the ester group on low-

temperature chain-branching. However, because influence of the ester group diminishes with increasing substituent size, an open question remains as to the alkyl size where ester-derived effects such as resonance-stabilized initial radicals, or alkoxy radicals, no longer impact overall oxidation. **Figure 53** shows the low-temperature chain-branching scheme augmented to emphasize pathways that are affected by the ester functional group.

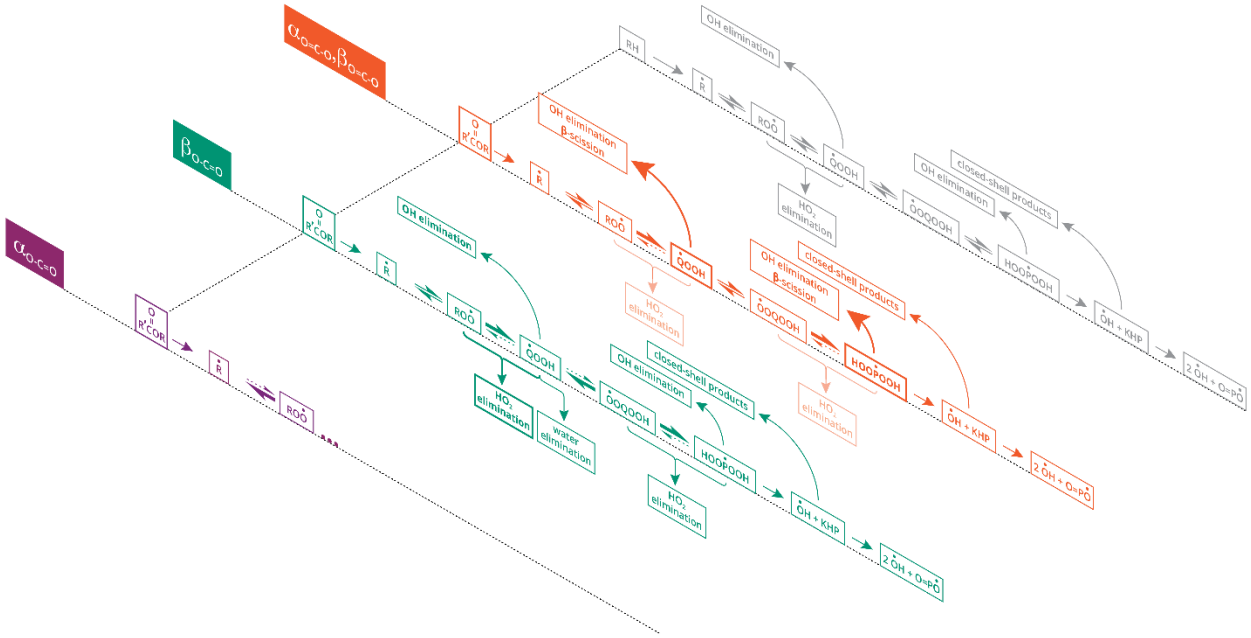

Figure 53. Summary of ester functional group effects on low-temperature chain-branching. The leftward-pointing and downward-pointing arrows indicate a shift in flux away from chain-branching pathways responsible for ignition. For initial radicals on the carbonyl side of the molecule, subsequent oxidation reactions are affected by the reduced reactivity of vinoxylic resonance stabilized radicals, similar to the chemistry of ketone fuels. For initial radicals on the ether side of the molecule the –O– group cannot donate a hydrogen, which reduces chain-inhibiting HOȮ formation, and can increase the role of chain-propagating *β*-scission. Each type of initial radical is depicted in a separate plane, with different colors used to guide the eye. The alkane oxidation mechanism is depicted in the back plane for reference. Pathways that are enhanced by the effects of the functional group are emphasized with bold arrows and labels, and those that are diminished are made lighter or omitted.

Branching fractions of esters from initiation reactions with ȮH and other radicals depends partly on bond energies and influence from pre-reaction complex formation. Thermochemical calculations indicate that bond energies on the methoxy group are lower by 3 – 4 kcal/mol compared to primary C–H bonds in alkanes due to the higher electronegativity of oxygen. On the alkyl substituent, because of resonance stabilization, C–H bond energy on α' carbon is 7 – 8 kcal/mol lower than the analogous secondary C–H bonds in alkanes. As in hydrocarbons, the presence of sp^2 carbon on the alkyl chain for larger methyl esters creates allylic hydrogen and, in cases where C=C bonds are separated by one methylene group (R–C=C–CH_2–C=C–R), *bis*-allylic hydrogens are created. Compared to secondary hydrogen in alkanes, allylic C–H bond energies are lower by ~15 kcal/mol and *bis*-allylic are lower by ~22 kcal/mol.

For H-abstraction by ȮH and HOȮ, branching fractions are reported only for small esters: methyl formate, methyl acetate, methyl propanoate, methyl butanoate, and *n*-butyl formate. The choice of using a single-transition-state model versus a two-transition-state model, to account for pre-reaction complexes, may not

strongly affect the total *k*(T), yet branching ratios are potentially impacted. For example, rate coefficients for methyl propanoate + ȮH from Tan et al. [646] (single transition state model) and Mendes et al. [620] (two-transition-state model) are within ~50% of one another. However, the temperature dependences of the branching ratios differ substantially. In contrast, for abstraction reactions of methyl propanoate with HOȮ, *k*(T) from Tan et al. [646] (two-transition-state model) differs from Mendes et al. [621] (two-transition-state model) by approximately a factor of 5, yet branching ratios agree closely over a wide temperature range.

Among the quantum chemical studies for reactions involving either ȮH or HOȮ, abstraction of hydrogen from β' carbon (on the alkyl chain) involves a pre-reaction complex and is favored in the high-pressure limit at temperatures up to 850 K for methyl butanoate and methyl pentanoate. As shown in MPIMS experiments [605, 606] and quantum chemical calculations [666], rates of formation of alkene + HOȮ from ROȮ radicals are higher than in analogous reactions of alkanes. In addition, ROȮ → Q̇OOH rates are lower, compared to alkanes, when the ester moiety is contained within the transition state [603]. The combined effect of preferential formation of β' radicals in the initiation step, higher rates of HOȮ formation, and lower rates of Q̇OOH formation contribute to the diminished chain-branching observed for smaller methyl esters.

3.3. ketones

The carbonyl moiety in ketones imposes two effects on initiation steps that precede $\dot{R} + O_2$ reactions that differ from analogous reactions in alkanes: (1) distinct hydrogen-abstraction sites influenced by the C=O group (**Figure 54a**), two of which introduce resonance-stabilization in subsequent ketonyl radicals (**Figure 54b**), and (2) the potential for forming pre-reaction complexes between the H atom in an abstracting radical (e.g. ȮH, HOȮ, …) and the O atom in the C=O group (**Figure 54c**). C–H bond energies on carbon sites in closest proximity to the carbonyl group (α and α') sites are reduced while bond energies on β, γ, and δ sites are similar to alkanes [723]. Hudzik and Bozzelli [723] conducted CBS-QB3 and G3MP2P3 calculations on the thermochemistry for a range of linear and branched ketones, indicating that C–H bonds in the α and α' sites are lower compared to the analogous bond in alkanes. Similar results were reported in Thion et al. [724] for cyclopentanone. Vinoxylic stabilization in α and α' ketonyl radicals (**Figure 54b**) disfavors O_2-addition because ROȮ well depths are ~15 kcal/mol shallower than alkylperoxy radicals owing to the loss of resonance stabilization (upon addition to O_2). With increasing temperature, the weaker-bound ROȮ adduct preferentially dissociates back into reactants $\dot{R} + O_2$, restricting the formation of ȮOOH either through isomerization or direct pathways, which subsequently inhibits chain-branching.

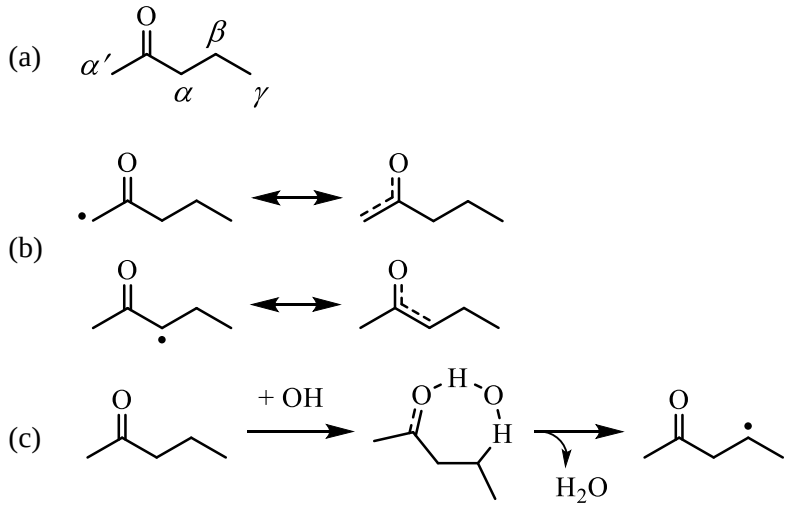

Figure 54. (a) Molecular structure of 2-pentanone with labeled H-abstraction sites. (b) 2-pentanon-1-yl and 2-pentan-3-yl radicals with resonance structures. (c) Formation of 2-pentanon-4-yl via 7-membered hydrogen-bonded adduct complex [725, 726] formed in ȮH-initiated H-abstraction from β carbon in 2-pentanone.

Aldehydes, where a hydrogen atom is one of the substituents bound to the carbonyl group, are a special case and are common combustion intermediates [727] yet are not regarded as biofuels. On the alkyl side, the effect of the carbonyl group on the neighboring C–H bond is similar to that in ketones. The weakest C–H bond is the aldehydic hydrogen, and loss of that hydrogen leaves an acyl radical that rapidly decarbonylates to give CO and an alkyl radical.

3.3.1. initiation reactions and branching fractions

A positive temperature dependence is observed in rate coefficients for acetone + ȮH and near-zero temperature dependence in butanone + ȮH [728, 729], whereas negative temperature dependence becomes pronounced in ketones with substituents larger than ethyl, with minima occurring near 600 K [728, 729]. The formation of a hydrogen-bonded pre-reaction complex (cf. **Figure 54c**) facilitates ȮH-initiated H-abstraction at lower temperatures primarily from β carbon, which becomes the dominant initiation step for ketones larger than butanone [662, 725, 726, 730-733] The analogous mechanism involving α carbon is of comparatively smaller influence [734], and rate coefficients for H-abstraction by ȮH from other sites (e.g. γ, δ, …) are unaffected by the carbonyl group [732]. Negative temperature dependence is observed when complex-mediated abstraction is of secondary or tertiary hydrogen on β carbon [730-732].

Complex-mediated abstraction was proposed in Wallington and Kurylo [662], inferred from a shift in the activation energy from positive ($E_a > 0$) in ȮH + acetone, to $E_a \approx 0$ in butanone and 3-pentanone, to negative ($E_a < 0$) in reactions of ȮH with ketones containing alkyl chains larger than ethyl. Wallington and Kurylo [662] modeled branching fractions by a structure-activity relationship (SAR) with k(T) for abstraction from α carbon similar to alkanes and for β carbon a factor of ~3 higher, which is in agreement with Atkinson [735]. Subsequently, the SAR results were supported in Dagaut et al. [730] from rate coefficient measurements of ȮH + dione species over the same temperature range: 2,3-butanedione, 2,4-pentanedione, and 2,5-hexanedione. Le Calvé et al. [732] confirmed the results of ȮH + acetone/butanone/2-hexanone in [662, 730] and expanded on the measurements of acyclic ketones to include branched ketones methyl-butanone and 4-methyl-2-pentanone from 243 – 372 K. The negative temperature dependence in the trends of k(T) in reactions of ȮH with branched ketones with more than one β carbon were consistent with [662, 730] and the experiments in Jiménez et al. [731].

Wallington and Kurylo [662] postulated a 6-membered *oxygen*-bonded adduct complex formed between the O atom in ȮH and the O atom in the C=O group, with the ȮH abstracting hydrogen from the β carbon, and a similar 7-membered complex involving γ carbon. Klamt [725] proposed the 7-membered *hydrogen*-bonded adduct complex (cf. **Figure 54c**) for abstraction at the β carbon. The molecular dynamics simulations in Frank et al. [726] of H-abstraction from 3-hexanone and the calculations of Zhou et al. [734] and Alvarez-Idaboy et al. [733] lend support for the mechanism proposed by Klamt [725].

Tranter and Walker [736] measured k(753 K) and products from reactions of acetone, butanone, and 3-pentanone with ȮH and with Ḣ at 500 Torr, reporting a rate coefficient 30 – 40% lower compared to alkanes. Similar conclusions were drawn in Carr et al. [737]. The implicit result in both [736] and [737] is that the adduct complex and abstraction from β carbon is of lower importance to the overall rate of H-abstraction from ketones by ȮH at higher temperature.

Using *ab initio* calculations, reaction mechanisms and rate coefficients of HOȮ with butanone are reported in Mendes et al. [78] for site-specific H-abstraction and in Zhou et al. [738] for HOȮ-addition to butanone. Reactions of several ketones with HOȮ were included in Mendes et al. [78]: acetone, butanone, 2-pentanone, methyl-butanone, and 4-methyl-penta-2-one. Transition states were identified in abstraction reactions of H atoms resulting in the formation of a pre-reaction complex formed via hydrogen-bonding between the H atom of the hydroperoxyl radical and the O atom of the carbonyl group and the abstraction coordinate between the O atom of hydroperoxyl and the H being abstracted (**Figure 55**). With the exception

of abstraction reactions from tertiary (β) carbon in 4-methyl-penta-2-one, binding energies of the complexes were approximately 10 kcal/mol and because hydrogen bonding leads to the loss of rotors in the transition state, the high-pressure limit rate coefficients for ketone + HOȮ were lower by more than a factor of 10 compared with analogous reactions in alkanes [78].

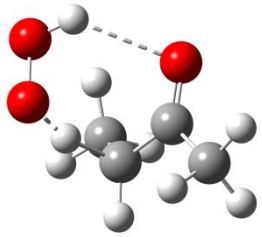

Figure 55. In-plane (complex-mediated) transition state for α-hydrogen abstraction from butanone by HOȮ [78].

Zhou et al. [738] reported a series of *ab initio* calculations on the kinetics and mechanisms of HOȮ-addition to butanone, which forms hydroxy-substituted peroxy radicals (HO–ROȮ) where both the OH and peroxy groups are bonded to the same carbon. Zhou et al. [738] concluded that, over the temperature range 600 – 1600 K, abstraction exceeds the addition of HOȮ to the functionalized carbon in butanone by ~10^2 at 1 atm.

Kopp et al. [739] computed rate coefficients using *ab initio* methods for H-abstraction from butanone by $\dot{C}H_3$ and for subsequent unimolecular reactions of butanonyl radicals, including isomerization and C–C β-scission. The effects of non-Boltzmann distributions were also examined and were deemed negligible at temperatures below 1000 K and pressures above 1 atm. Total rate coefficients were ~10^{-16} cm^3 s^{-1} at 500 K and ~10^{-15} cm^3 s^{-1} at 1000 K. Abstraction from the secondary (vinoxylic) site was favored, while branching fractions were similar for the other two sites.

Rate coefficients for H-abstraction from butanone by ȮH [734] and HOȮ [78] are compared in **Figure 56a**. For reactions with ȮH, Zhou et al. [734] used the Møller-Plesset MP2 method with the 6-311G(*d*,*p*) basis set, MP2/6-311G(*d*,*p*), for geometry optimization and energies were computed using the CCSD(T) method with correlation-consistent polarized split-valence multiple-ζ basis sets extrapolated to the complete basis set (CBS) limit. High-pressure limit rate constants were computed with variational transition state theory and conventional transition state theory as implemented in VariFlex [468], which were largely consistent with experiments [728, 729, 736, 737, 740]. Mendes et al. [78] employed a similar computational approach for calculating rate coefficients of HOȮ + butanone → H_2O_2 + Ṙ. As with other systems, the total rate coefficient for abstraction by ȮH is several orders of magnitude larger than for abstraction by HOȮ, even at 1000 K. Zhou et al. [734] and Mendes et al. [78] also reported site-specific rate coefficients, which are depicted in **Figure 56b**. For both radicals, abstraction from the (secondary) α carbon is favored from 500 – 1000 K, followed by abstraction from β carbon. For ȮH, branching fractions are α:β:α' (500 K) = 0.70:0.21:0.09 and α:β:α' (1000 K) = 0.54:0.27:0.19, respectively. For HOȮ, α:β:α' (500 K) = 0.83:0.13:0.03 and α:β:α' (1000 K) = 0.60:0.27:0.13. Abstraction from α carbon is favored by both radicals in part because the pathways are the lowest lying channels on the respective potential energy surfaces. For abstraction by HOȮ, the barrier height relative to the pre-reaction complex is the lowest by ~4 kcal/mol and similarly for abstraction of α carbon by ȮH.

Zhou et al. [79] employed the G4 method, benchmarked against CCSD(T)/CBS, to calculate high-pressure-limit rate coefficients for H-abstraction from cyclopentanone, including reactions with ȮH and HOȮ (**Figure 56c**). Rate coefficients for axial and equatorial positions of hydrogen atoms were calculated separately and, for both α and β carbon, abstraction of hydrogen in the axial position is favored. In contrast to reactions with acyclic ketones, where selectivity in H-abstraction by ȮH and HOȮ favors α carbon, the calculations of Zhou et al. [79] revealed that, although abstraction from α carbon remains favored in reaction with HOȮ, abstraction from β carbon dominates reactions with ȮH (**Figure 56d**). Similar results were reported in Thion et al. [724] at the MP2/aug-cc-pVDZ level of theory, which predicted a pre-reaction complex of ȮH with cyclopentanone stabilized by 5.4 kcal/mol.

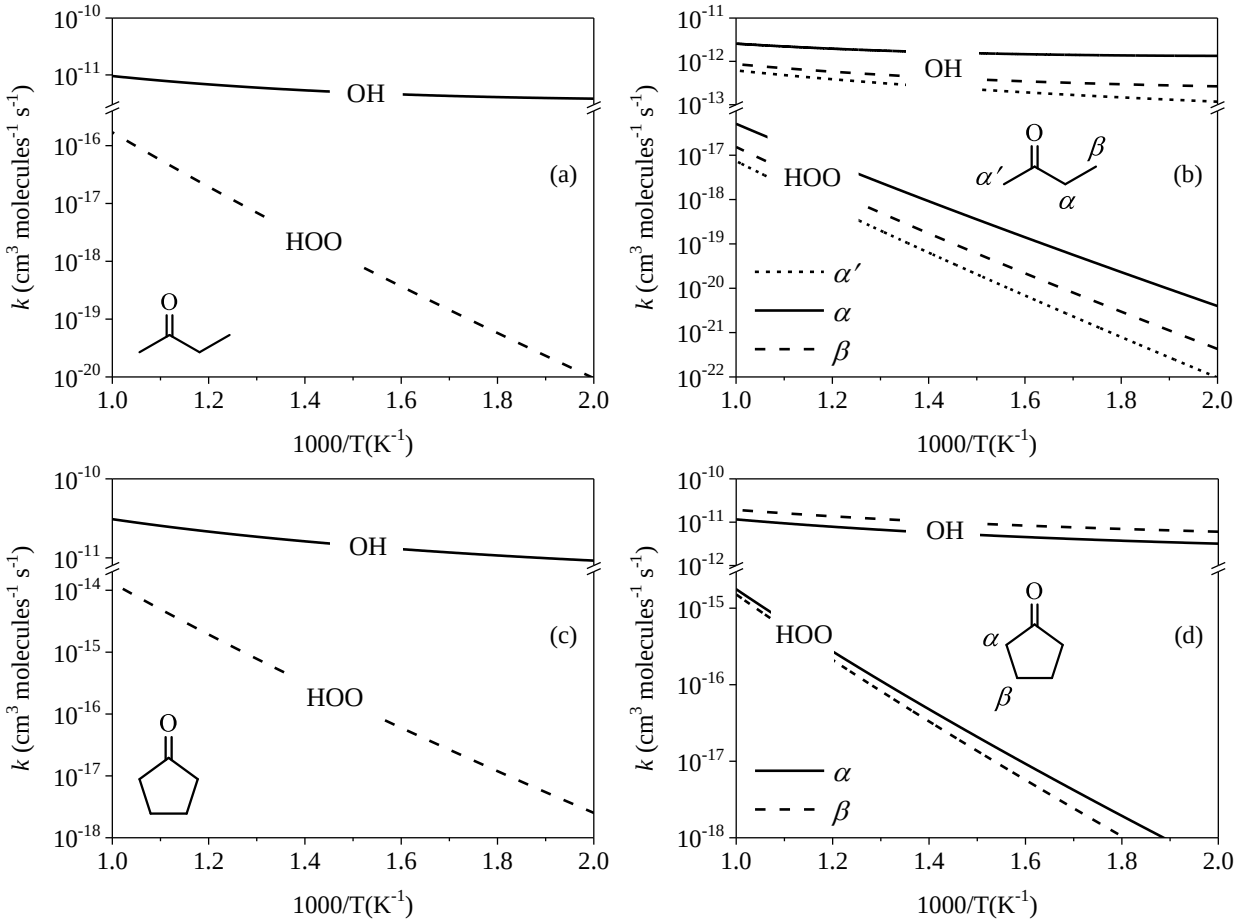

Figure 56. High-pressure-limit rate coefficients for H-abstraction from butanone by ȮH (Zhou et al. [734]) and HOȮ (Mendes et al. [78]) and from cyclopentanone by ȮH and HOȮ (Zhou et al. [79]); (a) total, (b) site-specific.

Figure 57 compares the temperature dependence of branching fractions for ȮH + cyclopentanone → Ṙ + H_2O from Zhou et al. [79] and Thion et al. [724]. Over the temperature range 500 – 1000 K, branching towards β is favored by a factor of ~2 above 650 K. Both studies reflect a relatively weak dependence on temperature. Rate coefficients and branching fractions for other H-abstraction reactions were also calculated in Zhou et al. [79], including for Ö, Ḣ, and $\dot{C}H_3$, and ring-opening reactions of initial cyclopentanonyl radicals, and Thion et al. [724] calculated k(T) for $\dot{C}H_3$ + cyclopentanone → CH_4 + Ṙ.

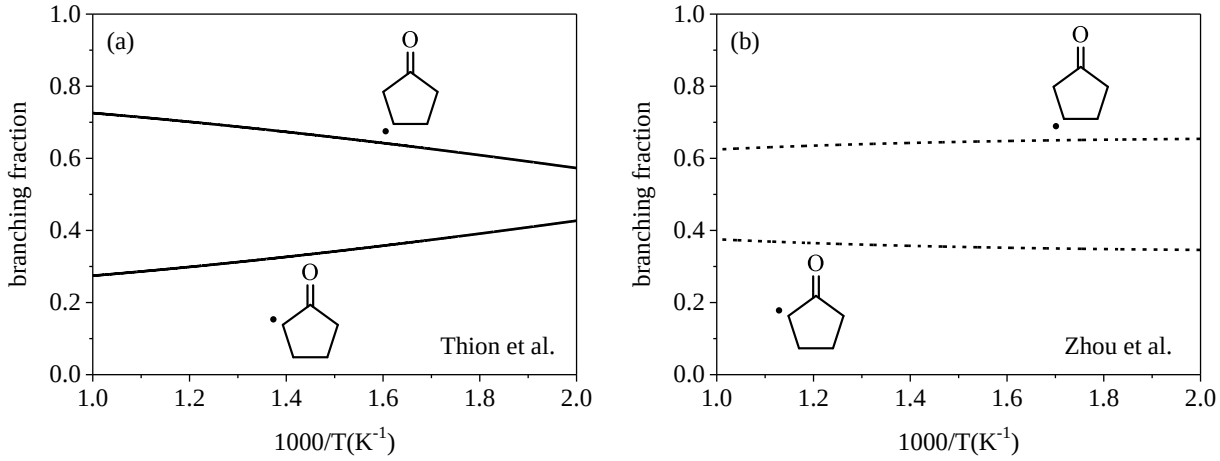

Figure 57. Branching fractions for ȮH + cyclopentanone from (a) Thion et al. [724] and (b) Zhou et al. [79].

Liu et al. [741] employed shock tube experiments and UV laser-absorption spectroscopy to measure *k*(T) for ȮH-initiated H-abstraction from cyclopentanone and cyclohexanone at 1.2 atm and from 900 – 1330 K. The measurements were fit to an Arrhenius expression that included measurements from Dagaut et al. [730] at 296 K, which enabled the rate parameters to include temperatures relevant to low-temperature combustion conditions (i.e. ~500 – 800 K) where no such measurements exist. The absence of any significant negative temperature dependence led to the conclusion that, in both cases, ȮH-addition to the carbonyl group is insignificant, which is similar to reactions with acetone where addition contributes to <1% of the total rate coefficient from 500 – 2000 K [734]. Site-specific rate coefficients were not determined explicitly in Liu et al. [741], although analytical estimates were made based on Zhou et al. [742] and indicated that branching fractions favor the formation of β radicals, which is the same conclusion drawn in Thion et al. [724].

Rate coefficients for ȮH + cyclopentanone from Liu et al. [741], Dagaut et al. [730], Thion et al. [724], and Zhou et al. [742] are plotted in **Figure 58a**. The theoretical calculations for cyclopentanone [724, 742] are within 15% of one another above 750 K, below which the two trends deviate due to differences in activation energy and temperature dependence. The barrier to abstraction from α carbon in Zhou et al. [742] is lower than Thion et al. [724] by ~1 kcal/mol and ~0.5 kcal/mol lower for β carbon. Weaker temperature dependence is also predicted in [742] on both sites. In comparison with the experimental trend for cyclopentanone, Zhou et al. [742] is within a factor of ~2 over the temperature range whereas Thion et al. [724] varies from a factor of ~3 at 1000 K to ~20% at 500 K.

The *k*(T) measurements for ȮH + cyclohexanone from Liu et al. [741] are plotted in **Figure 58b** with the Dagaut et al. [730] value at 296 K and predictions from Thion et al. [743] and Serinyel et al. [744]. The latter model utilized rates for abstraction of secondary hydrogen in alkanes for β and γ carbon and drew analogy for α carbon on cyclohexanone from ȮH + acetone [745]. High-temperature predictions using the Serinyel et al. mechanism [744] are consistent with the experimental results of Liu et al. [741] to within 20%. Deviations are evident at lower temperatures that are less relevant to combustion.

Theoretical calculations for k(T) of analogous reactions for cyclopentane and cyclohexane from Sivaramakrishnan and Michael [746], conducted at the B3-LYP/6-31G(*d*) and G3//B3LYP levels of theory and remarkably consistent with experiments [747-756], are compared in **Figure 58** to highlight the influence of the carbonyl group. In both cases, k(T) for the ketone species is lower by a factor of ~2. On a per-H-atom basis, β-sites rates are similar among the various studies to within ~30% (**Figure 58c and 58d**), which indicates that the lower rate coefficients reflect reduced abstraction at the α site, largely because of hydrogen bonding in the pre-reaction complex.

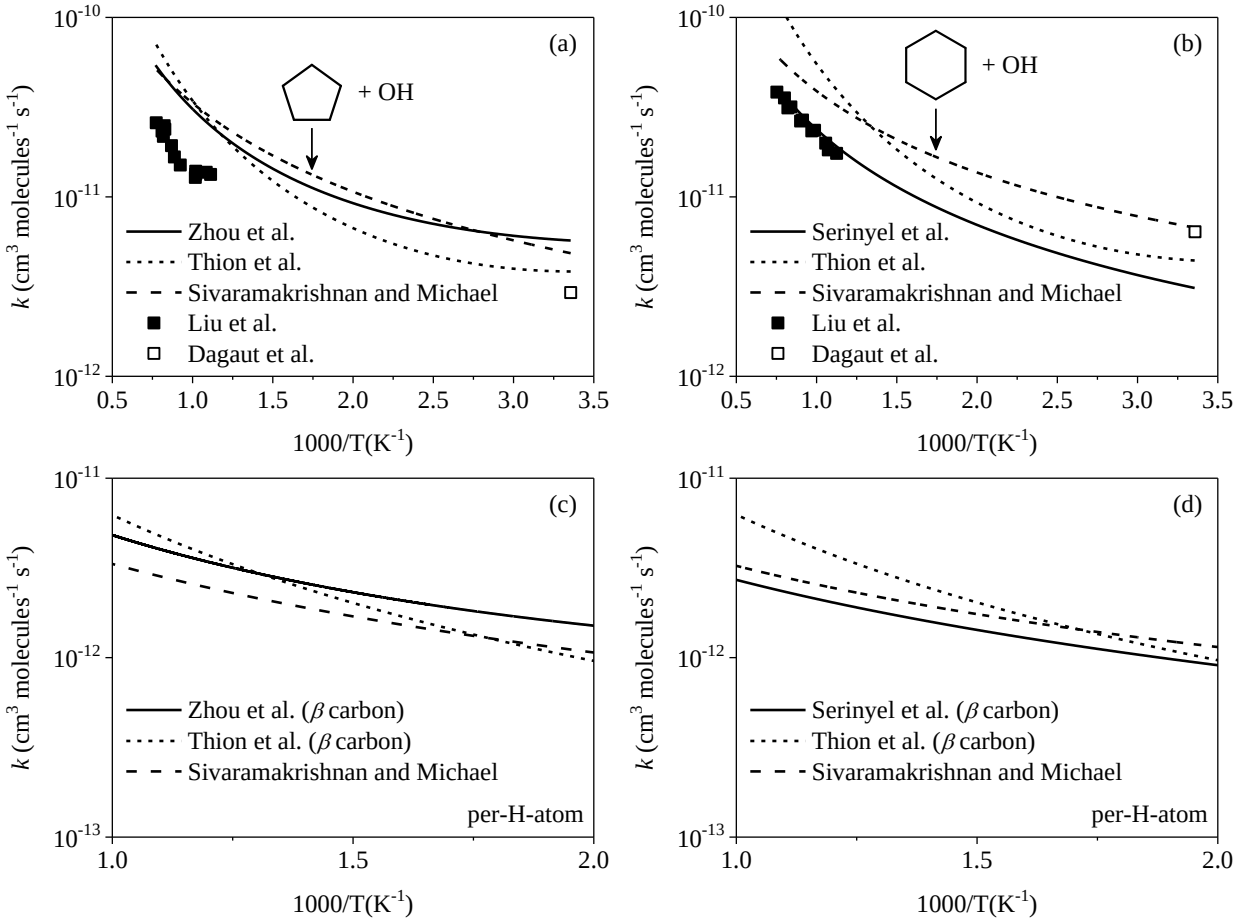

Figure 58. (a) Rate coefficients for ȮH + cyclopentanone from Dagaut et al. [730], Liu et al. [741], Thion et al. [724], and Zhou et al. [742] compared with ȮH + cyclopentane [746]. (b) Rate coefficients for ȮH + cyclohexanone from Liu et al. [741], Dagaut et al. [730], Serinyel et al. [744], and Thion et al. [743] compared with ȮH + cyclohexane [746]. Rate coefficients for the cycloalkanes are from Sivaramakrishnan and Michael [746]. (c) and (d) depict abstraction from β-carbon compared to analogous cycloalkane on a per-H-atom basis.

3.3.2. reactions of initial radicals with O_2

Scheer et al. [299, 302, 757, 758] employed MPIMS experiments to examine reaction mechanisms of ketonyl radicals with O_2 from measurements of oxidation intermediates of acyclic ketones [299, 302, 758] cyclic ketones [757] and branched ketones [302]. Chain-inhibition via conjugate alkene + HOȮ dominated the oxidation of α radicals of cyclopentanone, cyclohexanone, and 2-methylcyclopentanone and chain-

propagation via cyclic ether + ȮH were stated as being of lower importance due to weak signal detected at the corresponding nominal *m/z* in all three cases [757]. A Dowd-Beckwith ring-expansion reaction (**Figure 59**) was postulated in the oxidation of 2-methylcyclopentanone (forming 2-cyclohexen-1-one), although the mechanism was not confirmed experimentally due to nearly identical photoionization spectra of 2-methylcyclopenten-1-one and the expanded product 2-cyclohexen-1-one. Analogous ketonyl rearrangement reactions via 1,2-acyl migration (**Figure 59b**) were confirmed by Scheer et al. [302] in *tert*-butyl ketones and were critical to explaining HOȮ forming reactions at temperatures above 550 K. The reaction is facilitated by a thermodynamic driving force (conversion of a primary radical to a tertiary radical) and the tertiary radical 4-methylpentan-2-on-4-yl subsequently undergoes oxidation via chain-inhibiting HOȮ forming pathways. Radical rearrangement of ȮOOH radicals was also postulated [302].

MPIMS results by Scheer et al. from Cl-initiated oxidation of 3-pentanone at 8 Torr from 550 – 650 K [299], and from the oxidation of deuterated isotopologues of 3-pentanone, with expanded experimental conditions to lower temperature (450 K) and higher pressure (2 atm) [758], indicate that resonance-stabilized ȮOOH radicals play a central role and undergo facile chain-propagation reactions. In 3-pentanone oxidation, below 550 K, the predominant cyclic ether is 2,4-dimethyloxetan-3-one, formed via resonance-stabilized ȮOOH produced by reaction of resonance-stabilized 3-pentanon-2-yl with O_2 [758]. At temperatures above 550 K the photoionization spectrum at the *m/z* corresponding to cyclic ether is dominated by 2-methyltetrahydrofuran-3-one, a product of oxidation of the non-resonance stabilized 3-pentanon-1-yl radical. Similar to Rotavera et al. [759] in a study on oxidation of *iso*-propyl toluene isomers, a shift in the chain-propagation mechanism with temperature was observed, where higher temperature favors mechanisms derived from non-resonance-stabilized initial radicals. With increasing temperature and increasing contribution from reverse RȮ reactions into Ṙ + O_2, C–C β-scission becomes a major consumption channel for vinoxylic ketonyl radicals. The use of pentan-3-one-1,1,1,5,5,5-d_6 in [758] at high oxygen concentrations (> 10^{17} molecules cm^{-3}) led to the detection and identification of a specific ketohydroperoxide species, 4-hydroperoxypentane-2,3-dione, as the lone γ ketohydroperoxide isomer derived from 3-pentanone oxidation. Experimental evidence for the decomposition of 4-hydroperoxypentane-2,3-dione via three channels was reported: (1) Korcek decomposition into acetic acid and methylglyoxal; (2) water-elimination forming pentane-2,3,4-trione; and (3) β-scission of oxy radical formed via O–O bond-scission, into acetaldehyde + CO + CO + $\dot{C}H_3$ (**Figure 59c**).

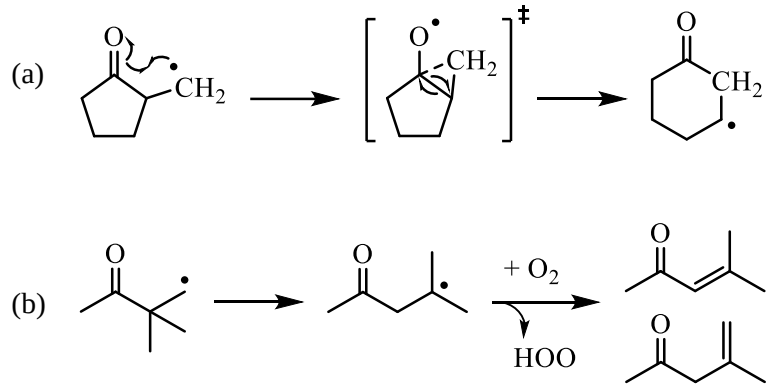

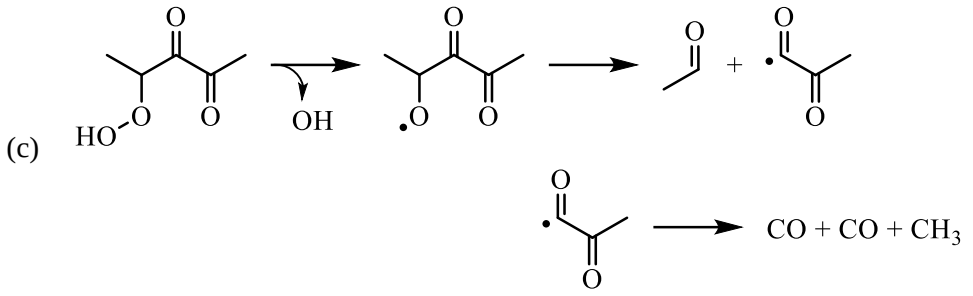

Figure 59. Reaction pathways in ketone oxidation facilitated by the carbonyl functional group: (a) Dowd-Beckwith ring-expansion reaction of 2-methylene-cyclopentan-1-one forming 2-cyclohexen-1-one [757]. (b) Similar rearrangement reaction in methyl-*tert*-butyl ketone [302]. Subsequent reaction of the rearranged 4-methyl-penta-2-on-4-yl with O_2 led to the formation of 4-methyl-3-penten-2-one in methyl-*iso*-butyl ketone oxidation at 550 K and 4-methyl-4-penten-2-one at 650 K [302]. (c) ȮH-loss from γ-ketohydroperoxide of 3-pentanone (4-hydroperoxypentane-2,3-dione) via O–O bond-scission followed by β-scission of the resulting oxy radical into acetaldehyde + CO + CO + $\dot{C}H_3$ [758].

Sebbar et al. [760-762] conducted a series of quantum chemical calculations on thermochemistry and pressure- and temperature-dependent rate coefficients for reactions derived from 2-butanon-1-yl + O_2 [760] and 2-butanon-3-yl + O_2 [761] over the temperature range 500 – 2500 K. In addition to potential energy surface calculations for 2-butanon-4-yl + O_2, Sebbar et al. [762] calculated several surfaces for decomposition products of ȮOOH radicals. Several methods were employed for all three systems, including G3MP2B3, G3, G3MP3. Sebbar et al. [762] noted a substantial range of energy estimates among the B3LYP, G3MP2B3, and G3 methods used for most of the calculations, and carried out G3MP2, CBS-QB3, and CBS-APNO calculation methods for some transition states. As part of an investigation of second O_2 addition reactions by Kuzhanthaivelan and Rajakumar [763] (*vide infra*), higher accuracy (CBS-QB3) quantum chemistry on the initial butanone oxidation steps was reported, which is in qualitative agreement with the pathways outlined earlier in Sebbar et al. [760-762]. However, in several cases, such as ȮH-elimination from ȮOOH, the barrier heights calculated using CBS-QB3 differed by more than 3 kcal/mol from Sebbar et al. [760, 761].

Sebbar et al. [760] found the 2-butanon-1-yl + O_2 reaction forms a chemically activated ROȮ with 27 kcal/mol of excess energy for which stabilization, isomerization to ȮOOH, and forward/reverse reactions were considered. Two previously unreported chain-propagating reactions of ȮOOH were proposed [760]: water-elimination leading to an oxy radical (Ȯ–$CH_2C(=O)CHCH_2$) coincident with H_2O **(Figure 60a)** and an OH-elimination reaction leading to 2-hydroxybut-2-enal. The latter reaction is initiated by hydrogen transfer from the –OOH group in $H_2C(OOH)C(=O)\dot{C}HCH_3$ to the oxygen of the carbonyl group to form a peroxy-substituted enol **(Figure 60b)**, which was competitive below 1000 K with the most-favored being reverse-isomerization to the initial ROȮ. Subsequent ROȮ ⇌ ȮOOH isomerization via a four-membered transition state and OH-elimination leads to 2-hydroxybut-2-enal, although the barrier for the four-center isomerization exceeds the $\dot{R}$ + O_2 entrance channel. Rate coefficients were calculated at 1 atm for unimolecular reaction of two of the hydroperoxyketonyl radicals. Decomposition of the non-resonance-stabilized $H_2C(OOH)C(=O)CH_2\dot{C}H_2$ is dominated by chain-propagation into tetrahydrofuran-3-one + ȮH, with a barrier similar to reverse isomerization (ȮOOH → ROȮ). In contrast, the resonance-stabilized $H_2C(OOH)C(=O)\dot{C}HCH_3$ reacts primarily via dissociation back into ROȮ and the hydrogen transfer from

the HOȮ group to the carbonyl resulting in an enol-peroxy radical, with some competition from water-elimination and concerted O–O and C–C bond fission into methyl ketene + formaldehyde + ȮH. Because the Ṙ + O_2 ⇌ ROȮ reaction is reversable at moderate temperatures, the *β*-scission reaction of 2-butanon-1-yl into ketene + ethyl is also important to consider and can compete with the forward reaction.

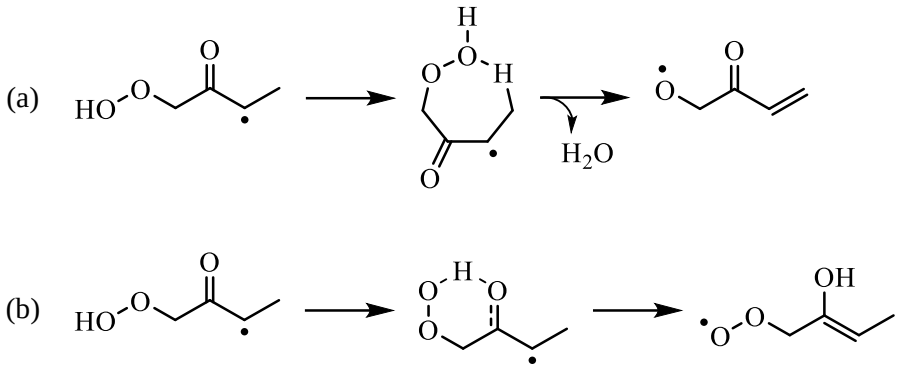

Figure 60. Alternative unimolecular decomposition pathways of 1-hydroperoxy-butanon-3-yl (ȮOOH) identified in Sebbar et al. [760]. (a) water-elimination via a mechanism similar to that of *γ*-ȮOOH in alcohol oxidation proposed by Welz et al. [301]. (b) Hydrogen-transfer from the hydroperoxy group to the carbonyl group forming peroxy-substituted enol.

In the 2-butanon-3-yl + O_2 reactions below 1000 K, two product channels were dominant [761]: direct formation of methylvinyl ketone + HOȮ and isomerization of the peroxy adduct $H_3CC(=O)CH(OȮ)CH_3$ to the resonance-stabilized hydroperoxyketonyl radical $H_2ĊC(=O)CH(OOH)CH_3$. The reverse reaction to ROȮ dominates, followed by the chain-branching channel acetaldehyde + acetyl + Ö and chain-propagating channel 2-methyl-oxetan-3-one + ȮH. Isomerization to the non-resonance-stabilized hydroperoxyketonyl $H_3CC(=O)CH(OOH)ĊH_2$ was of minor importance. In contrast to the resonance-stabilized hydroperoxyketonyl, the non-resonance-stabilized hydroperoxyketonyl $H_3CC(=O)CH(OOH)ĊH_2$ predominantly reacts via chain-propagation, to 1-(oxiran-2-yl)-ethanone + ȮH, and via chain-inhibiting, to methylvinyl ketone + HOȮ, while reverse reaction to the peroxy adduct $H_3CC(=O)CH(OȮ)CH_3$ is insignificant.

2-butanon-4-yl + O_2 → ROȮ forms a chemically activated adduct with 35 kcal/mol of excess energy [762]. The barriers for both possible cyclic ether + ȮH channels (forming either dihydrofuran-3(2*H*)-one or 1-(oxiran-2-yl)-ethanone) are below the 2-butanon-4-yl + O_2 reactants. However, no speciation measurements are reported in the literature, as noted in Hemken et al. [764]. In comparison to the 2-butanon-3-yl + O_2 [761] calculations, direct ROȮ → methyl vinyl ketone + HOȮ is favored more in 2-butanon-4-yl + O_2 due to the combination of a deeper ROȮ well (by ~10 kcal/mol) and to the lower C–H bond energy on the vinoxylic site.

Sebbar et al. [762] discovered an alternative chain-propagation pathway via the formation of a 5-membered cyclic peroxy radical intermediate (**Figure 61**) by attack of the –OȮ group on the electrophilic carbon end of the carbonyl. The barrier height is similar to that for ROȮ → ȮOOH via a 7-membered transition state and the two channels were the lowest on the ROȮ surface. The cyclic peroxy radical rearranges over a ~5.5

kcal/mol barrier and subsequent decomposition of the rearranged radical leads to oxirane and acetyloxy radical, $CH_3C(=O)\dot{O}$, requiring ~12 kcal/mol. Acetyloxy rapidly decarboxylates to $\dot{C}H_3 + CO_2$.

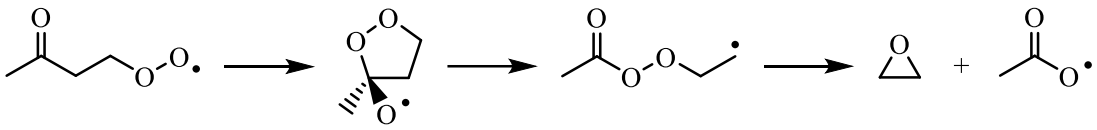

Figure 61. Alternative chain-propagation reaction sequence proposed in Sebbar et al. [762] yielding oxirane + acetyloxy radical.

Khanniche and Green [765] calculated stationary point energies using CBS-QB3 on potential energy surfaces and high-pressure limit rate coefficients using CanTherm [766] for reactions of α-cyclopentanonyl and β-cyclopentanonyl with O_2. The reaction of resonance-stabilized α-cyclopentanonyl + O_2 forms a weakly bound $RO\dot{O}$ (19.4 kcal/mol below the entrance channel), due to the loss of resonance in α-cyclopentanonyl upon O_2 addition. On the surface of α-cyclopentanonylperoxy (α-$RO\dot{O}$), $HO\dot{O}$ elimination to form cyclopent-2-en-1-one is the only channel with barriers below the α-cyclopentanonyl + O_2 reactant energy. The surface for β-$RO\dot{O}$ is significantly more complex, with several competing channels, including conventional pathways such as HOO-elimination forming both cyclopent-2-en-1-one and cyclopent-3-en-1-one, cyclic ether + $\dot{O}H$, and a $\dot{Q}OOH$ ring-opening mechanism. Transition states for hydrogen transfer from the –OOH group to the carbonyl group to form an enol-peroxy radical (**Figure 62a**) were identified on both $\dot{Q}OOH$ surfaces. However, only on the α-$RO\dot{O}$ surface is the reaction competitive with other $\dot{Q}OOH$ decomposition pathways.

Because the equilibrium α-cyclopentanonyl + $O_2 \rightleftharpoons$ α-$RO\dot{O}$ favors the reactant side at combustion-relevant conditions, calculations were also conducted on the surface of the adduct from $HO\dot{O}$ + α-cyclopentanonyl, 2-hydroperoxycyclopentan-1-one. On the surface of 2-hydroperoxycyclopentan-1-one – a ketohydroperoxide structure – the well-depth is 54.5 kcal/mol below the energy of the entrance channel. Transition states for five reaction pathways of 2-hydroperoxycyclopentan-1-one were calculated, four of which were submerged: two water-elimination mechanisms, yielding 1,2-cyclopentadione + H_2O, an OH-elimination channel occurring via O–O bond-scission (**Figure 62b**), and a concerted OH-transfer/ring-opening reaction (**Figure 62c**) yielding 4-formylbutyric acid ($HO–C(=O)(CH_2)_3CHO$). The rates of the concerted reaction and of the OH-elimination channels are more than an order of magnitude higher than water-elimination at 700 K [765].

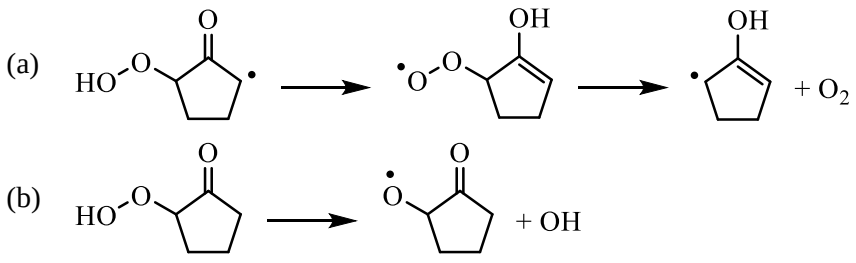

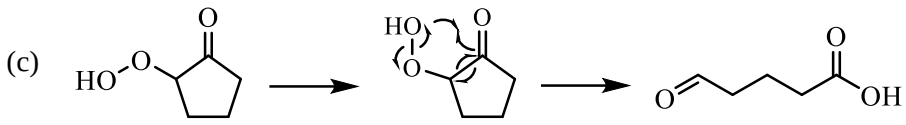

Figure 62. Reaction mechanisms of cyclopentanone-derived radicals from Khanniche and Green [765]: (a) formation of enol-peroxy from ȮOOH, producing an allylic enol radical upon loss of O_2; (b) OH-elimination yielding an carbonyl-oxy radical; (c) OH-transfer/ring-opening reaction producing carboxylic acid (5-oxopentanoic acid). Reactions in (b) and (c) are initiated from addition of HOȮ to α-cyclopentanonylperoxy.

Zhang et al. [767] used the CBS-QB3 level of theory and calculated site-specific rate coefficients for ROȮ → alkene + HOȮ reactions in cyclopentanone oxidation by canonical transition state theory in CanTherm [766] including hindered-rotor and one-dimensional Eckart tunneling corrections. The barrier heights for the pathways leading to cyclopent-2-en-1-one from both α-ROȮ and β-ROȮ differed by ~1.5 kcal/mol, which is within the limit of uncertainty of the method, and both were lower than the pathway from β-ROȮ to cyclopent-3-en-1-one because of the reduced bond energy on α carbon. **Figure 63** compares rates of direct HOO-elimination from [767] for the two peroxy radicals. Below 1000 K, the rate of formation of cyclopent-2-en-1-one exceeds the other isomer by ~10^1 – 10^2. The MPIMS experiments of Scheer et al. [757] at 550 K and 650 K observed substantial cyclopent-2-en-1-one, yet detected no cyclopent-3-en-1-one.

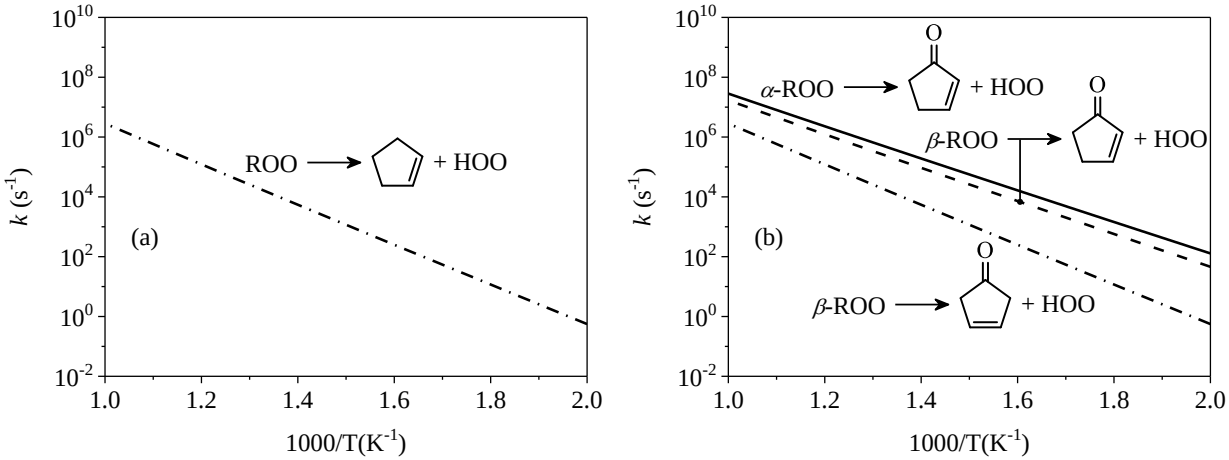

Figure 63. Unimolecular decomposition rates for ROȮ → conjugate alkene + HOȮ in the high-pressure limit for (a) cyclopentylperoxy → cyclopentene + HOȮ from Al Rashidi et al. [768] and (b) peroxy radicals of cyclopentanone calculated in Zhang et al. [767].

Similar resonance stabilization effects occur in diones. Yommee and Bozzelli [769] calculated rate coefficients for Ṙ + O_2 reactions in cyclopentadienone and related thermochemical properties of the species involved including adducts and decomposition products. Wang and Brezinsky [770] also calculated pathways and reaction rate coefficients, for thermal decomposition of cyclopentadienone, using molecular orbital and RRKM calculations. Although not regarded as a biofuel, cyclopentadieneone is formed via oxidation of cyclopentenone isomers, which are relevant to cyclopentanone combustion [724, 757].

Kuzhanthaivelan and Rajakumar [763] calculated high-pressure limit rate coefficients for unimolecular reactions of hydroperoxyalkylperoxy (ȮOQOOH) radicals derived from butanone oxidation using CBS-QB3 and canonical variational transition state theory. Reverse reactions ȮOQOOH → Q̇OOH + O_2 were neglected. Below 1000 K, rates for ȮOQOOH interconversion (**Figure 64a**) were the highest, by several orders of magnitude, for all four radicals. With one exception, an HOO-elimination pathway (**Figure 64b**), the second highest reaction rates were conventional isomerization (**Figure 64c**), where hydrogen is removed by the peroxy group from the carbon to which the –OOH group is bonded. Carbon-centered radicals produced from that isomerization lead subsequently to ketohydroperoxide + ȮH. Potential energy calculations for cyclic ether + ȮH from HOOQ̇OOH were also included, namely the formation of substituted oxetane species. However, for both cases the barrier heights were ~20 kcal/mol and are negligible compared to the (barrierless) O–O bond scission to ȮH + ketohydroperoxide. Calculations were also conducted by Kuzhanthaivelan and Rajakumar [771] on analogous radicals derived from 2-pentanone, which included pressure-dependent rates determined using RRKM theory.

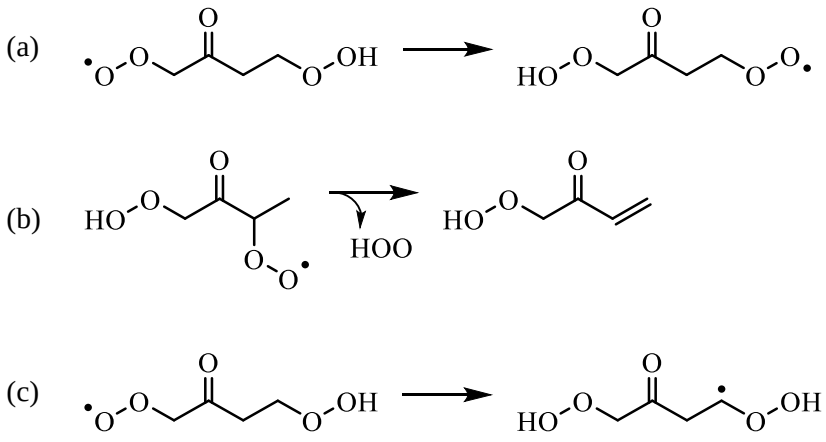

Figure 64. Major reactions from canonical variational transition state theory calculations of Kuzhanthaivelan and Rajakumar [763] on forward unimolecular reactions of ȮOQOOH radicals derived from butanone.

3.3.3. speciation from thermally initiated experiments

Speciation experiments from JSR and other thermally initiated flow reactors on ketone oxidation include butanone [764, 772-776], 2-pentanone and 3-pentanone [777], and two cyclic ketones, cyclopentanone [724], and cyclohexanone [743, 744].

Initial studies of butanone oxidation at low temperatures (< 750 K) were conducted by Bardwell and Hinshelwood [772-775]. More recently, FTIR and gas-chromatographic speciation measurements of butanone oxidation were obtained by in Thion et al. [776] at 1 and 10 atm and from 725 – 1250 K, using a jet-stirred reactor. Hemken et al. [764] conducted speciation measurements from butanone oxidation at 1 atm using a laminar flow reactor equipped with EI-MBMS, which utilized 17 eV electrons for ionization, and focused on product formation relevant to low-temperature autoignition. Several key species were quantified, including H_2O_2, β-scission products of initial butanonyl radicals – ethene, ketene, and methyl

ketene – and an unconfirmed oxygenated species with the molecular formula $C_4H_6O_2$. Methyl ketene was detected by MBMS and is an important species that forms exclusively from unimolecular decomposition of butanon-3-yl. Hemken et al. [764] ascribed the majority of the mole fraction of $C_4H_6O_2$ (*m/z* 86) to 2-methyloxetan-3-one, which is the lone cyclic ether formed along a pathway involving both resonance-stabilized Ṙ and Q̇OOH radicals. However, the authors noted that the uncertainty for 2-methyloxetan-3-one is significant (factor of ~5) because of missing cross-section measurements in the literature; Hemken et al. [764] employed the procedure of Schenk et al. [778] to estimate the cross-section. The discrepancies may also arise from an incomplete description of cyclic ether sub-mechanisms. Thion et al. [776] considered only diacetyl formation and excluded cyclic ether formation. However, Hemken et al. [764] disregard diacetyl on the basis of barrier height calculations from Sebbar et al. [761]. Because several isomers are possible, the identity of the $C_4H_6O_2$ species remains unresolved.

Fenard et al. [777] measured species profiles for 2-pentanone and 3-pentanone oxidation, using the laminar flow reactor/EI-MBMS approach of Hemken et al. [764], at 1 atm and from 800 – 1050 K. Several species were quantified, including CO, CO_2, H_2O, C_2H_4, as well as species related to RO$\dot{O}$ chemistry, such as methyl ketene. Cyclic ethers, which were predicted as abundant intermediates from chemical kinetics modeling, were not reported and the isomeric composition of HO$\dot{O}$-elimination products in 2-pentanone oxidation was not determined.

Cyclopentanone oxidation experiments were conducted in Thion et al. [724] at 1 atm and 10 atm using a JSR. Species profiles were measured from 730 – 1280 K and exhibited no NTC chemistry. With the exception of cyclopent-2-en-1-one and cyclopent-3-en-1-one, which were not isomer-resolved, profiles were measured for alkenes, carbonyls, and other species such as acetylene that were produced from ring-opening reactions. Reaction mechanisms were proposed for several of the species detected, including acetylene via H-abstraction from cyclopent-2-en-1-one from the α carbon and subsequent ring-opening of the resonance-stabilized radical.

Serinyel et al. [744] reported JSR experiments on cyclohexanone oxidation, which were conducted at 10 atm and from 530 – 1220 K over a range of equivalence ratios. Cyclic intermediates formed via ring-opening reactions were detected, namely cyclopentene and cyclopentadiene. Below 1000 K, several other ring-opened products were detected, including methyl vinyl ketone, 1,5-hexadiene, propene, and formaldehyde. In subsequent JSR experiments, conducted at 1 atm and 10 atm, Thion et al. [743] reported similar speciation results. Both studies detected only one of the two alkene isomers formed via Ṙ + O_2 reactions, cyclohex-2-en-1-one, which is consistent with the MPIMS results in Scheer et al. [757]. Similar to cyclopentanone, two-stage chemistry is not evident in cyclohexanone oxidation.

3.3.4. influence of ketone oxidation pathways on autoignition chemistry

Ignition delay time measurements below 1000 K have been reported for butanone [764, 779, 780] and di-*iso*-propyl ketone [781], 2-pentanone [777], 3-pentanone [777, 782], and cyclopentanone [767]. NTC behavior is seen in di-*iso*-propyl ketone, 2-pentanone and 3-pentanone. Other measurements of ignition delay times, above 1000 K, include acetone [783], butanone [740, 784] and 2-pentanone [783], 3-pentanone [783, 785], and cyclohexanone [786]. Lam et al. [728] conducted shock tube measurements on ignition of a series of ketones from 1100 – 1400 K. **Table 4** summarizes the chemical kinetics mechanisms produced for ketone oxidation. Two mechanisms are reported for 3-pentanone, Serinyel et al. [785] and Fikri et al. [782], yet neither include RO$\dot{O}$ chemistry since the mechanisms were developed for high-temperature

combustion where the ketone is used as a chemiluminescence tracer in visualization experiments. Fenard et al. [777] developed a mechanism for both 2-pentanone and 3-pentanone, which includes low-temperature chemistry.

Table 4. Chemical kinetics mechanisms for acyclic and cyclic ketones.

species	*reference*
butanone	[764, 776, 780, 784]
2-pentanone	[777]
3-pentanone	[782, 785] [777]
di-*iso*-propyl ketone	[781, 787]
cyclopentanone	[724, 767]
cyclohexanone	[743, 744, 786]

3.3.4.1. ignition delay time experiments

The RCM ignition measurements of stoichiometric butanone in Hoppe et al. [779] covered 850 – 950 K and did not exhibit NTC behavior at either 20 atm or 40 atm. Burke et al. [780] extended the temperature range up to 1280 K for the same pressures. Hemken et al. [764] expanded the conditions over which RCM experiments were reported in [780], measuring ignition delay times at 40 atm from $\phi = 0.5 – 2.0$. In contrast to butanone ignition, *n*-butane exhibits two-stage chemistry due to the formation of ketohydroperoxides [788, 789] with an NTC region starting near 750 K [551]. The difference in ignition behavior between the two C4 molecules implies that the C=O group in butanone facilitates HOO-elimination via $\dot{R} + O_2$ reactions or acts as an impediment to the formation of $\dot{Q}OOH$ and/or subsequent consumption via second-O_2-addition reactions leading to ketohydroperoxide formation. **Figure 65a** compares stoichiometric ignition delay times of *n*-butane [96] and butanone [780] near ~20 atm.

In contrast, NTC behavior is displayed in ignition delay time trends of 2-pentanone and 3-pentanone. Fenard et al. [777] conducted RCM experiments at 20 atm and 40 atm covering from 650 – 950 K. Despite the longer alkyl chain, which typically enhances low-temperature chemistry, chain-branching was less pronounced in 2-pentanone. For example, at 40 atm and 700 K, ignition delay times for 2-pentanone was ~80 ms and for 3-pentanone ~25 ms. The lower reactivity of 2-pentanone was ascribed to increased flux of initial $\dot{R}$ radicals through both HOO-elimination and C–C β-scission reactions, both of which are inhibited to a larger extent in 3-pentanone. In addition, at both pressures, the temperature ranges over which NTC chemistry is evident differed substantially: ~150 K for 3-pentanone and ~50 K for 2-pentnaone.

Figure 65b compares ignition delay times at 20 atm of 2-pentanone and 3-pentanone from Fenard et al. [777] to *n*-pentane from Bugler et al. [554], which exhibits an NTC region. All three trends overlap within experimental uncertainty above 1000 K, below which the ignition delay times for *n*-pentane are significantly shorter due to more favorable chain-branching (arising from a larger number of pathways and higher amount of secondary hydrogen available for abstraction and intramolecular isomerization). At 800 K, compared to 2-pentanone, *n*-pentane ignition times in **Figure 65b** are shorter by a factor of ~50, and by a factor of ~30 compared to 3-pentanone. Fikri et al. [782] conducted ignition delay time measurements of 3-pentanone at 10 atm, 20 atm, and 40 atm using a shock tube and covered a broad range of temperatures (~750 – 1200 K). The strong NTC behavior measured in the RCM experiments of Fenard et al. [777] was

not observed in Fikri et al. [782] because the lower limit of temperature is near the inflection point where continued decrease in temperature starts leading to shorter ignition times (i.e. the end of the NTC region).

Zhang et al. [767] measured ignition delay times for cyclopentanone using both shock tube and RCM experiments and no NTC behavior was observed. The experiments were conducted using several equivalence ratios, two pressures (15 atm and 30 atm), and over the temperature range 794 – 1368 K. Time histories of CO formation behind reflected shock waves were also measured. **Figure 65c** compares the cyclopentanone ignition measurements in Zhang et al. [767] to cyclopentane ignition measurements [553]. However, the temperatures where ignition delay times overlap is limited to 1000 K and above.

Allen et al. [781] measured ignition delay times for di-*iso*-propyl ketone from 590 – 720 K at a nominal pressure of 10 atm using an RCM. Despite the highly branched molecular structure, di-*iso*-propyl ketone ignition exhibits appreciable two-stage chemistry, facilitated in part by 1,2-acyl shift rearrangement of initial ketonyl radicals enabling ȮOOH radical formation [781]. NTC behavior started near 650 K in the experiments.

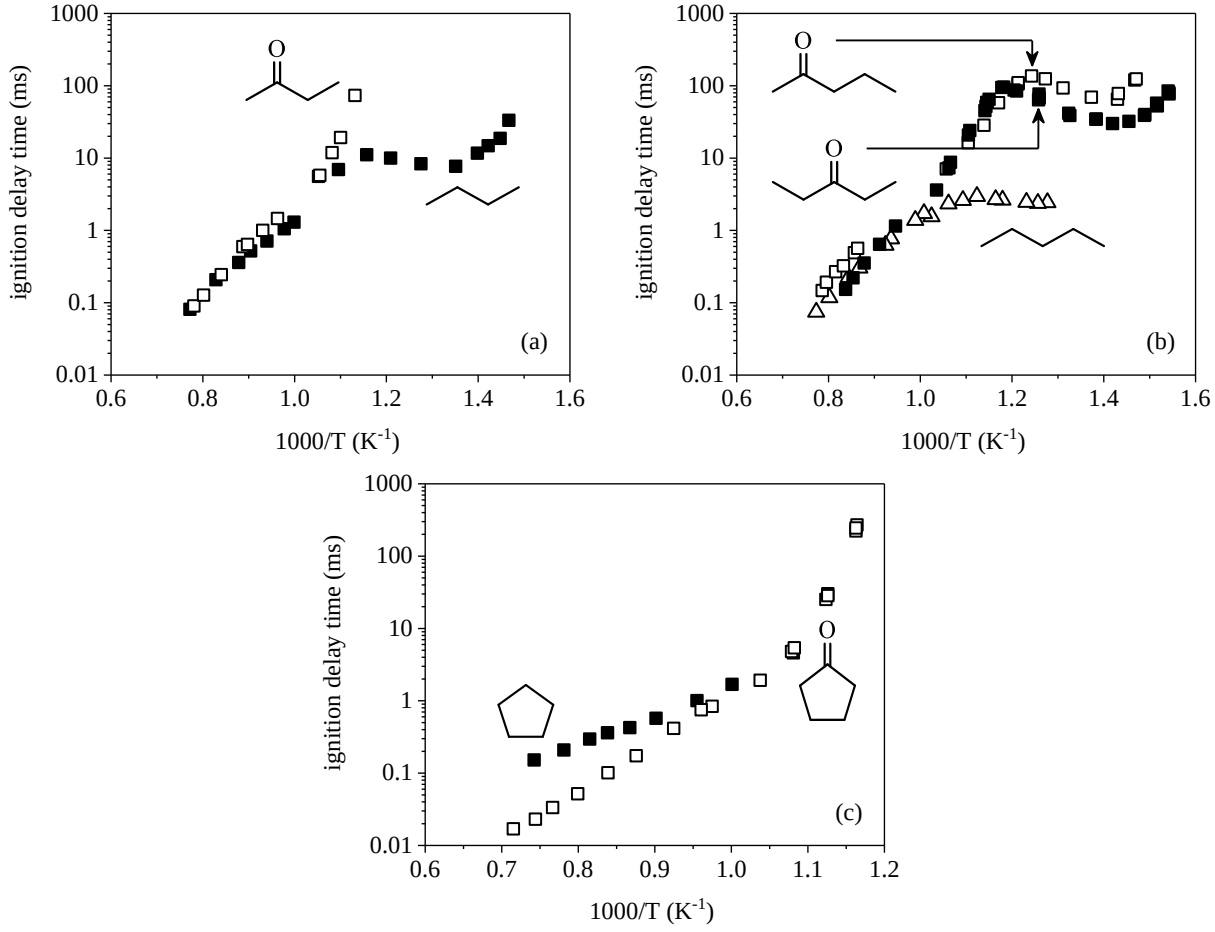

Figure 65. Comparison of stoichiometric ignition delay time trends of ketones and alkanes. (a) butanone (20 atm), Burke et al. [780], and *n*-butane (18 atm), Healy et al. [96]. (b) 2-pentanone/3-pentanone, Minwegen et al. [783] and Fenard et al. [777], and *n*-pentane (20 atm), Bugler et al. [554]. (c) cyclopentanone (15 atm), Zhang et al. [767], and cyclopentane (13 atm), Al-Rashidi et al. [553]. Ignition delay times below 1000 K in (b) are from RCM experiments

in Fenard et al. [777] while high-temperature measurements are from shock tube experiments in Minwegen et al. [783]. RCM ignition times for 3-pentanone were measured at a nominal pressure of 25 atm [777].

3.3.4.2. detailed chemical kinetics mechanisms

Four chemical kinetics mechanisms exist for butanone oxidation: Serinyel et al. [784], Burke et al. [780], Hemken et al. [764], and Thion et al. [776]. The first-generation mechanism of Serinyel et al. [764, 776, 780, 784] excluded peroxy radical chemistry because high-temperature shock tube ignition delay times were used as benchmark measurements. Burke et al. [780] produced the first low-temperature combustion mechanism of butanone by developing a sub-mechanism for peroxy radicals using rate rules from Curran et al. [385]. RCM and shock-tube ignition delay times were simulated and, consistent with the experiments, exhibited no significant NTC behavior. Reaction flux analyses in [780] predicted that a major pathway for consumption of initial ketonyl radicals is via C–C β-scission or disproportionation reactions leading to alkoxy radicals, both disfavoring ROȮ formation necessary for low-temperature chain-branching. Despite no indication of NTC behavior, the addition of low-temperature oxidation pathways, particularly HOȮ-elimination reactions, were essential in accurately predicting the ignition delay times.

Thion et al. [776] produced a revised chemical kinetics mechanism for butanone based on Serinyel et al. [784]. Utilizing potential energy surface calculations at the G3//MP2/aug-cc-pVDZ level of theory, high-pressure limit rate coefficients were calculated for H-abstraction by Ḣ and $\dot{C}H_3$ using conventional transition state theory. Pressure-dependent rate coefficients were calculated for β-scission and isomerization of the three butanon-x-yl radicals (where x = 1, 3, or 4) and homolysis of butanone. Rate parameters were also calculated for ȮH-addition and HOȮ-addition reactions to resonance-stabilized butanon-3-yl radicals. The revised rate coefficients were combined with the addition of several reactions relevant to low-temperature oxidation into the mechanism [776].

Hemken et al. [764] revised the Burke et al. [780] mechanism to include updated unimolecular decomposition reactions of butanone and butanonyl radicals from calculations of Thion et al. [764, 776, 780, 784], higher rates for H-abstraction by HOȮ, and a revised methyl ketene sub-mechanism that included thermal decomposition (accounting for pressure-dependence using Troe parameters), H-abstraction, and disproportionation with ȮH and other radicals. Subsequent reactions of radicals from methyl ketene were also included.

To compare the role of the ketone group on low-temperature oxidation, **Figure 66a** compares simulations of the temperature dependence of butanone consumption using the mechanism of Thion et al. [776] and *n*-butane consumption using the mechanism of Healy et al. [96]. Both were conducted using the PSR module in ChemKin. The conditions of the simulations are 10 atm, stoichiometric, isothermal conditions at a residence time of 1000 ms, under dilute conditions (initial concentrations were 1000 ppm). Using the mechanism of Hemken et al. [764], a similar butanone consumption profile is predicted. Low-temperature chain branching and NTC behavior is evident for *n*-butane, starting around 600 K, which is due to ȮOOH + O_2 reactions forming ketohydroperoxides (**Figure 66b**). Owing to the reaction pathways including favorable reverse reaction rates of ketonylperoxy radicals (ROȮ) to Ṙ + O_2 [760, 761] and of ȮOOH products, as well as facile C–C β-scission reactions of ketonyl and hydroperoxyketonyl radicals competing

with O_2-addition [736], chain-branching and subsequent two-stage ignition that is observed in *n*-butane oxidation is suppressed for butanone (**Figure 66c**).

(a)

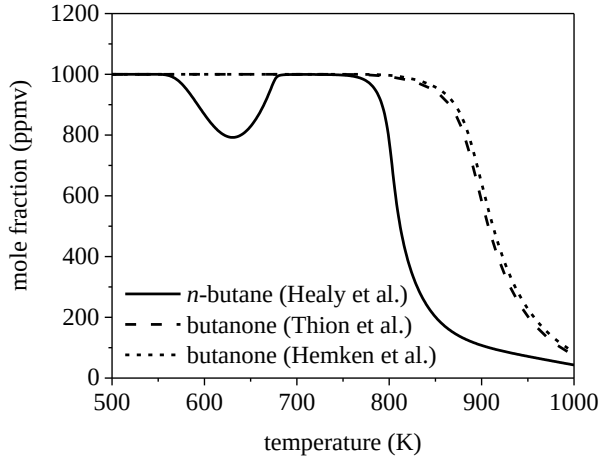

(b)

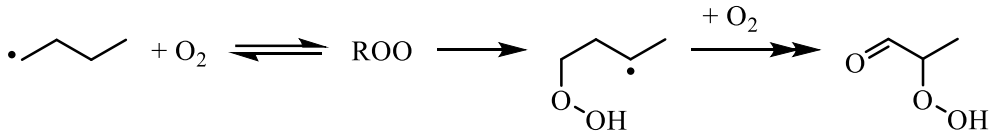

(c)

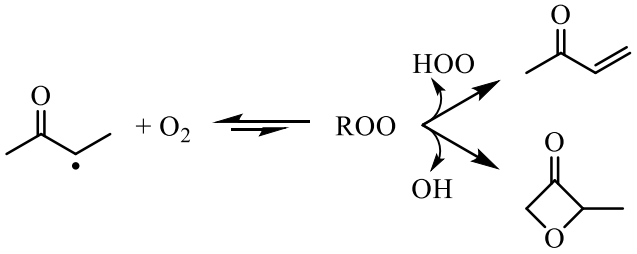

Figure 66. (a) Model simulations of stoichiometric consumption of *n*-butane [96] and butanone (Thion et al. [776] and Hemken et al. [764]) at 10 atm and residence time of 1000 ms. NTC behavior is not exhibited in butanone due to the impact of the carbonyl functional group on reaction mechanisms preceding chain-branching. Representative reaction pathways at 625 K in *n*-butane (b) and butanone (c). The chain-branching pathway in *n*-butane is responsible for accelerated depletion in the range ~575 – 675 K. Analogous second-O_2-addition reactions are hindered in butanone oxidation in favor of HOO-elimination, cyclic ether formation, or back dissociation of ROȮ into Ṙ + O_2.

Using a chemical kinetics mechanism produced by Reaction Mechanism Generator (RMG), simulations were conducted in Allen et al. [781] on ignition delay time and speciation results for di-*iso*-propyl ketone from RCM and MPIMS experiments. In the ignition delay time results at 10 bar, NTC behavior became evident over the temperature range 625 – 725 K and was ascribed to three reactions: (1) increased rates of *β*-scission of primary radicals with increasing temperature leading to the formation of methyloxirane + propene + CO + ȮH, a reaction pathway confirmed in the MPIMS experiments, (2) 1,2-acyl shift in primary radicals of di-*iso*-propyl ketone and subsequent reaction of the rearranged radicals with O_2, similar to methyl *tert*-butyl ketone (cf. **Figure 59b**), and (3) chain-branching derived from unsaturated ketohydroperoxides formed via HOȮ-elimination from tertiary-tertiary ȮOQOOH radicals (**Figure 67**). Coordination of the reaction mechanism details produced from the MPIMS experiments along with the PES

calculations led to an initial mechanism produced using RMG. The initial simulations of ignition delay times predicted less-pronounced NTC behavior, although the mechanisms predictions were improved significantly by accounting for resonance-stabilization in the underlying thermochemistry.

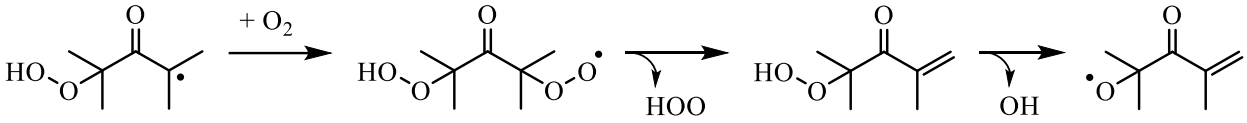

Figure 67. Chain-branching pathway in di-*iso*-propyl ketone [781]. The lack of tertiary hydrogen for conventional ȮOQOOH ⇌ HOOṖOOH isomerization and availability of adjacent hydrogen leads via HOO-elimination to an unsaturated ketohydroperoxide (4-hydroperoxy-2,4-dimethylpent-1-en-3-one), which may decompose via O–O bond-scission into an oxy radical.

Thion et al. [724] constructed a chemical kinetics mechanism for cyclopentanone oxidation, which built upon prior mechanisms for butanone [776] and for butene isomers [790, 791], and predicted species profiles from jet-stirred reactor experiments. Reaction pathway analysis using the mechanism indicated that ring-opening reactions were of central importance, e.g. cyclopentanon-3-yl → CO + but-1-en-4-yl. Thion et al. [724] remarked on the need to refine the sub-mechanism for cyclopent-2-en-1-one due to inconsistencies between predictions and experiment related to acetylene formation (**Figure 68**), particularly at high pressure, in addition to the formation of cyclopent-2-en-1-one [776]. Cyclic ether formation pathways were not included in the mechanism despite analogous reactions being submerged on the potential energy surface of cyclopentanyl peroxy radicals [768].

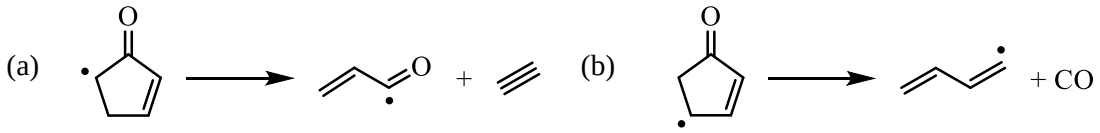

Figure 68. Reaction mechanisms in Thion et al. [724] for decomposition of radicals of cyclopent-2-en-1-one leading to acetylene production via (a) direct and (b) indirect pathways (decomposition of 1,3-butadien-4-yl yields acetylene + vinyl).

The chemical kinetics mechanism of Zhang et al. [767] for cyclopentanone was constructed from the mechanism of Thion et al. [724] and using existing mechanisms for alkanes [792]. The Zhang et al. [767] mechanism included peroxy radical chemistry, deriving the core reaction classes and rate parameters from cyclopentane [793] with modifications to account for bond energy differences. High-pressure-limit rates were calculated for Ṙ + O_2 → cyclopentenone + HOȮ for both isomers from 500 – 2000 K (cf. **Figure 63**). The chemical kinetics simulations indicated that, in addition to HOO-elimination, cyclic ether formation is competitive with second-O_2-addition and with ȮOOH-ring-opening reactions. However, no speciation data for the cyclic ethers are available and the isomeric branching for cyclic ether formation from ȮOOH radicals of cyclopentanone remains unknown.

Three chemical kinetics mechanisms exist for cyclohexanone oxidation: Serinyel et al. [744], Thion et al. [743], and He et al. [786]. The last is built from the first-generation mechanism of Serinyel et al. [744] and utilizes high-temperature shock tube ignition for assessing performance. Thion et al. [743] revised the first-

generation mechanism of Serinyel et al. [744] by including the reaction class $\dot{R} + O_2 \rightarrow$ conjugate alkene + $HO\dot{O}$ and directly calculating rate coefficients for several reaction classes using G3//MP2/aug-cc-pVDZ, RRKM theory, and master equation analysis. Rate coefficients were calculated using transition state theory for H-abstraction from cyclohexanone by $\dot{H}$, $\dot{O}H$, and $\dot{C}H_3$, and for isomerization and decomposition of initial α, β, and γ radicals. While the formation of β radicals remains the most favorable from 500 – 1000 K, the direct calculations for H-abstraction in Thion et al. [743] affected predictions of branching fractions of initial radicals compared to [744] (**Figure 69**).

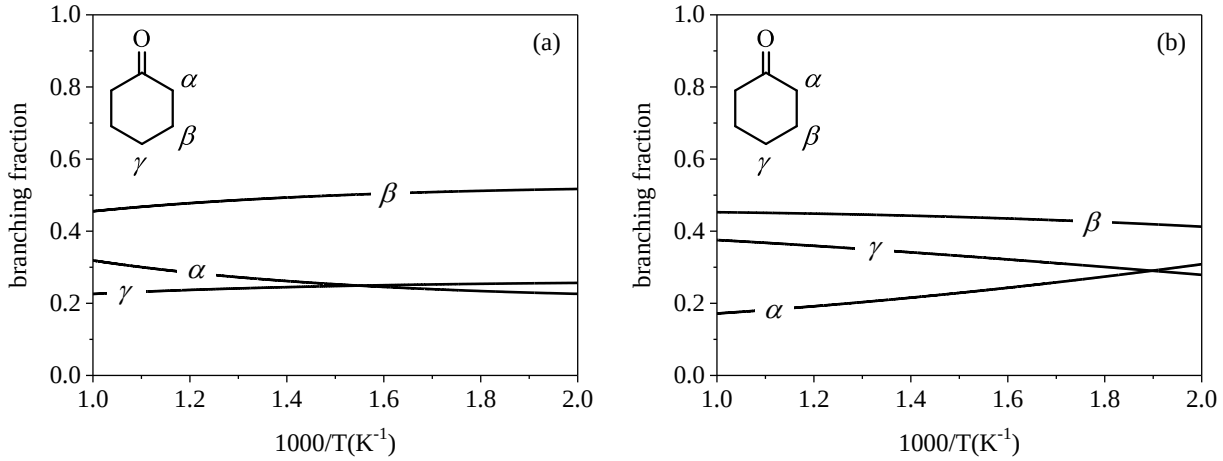

Figure 69. Branching fractions for $\dot{O}H$ + cyclohexanone $\rightarrow H_2O + \dot{R}$ from (a) Serinyel et al. [744] and (b) Thion et al. [743].

Oxidation reactions of initial radicals are limited in both cyclohexanone mechanisms [743, 744], which contain only $\dot{R} + O_2 \rightarrow$ alkene + $HO\dot{O}$ and exclude $\dot{Q}OOH$-mediated reactions. While both conjugate alkenes cyclohex-2-en-1-one and cyclohex-3-en-1-one are included in the two mechanisms, only the former was detected in the experiments of Thion et al. [743] and Serinyel et al. [744]. Despite being an important intermediate below 1000 K, model-predicted species profiles of cyclohex-2-en-1-one were inconsistent with experimental profiles. The discrepancies may indicate deficiency in the sub-mechanism, which only includes abstraction reactions forming an allylic-type radical using rate coefficients from Battin-Leclerc et al. [99], and subsequent unimolecular decomposition into species such as acetylene, ethene, and CO. Serinyel et al. [744] included one additional reaction: $\dot{O}H$-addition to cyclohex-2-en-1-one using rate parameters from Heyberger et al. [794] for $\dot{O}H$ + propene. $\dot{O}H$-addition reactions were not included for cyclohex-3-en-1-one. Unimolecular loss of H_2 and C–H β-scission reactions from cyclohexanone were also included, yet are not relevant below 1000 K. Other reactions, which are relevant to low-temperature chemistry, such as $\dot{Q}OOH \rightarrow$ cyclic ether + $\dot{O}H$, were excluded in both mechanisms. The MPIMS experiments of Scheer et al. [757] on cyclohexanone, which were reported subsequent to the Serinyel et al. [743, 744] mechanism, observed ion signal at the mass-to-charge ratio (*m/z* 112) corresponding to cyclic ether products, yet isomers were not identified. Cyclic ether formation in cyclohexanone oxidation is likely, given the detection of similar species in both cyclohexane [522, 795] and in cyclohexene oxidation [796].

3.3.5. summary of ketone functional group effects

The carbonyl functional group creates distinct hydrogen-abstraction sites in ketone biofuels, two of which introduce resonance-stabilization in subsequent ketonyl radicals, and the potential for pre-reaction complex formation in the initiation reactions with ȮH and HOȮ. Because of resonance stabilization, and depending on the type of carbon (primary, secondary, or tertiary), C–H bond energies are lower by 5-10 kcal/mol compared to alkanes. For O_2-addition to resonance-stabilized ketonyl radicals, peroxy radical well depths are ~15 kcal/mol higher in energy due to the loss of resonance. Reactions of resonance-stabilized Ṙ and ȮOOH radicals – in particular, the competition between C–C β-scission and reaction with O_2 – is the main distinguishing characteristic governing chain-branching reactions in ketone oxidation.

In ȮH-initiated H-abstraction reactions from acyclic ketones, α radicals (adjacent to carbonyl group) are formed via direct abstraction while β radicals are produced via pre-reaction complexes and are competitive below ~700 K. Reactions at other sites that are further from the carbonyl group (γ, δ, …) undergo only direct abstraction. In contrast to ȮH, where hydrogen-bonded pre-reaction complexes occur primarily at β carbon, such complexes are significant in the majority of HOȮ-initiated H-abstraction reactions from ketones. For ȮH-initiated H-abstraction from cyclopentanone, branching fractions are weakly temperature dependent and β radicals are favored over α radicals (β ~0.6 versus α ~0.4 at 500 K and β ~0.7 versus α ~0.3 at 1000 K). Similar results are reported for cyclohexanone in that β radicals are favored and all abstraction sites are important. Abstraction from α and γ carbon vary from 0.2 – 0.3 from 500 – 1000 K. On a per-H-atom basis, for cyclic ketones, rate coefficients for H-abstraction from β carbon are similar among the computational studies to within ~30%, yet are lower than analogous reactions in alkanes because of the effects of hydrogen bonding in the pre-reaction complex lowering the rate of abstraction from α carbon.

Several reaction mechanisms that are relevant to chain-branching chemistry and characteristic of ketones are reported: (i) ȮH-loss from γ-ketohydroperoxide via O–O bond-scission is potentially facilitated by the ketone group, given that the decomposition pathway involves production of a resonance-stabilized radical; (ii) alternative unimolecular decomposition pathways of ȮOOH including a water-elimination reaction, via a mechanism similar to that of γ-ȮOOH in alcohol oxidation, and a hydrogen-transfer reaction from the hydroperoxy group to the carbonyl group forming peroxy-substituted enol; (iii) rearrangement reaction mechanism in ketonylperoxy radicals via a chain-propagation pathway mediated by to the formation of a 5-membered cyclic peroxy radical intermediate. Other characteristic reactions of ketones include Dowd-Beckwith ring-expansion (occurring in 2-methylcyclopentanone oxidation) and related rearrangement reaction (e.g., from primary radicals occurring in methyl *iso*-butyl ketone oxidation). **Figure 70** shows the low-temperature chain-branching scheme augmented to emphasize pathways that diminish chain-branching and that are enhanced by the ketone functional group.

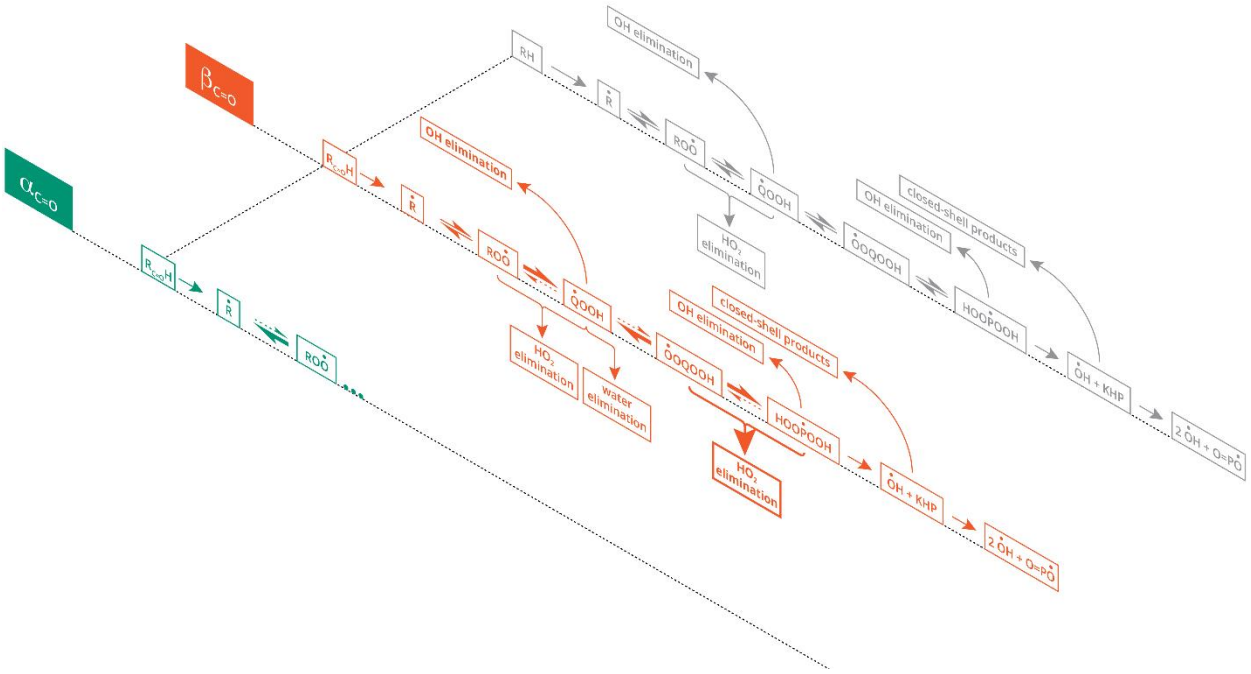

Figure 70. Summary of ketone functional group effects on low-temperature chain-branching. The leftward-pointing and downward-pointing arrows indicate a shift in flux away from chain-branching pathways responsible for ignition. Vinoxylic resonance stabilization reduces the reactivity of α- radicals and the corresponding lower exothermicity of ROȮ formation inhibits the transformations required to proceed towards chain branching. For oxidation with initial radical sites farther removed from the carbonyl group, vinoxylic resonance can stabilize ȮQOOH or other intermediates, changing the thermochemistry of isomerization steps. Each type of initial radical is depicted in a separate plane, with different colors used to guide the eye. The alkane oxidation mechanism is depicted in the back plane for reference. Pathways that are enhanced by the effects of the functional group are emphasized with bold arrows and labels, and those that are diminished are made lighter or omitted.

3.4. acyclic ethers

Figure 71 depicts the molecular structure and site-labeling nomenclature for three representative acyclic ethers: dimethyl ether, diethyl ether, and *iso*-propyl methyl ether. The ether group lowers C–H bond dissociation energies on α carbon due to hyperconjugation in the resultant radical between the lone-pair orbital of the oxygen atom and the singly-occupied orbital of the carbon atom – the lone pair on the –O– group delocalizes to adjacent C–H antibonding orbitals, weakening C–H bond energy on α carbon. Cai et al. [797] utilized G4 and CBS-QB3 methods to calculate bond energies of di-*n*-butyl ether, which differed consistently from one another by ~1.5 kcal/mol. C–H bond energies for the latter method were 95.0, 100.0, 96.7, and 101.2 kcal/mol for α, β, γ, and δ sites. Similar results were produced by Thion et al. [798] using G3B3 with the exception of the γ site (98.8 kcal/mol) that differed by 2.1 kcal/mol. The main influence of the ether group is a reduction of C–H bond energy on α carbon by ~3.5 kcal/mol compared to secondary carbon on alkanes.

Poly ethers are potential biofuels [799-805]. The ether functional group is repeated in poly(oxymethylene) dimethyl ethers (**Figure 71d**), the simplest example of which is dimethoxymethane (DMM) [806] shown in **Figure 71e**. The reactions of such polyethers share some chemical characteristics with reactions of dimethyl ether [807-809]. However, Vermeire et al. [810] note some differences. Kopp et al. [808] report a C–H bond energy of 95.67 kcal/mol for the terminal methyl groups in DMM and slightly higher (96.01 kcal/mol) for the central methylene group (at the CCSD(T)/aug-cc-pV(D+T)Z//B2PLYPD3BJ/6-311++g(*d*,*p*) level).

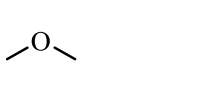

(a) dimethyl ether

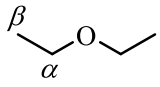

(b) diethyl ether

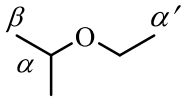

(c) *iso*-propyl methyl ether

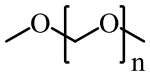

(d) dimethoxymethane

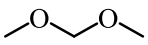

(e) poly(oxymethylene) dimethyl ethers

Figure 71. Structure and site nomenclature of acyclic ethers: (a) dimethyl ether, (b) diethyl ether, (c) *iso*-propyl methyl ether, (d) polyether with n monomer units, and (e) dimethoxymethane.

The sections below are separated into the following areas: (1) initiation reactions, RH + $\dot{X}\rightarrow \dot{R}$ + HX, (2) reactions of linear radicals with O_2, including methoxymethyl and diethyl ether radicals, and reactions of branched ether radicals with O_2; (3) thermally initiated experiments in which speciation measurements were conducted, e.g. jet-stirred reactors; (4) detailed chemical kinetics mechanisms; (5) ignition delay time measurements. Interwoven into the sections are relevant theoretical studies and particular attention is paid to connecting with experiments in order to highlight areas of both agreement and disagreement.

3.4.1.initiation reactions and branching fractions

Because of the importance of ether oxidation in atmospheric chemistry, there are many studies of initiation reactions at lower temperature. These temperature dependent results are useful in connecting to other, higher-temperature measurements in cases where there is an inflection in temperature due to the formation of pre-reaction complexes. Rate coefficients for abstraction reactions above 300 K involving ȮH and linear ethers are reported for dimethyl ether [750, 811-826], diethyl ether [812, 813, 815, 821, 822, 826-828], and several other ethers [803, 813, 815, 821-823, 827-833] using both experimental and computational methods.

Measurements of rate coefficients for ȮH + H_3COCH_3 → H_2O + $H_2\dot{C}OCH_3$ span a broad range of temperature and pressure: 230 – 850 K and 0.03 – 21 bar, respectively. No significant pressure dependence is exhibited [824, 825] and the overall reaction follows positive temperature dependence [750, 811, 812, 814, 815, 818, 824-826]. Theoretical calculations of high-pressure limit rate coefficients cover a broader range of temperature, 200 – 3000 K [817, 819-825, 831] and are largely consistent with the experimental results. Ogura et al. [821] concluded using *ab initio* calculations on a range of ethers that the presence of an ether group lowers the barrier height to abstraction by 3 – 4 kcal/mol relative to alkanes. Rate coefficients from OH laser-induced fluorescence experiments measured in Bänsch et al. [825] were convolved with the majority of literature measurements, which produced the rate coefficient of modified Arrhenius form, $k(T) = 8.45 \cdot 10^{-18}\ T^{2.07} exp(262.2\ K\ /T)\ cm^3\ s^{-1}$. **Figure 72** compares the rate coefficient produced from [825] to the calculations of Hu et al. [834] for reaction with the analogous alkane ȮH + $CH_3CH_2CH_3$ → H_2O + $\dot{C}H_2CH_2CH_3$, which employed VTST with microcanonical-optimized multidimensional tunneling. The comparison highlights the larger rate coefficient for dimethyl ether + ȮH at temperatures below 1000 K; at 500 K, the two differ by ~65%.

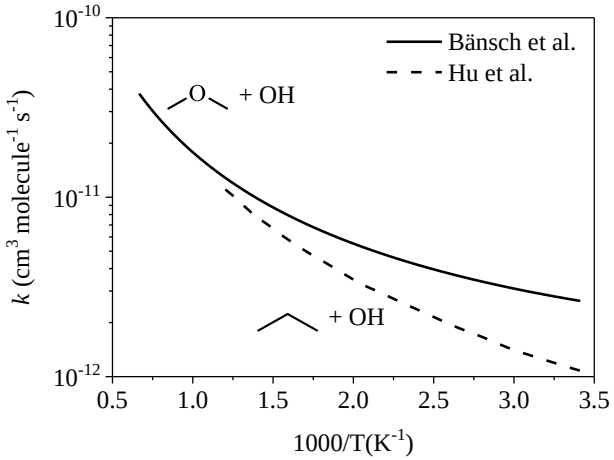

Figure 72. Comparison of rate coefficients for H-abstraction by ȮH from dimethyl ether (Bänsch et al. [825]) and from propane (Hu et al. [834]).

The *ab initio* calculations showed differences between out-of-plane and in-plane transition states in reactions of ȮH with dimethyl ether. The formation of a reactant complex (**Figure 73a**) precedes an out-of-plane, indirect abstraction reaction (**Figure 73b**) – the transition state for which is submerged relative to the ȮH + CH_3OCH_3 entrance channel by 1 – 4 kcal/mol [816, 817, 819, 820, 823-825] depending on the

level of theory applied. The complex provides 4 – 9 kcal/mol of stabilization, depending again on the level theory applied. In contrast, transition states located for in-plane, direct abstraction (**Figure 73c**) lie above the entrance channel by approximately 3 – 4 kcal/mol [816, 817, 819, 820, 823, 824] Bänsch et al. [825] identified transition states connecting to both the out-of-plane *and* in-plane transition states using both CCSD(T)/cc-pV(T,Q)Z//MP2/6-311G(*d*,*p*) and CCSD(T)/cc-pV(T,Q)Z//CCSD/cc-pVDZ levels of theory. A third method applied, CBS-QB3, did not locate an in-plane transition state and some variability amongst the different methods in predicting transition state geometries was noted [825]. Calculated branching fractions [816, 817, 819, 820, 822-824], show more than 90% of radicals formed by abstraction via the out-of-plane transition state below 500 K.

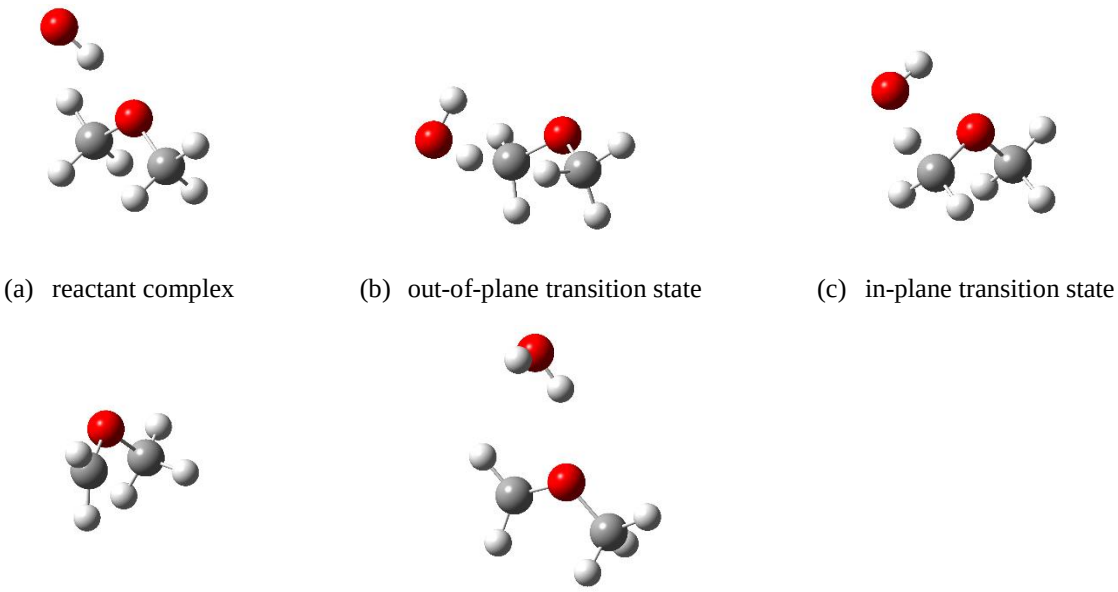

(a) reactant complex (b) out-of-plane transition state (c) in-plane transition state

(d) methoxymethyl (e) product complex

Figure 73. Structure of reactant complex (a), transition states (b, c), $\dot{C}H_2OCH_3$ product (d), and (e) product complex from $\dot{O}H + CH_3OCH_3$ calculated at the MP2/6-311G(*d*,*p*) level of theory in Zhou et al. [823].

The respective geometries of the out-of-plane and in-plane transition states, calculated at various levels of theory, are largely similar [816, 817, 819, 820, 823-825]. To explain the reason for lower barrier height of the out-of-plane transition state Zhou et al. [823] noted an inverse relationship between the barrier height and length of the C–O bond (on the abstraction site) in the transition state: longer C–O bond length being consistent with a lower barrier height. Zhou et al. [823] also remarked on the C–H bond energy being lower for out-of-plane H atoms as a means of explaining the lower barrier height. However, no energy differences were reported and bond lengths differed by only 0.019 Å. Bottoni et al. [816] conducted an extensive series of calculations on transition state geometries and potential energy surfaces using nine combinations of functionals and basis sets. The results in [816] and in other studies [817, 820] point to appreciable dependence on method, which provides a plausible explanation of the aforementioned differences in the barrier heights.

Figure 74a compares rate coefficients for ȮH + CH_3OCH_3 → H_2O + $\dot{C}H_2OCH_3$ calculated in Wu et al. [819], Zhou et al. [823], Bänsch et al. [825], and Carr et al. [824] with the group rate expression produced in Ogura et al. [821]. The overall rate coefficients all follow positive temperature dependence and are consistent below 1000 K to within approximately 50%. **Figure 74b** shows branching fractions calculated from Wu et al. [819], El-Nahas et al. [820], Zavala-Oseguera et al. [822], and Zhou et al. [823]. The temperature dependence for in-plane abstraction is positive while out-of-plane pathways, which proceed via formation of a reactant complex (c.f. **Figure 73a**), follow negative temperature dependence [819, 820, 822, 823, 825], as evident in branching fraction calculations in **Figure 74b**. Out-of-plane abstraction is predicted to be the dominant branching channel at temperatures below 1000 K, with the exception of the lower level results from [820], because of the reaction complex [819, 820, 822, 823], which lowers the barrier height.

In addition to pre-reaction complex formation, a product complex (c.f. **Figure 73e**) that precedes H_2O + $\dot{C}H_2OCH_3$ – stabilized via hydrogen-bonding between one H atom in H_2O and the O atom in the methoxymethyl radical – is included in the overall rate coefficient for ȮH + CH_3OCH_3 → H_2O + $\dot{C}H_2OCH_3$ [819, 820, 823, 825]. The product complex is expected to undergo facile dissociation to products, given that the H···O energy (ca. 3.5 kcal/mol) is lower than the reverse H-abstraction barriers.

Carr et al. [824] adopted a one-transition-state model to conduct master equation calculations for ȮH + CH_3OCH_3 → H_2O + $\dot{C}H_2OCH_3$ using MESMER and reproduced literature measurements, along with results from OH LIF experiments, covering a combined temperature range of 195 – 1423 K. The consistency of the one-transition-state calculations with the experimental results [750, 811-814, 818, 835-837] indicates that the formation of a reactant complex may impact rate coefficients only at temperatures below ~200 K, and is of diminished importance at combustion-relevant temperatures.

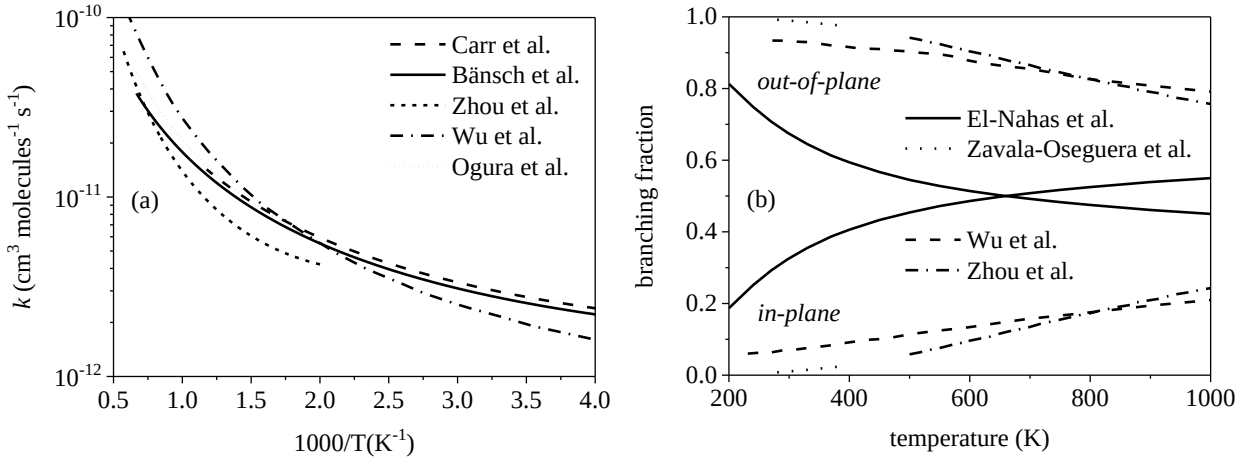

Figure 74. (a) High-pressure limit rate coefficients for ȮH + CH_3OCH_3 → H_2O + $CH_3O\dot{C}H_2$ from Wu et al. [819], Zhou et al. [823], Bänsch et al. [825], Carr et al. [824], and Ogura et al. [821]. (b) Branching fractions for out-of-plane and in-plane abstraction from Wu et al. [819], El-Nahas et al. [820], Zavala-Oseguera et al. [822], and Zhou et al. [823].

Reactions of poly(oxymethylene) methyl ethers with ȮH may be expected to follow similar behavior. The reaction with dimethoxymethane shows a negative temperature dependence at low temperature in experimental determinations from Porter et al. [838] and Wallington et al. [832]; at higher temperature there is a disagreement between the results of Vovelle et al. [833], which show a turn towards a positive temperature dependence above ~350 K, and the measurements of Bänsch and Olzmann [803], which show a continued weak negative temperature dependence over the range covered (297 – 570 K). Theory (CCSD(T)-F12a/aug-cc-pVTZ//M06-2X/def2-TZVP) by He et al. [839] shows an initial reactant complex in the ȮH + DMM reaction that can connect to abstraction over submerged barriers at either the terminal or central carbon. As in dimethyl ether, a product complex also exists between H_2O and radical products of the ȮH + DMM reaction. Canonical transition state theory calculations [839] predicted non-Arrhenius behavior in reasonable agreement with the measurements from Vovelle et al. [833], and showed a dominance of abstraction at the central site, which exhibits a looser transition state for abstraction.

Rate coefficients for initiation reactions of diethyl ether ($C_2H_5OC_2H_5$) with ȮH below 1000 K were measured in several experiments using laser photolysis laser-induced fluorescence [812, 813, 826, 827], UV-irradiation [828], or a reacting H_2/O_2 flow [815]. High-temperature rate coefficients were also measured from 1054 – 1505 K by Sela et al. [840] using a shock tube. However, with the exception of Tranter and Walker [815], the reported measurements are below 450 K and only a relatively narrow range of pressures are covered: 25 – 720 Torr. Negative temperature dependence is exhibited starting from the lower extremum of the measurements, 230 K [813], up to approximately 400 K as evident in [815]. The *ab initio* calculations of $C_2H_5OC_2H_5$ + ȮH in Ogura et al. [821] and Zavala-Oseguera et al. [822] support the experimental results. Notably, hydrogen-bonded pre-reaction and product complexes were included in [822], yet in [821] direct and indirect transition states were not considered. Branching fractions calculated in Zavala-Oseguera et al. [822] – at 400 K, the highest temperature for which branching fractions were reported – indicate that >90% of abstraction occurs from α carbon in diethyl ether, due largely to the 3 – 5 kcal/mol lower C–H bond energy caused by the proximity to the ether group. However, branching fractions calculated from the group rate expressions in Ogura et al. [821] suggest a more competitive reaction, where α radicals range from 40 – 60% up to 1000 K. **Figure 75** compares rate coefficients determined using group rate expressions for ȮH + diethyl ether from Ogura et al. [821] against ȮH + *n*-pentane from Sivaramakrishnan et al. [841], showing that H-abstraction is approximately a factor of ~2 higher from diethyl ether from 500 – 1000 K.

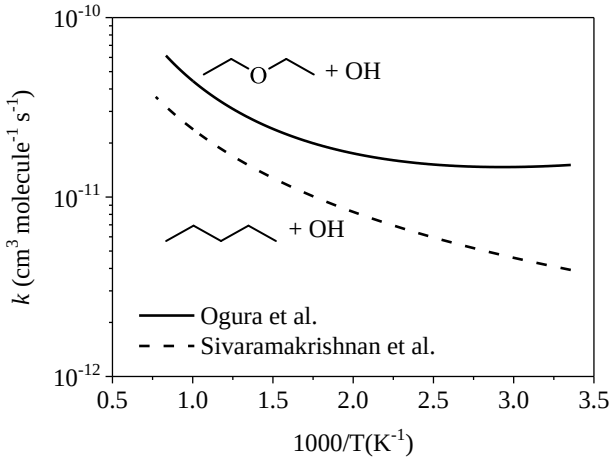

Figure 75. Comparison of rate coefficients for H-abstraction by ȮH from *n*-pentane [841] and for diethyl ether calculated in Ogura et al. [821] from group rate expressions.

For H-abstraction by ȮH from branched ethers, including di-*iso*-propyl ether [813, 821, 826], ethyl *tert*-butyl ether [815, 821, 829], and others [813-815, 817, 818, 821-823, 826, 829, 830, 842], rate coefficients are reported experimentally and computationally. *iso*-propyl substituents in ethers such as di-*iso*-propyl ether [813, 821, 826] and methyl *iso*-propyl ether [821-823] introduce tertiary C–H bonds into the molecular structure, which are approximately 5 kcal/mol lower in energy compared to primary C–H bonds. Reactive complex formation for ȮH + methyl *iso*-propyl ether was reported in Zhou et al. [823], which is consistent with the negative temperature dependence observed experimentally [815] and likely explains similar behavior in ȮH + di-*iso*-propyl ether [813, 826].

In contrast, the quaternary carbon that is present on *tert*-butyl substituents in ethers restricts the formation of a pre-reaction complex, leading to positive temperature dependence of the rate coefficient methyl *tert*-butyl ether + ȮH [814, 815, 817, 818, 822], and is the principal reason for inhibition of chain-branching reactions that require Q̇OOH formation and subsequent second O_2-addition. Tranter and Walker [815] conducted rate coefficient measurements for H-abstraction by Ḣ and ȮH, in addition to speciation of reaction products from methyl- and ethyl-*tert*-butyl ether oxidation.

Zhou et al. [823] conducted a series of calculations on dimethyl ether, ethyl methyl ether, and *iso*-propyl methyl ether to examine the influence of branched substituents on k(T) for ȮH + ether → Ṙ + H_2O (**Figure 76**). Branching ratios were reported, and in the latter two cases abstraction of hydrogen on tertiary carbon – forming α radicals – were favored at temperatures below 1000 K. Similarly, Zavala-Oseguera et al. [822] conducted a systematic series of computations wherein substituents were varied from dimethyl ether to *n*-propyl methyl ether, and in branched systems from *iso*-propyl methyl ether to *iso*-butyl methyl ether and methyl *tert*-butyl ether, concluding that abstraction dominated at the carbon atom located α to the ether group on the side with the larger alkyl substituent. For example, branching fractions from ȮH + diethyl ether favor α radicals by more than 90% at the peak temperature considered, 400 K. Similarly, at the same temperature, ȮH + *iso*-butyl methyl ether favors abstraction at the (secondary) α' carbon with a branching fraction of ~45%, compared to ~10% from the α carbon on the opposite side of the ether group (i.e. H_2Ċ–O–). The *tert*-butyl substituent does not support the complex formation that leads to negative temperature dependence, evidenced by the comparison of methyl *tert*-butyl ether to that of ethyl *tert*-butyl ether – the latter displays dk/dT < 0 due to the ethyl group [829].

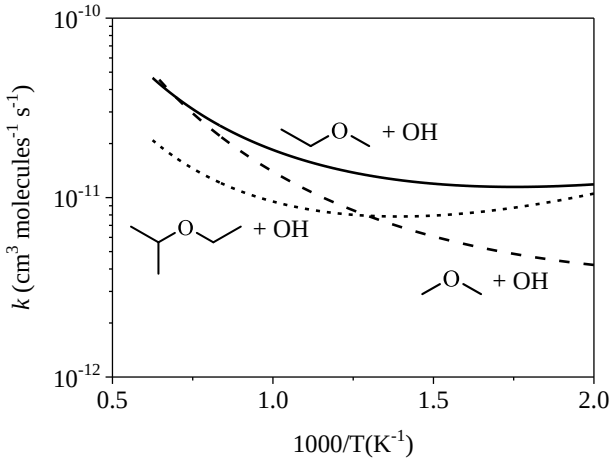

Figure 76. Rate coefficients calculated at the CCSD(T)/CBS level of theory in Zhou et al. [823] for ȮH + linear and branched ethers. Negative temperature dependence is evident in *iso*-propyl methyl ether up to ~800 K and up to ~600 K in ethyl methyl ether due to the formation of a pre-reaction complex, while positive temperature dependence is exhibited for dimethyl ether + ȮH.

Only a limited number of studies on hydrogen abstraction from acyclic ethers by HOȮ [77] and ĊH$_3$ [843-847] exist at temperatures below 1000 K. Mendes et al. [77] report the only calculated rate coefficients for H-abstraction by HOȮ from ethers above 300 K, and no measurements are reported in the literature. High-pressure limit rate coefficients for HOȮ + RH → Ṙ + H_2O_2 were calculated in [77] from 500 – 2000 K using conventional transition state theory that included asymmetric Eckart tunneling corrections. Site-specific and overall rate coefficients were reported. Using MP2-based functionals with the 6-311G(*d,p*) basis set for geometry optimization and frequency calculations, and the CCSD(T) coupled cluster method for energy calculations, Mendes et al. [77] assessed the effects of linear and branched substituents, ranging from methyl to butyl. Reactions of HOȮ with six ethers were studied: dimethyl ether (CH_3OCH_3), ethylmethyl ether ($CH_3OC_2H_5$), *n*-propyl methyl ether ($CH_3OC_3H_7$), *iso*-propyl methyl ether ($CH_3OCH(CH_3)_2$), *n*-butyl methyl ether ($CH_3OC_4H_9$), and *iso*-butyl methyl ether ($CH_3OCH_2CH(CH_3)_2$). Similar to reactions with ȮH, reactant and product complexes were identified in the entrance and exit channels on all of the potential energy surfaces, most of which involved hydrogen bonding between the –O– group and the H atom of HOȮ. In all cases, branching fraction calculations revealed that reactions occur predominantly at α and α' sites, where the latter designates the methyl substituent and α is either 1°, 2°, or 3° depending on the nature of the substituent. Below 1000 K, abstraction from α and α' sites combined to account for over 90% of initial radical production via HOȮ + RH → H_2O_2 + Ṙ, with the α site favored – remaining above ca. 60%. The influence of the ether group in such reactions is negligible for β, γ, and δ sites. Moreover, rate coefficients for abstraction at α sites were approximately 10^2 higher than for corresponding sites in alkanes, and several orders of magnitude higher than the analogous site in ketones and esters [77].

Rate coefficients of H-abstraction by ĊH$_3$ were measured for dimethyl ether in Tranter et al. [843] and for diethyl ether in Long and Skirrow [844]. Tranter et al. [843] conducted laser schlieren densitometry experiments behind incident shock waves at temperatures above 1000 K; at the lowest experimental temperature, 1163 K, $k = 9.8 \cdot 10^{-14}$ cm^3 molecule^{-1} s^{-1} [843]. Similar to reactions with ȮH, no pressure dependence was observed from 60 – 240 Torr. The rate coefficients for ĊH$_3$ reaction with dimethyl ether

showed a substantial activation energy, in concert with the experimental results of Pacey [845], Hidaka et al. [846], and Held et al. [847], which were conducted at temperatures below 1000 K, and with the mechanism of Curran et al. [848]. Saheb et al. [849] calculated kinetics for based on a single transition state for $\dot{C}H_3$ abstracting a H atom from dimethyl ether. Guan et al. [850] characterized a single reaction pathway that included transition states for in-plane and out-of-plane abstraction by $\dot{C}H_3$, linked by an internal rotation, and calculated kinetics using a detailed treatment of torsional modes. Similar to other ethers, $k(T)$ for $\dot{C}H_3$ + R–O–R → CH_4 + R–O–$\dot{R}$ are several orders of magnitude lower compared to reactions with ȮH at temperatures below 1000 K: at 450 K, $k = 6.8 \cdot 10^{-17}$ cm^3 s^{-1} for $\dot{C}H_3$ + diethyl ether [844], and $8.3 \cdot 10^{-18}$ cm^3 s^{-1} for $\dot{C}H_3$ + dimethyl ether [843].

3.4.2.reactions of initial radicals with O_2

Initiation reactions described above, involving ȮH, HOȮ, or $\dot{C}H_3$, yield the initial ether radicals with which O_2 reacts. **Figure 77** depicts relevant pathways considered in the literature for the simplest acyclic ether, dimethyl ether. Other, more structurally complex ethers follow similar general schemes although with additional pathways to, for example, cyclic ether + ȮH in chain-propagating steps. The balance among the competing pathways for ether radicals is responsible for the differences in autoignition chemistry. Connecting product formation to initial radicals with O_2 is therefore a critical step to enable quantitative chemical kinetics modeling. Two critical steps for chain-branching are isomerization reactions ROȮ → Q̇OOH and ȮOQOOH → HOOṖOOH, which may also play a role in tropospheric oxidation, as computed by Wang and Wang [851]. Results from experimental and computational studies for several ethers are described in detail in the ensuing sections in relation to the pathways in **Figure 77**. For dimethyl ether, the main aspects of low-temperature oxidation are: (1) second-O_2-addition is favored over Q̇OOH → products due to high barriers for cyclic ether formation and since no conjugate alkene + HOȮ pathways are available; (2) the pathway to formic acid + Criegee intermediate, Channel I, is unconfirmed since no detection of formaldehyde oxide ($\dot{C}H_2O\dot{O}$) is reported; (3) formic anhydride (CHO(–O–)CHO), formed via Channel II, was detected in JSR experiments of Moshammer et al. [344]; (4) formic acid may arise from several competing pathways, including via hydroperoxymethyl formate (Channels I, II, II, and V), from reaction of formaldehyde with ȮH, or via secondary chemistry initiated by HOȮ + formaldehyde; and (5) performic acid, formed via Channel IV, was detected in Moshammer et al. [852], despite a high barrier on the potential energy surface for hydroperoxymethyl formate [853].

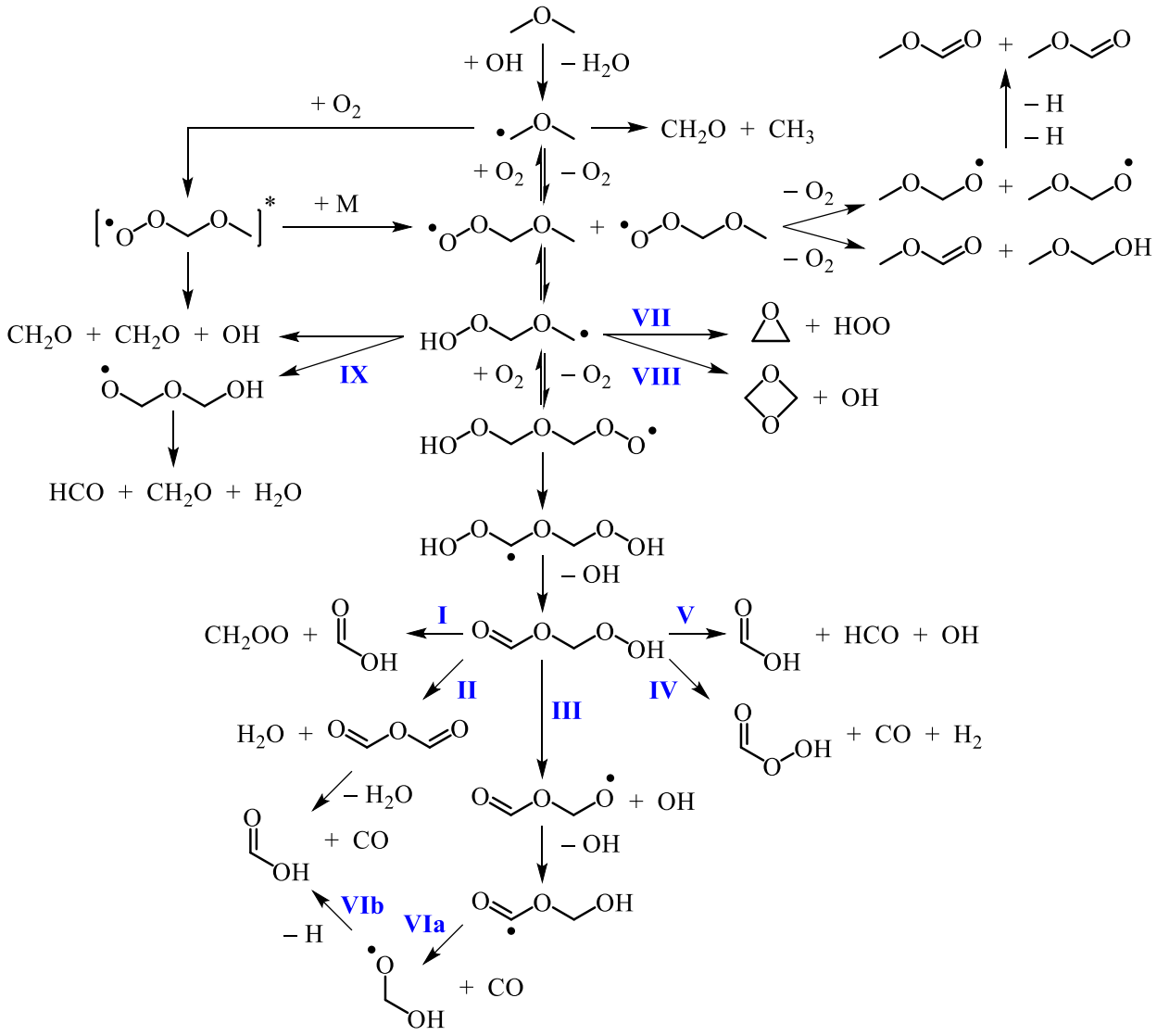

Figure 77. Oxidation mechanism for dimethyl ether showing reaction pathways and products relevant to low-temperature combustion. Hydroperoxymethyl formate decomposition reactions via Channels I, II, IV and V were proposed in Andersen and Carter [853], Channel IX is from Suzaki et al. [854], and the bimolecular ROȮ + ROȮ channels leading to methyl formate and methoxymethanol were proposed in Wallington et al. [855] and Jenkin et al. [856].

3.4.2.1. methoxymethyl + O_2

Dimethyl ether oxidation presents an apparent simplicity: upon H-abstraction, dimethyl ether yields one radical isomer (methoxymethyl, $H_2\dot{C}OCH_3$), which can add to O_2 and form one peroxy radical (methoxymethyl-peroxy, ROȮ), which can isomerize to one hydroperoxy-substituted radical (hydroperoxymethoxymethyl, ȮOOH). The reaction of the latter radical with O_2 leads to the formation of the lone γ-ketohydroperoxide isomer from dimethyl ether, hydroperoxymethyl formate. However, several alternative reaction pathways exist, as proposed in Andersen and Carter [853] as part of a series of computational studies on chain-propagation and chain-branching kinetics and mechanisms of dimethyl

ether oxidation (**Figure 77**): Criegee channel (I), dehydration channel (II), alternative chain-branching channel (V), performic acid channel (IV).

Reaction of $\dot{C}H_2OCH_3$ radicals with O_2 can form a vibrationally excited complex, (ROȮ)*, which either leads directly to $CH_2O + CH_2O + \dot{O}H$ (direct formaldehyde channel), or a collisionally stabilized peroxy radical (adduct-stabilized channel). The latter may subsequently undergo isomerization via $\dot{O}OCH_2OCH_3 \rightarrow HOOCH_2O\dot{C}H_2$ (Q̇OOH) and dissociate, leading to the same, yet Q̇OOH-mediated, set of products. The two channels in **Figure 78** show the reactions that define the branching fraction for $\dot{C}H_2OCH_3 + O_2$.

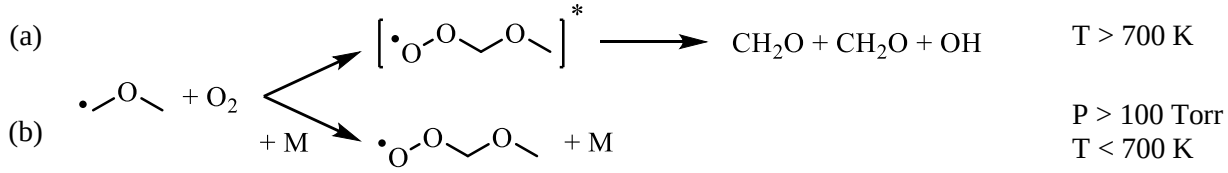

Figure 78. Product formation from reaction of methoxymethyl ($H_2\dot{C}OCH_3$) with O_2. The branching fraction is defined by two channels: (a) direct formaldehyde channel and (b) adduct-stabilized channel.

Several experimental and computational studies report rate coefficients and/or product formation from methoxymethyl ($H_2\dot{C}OCH_3$) + O_2 reactions [857-865]. Lower pressure/higher temperature favors the direct formaldehyde channel, and higher pressure/lower temperature favors the adduct-stabilization channel. Maricq et al. [857] measured the pressure-dependence of rate coefficients for $\dot{C}H_2OCH_3 + O_2$ from ~10^{-3} – 0.9 atm over the temperature range 230 – 350 K; rate coefficients for the $\dot{C}H_2OCH_3 + \dot{C}H_2OCH_3$ self-reaction were also measured. Direct detection and quantification of methoxymethyl-peroxy ($\dot{O}OCH_2OCH_3$) and formaldehyde time profiles was conducted using transient UV- and IR-absorption spectroscopy, respectively, during Cl-initiated oxidation experiments and were used to develop an analytical model for predicting $k(T)$ and related product yields. The results confirmed that the $\dot{C}H_2OCH_3 + O_2$ reaction exhibits negative temperature dependence, similar to other systems, and formation of the peroxy adduct dominated over the direct yield of formaldehyde starting near 100 Torr.

Rosado-Reyes and Francisco [858] employed time-dependent IR-absorption spectroscopy to probe product formation from both thermally- and photolytically-initiated oxidation experiments from 20 – 200 Torr and 295 – 600 K with the aim of determining the pressure- and temperature-dependence of branching fractions in the $\dot{C}H_2OCH_3 + O_2$ reaction. Direct formaldehyde production, evident from an abrupt rise in IR-absorption signal near time-zero, exhibited inverse pressure dependence. Sehested et al. [859] expanded the conditions used in [858] to higher pressures, conducting experiments from 10^{-2} – 18 atm and from 296 – 473 K. The measurements revealed a weak dependence on both pressure and temperature, consistent with Hoyermann and Nacke [860] and Masaki et al. [861]. Rate coefficients were also measured for $\dot{C}H_2OCH_3 + \dot{C}H_2OCH_3$ and thermal decomposition rates for $\dot{C}H_2OCH_3$ at 18 atm and temperatures up to ~650 K [858].

Yamada et al. [862] employed the CBS-q and G2 composite quantum chemistry methods to calculate transition states and related rate coefficients for reactions on the $\dot{C}H_2OCH_3 + O_2$ potential energy surface. Quantum Rice-Ramsperger-Kassel (QRRK) theory and master equation analysis were subsequently used to calculate energy-dependent rate coefficients and to account for collisional stabilization of the adduct methoxymethyl-peroxy and Q̇OOH isomer, hydroperoxymethyl-peroxy. Consistent with the experimental results of Hoyermann and Nacke [860], Maricq et al. [857], Sehested et al. [859], and Masaki et al. [861],

the association reaction $\dot{C}H_2OCH_3 + O_2 \rightarrow$ products approaches the high-pressure limit near 100 Torr at 298 K. The temperature dependence of $\dot{C}H_2OCH_3 + O_2 \rightarrow$ products, at 1 atm, revealed that below ~650 K the formation of collisionally stabilized methoxymethyl-peroxy ($\dot{O}OCH_2OCH_3$) dominates. Towards 700 K, direct formation of $CH_2O + CH_2O + \dot{O}H$ becomes competitive along with the reverse reaction back to the reactants. With increasing pressure, the temperature at which the formaldehyde channel and reverse reaction become competitive increases: at 10 atm, formation of $\dot{O}OCH_2OCH_3$ dominates below ~850 K, and the formaldehyde channel and back dissociation become relevant at 950 K.

Andersen and Carter [866] calculated k(T) for both the forward and reverse reactions of methoxymethyl + O_2 using microcanonical *E*/*J*-resolved variational/flexible RRKM theory (VRRKM) with an adjusted Varshni potential, leading to high-pressure limit rate coefficients of $6.18 \cdot 10^{12} \cdot T^{0.69}\exp(1.2 \text{ kcal mol}^{-1}/RT)$ $\text{cm}^3 \text{ mol}^{-1} \text{ s}^{-1}$ for the forward reaction and $3.59 \cdot 10^{19} \cdot T^{-1.03}\exp(-29.5 \text{ kcal mol}^{-1}/RT)$ s^{-1} for the reverse dissociation. Andersen and Carter [866] remarked that their DFT-B3LYP//6-311G** calculations could lead to artificially lower bond dissociation energies, and so also carried out calculations with bond enthalpy parameters adjusted to match thermochemistry from Curran et al. [848, 867]. **Figure 79** compares the calculations in Andersen and Carter [866] with the experimental results from Maricq et al. [857], Sehested et al. [859], and Hoyermann et al. [860]. Despite the state-resolved variational treatment, the rate coefficient for the forward reaction, even after adjusting the bond enthalpy, is higher than experimental rate coefficients [857, 859, 860]. The discrepancies were ascribed partly to an incomplete description of the bond-breaking mechanism, particularly the bending motion orthogonal to the reaction coordinate, and interactions between excited-state O_2 and neutral methoxymethyl and ionic $[\text{methoxymethyl}]^+ + O_2^-$ [866]; the latter interaction was invoked by Ruiz and Bayes [868] in rate coefficient measurements of *n*-propyl and *iso*-propyl with O_2.

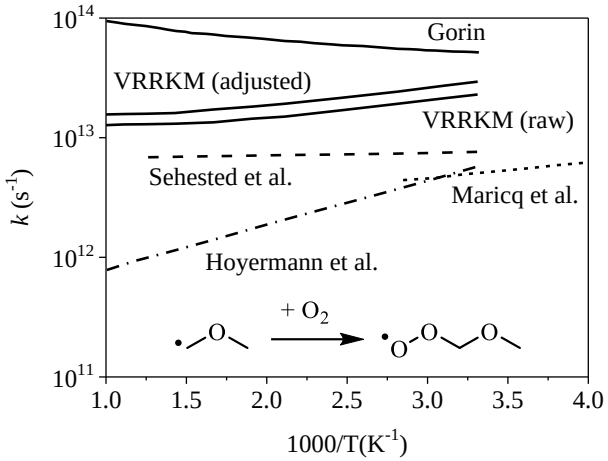

Figure 79. High-pressure limit rate coefficients from the RRKM calculations in Andersen and Carter [866] for methoxymethyl + $O_2 \rightarrow$ methoxymethyl-peroxy compared with measurements from Hoyermann et al. [860] (~0.8 – 3.8 Torr), Sehested et al. [859] (~20 – 760 Torr), and Maricq et al. [857] (5 – 690 Torr). 'Raw' refers to calculations using the DFT/ B3LYP//6-311G** values [866] and 'adjusted' calculations have the R–O$\dot{O}$ bond dissociation enthalpy changed to agree with Curran et al. [848].

Product formation and reaction kinetics involving collisionally stabilized ether-peroxy radicals were examined in both computational and experimental studies [853, 854, 856, 858, 863, 866, 869-871], which provide clarity on the oxidation mechanism depicted in **Figure 77**. Unimolecular reactions of RO$\dot{O}$ involve

either back-dissociation to $\dot{R}$ + O_2 or isomerization to $\dot{Q}OOH$ followed by chain-propagation or chain-branching mechanisms.

Yamada et al. [862] found at the CBS-q/MP2//6-31G(*d,p*) level of theory that the isomerization step $\dot{O}OCH_2OCH_3 \rightarrow HOOCH_2O\dot{C}H_2$ encounters a barrier of ~ 16 kcal/mol; they applied canonical transition state theory to calculate rate coefficients in the high-pressure limit. Rodriguez et al. [872] derived a similar expression using stationary points calculated with the G4 composite method. Andersen and Carter [866] applied canonical transition state theory to stationary points from DFT-B3LYP//6-311G** calculations that give a significantly higher barrier to isomerization. Their results differ in both *A*-factor and in activation energy with the results of Yamada et al. [862], Rodriguez et al. [872], and with the estimate in Curran et al. [848], where *A* is derived using an analogous reaction from *n*-heptane oxidation [385] and E_a is determined using the sum of the enthalpy of reaction, ring-strain energy of the transition state, and H-abstraction energy determined from analysis of the relevant Evans-Polanyi plot. Hindered rotor treatment was neglected in [866] partly because of issues related to low-frequency modes and mode-mixing. Wang and Wang [851] carried out more accurate RRKM-master equation calculations for the internal hydrogen transfer isomerization of peroxy radicals from dimethyl-, diethyl-, and di-*iso*-propyl ethers, employing complete basis set methods (UCSB-QB3 and ROCBS-QB3) on M06-2X/6-311++G(2*df*,2*p*) structures and treating internal rotations as hindered rotors using M06-2X calculations of the torsional potential. Wang and Wang concentrated on lower temperatures (233 – 343 K) for tropospheric applications and yielded high-pressure limit results ($3.10 \cdot 10^7$ exp(–5903/T) s^{-1}) that are higher than an extrapolation of the results of Yamada et al. [862] or Rodriguez et al. [872], which may partially reflect tunneling effects [851]. The extrapolated results from Andersen and Carter [866] are lower still because of the higher isomerization barrier in their B3LYP calculations [870]. **Figure 80** compares the methoxymethyl-peroxy → hydroperoxymethyl-peroxy rate coefficients in the high-pressure limit from Andersen and Carter [866], Yamada et al. [862], Wang and Wang [851], Curran et al. [848], and Suzaki et al. [854] in which the rate coefficient was inferred via modeling and analysis of time-dependent ȮH and HOȮ measurements.

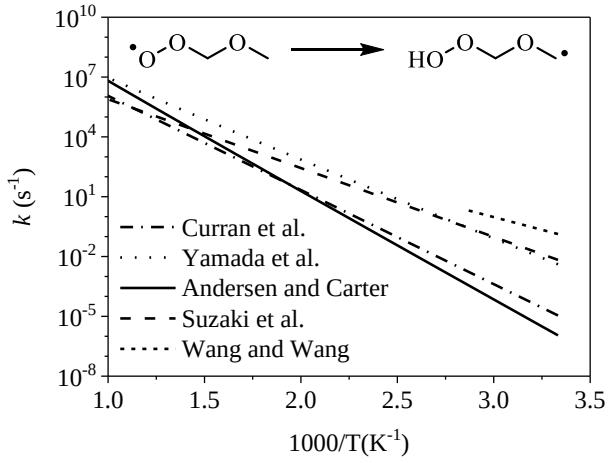

Figure 80. High-pressure limit rate coefficients for the isomerization reaction methoxymethyl-peroxy → hydroperoxymethyl-peroxy. Andersen and Carter [866]: $k(T) = 9.22 \cdot 10^9 \cdot T^{0.72}$exp(–24.3 kcal mol^{-1}/RT) s^{-1}; Yamada et al. [862]: $k(T) = 1.18 \cdot 10^7 \cdot T^{1.21}$exp(–17.1 kcal mol^{-1}/RT) s^{-1}; Wang and Wang [851]: $k(T) = 4.06 \cdot 10^7$exp(–5858/T); Curran et al. [848]: $k(T) = 6.00 \cdot 10^{10} \cdot$ exp(–21.6 kcal mol^{-1}/RT) s^{-1}; Suzaki et al. [854]: $k(T) = 2.20 \cdot 10^9 \cdot$ exp(–15.8 kcal mol^{-1}/RT) s^{-1}.

In principle, the formation of ȮOOH radicals can lead to cyclic ether formation (oxirane + HOȮ or 1,3-dioxetane + ȮH; pathways VII and VIII in **Figure 77**); Moshammer et al. [852] experimentally identified 1,3-dioxetane in JSR measurements of dimethyl ether oxidation. The ether group opens another decomposition channel via β-scission to CH_2O + CH_2O + ȮH. Yamada et al. [862] found this decomposition to be the primary unimolecular channel for the ȮOOH species and predicted that formation of the cyclic ether 1,3-dioxetane is unimportant with a CBS-q barrier height being nearly 8 kcal/mol higher. Pressure-dependent formaldehyde yields were calculated and a 3.3 kcal/mol reduction in barrier height for decomposition (to 21.4 kcal/mol) was required to match formaldehyde yields measured in photolytically initiated oxidation experiments of Sehested et al. [873], suggesting that the CBS-q barriers could be uncertain by ~3.5 kcal/mol [862]. Similarly, Andersen and Carter [866] focused on the decomposition reaction forming CH_2O + CH_2O + ȮH, discounting the reactions forming cyclic ether + ȮH on the basis of B3LYP saddle point energies [870]. Pressure-dependent calculations in [866] reveal that ȮOOH → CH_2O + CH_2O + ȮH is not in the high-pressure limit at 40 atm above 500 K, and the authors remarked on the need to account for such pressure-dependence in combustion modeling. In contrast with Yamada et al. [862] and Curran et al. [848], Andersen and Carter [866] find that breaking the O–OH bond in ȮOOH, rather than β-scission to produce formaldehyde, is the transition state to forming 2 CH_2O and ȮH. However, Eskola et al. [863] (*vide infra*) demonstrated that the transition states for $H_2\dot{C}OCH_2OOH$ decomposition show significant multireference character and different methods yield dramatically different energies (by nearly 10 kcal/mol), compelling caution when evaluating such reactions. Even with the uncertainty, in the case of dimethyl ether oxidation, the two major channels for ȮOOH are CH_2O + CH_2O + ȮH or second-O_2-addition to form ȮOQOOH radicals [863, 864, 872]. In the case of the latter, isomerization via a 6-membered transition state, leads to HOOṖOOH, the decomposition of which gives the lone γ-ketohydroperoxide isomer of dimethyl ether, hydroperoxymethyl formate.

Addition of ȮOOH to a second O_2 is barrierless. Andersen and Carter [866] calculated a high-pressure limit for this addition of $k(T) = 2.69 \cdot 10^{12} \cdot T^{0.5}$ cm^3 mol^{-1} s^{-1} by applying canonical transition state theory to stationary points from DFT/B3LYP//6-311G**. A benchmark temperature of 600 K was used to compare with Curran et al. [848], because this was the peak temperature where formic acid, formed via chain-branching, was observed in [848] and in Liu et al. [874]. Curran et al. [848] estimated k(600 K) of $7.00 \cdot 10^{11}$ cm^3 mol^{-1} s^{-1} to reach agreement with experimental yields. The rate coefficient calculated in [866] is approximately 10^2 higher than [848], and the difference ascribed to the same issue that occurred for Ṙ + O_2 reactions: inadequate description by DFT methods because of multi-reference contributions. Further refinements by [866], employing variational RRKM, reduced the discrepancy yet the value remained more than 10^1 higher than Curran et al. [848], leading the authors in [866] to remark on the need for more-accurate portrayal of the relevant PES and of the bending potential involved in the reaction.

Once ȮOQOOH is formed, the next step in the sequence leading to chain-branching is isomerization to HOOṖOOH, for which reverse reaction is negligible in the temperature range where low-temperature chain branching is prevalent: 500 – 700 K. Some discrepancies in k(T) were noted in [866]. The Curran et al. estimate [848] of $4.00 \cdot 10^{10}\exp(-18.6/RT)$ s^{-1} differs by more than 10^1 at 600 K compared to Andersen and Carter [866]: $2.32\ 10^{11}\ T^{0.81}\exp(-22.9/RT)$ s^{-1} gives $1.88 \cdot 10^5$ s^{-1} [866]. The large differences in A-factor (up to 10^3) and in E_a (up to 7 kcal/mol) suggested that further computational studies are required to provide more precise constraints. Wang and Wang [851] found a lower ȮOQOOH → HOOṖOOH isomerization barrier (21.2 kcal mol^{-1} by UCBS-QB3) than the Andersen and Carter B3LYP/6-311G(*d*,*p*) value of 22.7 kJ mol^{-1} [866]. Scission of the O–O bond adjacent to the carbon radical center is accepted as

the sole fate of HOOṖOOH and gives hydroperoxymethyl formate + ȮH as products. Born-Oppenheimer molecular dynamics (BOMD) simulations by Andersen and Carter [871] found that O–O bond-scission in HOOṖOOH occurs within 500 fs.

The chain-branching step in dimethyl ether oxidation occurs from the production of additional radicals from the decomposition of hydroperoxymethyl formate, for which several channels are possible [853] (**Figure 77**). In addition, the detection of formic anhydride (via the non-chain branching Channel II in **Figure 77**) in hydroperoxymethyl formate decomposition [875] raises the potential for acid-catalyzed dehydration reactions. Channel V is a chain-branching pathway alternative to the O–O bond-scission pathway considered to be the primary decomposition channel for hydroperoxymethyl formate, and it produces formic acid + HCȮ + ȮH, giving a connection to the production of formic acid from second-O_2-addition reactions. However, the *A*-factor for the reaction to formic acid + HĊO + ȮH computed in [866], $1.96 \cdot 10^{14}$ s^{-1} at 600 K, is considerably smaller than that for the simple O–O bond-scission. Application of variational RRKM to both reactions in [853] shows that bond scission is favored by more than 10^1 at 600 K. Channel I is an energetically competitive pathway leading to the production of formaldehyde oxide ($ĊH_2OȮ$) – the smallest Criegee intermediate. Andersen and Carter [853] suggested that the Criegee intermediate channel may compete with O–O scission, given that the pathway lies 25 kcal/mol below the ȮOOH + O_2 entrance channel with a barrier height (at B3LYP/6-311G(*d,p*)) similar to the dissociation energy of the O–O bond. However, the kinetics calculations in [866] show Criegee intermediate formation as a minor channel. **Figure 81** compares the unimolecular reaction rate coefficients calculated for the most favorable dissociation channels in **Figure 77**. Channel IV – performic acid + CO + H_2 – is not shown because it has a barrier more than 20 kcal/mol higher than the other channels.

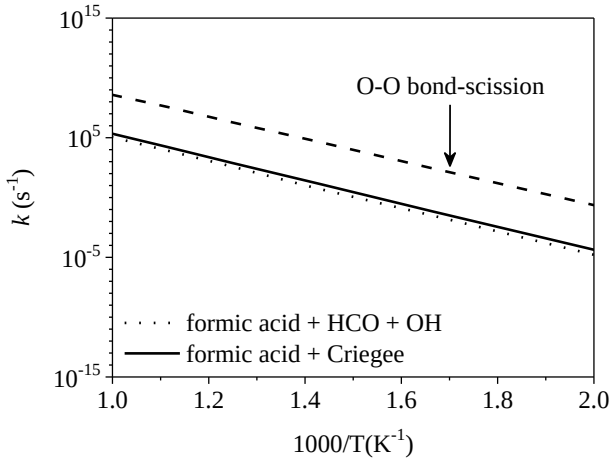

Figure 81. Unimolecular decomposition rates of hydroperoxymethyl formate ($HOOCH_2OCHO$) calculated in Andersen and Carter [866].

Several groups have measured product formation from methoxymethyl + O_2 reactions using pulsed-photolysis initiation [854, 858, 863, 869]. Rosado-Reyes and Francisco [858] employed both photolytically- and thermally-initiated experiments in conjunction with transient IR-absorption spectroscopy to determine the temperature- and pressure-dependence of the branching fraction of Ṙ + O_2 (cf. **Figure 78**, direct formaldehyde channel versus the adduct-stabilized channel). Time profiles of formic acid, formaldehyde,

and methyl formate were directly probed over the first 900 μs of oxidation at pressures from 20 – 200 Torr and temperatures up to 600 K. One of the more salient points was the absence of formic acid in the photolysis experiments, indicating production in the thermally initiated experiments arising from secondary reactions indirectly related to ROȮ, e.g. $HOCH_2O + O_2 \rightarrow$ formic acid + HOȮ, where $HOCH_2O$ forms via a reaction sequence initiated by HOȮ + formaldehyde. However, formic acid was observed in thermally initiated experiments of Rosado-Reyes and Francisco [858], similar to Curran et al. [848] in which flow reactor experiments were conducted using residence times of 2 – 4 s. Formaldehyde yields were in the high-pressure limit above ~100 Torr in [858], indicating the dominance of the adduct-stabilized channel at practical combustion pressures, and within the 900-μs measurement time formaldehyde was suppressed towards the higher pressures used in the experiments. Rosado-Reyes and Francisco [858] postulate that the primary fate of ROȮ radicals at the high initial radical concentrations ($>10^{14}$ cm^{-3}) in their experiments is not isomerization to ȮOOH, rather self-reaction to yield RȮ + RȮ + O_2. The unimolecular decomposition of RȮ is deemed responsible for the methyl formate observed, which was negligibly affected by temperature or pressure.

Subsequent pulsed photolysis experiments and potential energy surface calculations in Suzaki et al. [854, 869] extended the insight into the oxidation mechanism of dimethyl ether using a frequency-modulated near-infrared (FM-NIR) absorption spectroscopy for direct measurements of ȮH and HOȮ time histories [854, 869] and UV-absorption spectroscopy for direct measurements of HOȮ, $H_2\dot{C}OCH_3$, and $\dot{O}OCH_2OCH_3$ [869]. The FM-NIR measurements and kinetics analysis in [854] confirmed that HOȮ is not formed directly, as a primary product, from ȮOOH → HOȮ + oxirane. Instead, formaldehyde formed via β-scission of ȮOOH serves as the precursor via the production of formyl radical (ȮH + $CH_2O \rightarrow H\dot{C}O$ + H_2O) followed by O_2 ($H\dot{C}O + O_2 \rightarrow$ HOȮ + CO). In addition, the experimental ȮH and HOȮ profiles were modeled using a refinement of the Curran et al. [867] mechanism; the initial version did not reproduce the ȮH and HOȮ time histories despite accurately capturing ignition delay times [867]. Suzaki et al. [869] later identified an alternative reaction pathway for ȮOOH decomposition, which is 2 – 3 kcal/mol lower than the conventional β-scission pathway yielding $CH_2O + CH_2O +$ ȮH. The mechanism involves a transition state for an ȮH-transfer reaction from the –OOH group to the carbon radical site and forms a hydroxy-alkoxy radical that decomposes into $H\dot{C}O + CH_2O + H_2O$.

Eskola et al. [863] conducted LIF experiments to measure ȮH time histories in dimethyl ether oxidation and master equation calculations using MESMER to simulate the results. Several important details were noted. As noted above, transition states on the first-O_2-addition potential energy surface displayed significant multi-reference character, with T1 diagnostics exceeding 0.02, revealing model-chemistry-dependent saddle point energies spanning 6 kcal/mol for ROȮ → ȮOOH and 10 kcal/mol for subsequent ȮOOH decomposition reactions. Rate coefficients were determined at their best estimate CBS-q//MPW1K/aug-cc-pVTZ level of theory using MESMER, and comparisons were drawn against the Curran et al. [848] mechanism. In the context of autoignition chemistry, two principal differences were noted. For both forward and reverse reactions in ROȮ ⇋ ȮOOH, the master equation analysis in [863] produced rate coefficients 10^1 higher, which impacted the predicted time-dependence of ȮOQOOH – the radical precursor to the chain-branching agent, hydroperoxy methyl formate.

Product formation from bimolecular reactions in dimethyl ether oxidation, other than Ṙ + O_2 and related reactions, include studies on self-reactions of methoxymethyl-peroxy radicals [856] and HOȮ + $H_2\dot{C}OCH_3$ [855]. Wallington et al. [855] applied Fourier Transform Infrared Spectroscopy (FT-IR) to measure

methoxy hydroperoxide (H_3COCH_2OOH) and methyl formate from reactions of HOȮ with $H_2ĊOCH_3$ at 700 Torr. The experiments were conducted at a temperature not directly relevant to combustion (298 K), however a mechanism by which the products are formed was postulated. The mechanism for methoxy hydroperoxide formation involved a 4-membered transition state involving only the terminal O atom and the HOȮ reactant. However, the 6-membered transition state leading to methyl formate (+ H_2O + O_2), additionally involved the secondary H atom on methoxymethyl-peroxy, indicating a potential dependence of the rate coefficient on the type of Ṙ group. Jenkin et al. [856] employed UV-absorption to probe the kinetics of the methoxymethyl-peroxy self-reaction and resulting product formation including methoxy hydroperoxide, methyl formate, and hydroxymethyl methoxy (H_3COCH_2OH). The latter species, assigned an upper limit of 15% of the total yield of products from self-reaction, is suspected to form via decomposition of the RȮ radicals, although no distinguishing spectral features were observed in the infrared spectra. Although not included in the calculations, Andersen and Carter [866] noted the potential importance of ROȮ self-reaction in dimethyl ether oxidation at high pressures due to appreciable stabilization of the adduct at 1 atm – significantly below practical combustion pressures; branching fraction calculations for methoxymethyl + O_2 reactions in [866] indicated nearly 90% is stabilized ROȮ at 100 Torr.

The functional group effects on dimethyl ether oxidation are also present in the oxidation of poly(oxymethylene) dimethyl ethers such as dimethoxymethane, and their reaction mechanisms are often built from analogy to dimethyl ether [807, 808]. Döntgen et al. [876] have collected the relevant thermochemistry for polyether oxidation. He et al. [839] explicitly calculated stationary points for the addition of dimethoxymethane radicals to O_2, the subsequent isomerization reactions of the ROȮ radicals, and decomposition of ȮOOH species at the CBS-QB3/B3LYP/CBSB7 level of theory, and applied canonical transition state theory with hindered rotor treatment of torsions to compute rate coefficients for the unimolecular reactions. As in the case of dimethyl ether oxidation, carbonyl formation from the ȮOOH species competes with dissociation to cyclic ethers.

3.4.2.2. reactions of diethyl ether radicals with O_2

Several theoretical studies have focused on the diethyl ether oxidation mechanisms. Wang and Wang [851] calculated potential energy surfaces at M06-2X/6-311++G(2*df*,2*p*) level of theory for isomerization of first- and second-O_2-addition adducts, i.e. ROȮ → ȮOOH and ȮOOQOOH → HOOṖOOH , for diethyl ether, dimethyl ether, and di-*iso*-propyl ether. Rate coefficients were calculated with RRKM theory using MESMER [851]. Di Tommaso et al. [877] employed a lower level of theory, B3LYP/6-31+G(*d*,*p*), to calculate stationary points for several types of reactions in diethyl ether oxidation, including peroxy radicals, γ-ketohydroperoxide (HOOQ'=O), and hydroperoxide (ROOH) species. On the surface for γ-ketohydroperoxide decomposition, transition states and reaction enthalpies were determined for six pathways, one of which involved a highly exothermic dehydration reaction facilitated by the –O– group, leading to acetic acid, H_2O, and ketene ($O=C=CH_2$). A similar dehydration reaction was also found on the surface of the secondary ROOH species. Di Tommaso et al. [878] subsequently conducted a series of calculations on linear and branched ethers, including dimethyl ether, *tert*-amyl methyl ether, and di-*iso*-propyl ether, and compared barrier heights for several reaction types against similar reactions in alkanes. The determinations in [878] suggest that the barrier height for C–O β-scission is ca. 10 kcal/mol lower than for analogous dissociations of alkyl radicals, and the barrier to ROROȮ isomerization is ca. 4 kcal/mol lower than for analogous isomerizations in alkylperoxy radicals.

A higher level study by Sakai et al. [879] employed variational transition state theory for reactions of diethyl ether radicals with O_2, using CASPT2(7,5)/aug-cc-pvdz single-point calculations and UB3LYP/CBSB7 geometries and frequencies for the oxygen association reactions, and conventional transition state theory at the CBS-QB3 level of theory for unimolecular reactions of ROȮ and ȮOOH radicals. The *ab initio* rate coefficients for the ether were then compared against rate-rules-derived rate coefficients of analogous alkanes. Several differences relevant to low-temperature oxidation were noted in this comparison. Isomerization rates for ROȮ ⇋ ȮOOH were similar, with the exception of the case where the peroxy group is located on the α carbon to the ether link and abstraction occurs on the opposite α carbon via a 6-membered transition state. For such an isomerization the rate was larger than the analogous alkane by a factor of 10 near 700 K. When the peroxy group is located on the β carbon, however, the reverse reaction to Ṙ + O_2 is higher by ca. 10^1 at 700 K than analogous alkane. Compared to *n*-pentane, the rate of cyclic ether + ȮH via unimolecular ȮOOH decomposition is higher by ~10^1 for diethyl ether when the radical site is adjacent to the ether group (**Figure 82a**), i.e. the formation of a substituted oxirane. Spin-contamination corrections were noted as a source of error. A transition state was located and rate coefficients were calculated for an OH-transfer reaction in β-α-ȮOOH radicals with a barrier height only 4 – 5 kcal/mol higher than ring-closure forming cyclic ether + ȮH; β refers to the location of the peroxy group and α the carbon radical site.

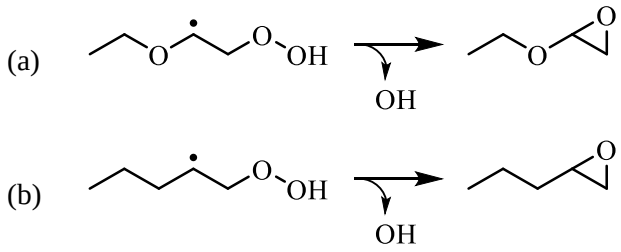

Figure 82. Rates for ȮOOH decomposition into oxiranes are facilitated in diethyl ether oxidation and are higher by ~10^1 than analogous reactions in alkanes.

Subsequently, Sakai et al. [880] compiled a detailed chemical kinetics mechanism and revised rate coefficients for twenty-four product channels from second-O_2-addition reactions using the composite CBS-QB3 level of theory to calculate barrier heights directly, which were determined in [879] by estimation. The barrier heights were largely similar to analogous alkane reactions except for six cases, which are separable into two types depending on the position of the –OOH (being α or β relative to the ether group), and both types involve entropically disfavored 8-membered transition states [880]. In cases where abstraction by the peroxy group occurs from the carbon to which the –OOH is bound (**Figure 83a**), leading ultimately to a ketohydroperoxide isomer, the barrier height is 4.3 kcal/mol lower than the analogous reaction in alkanes. In contrast, however, when the –OOH group is in the α position with respect to the ether group, and abstraction by the peroxy group occurs at the same (terminal) carbon, **Figure 83b**, the barrier height is higher by 6.7 kcal/mol. Of the six isomers of ȮOQOOH in diethyl ether, four are dominated by a single reaction at temperatures below 1000 K: isomerization to HOOṖOOH. In the remaining two cases, where the O–O and –OOH are adjacent to one another, HOȮ-forming channels either compete or exceed isomerization, in part due to lower C–H bond energy near the ether functional group.

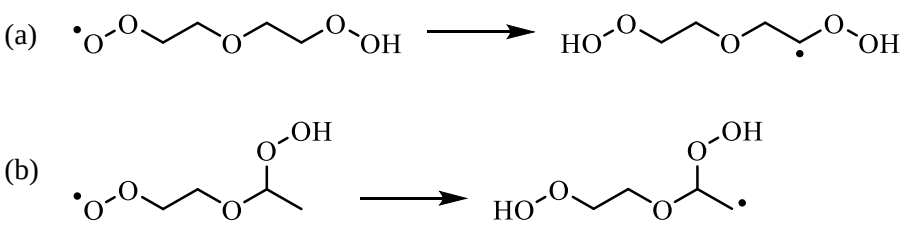

Figure 83. Decomposition pathways for ȮOQOOH radicals of diethyl ether in Sakai et al. [880] affected by the presence of the ether group. (a) E_a is 4.3 kcal/mol lower than in analogous alkane. (b) E_a is 6.7 kcal/mol higher than analogous alkane.

Fewer experimental studies exist of product formation from photolytically initiated $\dot{R} + O_2$ reactions in diethyl ether than for dimethyl ether. Orlando [881] carried out Cl-atom-initiated oxidation experiments on diethyl ether from 50 – 700 Torr, where 60 – 80% of the initial radicals led to the production of either ethyl formate or ethyl acetate. However, the experiments were conducted from 218 – 335 K, below combustion-relevant temperatures and where the role of radical-radical chemistry increases. Recently, Demireva et al. [882] used synchrotron photoionization mass spectrometry to measure both stable products and peroxy radical intermediates RȮ and ȮOQOOH in the Cl-initiated oxidation of diethyl ether at pressures up to 10 bar and temperatures from 450 – 600 K. They employed carbon balance in controlled experiments to deduce photoionization cross sections for the peroxy radical intermediates, allowing their quantification. Demireva et al. [882] observe that increasing temperature reduces yields of ȮOQOOH and KHP and increases acetaldehyde and RȮ, because thermal dissociation of ȮOOH increasingly competes with second O_2 addition; they also observe that increased stabilization at higher pressure tends to increase KHP and ȮOQOOH yields.

3.4.2.3. reactions of branched ether radicals with O_2

Direct kinetics studies of peroxy radicals formed from branched ethers are limited. The MPIMS experiments on ethyl *tert*-butyl ether oxidation in Winfough et al. [883], conducted from 550 – 700 K at pressures near 10 Torr, revealed that the favored reaction mechanism is the decomposition of the initial β radical on the *tert*-butyl group leading to *iso*-butene + acetaldehyde – the most abundant set of products quantified. Similarly, δ-ȮOOH radicals where the –OOH is located on the *tert*-butyl group also led to *iso*-butene and acetaldehyde (formed coincident with HOȮ). No cyclic ethers were observed in [883], despite submerged barrier heights on the potential energy surface calculated using CBS-QB3, perhaps due to experimental limitations such as unstable cations or poor Franck-Condon overlap. Giustini and Meloni conducted MPIMS experiments on di-*iso*-propyl ether oxidation [884] at 7 Torr and two temperatures, 550 K and 650 K. Two main species were propene and acetone. The branching fraction for the latter accounted for the majority of initial radical consumption and forms coincident with *iso*-propyl, via unimolecular decomposition of the tertiary radical, $(CH_3)_2\dot{C}(O)CH(CH_3)_2$, or via ȮOOH-mediated pathways yielding either acetone + acetone + ȮH, a chain propagating step, or acetone + propene + HOȮ, a chain-inhibiting step.

3.4.3. speciation from thermally initiated experiments

Speciation measurements from low-temperature oxidation of dimethyl ether [344, 848, 852, 867, 872, 874, 885-894], diethyl ether [895-900], and di-*n*-butyl ether [797, 798, 901, 902] are reported from JSR and laminar flow reactors.

Brumfield et al. [903] reported the first direct measurements of HOȮ from dimethyl ether oxidation under atmospheric pressure using mid-IR Faraday rotation spectroscopy (FRS) applied to a laminar flow reactor. The authors remarked on the uncertainty in the reaction of HĊO + O_2 → HOȮ + CO as one of the main causes of discrepancy between the concentration measurements and predictions using the Zhao et al. [904] mechanism. Guo et al. [905] reported the first direct measurements of hydrogen peroxide (H_2O_2) concentrations under atmospheric pressure in dimethyl ether oxidation using molecular beam mass spectrometry (MBMS) with electron-impact ionization. Several species were measured in addition to H_2O_2 over the temperature range 490 – 750 K, including CO, CO_2, H_2, formaldehyde, and acetaldehyde, and discrepancies were noted with the two mechanisms used for comparison, Zhao et al. [904] and Yasunaga et al. [906]. Kurimoto et al. [907] combined dual-modulation FRS and MBMS-EI techniques to atmospheric pressure flow reactor experiments of dimethyl ether oxidation to extend the temperature range up to 1150 K and also used different initial RH concentrations. The aim of the experiments in [907] was providing experimental constraints for improving predicted branching ratios for CH_2O-producing chain-propagation reactions and CO-producing chain-branching reactions. The authors developed a simplified 7-step analytical model to describe the low-temperature chemistry and emphasized the importance of improving the kinetics of unimolecular ȮOOH decomposition over second-O_2-addition as a means of reducing the higher reactivity predicted by the two mechanisms employed, Zhao et al. [904] and Liu et al. [908].

Two-stage oxidation chemistry is evident in species profile measurements in dimethyl ether [848, 852, 872, 874, 886, 888-891] and in the temperature oscillation measurements of Stoehr et al. [891]. The latter measurements were ascribed to shifts in the reaction mechanism at the cross-over temperature, defined as the temperature where ketohydroperoxide-mediated ȮH production ceases and the reaction mechanism moves away from second-O_2-addition (leading to chain-branching) and towards β-scission of ȮOOH (leading to chain-propagation via CH_2O + CH_2O + ȮH). The oscillatory behavior was captured by 5- and 13-step skeletal mechanisms developed by the authors and replicated predictions from the detailed kinetics mechanism of Curran et al. [848].

Dagaut et al. [887] reported measurements of stable intermediates, such as CO, CO_2, CH_2O, and ethene from dimethyl ether oxidation using jet-stirred reactor experiments at 1 and 10 atm and from 800 – 1300 K. Speciation measurements were subsequently extended to a lower limit of temperature (550 K) in Dagaut et al. [886], where NTC behavior spanned from 600 K to ~750 K.

Curran et al. [848], utilizing the Princeton variable pressure flow reactor (VPFR), confirmed via FT-IR measurements that formic acid (HOCHO) is a major intermediate in low-temperature dimethyl ether oxidation, with concentrations exceeding CH_2O, the β-scission product of methoxymethyl radicals, in the temperature range 550 – 650 K. The experiments were conducted from 12 – 18 atm, 550 – 850 K and were diluted in 98.5% N_2. Formic acid was not reported in dimethyl ether studies [886, 887] that preceded Curran et al. [848], which led to the inclusion of a formic acid sub-mechanism in a revised chemical kinetics mechanism. Two pathways were proposed: (1) isomerization of the carbonyl-oxy radical formed via O–O scission in hydroperoxy methyl formate, followed by two successive β-scission channels (**Figure 84**) – the

reaction also produces CO, which is formed in higher concentration than other species; (2) ȮH-addition to formaldehyde (**Figure 85**). However, the authors remarked on the uncertainty in the pressure dependence of ȮH + CH_2O, discussed initially in Stief et al. [909]. Pathways to HOȮ were neglected in the primary oxidation scheme proposed by Curran et al. [848]. However, the importance of HOȮ is evident from the experiments in Suzaki et al. [854, 869].

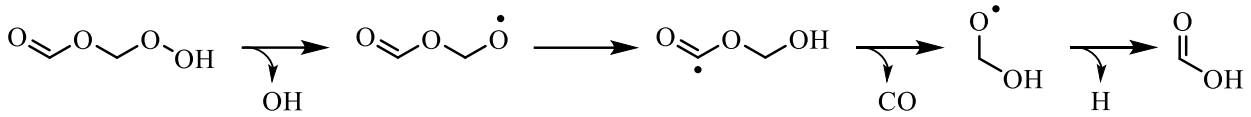

Figure 84. Formic acid pathway from hydroperoxymethyl formate decomposition.

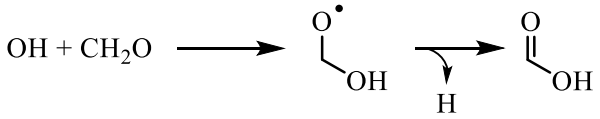

Figure 85. Formic acid pathway from reaction of formaldehyde with ȮH.

In subsequent experiments using a laminar flow reactor at atmospheric pressure to probe product formation from dilute dimethyl ether oxidation (340 ppm in 10% O_2), Liu et al. [874] also confirmed formic acid as a dominant product formed via the sequence in **Figure 84**. Liu et al. [874] did not, however, detect hydroperoxy methyl formate despite characteristic spectral features from the FT-IR measurements of Thamm et al. [875]. As a result of the absence, it was postulated that hydroperoxy methyl formate, the lone γ-ketohydroperoxide isomer of dimethyl ether, is either less thermally stable than assumed in literature mechanisms [867, 885, 886] or is removed by other, unknown reactions. Gao and Nakamura [910], utilizing laminar flow reactor experiments and computational modeling, concluded that a critical temperature of 540 K exists that is related to the transition between first- and second-stage ignition and is governed by hydroperoxy methyl formate decomposition, yet noted that the actual temperature is potentially lower due to insufficient contact time between the flames and thermocouples.

Methyl formate was detected in Liu et al. [874], yet only in the presence of NO (used in initial concentrations up to 600 ppm). The lack of methyl formate detection in absence of NO is in contrast to the experiments of Wallington et al. [855] and Jenkin et al. [856]. Herrmann et al. [888] conducted dilute (97% Ar) speciation experiments of dimethyl ether oxidation from 400 – 1200 K using an atmospheric-pressure laminar flow reactor coupled to a 20-eV electron impact time-of-flight mass spectrometer, where a pulsed electron beam generated via a hot-wire ionizer was used as the ionization source. Formic acid and methyl formate were detected in the low-temperature region, from around 500 – 750 K, and the latter was proposed to come from the ketohydroperoxide → carbonyl-oxy radical channel. However, formic acid was not quantified given the similarity in *m/z* (46.01) to the parent molecule, dimethyl ether (*m/z* 46.06), the latter of which was high in intensity and blurred the adjacent peak in the mass spectrum. However, the formic acid peak was separated quite clearly from the dimethyl ether signal using careful numerical integration over the conjoined peaks. Subsequently, Herrmann et al. [889] performed modeling analysis, which concluded that the measured concentrations were over-predicted by the Curran et al. [848] and the Zhao et al. [904] mechanisms. Modifications were then applied to both, yet the revisions did not capture the temperature dependence of methyl formate properly and remained higher by a factor of ~20.

Wang et al. [890] conducted an extensive series of experiments on dimethyl ether oxidation at 1 atm from 400 – 1160 K, using a combination of laminar flow reactor measurements, coupled with electron-impact and photoionization-based MBMS, and a jet-stirred reactor coupled with photoionization-MBMS. Several intermediate species were detected and quantified, including methyl formate. However, formic acid was not experimentally quantified in Wang et al. [890] unlike in Curran et al. [848] and in Liu et al. [874], both of which utilized FT-IR. Wang et al. [890] remarked on the detection of *m/z* 64, the molecular identity of which went unresolved. The two independent experiments both showed onsets in photoionization spectra near 10.4 eV at *m/z* 64. Two species were postulated: hydroxymethyl hydroperoxide ($HOCH_2OOH$) and trihydroxy methane ($(HO)_3CH$). Because of an absence of a reference photoionization spectra, Wang et al. [890] calculated adiabatic ionization energies to identify the species at *m/z* 64. For $HOCH_2O_2H$, adiabatic ionization energies were in the range 9.77 – 9.94 eV, (~0.5 eV lower than the experimental threshold). For $(HO)_3CH$, the energies were ~11.03 – 11.12 eV (above the experimental threshold by ~0.6 eV).

Potential energy surface calculations were also conducted in Wang et al. [890] on unimolecular decomposition pathways of the carbonyl-oxy radical formed via O–O bond-scission of hydroperoxymethyl formate, along with pressure- and temperature-dependent rate coefficients calculated using MESMER at 1 atm and 10 atm and in the high-pressure limit. The unimolecular decomposition pathways of methoxy formate ($\dot{O}CH_2OCHO$) were first optimized at the B3LYP/6-311++G(*d*,*p*) level of theory, followed by single-point determinations using quadratic configuration interaction with singles, doubles, and perturbative inclusion of triples (UQCISD(T)), as described in Harding et al. [911], with two basis sets: correlation-consistent, polarized-valence, triple-ζ (cc-PVTZ), and quadruple-ζ (cc-PVQZ) basis sets. The UQCISD(T) energies were extrapolated to the complete basis set limit (CBS) following the expression in Martin [912].

Figure 86a compares the five unimolecular decomposition rates of the methoxy formate radical ($\dot{O}CH_2OCHO$) from Wang et al. [890], which is depicted in **Figure 87**. Similar to Andersen and Carter [866], the rate for the pathway leading to formic acid + $H\dot{C}O$ is orders of magnitude larger than the competing pathways. The reactions with the next two highest rates lead to CO + $HOCH_2\dot{O}$, via a direct pathway, and to $\dot{H}$ + OCHOCHO, via C–H bond-scission and formation of a carbon-oxygen double bond. **Figure 86b** compares the rates from Andersen and Carter [866] for the formic acid channel and the isomerization step occurring via a 5-membered transition state to rates calculated in [890], which are likely to be more accurate. The calculations in Wang et al. [890] were used to amend 25 reactions in the mechanism of Zhao et al. [904], including revised rate parameters for both $RO\dot{O}$ formation and direct formaldehyde production via methoxymethyl + O_2 from Rosado-Reyes et al. [858], $\dot{R} + O_2 \rightarrow CH_2O + H\dot{C}O + H_2O$ from Suzaki et al. [869], and ten rate coefficients calculated from the potential energy surface for unimolecular decomposition of methoxy formate radical.

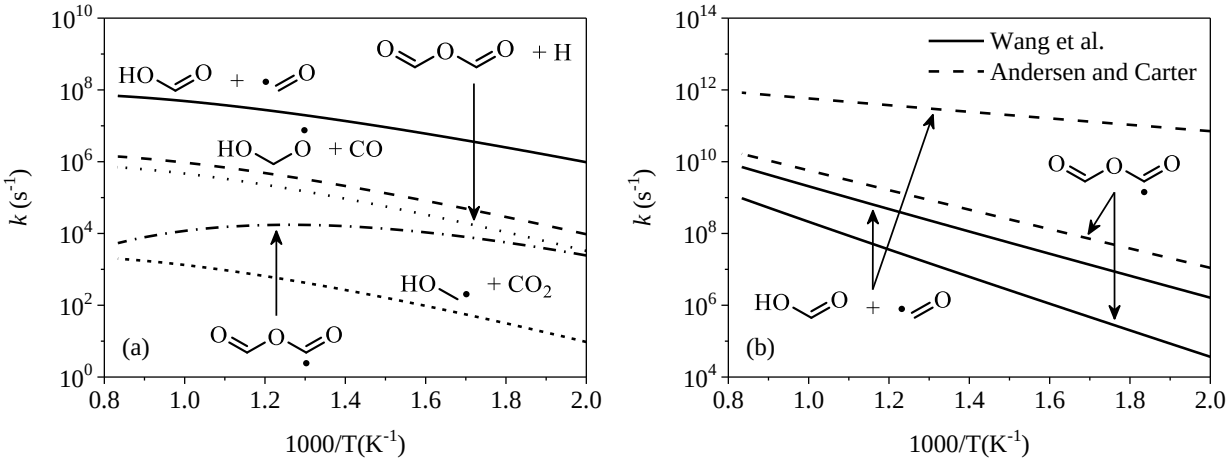

Figure 86. (a) Unimolecular decomposition rates methoxy formate radical ($\dot{O}CH_2OCHO$) from Wang et al. [890]. (b) Comparison of two reactions from (a) calculated in Wang et al. [890] and by Andersen and Carter [866].

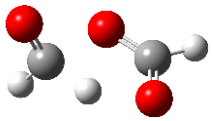

Figure 87. Transition state of methoxy formate → $H\dot{C}O$ + formic acid from Wang et al. [890].

Moshammer et al. [344] reported the first experimental detection of hydroperoxymethyl formate from dimethyl ether oxidation in jet-stirred reactor experiments at 1 atm using synchrotron-based photoionization MBMS. Several other species were also detected, some for the first time, and confirmed via *ab initio* calculations of adiabatic ionization energies and reference photoionization spectra including formic acid, methylhydroperoxide (H_3COOH), 1,3-dioxetane – the lone cyclic ether of dimethyl ether – formic anhydride, and carbonic acid which is a product formed via Korcek reaction. The Criegee intermediate, formaldehyde oxide ($H_2\dot{C}O\dot{O}$), was not detected. The detection of 1,3-dioxetane is one of several important results in Moshammer et al. [344] because of the implications on properly modeling chain-propagation in dimethyl ether oxidation. Previous determinations concluded that the cyclic ether was not relevant given the barrier height from $\dot{Q}OOH$ being 7 – 8 kcal/mol over the energy of the $\dot{R}$ + O_2 entrance channel [344, 870]. The authors in [344] postulated a mechanistic link connecting the observed performic acid (HOOCHO) to formic anhydride decomposition via CO and H_2 elimination as proposed in Andersen and Carter [853]; the formation of performic acid via recombination of $\dot{O}H$ with $\dot{O}CHO$ was proposed in Curran et al. [848].

In a subsequent study, Moshammer et al. [852] quantified hydroperoxymethyl formate and methylhydroperoxide for the first time using theoretical calculations of absolute photoionization cross-sections (**Figure 88**). Several other species were quantified in addition, including H_2O_2, formic acid, methyl formate, and performic acid. In cases where spectra were not available, e.g. hydroperoxymethyl formate, theoretical methods were applied to calculate cross-sections. Moshammer et al. [852] describe the deficiencies with the approach, yet also include several case studies where the simulation method accurately reproduced well-known photoionization spectra for acetylene, ethene, methanol, acetaldehyde, and several others, which lends support to the application of the method to hydroperoxymethyl formate. Comparisons

of the quantified mole fractions from the previous experiments [344] with several mechanisms [578, 872, 890] revealed inconsistences in two main areas: (1) the chemistry prescribed in the mechanisms, and (2) differences in thermochemistry. The appreciable influence of the latter is described for alkanes in Bugler et al. [710].

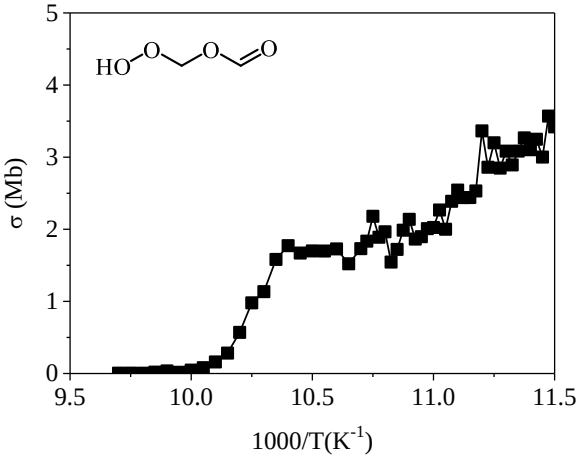

Figure 88. Photoionization cross-section of hydroperoxymethyl formate, the lone γ-ketohydroperoxide formed via dimethyl ether oxidation and quantified in Moshammer et al. [852].

Rodriguez et al. [872] applied gas chromatography and cw-CRDS to quantify products from JSR experiments on dimethyl ether near 1 atm and from 500 – 1100 K. Several species were quantified, including hydrogen peroxide and methyl formate. The concentration of the latter species relative to formaldehyde was lower by a factor of ~30, which is consistent with Kurimoto et al. [907] yet differs from Hermann et al. [889] where the mole fractions of the two species were of the same order of magnitude. Three main pathways were deemed most significant to the formation of methyl formate: (1) recombination reaction of methoxy + formyl ($CH_3\dot{O}$ + $HC\dot{O}$), (2) decomposition of the carbonyl-oxy radical (methoxy formate) formed via O–O scission in hydroperoxymethyl formate leading to methyl formate + $\dot{H}$, and (3) recombination of methyl and OCHO radicals. Reaction of carbonyl-oxy + O_2 yielding methyl formate + $H\dot{O}O$ was included in a mechanism produced using EXGAS, yet it did not impact the predicted methyl formate yields. Species observed in other studies, including formic acid [848, 852, 858, 874, 888] and 1,3-dioxetane [344], were not detected. The chemical kinetics mechanism in Rodriguez et al. [872] included sub-mechanisms for primary intermediates, e.g. methyl formate and 1,3-dioxetane.

In comparison to dimethyl ether, limited speciation experiments are reported for low-temperature oxidation of diethyl ether. Waddington [895] utilized a static reactor at a fixed temperature of 425 K to measure intermediates from diethyl ether oxidation, including formaldehyde, acetic acid, acetaldehyde, methanol, ethanol, and peracetic acid ($H_3CC(=O)OOH$). The proposed pathway to PA was acetaldehyde oxidation. Two important results from [895] were the role of peracetic acid in chain-branching, via decomposition into $CH_3C\dot{O}O$ + $\dot{O}H$, and the inhibiting effect of excess O_2 on the observed induction period. The latter effect was ascribed to inhibition of peracetic acid formation and an increase in hydroperoxides, specifically 1-ethoxy-1-hydroperoxyethane ($C_2H_5OC(OOH)HCH_3$), which were observed to increase with oxygen concentration. Griffiths and Inomata [896], similar to the dimethyl ether experiments of Stoehr et al. [891], observed oscillatory temperature in jet-stirred reactor experiments over the temperature range 430 – 590 K

and governed by a shift in the $\dot{R} + O_2 \leftrightharpoons ROO\dot{}$ equilibria to the reactant side and remarked on the significance of acetaldehyde oxidation in the overall reactions of diethyl ether, as noted in Waddington [895].

Tranter and Walker [815] conducted experiments on diethyl ether oxidation at 753 K and reported no evidence of conjugate alkene + $HO\dot{O}$ using GC-MS diagnostics. Similar results were concluded for other ethers, namely methyl ethyl ether and ethyl *tert*-butyl ether. Under the conditions of the experiments, suppression of the chain-inhibiting channel was ascribed to facile C–O homolysis, occurring at a rate ~10^2 higher than for analogous C–C homolysis in alkyl radicals at 753 K [815]. In addition, thermal decomposition of initial radicals outcompeting first-O_2-addition was concluded as the primary cause of low cyclic ether yield in methyl *tert*-butyl ether (~1%). Tranter and Walker found that in both methyl- and ethyl-*tert*-butyl ether oxidation, the yield of substituted dioxolanes via decomposition of $\dot{Q}OOH$ radicals remained less than 5% of the carbon balance, and for the latter, no detection of conjugate alkene + $HO\dot{O}$ was reported. Combined, the results led the authors to conclude that C–O β-scission rates exceeded rates of reaction with O_2. The concentrations of oxygen in [815] ranged from $9.0 \cdot 10^{17} – 4.6 \cdot 10^{18}$ cm^{-3}. Evidence for the decomposition of initial methyl-*tert*-butyl ether radicals was an appreciable yield of methanol (CH_3OH) formed via reaction of the β-scission product (methoxy) with H_2, used in the experiments of [815] for $\dot{O}H$ production, forming methanol + $\dot{H}$. In contrast, in ethyl *tert*-butyl ether, ethanol was not a substantial product (yield < 5%), yet *iso*-butene formed at 90% yield (the co-product with ethoxy from C–O β-scission of $\dot{R}$).

Serinyel et al. [897] conducted JSR experiments on diethyl ether oxidation at 1 and 10 atm from 450 – 1250 K and remarked on the importance of acetic acid in low-temperature kinetics. The primary mechanism postulated for acetic acid formation involved reaction of $CH_3C(=O)O\dot{O}$ (acetylperoxy) with either $HO\dot{O}$ or methyl peroxy, which yielded O_2 and either Ö or CH_2O as co-products. Species profiles for cyclic ether species were not reported.

Tran et al. [898] conducted a series of flow reactor experiments on diethyl ether oxidation at 1 atm using gas chromatography and MBMS. The latter diagnostic employed both electron-impact and photoionization mass spectrometer. Several species related either to $\dot{Q}OOH$ or ketohydroperoxide decomposition were quantified, including 2-methyl-1,3-dioxolane, acetaldehyde, acetic acid, and acetic anhydride. Two distinct NTC regions were identified in both JSR and plug-flow reactor measurements and were reflected in diethyl ether profiles, as well as CH_2O and CO profiles. A slight difference in the temperature of the NTC regions in the two flow reactors of ~50 K was noted. In the JSR experiments, the first NTC region occurred from ~525 – 575 K and was ascribed to a shift from second-O_2-addition towards unimolecular decomposition of $\dot{Q}OOH$, where both the –OOH group and unpaired electron are on opposing α carbons, into CH_3CHO + CH_3CHO + $\dot{O}H$. The second region occurred in the JSR from ~650 – 750 K and was attributed to enhanced C–O β-scission rates of α radicals, yielding $CH_3CHO + CH_3\dot{C}H_2$ and diminished first-O_2-addition, i.e. $\dot{R} + O_2 \rightarrow ROO\dot{}$. In effect, the existence of the first NTC region in diethyl ether is due not to a suppression of $\dot{Q}OOH$ chemistry, but to diminished second-O_2-addition reactions. The second NTC is due to a reduction in the flux of diethyl ether radicals towards the formation of $\dot{Q}OOH$. The latter change completely restricts chain-branching chemistry near ~750 K at 1 atm.

Subsequent experiments by Tran et al. [899] examined the effect of increased pressure on the bimodal NTC regions and also compared the oxidation of diethyl ether against *n*-pentane at the same conditions. Specifically, JSR experiments were conducted at 5 atm and showed that the first NTC region diminishes

with increased pressure because of increased rates of O_2-addition to both Ṙ and ȮOOH outcompeting C–O β-scission reactions. Mole fractions of acetic anhydride and acetic acid increased at higher pressure, ascribed to increased rates of second O_2-addition. Other ȮOOH-mediated species, such as 2-methyl-1,3-dioxolane were relatively insensitive to pressure. Temperature-dependent mole fraction profiles of analogous species in *n*-pentane oxidation were compared to understand the effect of the ether group on low-temperature chemistry. Two species ascribed to second-O_2-addition pathways, 1,3-pentadione and acetone, which are analogous to acetic anhydride and acetic acid in diethyl ether oxidation, were significantly lower indicating that the ether group facilitates both ketohydroperoxide formation and decomposition.

To account for the significant amount of acetic acid quantified in prior experiments, Tran et al. [898] proposed an alternative ketohydroperoxide decomposition pathway. The reaction involves the formation of a cyclic peroxy species (**Figure 89**), similar in structure to that formed via the Korcek mechanism [913]. Importantly, acetic acid concentration peaked near 575 K, the upper end of the first NTC region, which supports the explanation provided for the underlying mechanism being dependent on ketohydroperoxide formation. Two pathways to acetic anhydride ($CH_3C(=O)OC(=O)CH_3$) from ketohydroperoxide were also proposed and peak formation occurred near 500 K – providing additional supporting detail for the proposed mechanism. From analysis of photoionization spectra, 2-methyl-1,3-dioxolane was the only cyclic ether reported and, in contrast to the ketohydroperoxide-derived species, peak yield of the cyclic ether occurred towards the upper end of the second NTC region.

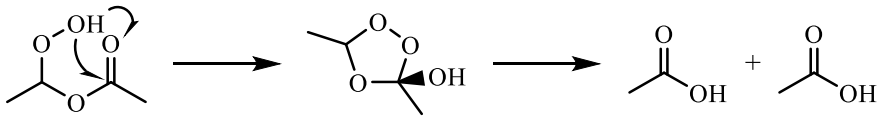

Figure 89. Alternative ketohydroperoxide decomposition pathway proposed in Tran et al. [898] from diethyl ether oxidation leading to the production of acetic acid.

Thion et al. [798] reported speciation measurements for di-*n*-butyl ether oxidation from JSR experiments conducted at 1 and 10 atm from 470 – 1250 K. While NTC behavior occurred at both pressures, the 10 atm experiments revealed two distinct regions of low-temperature chemistry, similar to diethyl ether in Tran et al. [898], which were separated by ~100 K. The first NTC region was ascribed to a shift of the main source of ȮH from decomposition of ether-derived ketohydroperoxides to decomposition of propylhydroperoxides derived from the propyl radicals produced in the ketohydroperoxide decomposition. The second NTC region (at higher temperature) was associated with decreasing effectiveness of the addition of fuel radicals to O_2 and a switch in the driving chemistry towards oxidation of *n*-butyl, which forms via C–O bond-scission of α radicals from di-*n*-butyl ether. In addition to the detection of common species, such as acetaldehyde and formic acid, 2,3-dihydrofuran was detected in the 10 atm experiments, which is also indicative of *n*-butyl chemistry. Oxidation of tetrahydrofuran, which is formed via decomposition of the ȮOOH isomer 1-hydroperoxy-4-butyl, leads to 2,3-dihydrofuran through the chain-inhibiting step tetrahydrofuranyl + O_2 → 2,3-dihydrofuran + HOȮ. Tran et al. [901] expanded on the work of Thion et al. [798], conducting speciation experiments using a JSR (with GC/MS/FID) and a plug flow reactor (with MBMS photoionization at 17 eV). Two distinct NTC regions were evident in the species profiles, consistent with [798], and Tran et al. [901] emphasized the importance of ȮOOH dissociation, and the concomitant decrease in second O_2 addition, in causing the lower-temperature NTC behavior. The experiments produced

19 previously undetected species, including alkylhydroperoxides, cyclic ethers, and ketohydroperoxides, although quantification was not possible due to missing reference electron-impact mass spectra and/or photoionization cross-sections. Several of the species were not included in the chemical kinetics mechanisms for di-*n*-butyl ether [797, 798].

Only a few studies exist on thermally initiated oxidation of branched ethers [496, 815, 914-916]. Brocard et al. [914] employed a static reactor to measure product formation from near-atmospheric methyl *tert*-butyl ether oxidation over a 200-K range of temperature, 575 – 775 K. The main products detected were *iso*-butene and methanol formed via a 4-centered decomposition reaction of methyl *tert*-butyl ether. Three conclusions were drawn in [914] to explain the resistance of methyl *tert*-butyl ether to chain-branching as marked in pressure and temperature measurements: (1) favoring of HOȮ-producing reactions derived from ȮOOH radicals over second-O_2-addition or ȮH-producing reactions, where the formation of ȮOOH is facilitated by weak C–H bond energy on the methoxy group and subsequent 7-membered transition state from ROȮ adducts; (2) unimolecular decomposition of α' radicals leading to *tert*-butyl and CH_2O, the former of which yields exclusively *iso*-butene and HOȮ upon reaction with O_2; (3) isomerization of the β radicals into α' radicals favored over unimolecular decomposition or reaction with O_2. Norton and Dryer [496] conducted experiments on methyl *tert*-butyl ether, although for temperatures greater than 1000 K, the results of which pointed to a favoring of unimolecular reactions of Ṙ forming *iso*-butene + methanol and lesser amounts of CO and other small-molecule species.

Goldaniga et al. [915] employed a jet-stirred reactor to measure product formation from oxidation of several ethers, methyl- and ethyl-*tert*-buytl ether, di-*iso*-propyl ether, and *tert*-amyl ether. Neither cyclic ethers nor conjugate alkenes were detected. Glaude et al. [916] conducted JSR experiments on methyl *tert*-butyl ether and ethyl *tert*-butyl ether at 10 atm from 750 – 1150 K and equivalence ratios from 0.5 – 2.0. EXGAS was utilized to produce a detailed kinetics mechanism and was augmented to accommodate ether-specific reactions. Specifically, activation energies were lowered for three reaction classes – H-abstraction from RH by O_2, β-scission of RȮ, and β-scission of Ṙ. For both cases, product formation below 1000 K was dominated by *iso*-butene and the corresponding alcohol: methanol for methyl *tert*-butyl ether and ethanol from ethyl *tert*-butyl ether.

3.4.4. influence of ether oxidation pathways on autoignition chemistry

Ethers such as dimethyl ether and diethyl ether are promising biofuels in compression-ignition applications because of high cetane numbers [917-923]. Ignition delay time trends of acyclic ethers, including dimethyl ether [578, 893, 924-927], diethyl ether [906, 928-930], and di-*n*-butyl ether [797, 902, 931] display pronounced NTC behavior. The sections below describe RCM, shock tube, and flow reactor measurements of ignition delay times and detailed chemical kinetics mechanisms in the context of alkane ignition chemistry.

3.4.4.1. ignition delay time measurements

Pfahl et al. [926] employed a high-pressure shock tube to measure stoichiometric ignition delay times of dimethyl ether and *n*-decane at 13 atm and ~45 atm from 650 – 1300 K to examine the NTC behavior and compare with established measurements of *n*-heptane [932]. The ignition delay time trend of dimethyl ether at 13 atm exhibited clear NTC behavior and nearly identical temperature dependence to both *n*-alkanes. However, below 1000 K, and despite the smaller molecular structure, ignition times of dimethyl ether were

approximately a factor of ~2 shorter than *n*-decane in the region where peroxy radical chemistry governs ignition. Mittal et al. [924] measured dimethyl ether ignition in an RCM from 10 – 20 atm over a narrower range of temperature (615 – 735 K), yet studied the effect of equivalence ratio ($0.4 < \phi < 1.5$) on first- and second-stage ignition. In agreement with the Zhao et al. [904] mechanism, the experimental measurements in [924] revealed that first-stage ignition delay times were insensitive to both equivalence ratio and pressure. In contrast, second-stage ignition is strongly influenced by both equivalence ratio and pressure. Li et al. [925] measured ignition delay times of dimethyl ether in air from ~700 – 1240 K near 23 atm, intermediate to the pressures of Pfahl et al. [926] and Mittal et al. [924], and examined the effect of N_2 dilution from 0 – 40% and equivalence ratio from 0.5 – 1.5. The level of dilution made no impact on the temperature dependence, yet the ignition times were shortened with decreasing dilution from 70 – 85%. The measurements also followed a power-law dependence similar to that for alkanes [933, 934]. Burke et al. [578] expanded the experimental regions for dimethyl ether ignition utilizing shock tube and RCM measurements, covering 7 – 41 atm and including $\phi = 0.3$ equivalence ratio measurements.

Ignition delay time measurements for diethyl ether are more limited than dimethyl ether, yet the results in Inomata et al. [929] and Werler et al. [928] confirm NTC behavior and higher reactivity than *n*-pentane. **Figure 90** compares ignition delay times of dimethyl ether Li et al. [925] to propane [533] (**Figure 90a**) and diethyl ether Werler et al. [928] to *n*-pentane [554] (**Figure 90b**). The higher reactivity of dimethyl ether compared to propane is due in part to the absence of direct, chain-inhibiting pathways leading to HOȮ. Instead, HOȮ forms mainly via reaction of formyl radicals with O_2 to give HOȮ + CO, where HĊO comes almost exclusively via H-abstraction from CH_2O.

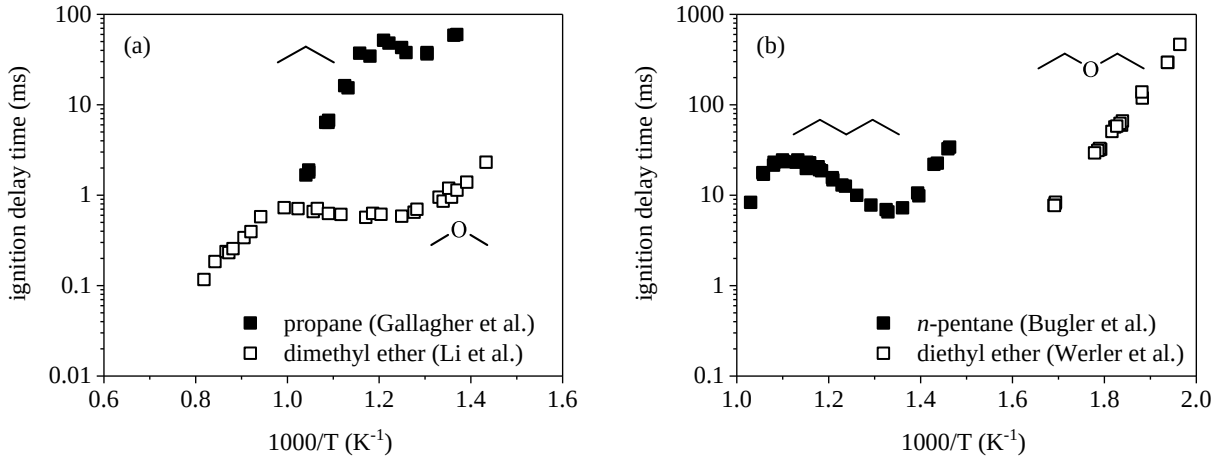

Figure 90. (a) Stoichiometric ignition delay times of dimethyl ether from Li et al. [925] (23 atm) compared to propane from Gallagher et al. [533] (27 atm). (b) Stoichiometric ignition delay times of diethyl ether from Werler et al. [928] (12 atm) to *n*-pentane from Bugler et al. [554] (10 atm). In both cases, the ether functional group appreciably shortens ignition delay times.

Cai et al. [797] reported ignition delay times from a laminar flow reactor for di-*n*-butyl ether in air at 1 atm using temperature profile measurements. The experiments were conducted over a narrow temperature range of 485 – 525 K using several equivalence ratios from $\phi = 0.5$ to $\phi = 1.0$. Within the temperature range, no equivalence ratio dependence was observed.

Ignition delay time measurements for branched acyclic ethers at low temperatures are lacking. Fieweger et al. [540] conducted shock tube experiments on methyl *tert*-butyl ether ignition at nominal pressures of 13 atm and 40 atm from ~750 – 1200 K. Two types of ignition delay times were measured: deflagrative (mild) ignition, measured using CH radical emission time profiles, and a secondary explosion (overall ignition) measured using pressure profiles. Both types of ignition times were compared to methanol, measured under the same conditions, and the two ignition delay time trends were nearly identical at 40 atm. For methyl *tert*-butyl ether, no secondary explosion occurred below 900 K (for methanol, the lower limit of temperature was ~800 K).

3.4.4.2. detailed chemical kinetics mechanisms

Chemical kinetics mechanisms for dimethyl ether oxidation are abundant [578, 848, 867, 872, 886, 887, 890, 894, 904, 906]. Dagaut et al. [887] developed the first chemical kinetics mechanism for dimethyl ether oxidation, which contained 43 species and 286 reactions. Subsequently, in Dagaut et al. [886], a revised mechanism (55 species and 331 reactions) was used to simulate the low-temperature intermediate species concentrations and the first- and second-stage ignition delay times measured in Pfahl et al. [926]. No new species profiles were reported relative to [887]. The mechanism achieved predictions within the experimental uncertainties. Curran et al. [867] expanded on the mechanism development in Dagaut et al. [886], leading to a revised mechanism with 78 species and 336 reactions, and conducted a modeling analysis of species profiles and ignition times. The main alterations to the initial mechanism were the rate coefficients for dimethyl ether homolysis and C–O β-scission of methoxymethyl radicals.

Toulson et al. [935] developed an multi-step analytical model for DME autoignition based in part on RCM ignition delay time measurements and using rate coefficients assigned to generic reactions to define the reaction mechanism – a technique based on Halstead et al. [936]. Burke et al. [578] reported that $CH_3O\dot{C}H_2 \rightarrow \dot{C}H_3 + CH_2O$ is not in the high-pressure limit at 100 atm and that the majority of $\dot{Q}OOH$ from dimethyl ether (> 80%) yields $CH_2O + CH_2O + \dot{O}H$ at 830 K for both 12 atm and 25 atm. Compared with preceding mechanisms of Zhao et al. [904] and Curran et al. [848], substantial changes were made to rate coefficients for H-abstraction from dimethyl ether by $H\dot{O}O$, $CH_3O\dot{O}$, and $\dot{C}H_3$.

Glarborg et al. [894] developed a chemical kinetics mechanism by integrating a sub-mechanism compiled for dimethyl based on literature rate coefficients with base chemistry prior mechanisms. The rate coefficients for the sub-mechanism were unaltered to reflect the status of knowledge of dimethyl ether combustion chemistry. As part of the mechanism development, Glarborg et al. [894] compared rate coefficients for three reactions (methoxymethyl + $O_2 \rightarrow RO\dot{O}$, $RO\dot{O} \rightarrow \dot{Q}OOH$, and $RO\dot{O} \rightarrow$ products + $\dot{O}H$) from the chemical kinetics mechanisms of Burke et al. [578] and Rodriguez et al. [872] to measurements from Sehested et al. [859] and Eskola et al. [863]. While the results from the two experimental studies were consistent, differences between rates in the mechanisms were 10^1 or higher, leading the authors to remark on the need for experimental measurements and theoretical calculations of reactions on the $CH_3OCH_2O\dot{O}$ potential energy surface to reconcile ignition delay measurements in the NTC region. Simulations were conducted on ignition delay times, including the experiments of Li et al. [925]. Above 1100 K, the predictions were consistent with the experiments.

However, within the NTC region, differences up to a factor of 5 were noted. In addition to the ignition delay times, species profiles from a high-pressure flow reactor in Glarborg et al. [894] were simulated using the newly developed chemical kinetics mechanism. Despite accurate predictions of dimethyl ether

consumption, CO, and other intermediates, other species profiles of CO_2 and CH_2O were in error. For the latter species, in addition to CO oxidation, two other pathways to CO_2 were postulated, both of which are mediated by formic acid. For CH_2O, the two major formation channels from dimethyl ether are: (1) unimolecular decomposition from methoxy methyl radicals outcompeting O_2-addition; (2) ȮOOH decomposition. Given the accuracy of species profile predictions for dimethyl ether, the CH_2O discrepancy may arise from uncertainty in the rate coefficients and/or reaction mechanisms of ȮOOH (hydroperoxymethyl-peroxy).

Numerous chemical kinetics mechanisms also exist for diethyl ether oxidation [880, 897-899, 906, 937-940]. Sakai et al. [880] calculated rate coefficients for second-O_2-addition reactions using quantum chemical methods along with rate coefficients specific to reactions of diethyl ether radicals with O_2 [879] and Burke et al. [578] as a base mechanism. Tang et al. [939] compiled a reduced mechanism based on Yasunaga et al. [906] and included the formation of only one of the four possible cyclic ethers (2-methyl-1,3-dioxolane). Only four consumption reactions for 2-methyl-1,3-dioxolane were included in the mechanism, namely reactions with either ȮH or HOȮ and subsequent ring-opening.

Hu et al. [940] conducted a series of *ab initio* and RRKM master equation calculations for H-abstraction and unimolecular decomposition reactions of diethyl ether. The rate calculations were combined with sub-mechanisms from other mechanisms [880, 906] and to develop a revised diethyl ether mechanism. Comparison of rate coefficients for H-abstraction by HOȮ and ȮH to other chemical kinetics mechanisms revealed differences of up to 10^1. The rate coefficients for the latter reactions from Yasunaga [906], which were derived from the ȮH + ether calculations of Zhou et al. [823] for abstraction from α carbon and, from β carbon, by analogy to secondary C–H in the methylcyclohexane model of Orme et al. [941] were lower by more than 10^2. Eble et al. [938] constructed a detailed mechanism and simulated the ignition delay time experiments of Werler et al. [928] and Sakai et al. [880] with a similar of success. The focus of Eble et al. [938] on reactions involved in first-stage ignition led to the identification of an additional chain-branching mechanism driven initially by ethyl formed via decomposition of α radicals of diethyl ether. Subsequently, ethyl + O_2 leads to ethyl peroxy, which upon reaction with diethyl ether forms ethylhydroperoxide (C_2H_5OOH), the decomposition of which yields two radicals: ethoxy + ȮH. Such a reaction sequence is favorable given the lower C–O bond energy in ether radicals compared with analogous alkyl radicals, e.g. 3-pentyl.

Serinyel et al. [897] developed a mechanism for diethyl ether based on Thion et al. [798]. Rate coefficients for O_2-addition reactions to Ṙ and to ȮOOH were adopted from calculations in Goldsmith et al. [534] on propyl radical and rate rules from Villano et al. [408, 409] were utilized for RȮ isomerization and ȮOOH → cyclic ether + ȮH. Rate coefficients for other reactions, such as H-abstraction, C–C and C–O β-scission of initial radicals, and related thermochemistry of species were also adopted from the literature.

The chemical kinetics mechanism of Tran et al. [898] for diethyl ether incorporated a detailed sub-mechanism defined by 31 reaction classes, which included the acetic acid channel in **Figure 89**. In addition, and despite only one species reported, all four cyclic ether formation channels were included with rates adopted from Sakai et al. [879]. 2-methyl-1,3-dioxolane mole fractions were quantified based on adiabatic ionization energy calculations and photoionization cross-section estimation [942]. Compared to Tang et al. [939], consumption channels for cyclic ethers were expanded in the Tran et al. [898] mechanism and

included reactions with ȮH, HOȮ, and other radicals. However, only simplified ring-opening reactions with no radical-specific mechanisms comprised cyclic ether consumption.

Danilack et al. [943] report UCCSD(T)-F12b/cc-pVTZ-f12 energies of structures optimized by B2PLYPD3/cc-pVTZ methods for stationary points along the diethyl ether oxidation pathway from initial addition of ethoxyethyl radicals to O_2 through to the dissociation of the ketohydroperoxide. Linked master equation calculations were then carried out along the full reaction sequence to characterize non-Boltzmann effects from reaction of energetic products from exothermic reactions, and the effects were incorporated into a detailed mechanism for diethyl ether oxidation. Notably, the inclusion of non-Boltzmann reactions could halve the ignition delay in the negative temperature coefficient region at 1 atm, pointing to substantial impact of non-Boltzmann chemistry in diethyl ether ignition.

Figure 91 compares species profiles of diethyl ether, dimethyl ether, and *n*-pentane during stoichiometric oxidation from 400 – 900 K at 1 atm. Tran et al. [898] noted the unusual presence of two distinct NTC regions in diethyl ether. Similar behavior was reported in di-*n*-butyl ether in Thion et al. [798]. However, from chemical kinetics modeling analysis, Tran et al. [898] differentiated the chemistry for diethyl ether from that for di-*n*-butyl ether oxidation in Thion et al. [798], in which the lower temperature NTC region was explained via subsequent reaction of ketohydroperoxide decomposition products, including *n*-propylhydroperoxide (*n*-C_3H_7OOH).

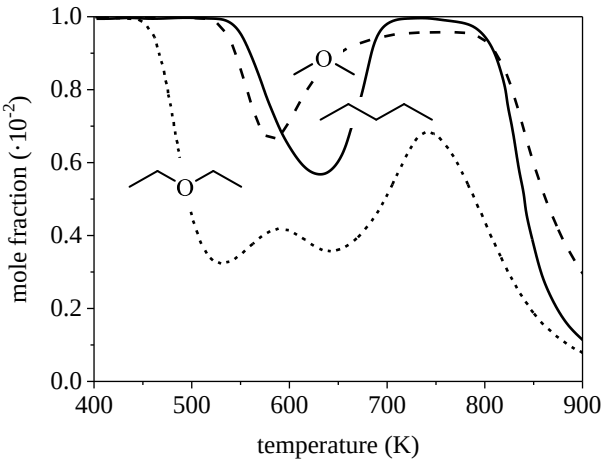

Figure 91. Species profiles of diethyl ether, dimethyl ether, and *n*-pentane oxidation predicted using the mechanism of Tran et al. [898]. Simulation conditions: initial concentration = 1000 ppm, residence time of 2000 ms, pressure of 1 atm, and equivalence ratio $\phi = 1.0$.

Cai et al. [797] and Thion et al. [798] independently developed chemical kinetics mechanisms for di-*n*-butyl ether oxidation. The former contains 2335 reactions and 426 species; the latter, 2732 reactions and 436 species. Ignition delay times were simulated in Cai et al. [797] and compared to alcohols (1-butanol and 1-pentanol) and to *n*-octane. The di-*n*-butyl ether ignition trends showed clear NTC behavior, more pronounced than 1-butanol or 1-pentanol, and were shorter than those for *n*-octane [797]. Al Rashidi et al. [944] calculated high-pressure limit rate coefficients from 300 – 2500 K for reactions of di-*n*-butyl ether radicals using the CBS-QB3 and G4 composite methods. Several reaction classes were considered, two of which are relevant for low-temperature conditions: isomerization reactions of Ṙ (i.e. intramolecular H-

migration) via 5-, 6-, and 7-membered transition states, and C–C and C–O β-scission of Ṙ. The authors placed emphasis on determining the applicability of estimating rate coefficients for ether reactions using analogous reactions in alkanes and alcohols and, in certain cases, analogies were deemed inappropriate including scission of C–C bonds adjacent to the –O– group. ROȮ → ȮOOH rates of α radicals were 10^2 – 10^3 lower than those for secondary *n*-octyl radicals due to higher barrier heights.

Only a limited number of detailed mechanisms exist for branched acyclic ethers. Goldaniga et al. [915] developed sub-mechanisms for several branched ethers using rate rules and incorporated these into a primary reference fuel mechanism. Using EXGAS, Glaude et al. [916] reported a chemical kinetics mechanism for methyl- and ethyl-*tert* butyl ether and simulated speciation measurements from several flow reactor experiments, including the time-dependent profiles from Norton and Dryer [496]. Yasunaga et al. [945] reported a combined mechanism for several branched species, including ethyl methyl ether, methyl *tert*-butyl ether, and ethyl *tert*-butyl ether. However, reactions relevant to low-temperature chemistry, namely ȮOOH formation, cyclic ether formation, and second-O_2-addition were neglected. Chain-inhibition reaction leading to HOȮ were included. The mechanism was utilized to simulate speciation measurements obtained via gas chromatography analysis of gases extracted from a shock tube.

3.4.5. summary of ether functional group effects

Despite relatively simple molecular structure, acyclic ethers undergo complex oxidation mechanisms due in part to facile C–O bond-scission reactions in Ṙ and ȮOOH radicals, which compete with O_2-addition, and to reduced bond dissociation energies for C–H adjacent to the ether group that affect initiation and isomerization reactions. **Figure 92** summarizes the low-temperature chain-branching scheme augmented to emphasize pathways attributed to the ether functional group. The ether group reduces C–H bond energy on α carbon by ~3 – 4 kcal/mol compared to analogous (secondary) carbon in alkanes. For all ethers, linear and branched, H-abstraction by ȮH is site-selective, and reactions with HOȮ occur predominantly from α carbon. In the case of dimethyl ether, only α radicals are possible. Branching fraction calculations for ȮH-initiated H-abstraction from diethyl ether indicate that both α and β radicals are relevant, while for branched ethers the formation of α radicals is favored because of tertiary carbon adjacent to the ether group.

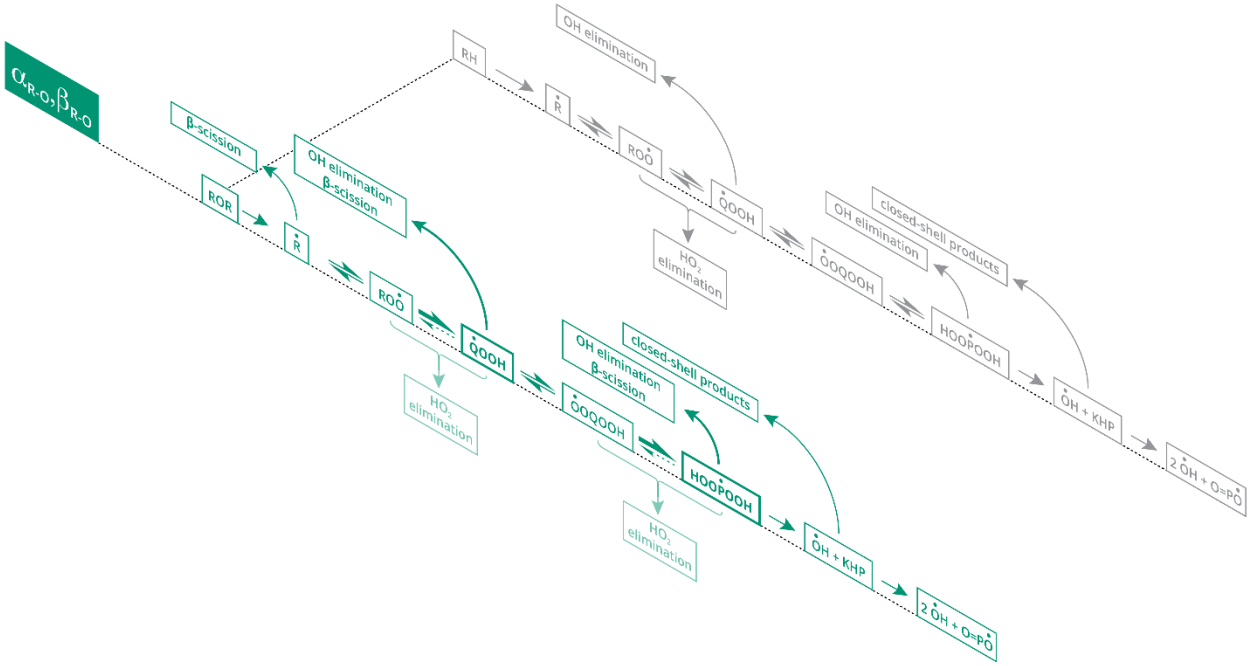

Figure 92. Summary of ether functional group effects in acyclic species on low-temperature chain-branching. The leftward-pointing and downward-pointing arrows indicate a shift in flux away from chain-branching pathways responsible for ignition. Because the –O– group cannot transfer a hydrogen to the radical site in the ROȮ or ȮOQOOH radicals, chain-inhibiting HOȮ elimination is less important for ethers. Dissociation at the –O– site to form carbonyls can lead to chain-propagation. Each type of initial radical is depicted in a separate plane, with different colors used to guide the eye. The alkane oxidation mechanism is depicted in the back plane for reference. Pathways that are enhanced by the effects of the functional group are emphasized with bold arrows and labels, and those that are diminished are made lighter or omitted.

Compared with ȮH + propane, rate coefficients for ȮH + dimethyl ether are similar below 1000 K (larger by ~65% at 500 K). Depending on the level of theory employed, transition states for both in-plane (direct) abstraction and out-of-plane (pre-reaction complex-mediated) abstraction may contribute. Regardless of the choice of including a pre-reaction complex, i.e. using a single- or two-transition-state model, rate coefficient calculations are largely consistent across several computational studies and are in remarkable agreement with experiment – within 50% over the range of temperatures relevant to low-temperature oxidation. Measurements of rate coefficients for ȮH + diethyl ether are reported only at temperatures below 450 K, with the exception of a single measurement at 753 K and, in the 500 – 1000 K range, are larger by a factor of ~2 compared with ȮH + *n*-pentane. Calculations of the total rate coefficient for ȮH + diethyl ether using group rate expressions, derived in part using transition state theory, are consistent with measurements.

Reactions of O_2 with $\dot{C}H_2OCH_3$ radicals produced from dimethyl ether form either a vibrationally excited complex (ROȮ)*, which can directly yield $CH_2O + CH_2O + \dot{O}H$, or a collisionally stabilized peroxy radical adduct. The formation of stabilized methoxymethyl-peroxy ($\dot{O}OCH_2OCH_3$) dominates below ~650 K, above which direct formation of $CH_2O + CH_2O + \dot{O}H$ becomes competitive due to facile C–O bond scission, along with the reverse reaction back to the reactants ROȮ → Ṙ + O_2. Second-O_2-addition of ȮOOH from dimethyl ether oxidation are favored over unimolecular decomposition to 1,3-dioxetane + ȮH. However, ȮOOH → $CH_2O + CH_2O + \dot{O}H$ is important and pressure-dependent calculations indicate that, above 500 K, the reaction is not in the high-pressure limit at 40 atm. Isomerization of ȮOQOOH in dimethyl ether

yields the ketohydroperoxide species hydroperoxymethyl formate, which may decompose via the Korcek mechanism or several other pathways (cf. **Figure 77**), producing formic acid, formic anhydride, CO, or performic acid. No experimental evidence of carbonyl oxide Criegee intermediate, formed coincident with formic acid via hydroperoxymethyl formate, is reported.

While ȮOOH → cyclic ether + ȮH is unimportant in dimethyl ether oxidation, because larger alkyl substituents enable facile RO$\dot{O}$ → ȮOOH isomerization, reactions that lead to cyclic ether formation are possible. Quantum chemical calculations indicate two distinguishing characteristics attributable to the ether group. Rates for RO$\dot{O}$ → ȮOOH via 6-membered transition state in diethyl ether, when the –O$\dot{O}$ and unpaired electron occupy opposing α sites, are higher by a factor of ~10 than for the analogous alkane reaction. Similarly, for β-ȮOOH in diethyl ether, decomposition into 2-ethoxyoxirane + ȮH is a factor of 10 higher below 1000 K than for the analogous process in pentane oxidation that produces *n*-propyl oxirane + ȮH. In both cases, the ether functional group facilitates the reaction. ȮOQOOH → HOOP$\dot{O}$OH isomerization rates are more complex and depend on the relative location of the –O$\dot{O}$ and –OOH groups. Barrier heights for reactions leading to the radical precursor for ketohydroperoxide are lower compared to alkanes, whereas barrier heights are higher for other isomerization reactions.

Ignition delay times for linear ethers are shorter compared to alkanes and exhibit clear NTC behavior. For species larger than dimethyl ether, namely diethyl ether and di-*n*-butyl ether, two distinct NTC regions that are separated by ~125 K are evident in species profile measurements. Multiple ignition stages are also evident in RCM experiments of di-*n*-butyl ether. The first NTC region is due to diminished second-O_2-addition reactions, rather than suppressed ȮOOH formation, and the increase in reactivity above the first NTC region in di-*n*-butyl ether is in part driven by secondary oxidation of the propyl radical products of KHP dissociation. The second NTC region is due to facile C–O bond-scission causing a reduction in the flux towards first-O_2-addition reactions of diethyl ether radicals, which otherwise may form ȮOOH. The net effect is inhibited chain-branching near ~750 K and 1 atm.

3.5. cyclic ethers

Understanding low-temperature oxidation kinetics of cyclic ethers is relevant to two areas of combustion chemistry. First, owing to advances in catalysis and synthetic chemistry, cyclic ethers including tetrahydrofuran [209, 244, 262, 267, 280], 2-methyltetrahydrofuran [115, 209, 244, 261, 262, 267, 280-285], 3-methyltetrahydrofuran [209, 261, 282], 2,5-dimethyltetrahydrofuran [209, 262, 277, 278, 281], 2-butyltetrahydrofuran [213, 292], and tetrahydropyran [286] may substantively contribute to sustainable energy objectives. Second, cyclic ethers are also primary intermediates [430, 946, 947] in low-temperature alkane oxidation formed coincident with ȮH via unimolecular Q̇OOH decomposition in a chain-propagating step [87, 595, 948, 949]. **Figure 93** shows the molecular structure of four representative cyclic ethers: tetrahydrofuran, 2-methyltetrahydrofuran, 3-methyltetrahydrofuran, and tetrahydropyran. The presence of the ether group creates distinct H-abstraction sites, e.g. α, β, and γ. The prime notation in **Figure 93** indicates carbon on the side of the ring where the substituent is located. Because of the electronegativity of the –O– group, C–H bond dissociation energy on secondary α carbon is lowered by approximately 4 – 5 kcal/mol relative to secondary carbon in alkanes [950-953]. For tertiary α' carbon, as in **Figure 93b**, the effect is smaller: ~2 kcal/mol [952-954]. However, unlike in ketones or ethers where the carbonyl group introduces resonance stabilization into initial α radicals, the well-depth of the adduct from $\dot{R} + O_2$ reactions in ethers is similar to that of alkylperoxy radicals (~36 kcal/mol) [951]. One important effect of the –O– group is a reduction in the C–H bond energy of α carbon, which results in a favoring of α radicals formed during the initiation step via abstraction by ȮH and HOȮ, among other radicals. As a result, subsequent reactions of α radicals play a central role in oxidation reactions of cyclic ethers.

(a) tetrahydrofuran (b) 2-methyltetrahydrofuran (c) 3-methyltetrahydrofuran (d) tetrahydropyran

Figure 93. Molecular structure of (a) tetrahydrofuran, (b) 2-methyltetrahydrofuran, (c) 3-methyltetrahydrofuran, and (d) tetrahydropyran with H-abstraction sites labeled. The –O– group reduces C–H bond energy on adjacent (α and α') carbon relative to secondary carbon in alkanes [950-953], while β and γ C–H energies are similar to analogous bonds in alkanes.

The sections below are separated into four main parts, divided according to ring size and number of substituents: tetrahydrofuran (*Section 3.5.1*), mono-substituted tetrahydrofuran (*Section 3.5.2*), di-substituted tetrahydrofurans, and tetrahydropyran (*Section 3.5.3*). Only one di-substituted tetrahydrofuran species is discussed, 2,5-dimethyltetrahydrofuran (*Section 3.5.4*), as no studies exist on 2,3-dimethyltetrahydrofuran or other isomers. As a subset of cyclic ethers, furans (*Section 3.5.5*) are also reviewed to the extent that low-temperature oxidation chemistry is concerned. For each section, initiation reactions by ȮH and HOȮ are discussed, followed by reaction mechanisms of initial radicals with O_2 from speciation experiments, then ignition delay times and chemical kinetics mechanisms.

3.5.1. tetrahydrofuran

Giri et al. [955] employed UV laser-absorption diagnostics in shock tube experiments to measure total rate coefficients for H-abstraction from tetrahydrofuran by ȮH from 800 – 1340 K and ~1.5 atm. The experiments were complemented using a coupled cluster quantum chemical method, CCSD(T)/cc-pV(D,T)Z//MP2/aug-cc-pVDZ, which identified both direct and indirect abstraction pathways – the latter involving formation of a pre-reaction complex formed via hydrogen bonding to the –O– group. The *ab initio* results indicated that both pathways were relevant at combustion conditions (**Figure 94**). At the lower end of temperature (800 K), branching towards α radicals was favored (α:β ~2:1) owing to reduced C–H bond energies [950-953] while towards the higher end (1200 K), α:β ~1:1. Rate coefficient measurements in other studies of ȮH + tetrahydrofuran → H_2O + Ṙ cover a lower temperature range of 263 – 400 K [822, 826, 956-958].

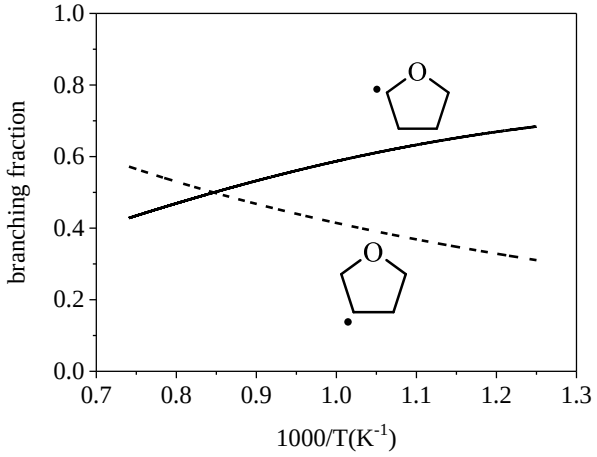

Figure 94. Branching fractions of α and β tetrahydrofuranyl radicals from Giri et al. [955].

Figure 95 compares high-pressure limit rate coefficients for H-abstraction from tetrahydrofuran via ȮH, from Giri et al. [955], and via HOȮ [959] with analogous reactions for cyclopentane [768]. The Fenard et al. [959] mechanism estimated the rate parameters for reaction with HOȮ based on similar calculations for 2-methyltetrahydrofuran and 2,5-dimethyltetrahydrofuran in Chakravarty and Fernandes [80]. The Sarathy et al. [768] mechanism utilized the ȮH + cyclopentane rate from Sivaramakrishnan and Michael [746] and rate rules [960] for HOȮ + cyclopentane. For both radicals, as evident in **Figure 95**, rate coefficients for abstraction are higher for tetrahydrofuran. For example, at 700 K, the difference is a factor of ~3 for ȮH and a factor of ~5 for HOȮ. Unlike for alkanes and some oxygenated biofuels, direct calculations of HOȮ + tetrahydrofuran are not reported, which is notable given the significance of HOO-elimination reactions [959, 961].

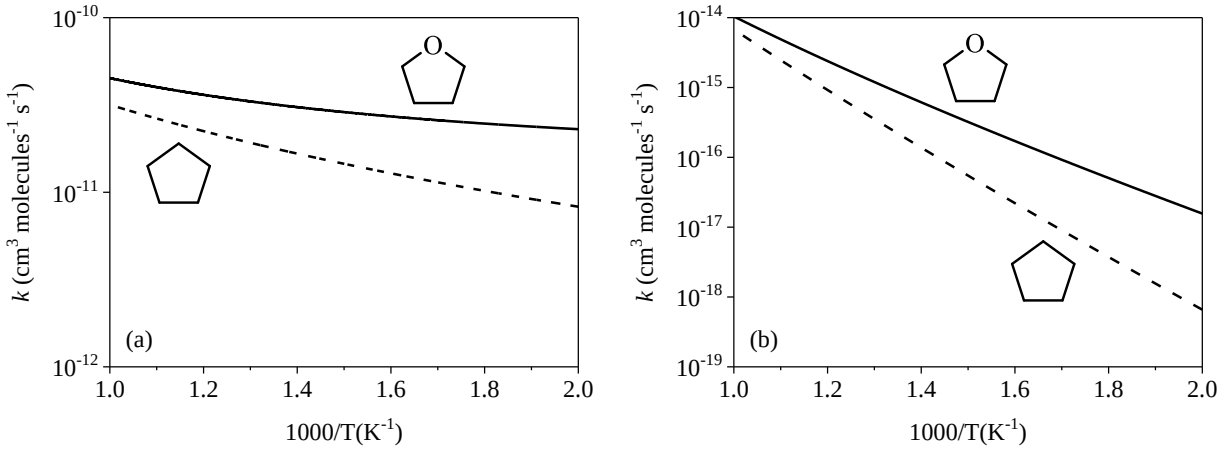

Figure 95. (a) Rate coefficients for H-abstraction by ȮH from Giri et al. [955] (tetrahydrofuran) and from Sarathy et al. [768] (cyclopentane). (b) Rate coefficients for H-abstraction by HOȮ from Fenard et al. [959] (tetrahydrofuran) and from Sarathy et al. [768] (cyclopentane).

Product formation from MPIMS experiments on Ṙ + O_2 reactions of tetrahydrofuran were conducted in Antonov et al. [961] at temperatures from 400 – 700 K and pressures of 10 – 2000 Torr. Ring-opening of initial α-tetrahydrofuranyl radicals became relevant near ~650 K, evident from propene formation via oxidation of *n*-propyl (**Figure 96**). In comparison to other reaction pathways, however, ring opening of initial radicals remained a minor channel. The majority of the products identified were derived from O_2-addition to the α radical and from second-O_2-addition to $\alpha\alpha'$-ȮOOH radicals. The main products confirmed via photoionization spectra were butanedial (+ ȮH), 2,3-dihydrofuran (+ HOȮ), γ-butyrolactone-5-hydroperoxide (+ ȮH), and 2-hydroperoxy-2,3-dihydrofuran (+ HOȮ). The latter two are formed via unimolecular decomposition of ȮOQOOH (**Figure 97**) and inhibit chain-branching.

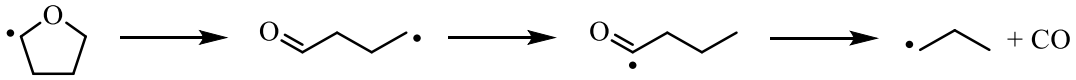

Figure 96. Ring-opening mechanism of tetrahydofuran-2-yl proposed in Antonov et al. [961] leading to the formation of propene via oxidation of *n*-propyl. The linear radical butan-4-yl-1-al isomerizes via a 5-membered transition state into butan-1-yl-1-al, which subsequently undergoes C–C β-scission to form *n*-propyl and CO.

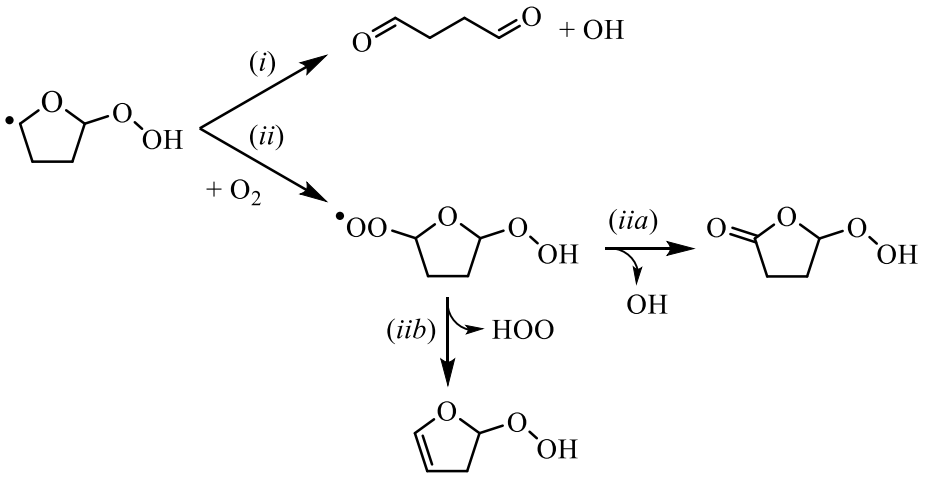

Figure 97. ȮOOH reaction pathways proposed from MPIMS experiments of Antonov et al. [961] on tetrahydrofuran oxidation: (i) ring-opening to butanedial + ȮH, (ii) second-O_2-addition leading either to (iia) γ-butyrolactone-5-hydroperoxide + ȮH or (iib) 2-hydroperoxy-2,3-dihydrofuran + HOȮ.

The identification of 2-hydroperoxy-2,3-dihydrofuran in **Figure 97** involves a previously undiscovered reaction pathway, which is effectively chain-inhibiting due to coincident HOȮ formation, and is relevant because ketohydroperoxide formation is diminished despite second-O_2-addition occurring. To quantify the significance of the ȮOQOOH → alkene + HOȮ reaction, rate coefficients were calculated in [961] with the MESS code [962], using CBS-QB3 energies, geometries and frequencies and B3LYP/6-311G(2*d*,*d*,*p*) to map 1-D hindered rotor potentials. Tunneling effects were accounted for using Eckart corrections. The results showed that 2-hydroperoxy-2,3-dihydrofuran is favored by ~4:1 over γ-butyrolactone-5-hydroperoxide at 400 K and by ~10:1 at 700 K.

Hansen et al. [342] utilized a JSR and molecular beam photoionization mass spectrometry (MBMS) to conduct tetrahydrofuran oxidation experiments, at 1 atm, and reported the first isomer-resolved detection of ketohydroperoxides. On the basis of photoionization spectra measurements, as well as *ab initio* calculations of ionization energies and appearance energies of cations formed from the loss of neutral OOH groups, four isomers were identified (**Figure 98**). Of the six isomers possible – three from each of the two initial α and β radicals – two were ruled out based on an absence of discernable spectral features in the measured ion signal. For the four isomers that were detected, quantum chemical calculations of photoionization cross-sections, using the methodology of Moshammer et al. [852], provided for quantification of ketohydroperoxide mole fractions, which reached a maximum at ~575 K. Using the first-generation chemical kinetics mechanism of Fenard et al. [959], mole fraction predictions for major species (isomers (a) and (b) in **Figure 98a**, derived from α-tetrahydrofuranyl) were remarkably consistent with the measurements. However, mole fractions of ketohydroperoxides produced from β-tetrahydrofuranyl (isomers (c) and (d) in **Figure 98**), which were ~10^2 lower than species from α-tetrahydrofuranyl, were underpredicted by at least 10^4. Because, as a class of molecules, direct experiments are difficult to conduct on ketohydroperoxides, the disparities may arise from incomplete understanding of decomposition mechanisms and associated rate parameters, inaccurate thermochemistry of the species involved, experimental issues with quantifying species that are formed in low concentrations, or in the case of photoionization detection, the theoretical methods by which cross-sections are calculated.

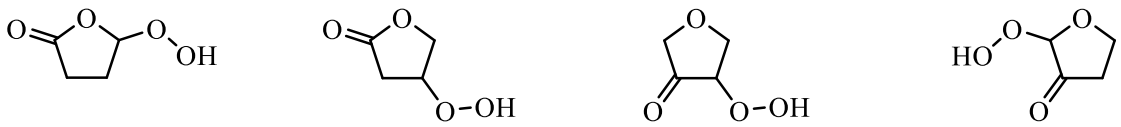

(a) (b) (c) (d)

Figure 98. Ketohydroperoxide isomers of tetrahydrofuran detected in Hansen et al. [342]. Isomers (a) and (b) are derived from oxidation of initial α-tetrahydrofuranyl radicals, while (c) and (d) are produced from β-tetrahydrofuranyl radicals.

Speciation measurements of tetrahydrofuran oxidation are reported from thermally initiated flow reactors [342, 959, 963-966] and from an RCM [965]. Molera et al. [963] conducted experiments using a static reactor operated at 473 K and 156 Torr. The majority of products were identified using gas chromatography, with the exception of H_2O_2 and organic hydroperoxides (ROOH), which were quantified using thin-layer chromatography. Primary products, formed in the initial stages of oxidation, were identified by molar ratios relative to the percent consumption of tetrahydrofuran and included CH_2O, CH_3CHO, CO, and hydroperoxides. Succinic acid was reported as a primary product and proposed to arise from ring-opening of HOOṖOOH species, where the peroxy and hydroperoxy groups are bonded to opposing α carbon [963]. An alternative water-catalyzed mechanism was also postulated: succinic anhydride + H_2O → succinic acid. However, noting that succinic acid is an oxidation product of butanedial, formed via ȮOOH ring-opening, secondary reactions involving the aldehyde may also contribute.

Dagaut [964] employed JSR experiments under dilute conditions (N_2 >98%) to measure mole fractions of products from tetrahydrofuran oxidation at 10 atm from 800 – 1100 K at a residence time of 500 ms. 2,3-dihydrofuran and 2,5-dihydrofuran, both formed coincident with HOȮ via Ṙ + O_2, were detected only in trace amounts. Neither species were detected in Molera et al. [963] either, although furan was quantified (~2% of product formation). Vanhove et al. [965] conducted speciation measurements utilizing both a JSR, with dilution of N_2 ~90%, and an RCM, operated under non-dilute conditions (N_2 ~76%). In the majority of cases, both sets of measurements qualitatively detected the same species, with several notable exceptions including allyl formate (CHO–O–CH_2CH=CH_2) and butanedial – both of which were detected only in the RCM measurements and ascribed to ring-opening of either ȮOOH or bicyclic ethers. As noted in Antonov et al. [961], butanedial is a major product of unimolecular ȮOOH decomposition owing to favorable energetics on the respective Ṙ + O_2 potential energy surface and to exclusive involvement of labile α radicals.

Belhadj et al. [966] conducted JSR experiments on tetrahydrofuran from 550 – 620 K at a residence time of 2000 ms, using a dilution level of N_2 ~94%, and focused on the detection of products from successive O_2-addition. Gas-phase species extracted from the reactor were condensed in acetonitrile for subsequent analysis via liquid chromatography and tandem mass spectrometry (MS/MS). Species were reported qualitatively and included ketodihydroperoxides, formed via third-O_2-addition. Other species included hydroperoxides (ROOH), dihydroperoxides, diols, and dicarbonyls. The latter species may arise from ketohydroperoxide decomposition. The majority of the species identified are not included in the mechanism of Fenard et al. [959].

Dagaut [964] reported the first detailed chemical kinetics mechanism for tetrahydrofuran, which focused on high-temperature oxidation pathways and, consequently, excluded peroxy radical chemistry. In a similar

vein, Tran et al. [967] developed a detailed mechanism for predicting species profiles in tetrahydrofuran flames. Fenard et al. [959] developed the first mechanism for tetrahydrofuran to include low-temperature chemistry of peroxy radicals. Ring-opening reactions of ȮOOH (**Figures 97 and 99**) were accounted for and rate parameters for both the ȮOQOOH-related kinetics reported in Antonov et al. [961] and for the ring-expansion reactions of ȮOOH in **Figure 100** were included. The latter reaction mechanism was postulated initially in Vanhove et al. [965]. High-pressure-limit rate coefficients were calculated in Fenard et al. [959] at the CBS-QB3 level of theory for RO$\dot{O}$ → Ȯ$\dot{O}$OH isomerization, concerted $\dot{R}$ + O_2 → alkene + HO$\dot{O}$ reactions, and unimolecular Ȯ$\dot{O}$OH decomposition reactions forming alkene + HO$\dot{O}$ and cyclic ether + $\dot{O}$H. The results were compared with alkane rate rules from Cai et al. [968] and differed appreciably, in several cases by ~10^1 – 10^2. In particular, rates for RO$\dot{O}$ → Ȯ$\dot{O}$OH isomerization via both 5-membered and 6-membered transition states and Ȯ$\dot{O}$OH → 3,4-epoxytetrahydrofuran + $\dot{O}$H deviated from rate rules.

Fenard et al. [959] noted that the predictions by the mechanism were sensitive to Ȯ$\dot{O}$OH branching fractions, i.e. the ratio of unimolecular decomposition rates to second-O_2-addition rates. The conclusion was drawn from the observation that adjustments in rate parameters related to Ȯ$\dot{O}$OH led to improved predictions of species profiles, but to the detriment of ignition delay time predictions. The uncertainty in Ȯ$\dot{O}$OH chemistry suggests an incomplete description of the underlying kinetics in one or both of the reaction channels. Notably, two of the major Ȯ$\dot{O}$OH ring-opening products – butanedial (**Figure 97**) and allyl formate (**Figure 99**) – were not quantified, which may add to the level of uncertainty. Several other species detected from the JSR experiments in Vanhove et al. [965], such as propanal and oxirane, exhibited significant formation near 600 K indicating a connection to low-temperature chemistry, yet were not reproduced by the chemical kinetics mechanism.

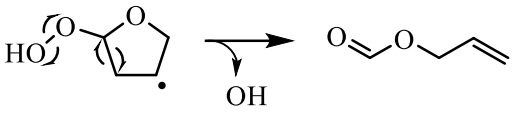

Figure 99. Ȯ$\dot{O}$OH ring-opening mechanism leading to allyl formate detected in Vanhove et al. [965].

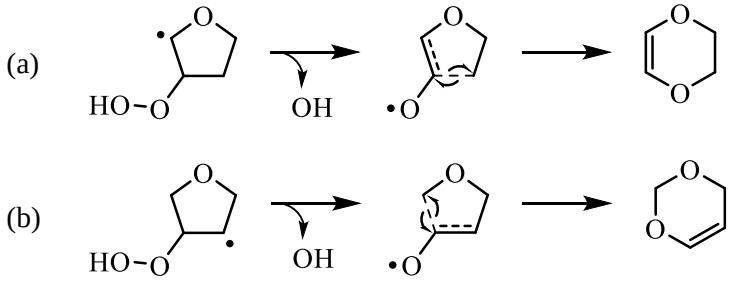

Figure 100. Ȯ$\dot{O}$OH ring-expansion mechanisms leading to (a) 1,3-dioxene and (b) 1,4-dioxene postulated in Fenard et al. [959] for 1,4-dioxene observed in Vanhove et al. [965].

Wu et al. [969] expanded on the mechanism of Fenard et al. [959] by combining sub-mechanisms for furan from Tran et al. [970] and 2,3-dihydrofuran from Fan et al. [971]. In addition, thermochemistry and rate parameters were added to describe reactions of 2,3-dihydrofuranyl radicals with O_2 to reconcile ignition delay time predictions. In Fenard et al. [959], both α and β isomers of 2,3-dihydrofuranyl exclusively yield furan + HO$\dot{O}$ upon reaction with O_2. Wu et al. [969] included O_2-addition to 2,3-dihydrofuranyl, isomerization of RO$\dot{O}$ adducts to Ȯ$\dot{O}$OH, unimolecular decomposition of Ȯ$\dot{O}$OH into cyclic ether + $\dot{O}$H,

and disproportionation the cyclic ether (2,6-dioxabicyclo[3.1.0]hex-3-ene) with ȮH to produce formyl + prop-1-en-1-yl-3-al (ĊHCHCH=O). The contrast in ignition delay time predictions between Fenard et al. [959] and Wu et al. [969] highlights the effect of sub-mechanisms for primary intermediates [428-430], which are commonly excluded from detailed chemical kinetics mechanism development. Ignition delay time predictions using the latter, expanded mechanism [969] were shorter and became consistent with RCM measurements below 700 K.

Measurements of tetrahydrofuran ignition delay times include the high-pressure shock tube experiments of Uygun et al [972] (691 – 1100 K; 20 and 40 atm), RCM experiments of Vanhove et al. [965] (640 – 900 K; 5 and 10 atm), and RCM experiments of Wu et al. [969] (680 – 905 K; 18 atm). The 20-atm results from [972] are plotted in **Figure 101a** against cyclopentane ignition delay times from Sarathy et al. [553]. While NTC behavior is evident in cyclopentane from ~750 – 825 K, the lower limit of temperature in Uygun et al [972] prevents a similar assessment for tetrahydrofuran. Within the range of overlapping temperature, ignition delay times are appreciably shorter for tetrahydrofuran than for cyclopentane: 4 ms compared to 225 ms at 780 K (1000/T = 1.28 K^{-1}).

Stoichiometric ignition delay time simulations were conducted in the present review using the mechanism of Fenard et al. [959] and compared to a recent mechanism for cyclopentane [553] at an initial pressure of 20 atm and with an N_2 mole fraction of ~0.76 (**Figure 101b**). In both cases, ignition was defined using the method of steepest ascent [361] applied to ȮH time histories, which were modeled using isobaric conditions with the 0D homogeneous reactor module in ChemKin. For simplicity, facility effects are neglected in the model predictions in **Figure 101b**, which contributes to any quantitative discrepancies with experiment. Similar to the experimental trends, NTC behavior, which is indicative of peroxy radical-mediated chemistry, is more prominent in cyclopentane than in tetrahydrofuran. In addition to the NTC difference, predicted ignition delay times for the cyclic ether are ~10^1 shorter than for the cycloalkane below ~800 K.

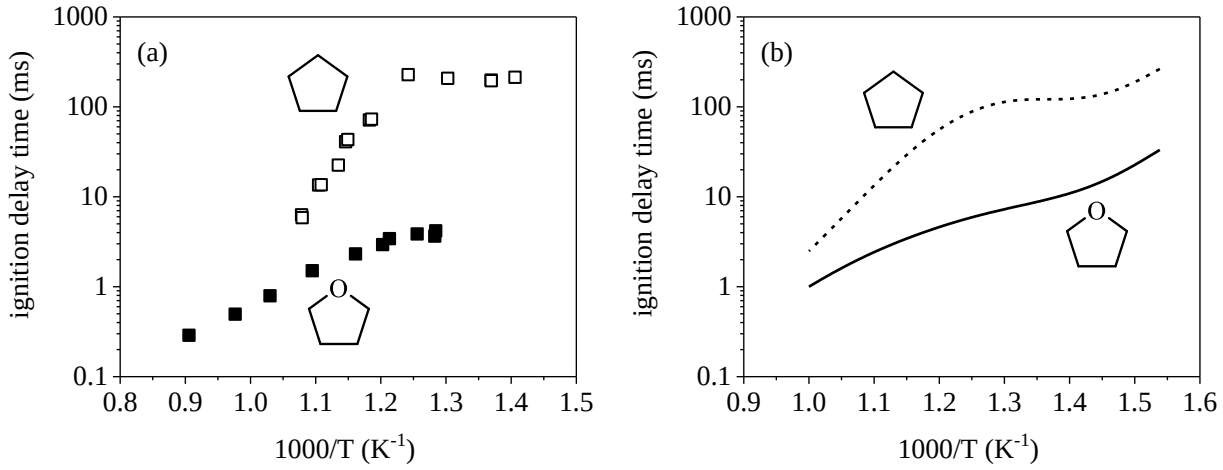

Figure 101. (a) Ignition delay time measurements of tetrahydrofuran (Uygun et al. [972]) and cyclopentane (Sarathy et al. [553]). (b) Predictions using chemical kinetics mechanisms of Fenard et al. [959] (tetrahydrofuran) and Sarathy et al. [959] (cyclopentane). 20 atm, ϕ = 1.0. N_2 mole fraction ~0.76.

The trends reflected in both the experimental and model-predicted ignition delay times in **Figure 101** suggest that second-O_2-addition and related decomposition steps are more facile in tetrahydrofuran and, in addition, raises questions as to the role of products formed via Ṙ or Q̇OOH ring-opening [309, 522, 951,

961]. In addition to mechanistic explanations, larger rate coefficients for H-abstraction by ȮH and HOȮ (cf. **Figure 95**) may play a role in facilitating shorter ignition delay times by contributing to higher rates of initiation reactions. NTC behavior, evident in cyclopentane ignition, results from combined effects of back dissociation of ROȮ into Ṙ + O_2 and a shift in the flux of remaining ROȮ radicals away from chain-branching and towards chain-inhibiting and chain-propagating pathways. Concerning the weak NTC region of tetrahydrofuran, potential causes may include: (1) favoring of products in Ṙ + O_2 ⇌ ROȮ equilibria, (2) facile ring-opening of tetrahydrofuranyl radicals reducing chain-propagation from first-O_2-addition, and (3) higher rates of HOO-elimination. For the latter type of reaction, several mechanisms are possible – direct elimination (Ṙ + O_2 → conjugate alkene + HOȮ), concerted elimination (ROȮ → conjugate alkene + HOȮ), or sequential elimination (ROȮ → ȮOOH → conjugate alkene + HOȮ).

Using rate parameters from the mechanism for tetrahydrofuran from Fenard et al. [959] and for cyclopentane from Al Rashidi et al. [768], rates for all three types of HOO-elimination in the high-pressure limit are compared in **Figure 102**. Fenard et al. [959] employed CBS-QB3 for electronic structure calculations canonical transition state theory with asymmetric Eckart potential for tunneling corrections, while Al Rashidi et al. [768] used UCCSD(T)-F12a/cc-pVTZ-F12//M06-2X/6-311++G(*d*,*p*) and the MESS code [962] for rate calculations. The largest difference between the two systems is in the direct pathway (**Figure 102a**), where the rate of α-tetrahydrofuranyl + O_2 → 2,3-dihydrofuran + HOȮ is more than an order of magnitude higher than for cyclopentyl + O_2 → cyclopentene + HOȮ up to 1000 K; approximately 10^3 at 500 K and ~10^2 at 750 K. For other HOO-elimination pathways, the differences are smaller or within the uncertainty of the computational method. **Figure 102b** compares rates of concerted HOO-elimination from cyclopentyl peroxy and from α-tetrahydrofuranyl peroxy, which are similar over the range relevant to low-temperature combustion. The effect of the ether group on rates of sequential HOO-elimination depends on the location of the hydroperoxy group. Compared to cyclopent-1-yl-2-hydroperoxy, the rate for tetrahydrofuran-2-yl-3-hydroperoxy is similar up to ~900 K (**Figure 102c**) and is lower for tetrahydrofuran-3-yl-2-hydroperoxy (**Figure 102d**). The net effect of higher HOO-elimination rates for tetrahydrofuran, largely derived from the direct HOO-elimination pathway, may lead to a more rapid accumulation of hydrogen peroxide via HOȮ + RH → H_2O_2 + Ṙ that provides accelerated intermediate-temperature chain-branching from thermal decomposition of H_2O_2.

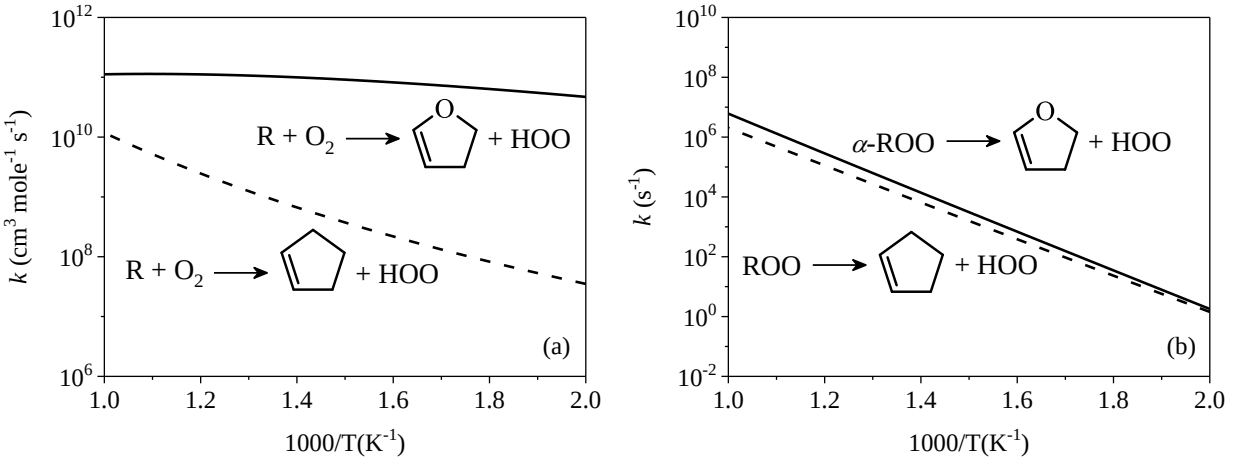

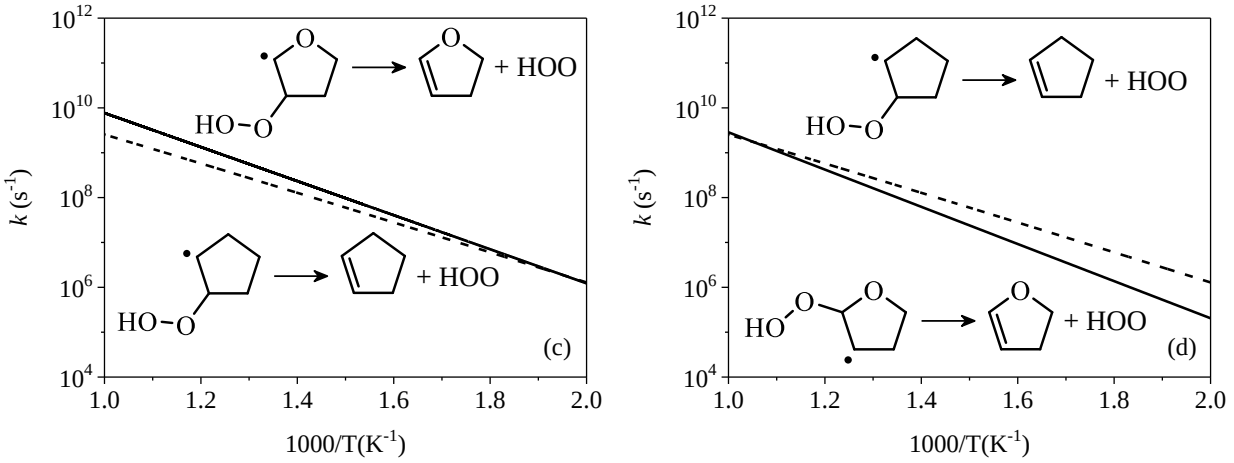

Figure 102. Comparison of high-pressure-limit rate coefficients for HOO-elimination from oxidation of α-tetrahydrofuranyl and cyclopentyl using rates from Fenard et al. [959] and Al Rashidi et al. [768], respectively.

3.5.2. monosubstituted tetrahydrofuran

Low-temperature oxidation studies of monosubstituted tetrahydrofuran include 2-methyltetrahydrofuran [80, 954, 973-975], 3-methyltetrahydrofuran [976, 977], and 2-butyltetrahydrofuran [968]. The sections below are separated by individual species. Initiation reactions are reviewed first, followed by reaction mechanisms of initial radicals with O_2. Ignition delay times and mechanism-based predictions are then discussed.

Chakravarty and Fernandes [80] calculated site-specific high-pressure-limit rate coefficients for H-abstraction reactions HOȮ + 2-methyltetrahydrofuran → H_2O_2 + Ṙ from 500 – 2000 K. The total rate coefficient displayed significant method dependence from the two different levels of theory employed: the composite CBS-QB3 method and a coupled cluster method, CCSD(T)/cc-pVTZ//B3LYP/cc-pVTZ. CBS-QB3 produced rate coefficients that were $>10^2$ larger compared with the coupled cluster method, due to the former predicting a lower activation energy (by ~4 kcal/mol). In order to assess the influence of the ether group, rate coefficients were also calculated in [80] for HOȮ + methylcyclopentane → H_2O_2 + Ṙ, using CBS-QB3. Rate coefficients for H-abstraction were higher in the case of 2-methyltetrahydofuran by ~4.4 at 750 K and ~1.9 at 1000 K. Site-specific k(T) were also calculated. Comparisons to methylcyclopentane revealed that rate coefficients were similar for H-abstraction from primary carbon (i.e. from the $–CH_3$ group), slightly lower in 2-methyltetrahydrofuran for abstraction from a secondary carbon adjacent to the $–CH_3$ group (i.e. β'), and higher by $>10^1$ for tertiary abstraction (i.e. α').

Branching fractions calculated in Chakravarty and Fernandes [80] indicated, using both levels of theory, that the principal hydrogen-abstraction site below 900 K is α and α' carbon, mainly the latter, and abstraction from β and β' carbon is negligible. However, while both methods are consistent in predicting the main channel, a dependence on computational method was evident in the branching fractions of secondary α carbon (opposite from the location of the $–CH_3$ group). For both computational methods, *cis*-/*trans*- conformations of HOȮ and $–CH_3$ groups in the transition state influenced abstraction from (secondary) α carbon. Using CBS-QB3, H-abstraction from the secondary α carbon on the *trans*- isomer was nearly 10^1 lower relative to the *cis*- isomer over the temperature range covered. Using the coupled

cluster method, however, the difference was less than a factor of 2 below 1000 K. For both methods, abstraction from the $–CH_3$ group became relevant (>10% of the branching fraction) only above ~900 K.

High-pressure-limit rate coefficients were calculated using transition state theory for ROȮ → ȮOOH isomerization reactions in 2-methyltetrahydrofuran at the CBS-QB3 level in Parab et al. [973]. The calculations included *cis*- and *trans*- isomers for all ROȮ radicals and branching fractions showed ROȮ-isomer-specific rates. For example, in isomerization reactions of α-ROȮ, the *trans*- isomer exclusively formed α'-ȮOOH over the 500 – 2000 K temperature range, while the *cis*- isomer formed several ȮOOH isomers including β-ȮOOH, β'-ȮOOH, and γ-ȮOOH.

Three detailed chemical kinetics mechanisms exist for 2-methyltetrahydrofuran [954, 974, 975], two of which contain peroxy radical chemistry [954, 974]. Utilizing rate coefficients for HOȮ + 2-methyltetrahydrofuran → H_2O_2 + Ṙ from Chakravarty and Fernandes [80], Fenard et al. [974] developed a chemical kinetics mechanism (507 species, 2425 reactions) and simulated speciation measurements from an RCM, in addition to ignition delay times from 640 – 900 K and from 3 – 20 atm. Reaction pathway analysis indicated that the tertiary α' radical predominately reacts with O_2, undergoing chain-inhibiting reactions that form HOȮ coincident with 5-methyl-2,3-dihydrofuran or 2-methylenetetrahydrofuran. The same analysis indicated that the secondary α radical proceeds via addition reactions with O_2 to form a stabilized peroxy radical, which subsequently reacts via unimolecular decomposition or second O_2-addition. β radical isomers were ~20% of the initial radical population and reacted with O_2 to form peroxy radicals. Similar to Fenard et al. [974], the mechanism of Tripathi et al. [954], developed using 250 species and 2494 reactions, predicts ~10% of α radicals undergo ring-opening at 650 K, with the remainder reacting with O_2. At 1100 K, ring-opening became the primary reaction path. For tertiary α' radicals, ring-opening reactions were slightly higher (branching fraction ~15%) and also became the primary reactions at 1100 K. Reactions forming and consuming β radicals were similar to [974].

Ignition delay times measured for 2-methyltetrahydrofuran in Fenard et al. [974] and Tripathi et al. [954] using an RCM and a shock tube from 10 – 40 atm and 640 – 1400 K displayed only slight NTC behavior, from ~750 – 950 K. The lack of two-stage ignition indicates that chain-propagation and chain-inhibiting reactions, including ring-opening reactions of initial radicals, are favored over second-O_2-addition reactions. Wang et al. [978] also report ignition delay times from 1 – 10 atm. However, the lowest temperature (1050 K) extends beyond the range where peroxy radical chemistry is relevant.

The *ab initio* calculations of Parab et al. [976] for ROȮ → ȮOOH isomerization and the ignition delay time/chemical kinetics modeling work of Tripathi et al. [977] are the only two studies on low-temperature oxidation of 3-methyltetrahydrofuran. Parab et al. [976] conducted an extensive series of calculations using the CBS-QB3 composite method, reporting high-pressure limit rate coefficients and branching fractions for ROȮ → ȮOOH over the temperature range 500 – 1250 K. Rate coefficients were computed for both *cis*- and *trans*-ROȮ and several isomer-specific results were noted. For all ROȮ species, internal H-abstraction occurs predominantly at α or α' carbon (cf. **Figure 93c**) via a 6-membered transition state: >90% over the entire temperature range for six of the eight isomers. The branching fraction towards α or α' radicals is the lowest for two of the *cis*-ROȮ species because of hydrogen-abstraction from the methyl group, also occurring via a 6-membered transition state, becoming relevant – approximately 20% of the branching fraction for α'-ROȮ and ~30% for β-ROȮ at 600 K. α' and β refer to carbon atoms adjacent to the methyl-substituted carbon (cf. **Figure 93c**). Branching fractions towards α or α' radicals remain above ~65% over

the temperatures covered, however. The results for 3-methyltetrahydrofuran were compared with calculations on analogous reactions in methylcyclopentane using the same level of theory in order to assess the influence of the ether group on ROȮ → ȮOOH isomerization rates. The main conclusion drawn was that the ether group increases the rate of isomerization by ~10^1 for the majority of the comparisons [976].

Figure 103 summarizes ROȮ → ȮOOH isomerization rates from Parab et al. on α-ROȮ radicals of 3-methyltetrahydrofuran [976] and 2-methyltetrahydrofuran [973] for abstraction from α carbon via 6-membered transition states. From comparison of the two sets of results from Parab et al. [973, 976], ROȮ → ȮOOH isomerization rates via 6-membered transition states for 3-methyltetrahydrofuran are not isomer-dependent, whereas some isomer dependence is evident for 2-methyltetrahydrofuran. For 2-methyltetrahydrofuranperoxy, isomerization rates for the *trans*- conformer (**Figure 103b**) are substantially higher (~10^5) than for the *cis*- isomer at 550 K and remain ~10^2 higher towards 1000 K. In contrast, conformational effects are negligible for isomerization rates of α-ROȮ radicals formed from 3-methyltetrahydrofuran. For context, comparisons were made in Parab et al. [973, 976] to analogous reactions for methylcyclopentane. Relative to *cis*-1-methylcyclopentyl-3-peroxy, isomerization rates for α-ROȮ of 3-methyltetrahydrofuran are appreciably higher, >10^1 at 750 K, while the rate at the same temperature for α-ROȮ of 2-methyltetrahydrofuran is lower by a factor of ~4 (**Figure 103a**). The reason for the lower rate in the latter case, despite lower C–H bond energies on α carbon, is the *trans*- position of the tertiary hydrogen atom relative to the –OȮ group. The opposite result is observed for *trans*-2-methyltetrahydrofuranyl-5-peroxy (**Figure 103b**), in which case the abstracting peroxy group occupies the same plane as the tertiary hydrogen. The effect of the favorable orientation is a significant increase in the isomerization rate: ~10^2 higher than both *trans*-1-methylcyclopentyl-3-peroxy and *trans*-3-methyltetrahydrofuranyl-5-peroxy at 750 K.

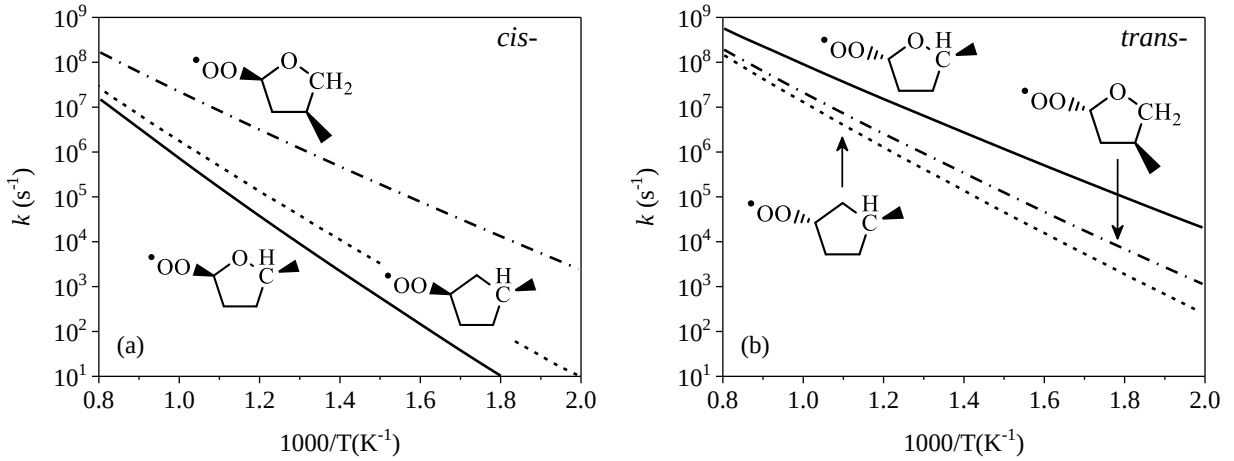

Figure 103. High-pressure limit rates for α-ROȮ → ȮOOH isomerization reactions via 6-membered transition states, calculated using CBS-QB3, for peroxy radicals of 2-methyltetrahydrofuran [973], 3-methyltetrahydrofuran [976], and methylcyclopentane [973, 976]. (a) *cis*-ROȮ. (b) *trans*-ROȮ.

Tripathi et al. [977] reported shock-tube and RCM ignition delay time measurements for 3-methyltetrahydrofuran, conducted at high pressure (10 – 40 bar) over 625 – 1250 K, and developed the first chemical kinetics mechanism. Because of the reduction in C–H bond energy, H-abstraction by ȮH at low temperature primarily occurs on α carbon (~75%) followed by abstraction from tertiary β' and secondary β carbon (both ~10%). Abstraction from the –CH_3 group is of minor importance. To a larger extent than in

2-methyltetrahydrofuran [973], the predictions indicate that ring-opening reactions of initial α radicals in 3-methyltetrahydrofuran are competitive with O_2-addition at temperatures below 750 K and ultimately become favored with increasing temperature.

The results in [977] were compared to 2-methyltetrahydrofuran from Tripathi et al. [954], which confirmed that chain-branching below 750 K is more pronounced in 3-methyltetrahydrofuran, and were consistent with the RCM measurements of Sudholt et al. [952]. One of the primary conclusions from the comparison in [977] was the impact of the methyl group location relative to the ether group. When the two are adjacent, as in 2-methyltetrahydrofuran where the $–CH_3$ group is in the α' position, chain-branching is restricted because of the lack of available hydrogen atoms for the ȮOQOOH isomerization step required for ketohydroperoxide formation (**Figure 104**).

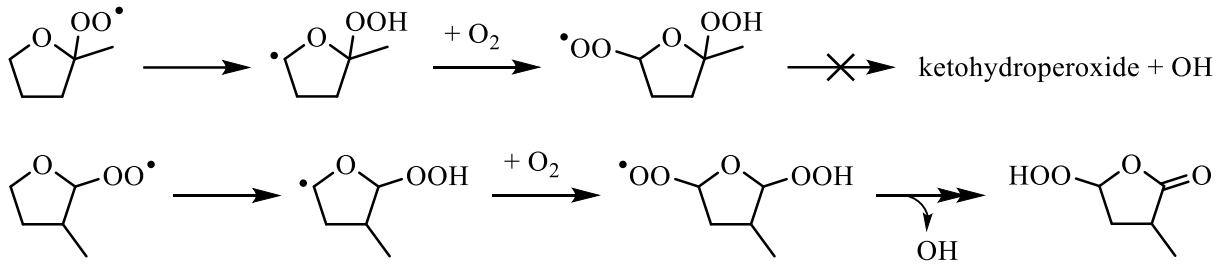

Figure 104. Second-O_2-addition reactions are hindered in 2-methyltetrahydrofuran oxidation because ȮOQOOH isomerization leading to ketohydroperoxide is not possible when the –OOH and methyl substituent are bonded to the same carbon [977].

Figure 105a shows stoichiometric ignition delay time measurements for 2-methyltetrahydrofuran from Tripathi et al. [954] and for 3-methyltetrahydrofuran from Tripathi et al. [977] at 20 atm. Differences between the two isomers, outside of the stated experimental uncertainty of ±15%, occur below ~800 K; at 650 K, 2-methyltetrahydrofuran ignition times are longer by a factor of ~3. As noted in [977] and depicted in **Figure 104**, the longer ignition delay times of 2-methyltetrahydrofuran are due to the lack of available hydrogen on α carbon for abstraction in ȮOQOOH isomerization reactions. In contrast, in the case of 2-methyltetrahydrofuran, four such carbon sites are present as is a tertiary C–H bond (i.e. β'). The latter point is additionally notable because ȮOQOOH isomerization involving that site undergoes a favorable 6-membered transition state. **Figure 105a** also compares the two cyclic ethers to methylcyclopentane, which exhibits NTC behavior over a similar range of temperature as cyclopentane. As observed with the tetrahydrofuran/cyclopentane comparison (cf. **Figure 101**), ignition delay times of both methylated cyclic ethers are significantly shorter than methylcyclopentane. At 780 K, the same temperature used in the previous comparison in **Figure 101**, the difference is more than one order of magnitude: methylcyclopentane (76.1 ms), 2-methyltetrahydrofuran (5.9 ms), and 3-methyltetrahydrofuran (2.7 ms).

Stoichiometric ignition delay time simulations were conducted in the present review at 20 atm using the mechanisms of Tripathi et al. [954] for 2-methyltetrahydrofuran and Tripathi et al. [977] for 3-methyltetrahydrofuran (**Figure 105b**). Simulations of methylcyclopentane ignition were also conducted using the mechanism of Fridlyand et al. [979]; N_2 mole fractions of ~0.76 were used in all cases. Ignition was defined using the method of steepest ascent [361] applied to ȮH time histories modeled using isobaric conditions with the 0D homogeneous reactor module in ChemKin PRO. The predictions are consistent with

the main observations in the experiments, namely that NTC behavior is more prominent in the alkane and that cyclic ether ignition delay times are significantly shorter. Note that facility effects are neglected in **Figure 105b**, which contributes to any quantitative discrepancy. The comparison in **Figure 105** highlights two aspects concerning ignition chemistry of functionalized molecules – the effect of ether group and the effect of methyl substituent location on methylated tetrahydrofuran. The explanation for the trends between the cyclic ethers and methylcyclopentane are likely similar to those for the tetrahydrofuran-cyclopentane comparison in that ring-opening reactions and peroxy radical formation play central roles.

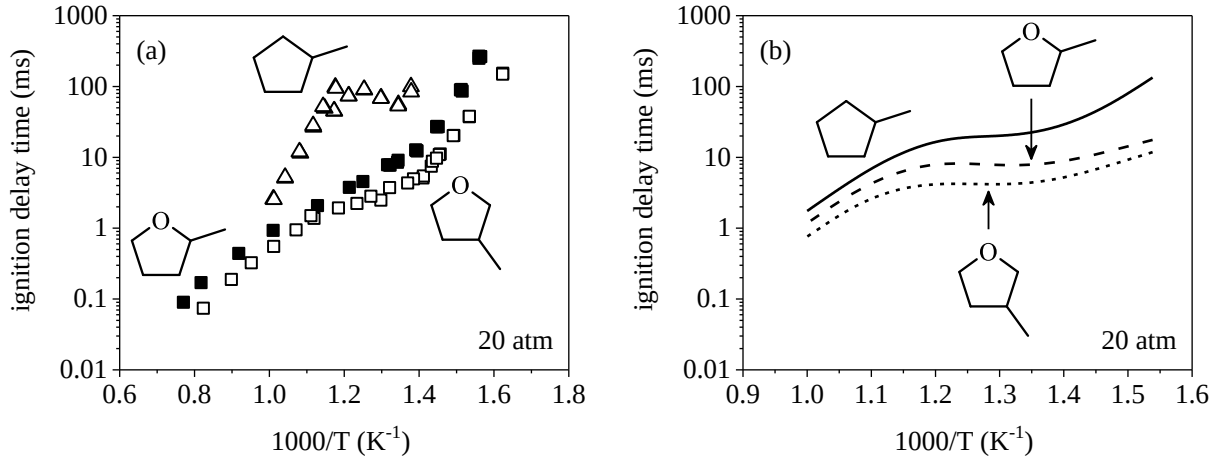

Figure 105. Stoichiometric ignition delay times of methylcyclopentane (Fridlyand et al. [979]), 2-methyltetrahydrofuran (Tripathi et al. [954]), and 3-methyltetrahydrofuran (Tripathi et al. [977]). ϕ = 1.0 and 20 atm. (a) experiment; (b) model.

Cai et al. [968] developed the first chemical kinetics mechanism for 2-butyltetrahydrofuran and reported shock-tube and RCM ignition delay time measurements at 20 atm. NTC behavior was evident from ~850 – 1000 K. Predictions of ignition delay times for 2-butyltetrahydrofuran were compared to other C8 species: *n*-octane [411], 1-octanol [548], and *n*-butyl ether [968]. None of the four trends overlapped one another over the range of temperatures simulated (650 – 1250 K), which underscores the complexity of functional group chemistry. Below 775 K, the ignition delay times trends were of the order: di-*n*-butyl ether < *n*-octane < 2-butyltetrahydrofuran < 1-octanol.

The core mechanism of [968] is built from the base mechanism of Blanquart et al. [980]. Additional ether-related chemistry is adapted from tetrahydrofuran [961, 967] and other cyclic ethers [950, 981]. Using the CBS-QB3 composite method, Cai et al. [968] expanded on prior work by calculating barrier heights for ring-opening of initial Ṙ radicals to include in the mechanism. For both types of α radicals, i.e. secondary and tertiary, ring-opening via C–O bond-scission requires ~23 kcal/mol, which is lower than the barrier height for the other radicals by 8 – 12 kcal/mol. Notably, peroxy radical formation and related chain reactions of products from ring-opening was included in the development of the mechanism, which resulted in shorter ignition delay times by 20 – 30% in the NTC region (~750 – 900 K). As a class of reactions, the inclusion of radical ring-opening appeared in sensitivity analysis calculations and inhibited ignition delay times to a similar degree as the formation of cyclic ether from unimolecular ȮOOH decomposition. Because of an absence of speciation studies on 2-butyltetrahydrofuran, however, open questions remain such as the

extent to which the alkyl chain interacts with the ether ring during oxidation and the importance of products from ring-opening reactions.

3.5.3. di-substituted tetrahydrofuran

Chakravarty and Fernandes [80] report the only computational study on 2,5-dimethyltetrahydrofuran relevant to combustion. Total high-pressure-limit rate coefficients for H-abstraction by HOȮ were calculated at the CCSD(T)/cc-pVTZ//B3LYP/cc-pVTZ level of theory with torsional mode treated using RRHO, Pitzer-Gwinn, 1D-Schrödinger, and 1D free rotor approximations. Tunneling effects were also accounted for using the unsymmetrical 1D Eckart approximation [982]. The CBS-QB3 method was also used and significant differences (~10^1) with the coupled cluster method were noted. In addition, the approximation for torsional energy of internal rotors led to differences of ~10^2 – ~10^3. Total high-pressure-limit rate coefficients were also calculated for 2-methyltetrahydrofuran and methylcyclopentane in order to assess the influence of molecular structure. **Figure 106** shows the rate coefficients for all three species from 500 – 1000 K over which 2,5-dimethyltetrahydrofuran is ~10^1 higher than for 2-methyltetrahydrofuran, which is likely due to the additional tertiary hydrogen since the barrier heights were nearly identical for analogous reactions in the two ethers. The rate coefficients for both ethers are notably higher than for methylcyclopentane, nearly 10^2 higher in the case of 2,5-dimethyltetrahydrofuran. Site-specific rate coefficients were also calculated and indicated that abstraction of hydrogen from α carbon is the only kinetically significant channel below ~900 K. With increasing temperature, abstraction from the methyl group becomes relevant, nearly equal to abstraction from α carbon above 1000 K.

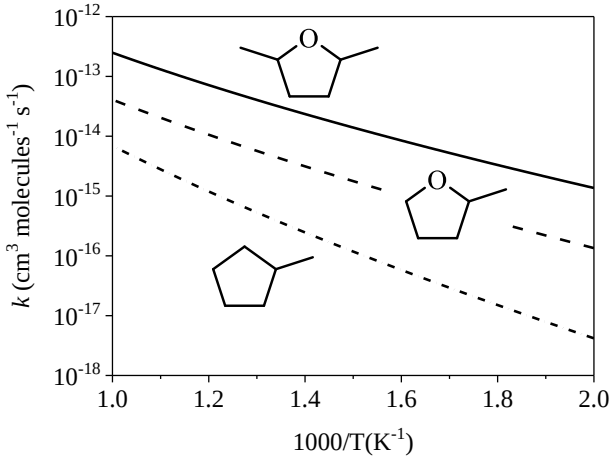

Figure 106. Total rate coefficients in the high-pressure limit for H-abstraction by HOȮ from 2,5-dimethyltetrahydrofuran, and 2-methyltetrahydrofuran, and methylcyclopentane calculated in Chakravarty and Fernandes [80] using energies at the CBS-QB3 level of theory.

Sudholt et al. [953] conducted derived cetane number (DCN) measurements of 2,3-dimethyltetrahydrofuran and 2,5-dimethyltetrahydrofuran, the results of which indicated that substituent proximity significantly impacts reactivity. The DCN of 2,3-dimethytetrahydrofuran (20) was ~20% higher compared to the other isomer (15.6). Fenard et al. [983] developed the first chemical kinetics mechanism and conducted a comprehensive study on 2,5-dimethyltetrahydrofuran combustion. Ignition delay times were measured using a shock tube from 10 – 40 atm and an RCM from 10 – 20 atm. NTC behavior was

observed. Speciation measurements were also reported from the RCM. Neither of the two HOO-elimination products (2,5-dimethyl-2,3-dihydrofuran and 2,5-dimethyl-2,5-dihydrofuran) were detected due to issues with chromatographic separation. Similar to Fenard et al. [959] for tetrahydrofuran, ȮOOH ring-expansion and ring-opening reactions were reported. In the case of 2,5-dimethyltetrahydrofuran, ring-expansion led to 2,4-dimethyl-4*H*-1,3-dioxine and hexa-2,5-dione was formed via ȮOOH ring-opening. Products from ring-opening reactions of initial Ṙ radicals were also observed, which included alkenes and carbonyl radicals via C–C β-scission of carbonyl radicals, e.g. 2-hexanon-5-yl → propene + acetonyl.

Figure 107 compares stoichiometric ignition delay time simulations at 20 atm using mechanisms for tetrahydrofuran [959], 2-methyltetrahydrofuran [954], 3-methyltetrahydrofuran [977], and 2,5-dimethyltetrahydrofuran [983]. N_2 mole fractions were ~0.76. The longer ignition delay times for 2,5-dimethyltetrahydrofuran is due in part to the lack of ketohydroperoxide formation pathways involving α carbon – the same explanation for the reason that low-temperature ignition times of 2-methyltetrahydofuran are longer than for 3-methyltetrahydrofuran (cf. **Figure 105**).

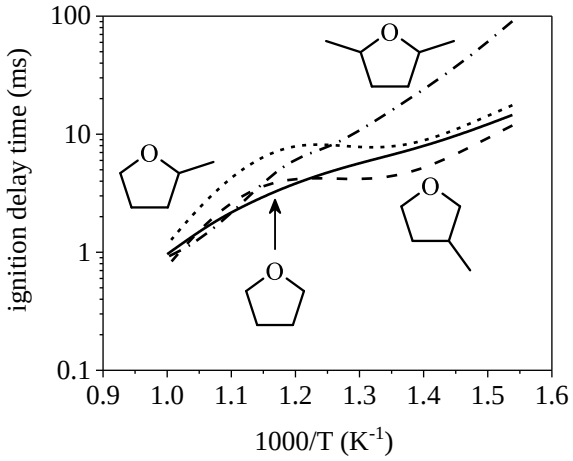

Figure 107. Stoichiometric ignition delay time simulations at 20 atm using mechanisms for tetrahydrofuran (Fenard et al. [959]), 2-methyltetrahydrofuran (Tripathi et al. [954]), 3-methyltetrahydrofuran (Tripathi et al. [977]), and 2,5-dimethyltetrahydrofuran (Fenard et al. [983]).

3.5.4. tetrahydropyran

Rotavera et al. [951] conducted MPIMS experiments to determine the influence of the ether group in tetrahydropyran on chain-inhibiting reactions, i.e. Ṙ + O_2 → conjugate alkene + HOȮ, in comparison to cyclohexane. The latter produces only one such alkene (cyclohexene), while tetrahydropyran produces two (3,4-dihydro-2*H*-pyran and 3,6-dihydro-2*H*-pyran). Branching fractions were measured from 500 – 700 K and were used to infer the effect of the ether group on the production of the set of conjugate alkenes. Below 700 K, chain-termination is favored in tetrahydropyran due to coupled effects of (1) lower C–H bond energy of α carbon, which leads to α-tetrahydropyranyl being the dominant initial radical, and (2) lower barrier to direct HOȮ formation on the α-tetrahydropyranyl + O_2 surface (by ~5 kcal/mol). With increasing temperature, however, competition from α-tetrahydropyranyl ring-opening reduces the flux through Ṙ + O_2 and subsequent product formation thereafter – an effect compounded by the fact that abstraction at the weakest C–H bond produces the initial radical most amenable to ring-opening. In contrast, analogous ring-opening reactions of cyclohexyl were not evident and are not relevant until ~800 K [303]. The results in

Rotavera et al. [951] highlight the fact that the ether group facilitates chain-inhibiting via HOO-elimination at lower temperature, whereas towards higher temperature the network of oxidation reactions grows more complex due to weak C–O bonds in α radicals that enable ring-opening reactions to become dominant. Subsequent reaction mechanisms of radicals produced from cyclic ether ring-opening remain an open question. Similar conclusions were drawn in measurements of ȮH and HOȮ time histories in Chen et al. [309].

Davis et al. [522] also conducted MPIMS experiments on cyclohexane and tetrahydropyran, at two pressures (10 Torr and 1520 Torr) and three temperatures (500 K, 600 K, and 700 K) to determine the effect of the ether group on ketohydroperoxide formation. Branching fractions of acyclic species were quantified and provided confirmation that ring opening of ȮOOH radicals, which ultimately diminishes second-O_2-addition reactions, was more pronounced in tetrahydropyran than in cyclohexane. In addition to branching fractions, species time profiles were also measured and a notable difference in the temperature dependence of ketohydroperoxide signal was observed. In cyclohexane experiments at 1520 Torr, ion signal at *m/z* 130 (corresponding to $C_6H_{10}O_3$) was evident at both 600 K and 700 K. In contrast, and as a result of ȮOOH ring-opening, ketohydroperoxide ion signal from tetrahydropyran (*m/z* 132, $C_5H_8O_4$) was detected only up to 650 K.

The main conclusion drawn in Davis et al. [522] is the importance of both Ṙ and ȮOOH radical ring-opening in tetrahydropyran oxidation, which depletes to some extent the already low steady-state concentration of ȮOOH. Four pathways were connected to unimolecular reactions of ȮOOH in [522] (**Figure 108**): (a) γ-ȮOOH → pentanedial + ȮH, (b) γ-ȮOOH → vinyl formate + ethene + ȮH, and (c – e) γ-ȮOOH → 3-butenal + formaldehyde + ȮH. Carbon balance calculations revealed that products from ring-opening accounted for >70% at 10 Torr and >55% at 1520 Torr. Analogous reaction mechanisms leading to similar intermediates from cyclohexane oxidation were examined in Davis et al. [522] to determine the extent to which ring-opening reactions were influenced by the ether group. On the basis of mass spectra measurements, no products from ring-opening reactions of cyclohexane-derived radicals were identified at the conditions of the experiments. The absence of products from such reactions, coupled with the detection of ketohydroperoxide signal at higher temperature than from tetrahydropyran oxidation, indicates that the ether group introduces ring-opening pathways that deplete ȮOOH radicals that may otherwise react via second-O_2-addition.

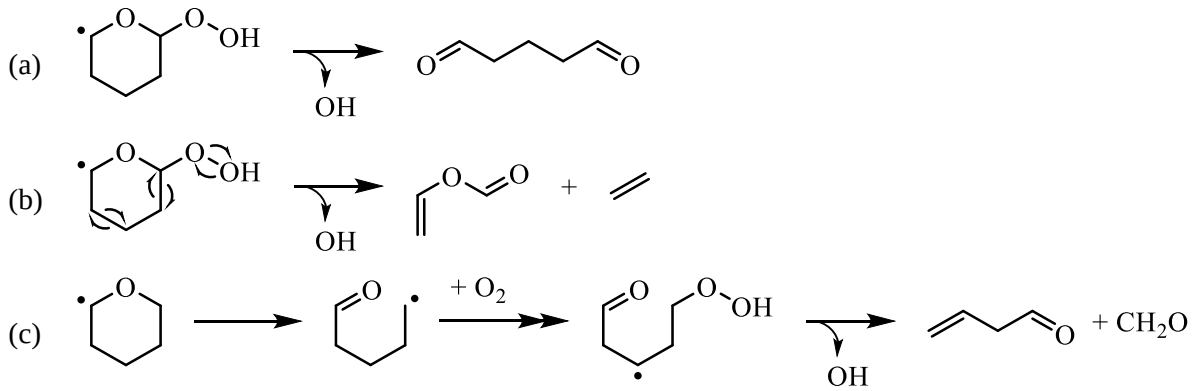

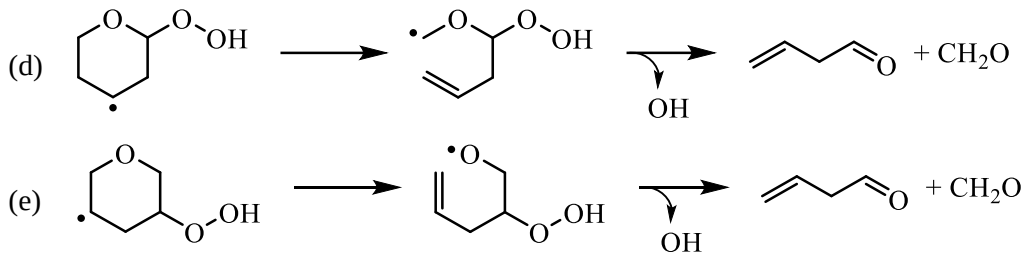

Figure 108. Ṙ and Q̇OOH ring-opening mechanisms in tetrahydropyran oxidation [522].

Dagaut et al. [984] measured ignition delay times for tetrahydropyran in a shock tube and species profiles in a jet-stirred reactor and also developed the first detailed chemical kinetics mechanism for pressure and temperature ranges of 2 – 10 atm and 800 – 1700 K, respectively. Labbe et al. [985] conducted speciation measurements on low-pressure flames and expanded on the mechanism of Dagaut et al. [984] using unimolecular quantum-RRK theory to calculate ring-opening rates of initial radicals. Tran et al. [986] studied the pyrolysis and high-temperature ignition and flame properties of tetrahydropyran. Tran et al. [986] also constructed a detailed chemical kinetics mechanism covering a broad parameter space in temperature, pressure, and concentration.

Ignition delay time measurements are not reported for tetrahydropyran below 1000 K. The shock tube measurements of Dagaut et al. [984] spanned ~1100 – 1580 K. In contrast, low-temperature ignition delay times were measured for cyclohexane in Lemaire et al. [987, 988] from 600 – 900 K using an RCM, and in Daley et al. [987, 988] from 850 – 1270 K using a shock tube. In addition, the three chemical kinetics mechanisms that exist for tetrahydropyran [984-986] were developed for flame conditions and do not include peroxy radical chemistry. Therefore, open questions remain as to the effect of the ether group on ignition delay times in the oxidation of 6-membered cyclic ethers. The impact of ring-opening reactions inhibiting ketohydroperoxide formation may lead to diminished NTC behavior compared to cyclohexane.

3.5.5. furans

Simmie and Curran [989] conducted *ab initio* calculations using three quantum chemical methods (CBS-QB3, CBS-APNO, and G3) on bond dissociation energies and enthalpies of formation for several alkyl-substituted furans. C–H bond energies of ~120 kcal/mol were computed and the high value, relative to abstraction of H atoms from saturated systems, was ascribed to an inability of the resulting radical to delocalize the unpaired electron. In a subsequent series of calculations, Feller and Simmie [990] utilized the Feller-Petersen-Dixon method [991] to conduct calculations on enthalpies of formation for 2,5-dimethylfuran, 2-methylfuran, and furan. Because of the unsaturated ring in furans (**Figure 109**) and the endothermicity of H-abstraction [989], peroxy radical chemistry leading to second-stage ignition is not observed. The lack of low-temperature chemistry makes furans suitable blending components for increasing efficiencies of premixed combustion systems [19, 779, 992] at levels of only 10% (vol.) [19].

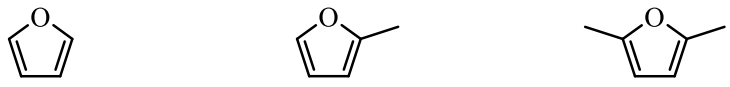

(a) furan (b) 2-methylfuran (c) 2,5-dimethylfuran

Figure 109. Molecular structure of (a) furan, (b) 2-methylfuran, and (c) 2,5-dimethyltetrahydrofuran. Owing to high C–H bond dissociation energies [989, 990] and resonance-stabilization, the aromatic ring minimizes the role of peroxy radical chemistry.

High-temperature studies of furan and alkyl-substituted furan are abundant, including pyrolysis [993-997] and flame structure [981, 998-1002]. Ignition delay time measurements are reported for furan [1003-1005] [969], 2-methylfuran [970, 972, 1001-1003, 1005, 1006], 2,3-dimethylfuran [969], and 2,5-dimethylfuran [1003, 1005-1009]. Qian et al. [1010] reviewed the status of 2,5-dimethylfuran related to both production and utilization. In all cases, the ignition delay time trends do not exhibit NTC behavior, indicating that ȮOOH-mediated chemistry is unimportant in furans. Despite the lack of low-temperature chemistry in furan oxidation, combustion studies of individual species below 1000 K include furan, 2-methylfuran, and 2,5-dimethylfuran. The sections below are organized into four parts: rate coefficients for initiation reactions, speciation measurements, reaction mechanisms of furanyl radicals, ignition delay times, and chemical kinetics modeling.

Whelan et al. [1011] conducted laser induced fluorescence spectroscopy experiments to measure rate coefficients for reactions of ȮH with furan, 2-methylfuran, and 2,5-dimethylfuran at temperatures up to 770 K and pressures up to 10 atm, which were complemented with master equation calculations. Rate equations and Troe fitting parameters were produced by including measurements in the literature at other conditions. Addition reactions of ȮH to only one location on each species – secondary α carbon in furan and tertiary α carbon in methylated furans – were considered in the kinetics modeling. The theoretical rates were consistent with the measurements and revealed that pressure dependence is weak and that (barrierless) ȮH-addition is the major channel over abstraction below 1000 K, even for 2,5-dimethylfuran where six primary C–H bonds are present that otherwise yield a resonance-stabilized radical upon abstraction. The lack of pressure dependence is ascribed to the formation of a ring-opened, resonance-stabilized radical submerged ~43 kcal mol^{-1} below the entrance channel.

Rate coefficients for ȮH + furan were measured in shock tube experiments from 1 – 2 atm in Elwardany et al. [1012] over the temperature range 924 – 1388 K. Wine and Thompson [1013] measured the temperature dependence of ȮH + furan at 900 Torr in Ar over the temperature range 254 – 425 K using time-resolved resonance fluorescence spectroscopy. Rate coefficients were also measured in [1012] for ȮH + 2-methylfuran from 890 – 1333 K and in Kim et al. [1014] from 948 – 1327 K at similar pressures. The latter work applied a two-step hierarchical Bayesian method to calibrate the experimentally determined rate parameters of the reaction ȮH + 2-methylfuranyl → products. Elwardany et al. [1012] report the only rate coefficient measurements of ȮH + 2,5-dimethylfuran → products, which were conducted from 915 – 1278 K and from 1 – 2 atm. Friese et al. [1015] measured rate coefficients in shock tube experiments from 970 – 1240 K and from 1.6 – 4.8 atm for Ḣ + 2,5-dimethylfuran reactions. Complementary calculations confirmed that addition-elimination – yielding 2-methylfuran + $\dot{C}H_3$ – was the primary reaction channel.

Only a limited number of experimental studies on speciation from low-temperature oxidation of furans exist [970, 1016-1019]. Speciation measurements were conducted on furan oxidation in a stirred reactor by Thornton et al. [1016] at 1 atm from 1000 – 1300 K. Product formation was detected near 1100 K and included species like acetylene, ethene, and formaldehyde, among others and oxidation mechanisms involving H-abstraction from furan and disproportionation reactions with O_2 leading to acetylene and others. Fathi and Meloni [1019] conducted MPIMS experiments on reactions of $O(^3P)$-initiated oxidation

of 2-methylfuran at 550 K and 650 K at 7 Torr. Potential energy surfaces were also calculated for O-atom addition to the ring using the CBS-QB3 composite method. Primary products, identified using analysis of species time histories, were ascribed to addition reactions and accounted for the majority of product formation while H-abstraction reactions were minor. The addition of Ö atoms to the furan ring led to singlet epoxide species via intersystem crossing [1020-1022] and derived from one of four triplet diradicals, which subsequently produced formaldehyde, propene, 2-butenal, and methyl vinyl ketone as major products; alkynes 1- and 2-butyne, 1,3-butadiene, and 3-butenal were also quantified. [1019]. Alexandrino et al. [1018] conducted flow reactor experiments on 2,5-dimethylfuran oxidation from 500 – 1400 K and from 1 – 40 atm. Species profiles for CO_2, CO, ethene, and H_2 were quantified.

Tran et al. [970] conducted laminar flow reactor experiments at 1 atm from 730 – 1170 K on furan, 2-methylfuran, and 2,5-dimethylfuran using 20-eV EI-MBMS. Over three dozen species were identified, including products from ring-opening reactions, such as acrolein and vinyl-acetylene, and higher molecular weight species, such as indane and naphthalene, indicating incipient soot formation processes. However, with the exception of furfural and 5-methylfurfural, potentially from ROȮ + ROȮ reactions, species containing two oxygen atoms, indicating product formation from ȮOOH chemistry, were not detected. Similar results were reported in Somers et al. [1007] on 2,5-dimethylfuran oxidation using a jet-stirred reactor and shock tube experiments. However, peroxy radical chemistry of furans may hold relevance for oxidative stability when used as blending components [1023]. As with other alkylated species, furans with longer alkyl chains, e.g. *n*-butylfuran [952], are more likely to display NTC chemistry as the number of secondary C–H bonds increase and favorable ROȮ → ȮOOH reactions are enabled.

Theoretical studies on reaction mechanisms of furans include ȮH + furan [1024-1026], O_2 + 2-methylfuran radicals [1027-1029], ȮH + 2-methylfuran [1026, 1027, 1030], ȮH + 3-methylfuran [1031], ȮH + 2,5-dimethylfuran [1026], and ȮH + 2-ethylfuran [1032]. Reactions of furans with ȮH lead predominantly to addition to α carbon and, subsequently, to the formation of ring-opened radicals [1024-1026]. The potential energy surfaces in Yuan et al. [1026] indicate that ȮH reaction with furans proceeds via a complex that leads to a chemically activated OH-substituted furan radical, which can undergo collisional stabilization or ring-opening to resonance-stabilized *E*/*Z* conformers that are able to interconvert. Upon reaction with O_2, the ring-opened radicals can form dicarbonyl species, e.g. *E*-butenedial and *Z*-butenedial in the case of furan. Because of the lack of chain-branching and generation of ȮH in the oxidation of furans, the relevance of such ring-opening reactions at combustion conditions remains unclear. At a minimum, however, in the presence of other highly reactive species, furans may act as a radical sink for ȮH.

Hudzik and Bozzelli [1028] conducted a series of thermochemical and kinetics calculations on species formed from 2-methyl-5-furanyl + O_2 reactions using a combination of CBS-QB3, M06-2X/6-31G(*d*,*p*), MP2, and PM3 levels of theory. The well-depth of the ROȮ adduct was 51 kcal/mol below the entrance channel and the energetically favorable pathway was abstraction of hydrogen from the methyl group, which led via a ring-expansion mechanism to 4-methyl-1,3-dioxane-2-one [1028]. Temperature- and pressure-dependent rate coefficient parameters were also calculated using QRRK and master equation analysis. Li and Cao [1029] conducted a series of pressure-dependent rate calculations for O_2-addition to radicals of 2-methylfuran.

Davis and Sarathy [1027] calculated potential energy surfaces and rate coefficients for reactions of Ḣ and ȮH with 2-methylfuran over the temperature range 300 – 2000 K. Since ȮH + 2-methylfuran reactions are

barrierless, addition reactions were favored energetically over abstraction reactions. Correspondingly, rate coefficients were calculated for subsequent reactions of OH-substituted 2-methylfuranyl radicals with O_2 using CBS-QB3 and G4 methods. *cis*-/*trans*- effects, with respect to –OH and –OȮ groups, were accounted for. In the ROȮ → ȮOOH transition states for *cis*- isomers, intramolecular hydrogen bonding between the two groups provided ~3 kcal/mol stabilization. Preceding reaction with O_2, addition of ȮH to α carbon on the furan ring produces resonance-stabilized radicals, whereas addition to β carbon yields non-resonance-stabilized radicals. On the potential energy surface for the latter type of radicals, isomerization via five-membered transition states and concerted elimination of HOȮ were favored. Barrier heights for isomerization/decomposition reactions stemming from O_2-addition to resonance-stabilized radicals were all above the entrance channel. However, within the uncertainty of the methods, Waddington mechanisms were the lowest lying pathways. An alternative Waddington channel, termed Waddington elimination, was proposed (**Figure 110**) – the similarity to the conventional channel being abstraction of hydroxylic hydrogen by the peroxy group and subsequent β-scission reactions. However, the difference is that, instead of two carbonyl species + ȮH, a multi-functional species is formed coincident with HOȮ rather than two carbonyl species and an ȮH.

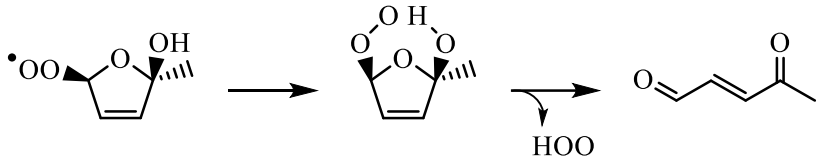

Figure 110. Waddington-type HOO-elimination mechanism derived from reaction of 2-hydroxy-2-methylfuran-5-yl with O_2. [1027].

Detailed chemical kinetics mechanisms for furan were developed in Tian et al. [999], Liu et al. [1000], and Tran et al. [970]. Similarly, mechanisms for 2-methylfuran were developed in Tran et al. [970, 1002] and for 2,5-dimethylfuran in Somers et al. [1007], Sirjean et al. [1009], Togbé et al. [1001], Alexandrino et al. [1018], and Tran et al. [970]. The mechanism in Tran et al. [970] is a single, joint mechanism for the three furan species and incorporates chemistry relevant to low-temperature combustion, including reactions of resonance-stabilized furanyl radicals with O_2 and with HOȮ.

3.5.6. summary of low-temperature oxidation of cyclic ethers

Reaction mechanisms of cyclic ethers are relevant to understanding biofuel combustion chemistry as well unimolecular decomposition rates of ȮOOH radicals in alkane oxidation [430, 947]. The presence of an ether group reduces C–H bond energies on α carbon by 4 – 5 kcal/mol, whereas bond energies on other carbon atoms are similar to analogous sites in cycloalkanes. As a result, for temperatures below 1000 K, α radicals are favored in initiation reactions with ȮH and HOȮ for tetrahydrofuran and methyl-substituted tetrahydrofuran species.

Reactions of α radicals with O_2 via the chain-inhibiting step Ṙ + O_2 → conjugate alkene + HOȮ are favorable due to lower barrier heights. In addition, as a result of the selectivity towards α radicals, an important aspect for both Ṙ and ȮOOH radicals produced from cyclic ethers is the propensity for radical ring-opening. In both cases, because of the adjacent unpaired electron, the C–O bond on the opposite side of the ether group is weakened. Subsequent ring-opening of the Ṙ radicals produces an aldehyde-alkyl

radical, e.g. α-tetrahydrofuranyl → butan-4-yl-1-al. Such reactions compete with first O_2-addition above ~650 K. Similar ring-opening reactions of ȮOOH follow chain-propagation pathways by producing an ȮH radical. Both types of ring-opening ultimately decrease the rate of second O_2-addition reactions and chain-branching steps thereafter owing to the depletion of ȮOOH radicals.

Rate coefficient calculations of first-O_2-addition to cyclic ether radicals or second-O_2-addition to ȮOOH, both of which are important to understand given the competition with ring-opening reactions, are absent in the literature. ROȮ well-depths of α peroxy radicals (α-ROȮ) are similar to alkylperoxy radicals (~35 kcal/mol below the Ṙ + O_2 entrance channel) and are likely central to understanding cyclic ethers. In addition to rates of formation of α-ROȮ, for methyl-substituted species such as 2-methyltetrahydrofuran, predicting ratios of *cis*-/*trans*- ROȮ is important given that rates of α-ROȮ → ȮOOH are isomer-dependent and because of the potential for inversion reactions [947]. Upon second-O_2-addition, the location of the methyl group relative to the peroxy group affects the flux of radicals towards ketohydroperoxide formation. Notably, isomer-specific rates are not included for any species in chemical kinetics mechanisms at present, which may impact predictions of ignition delay times and species profiles.

Several oxidation steps of cyclic ethers contribute to diminished NTC chemistry, as summarized in **Figure 111**, which is augmented to emphasize pathways influenced by the ether functional group contrasted against the low-temperature chain-branching scheme for alkanes. The main attributes of cyclic ether oxidation are favorable ring-opening of α-Ṙ radicals, ring-opening and ring-expansion of ȮOOH, and facile HOO-elimination from both Ṙ and ȮOOH, as well as from ȮOQOOH. Despite weak NTC chemistry in all the cyclic ethers for which measurements are reported – tetrahydrofuran, 2-methyltetrahydrofuran, and 3-methyltetrahydrofuran – ignition delay times in all cases are shorter than the corresponding cycloalkane analog. One plausible reason is larger rate coefficients for H-abstraction from cyclic ethers by both ȮH and HOȮ. Compounded with higher k(T) for the latter reaction, is facile production of HOȮ via ROȮ → conjugate alkene + HOȮ due to lower barrier heights when α carbon is involved. Low-temperature chain-branching in cyclic ethers is inhibited because of several reactions diminishing an already low steady-state concentration of ȮOOH, which effectively reduces reaction rates for second-O_2-addition. Specific types of reactions include ring-opening of α-Ṙ, which forms an acyclic carbon-centered radical with a distant carbonyl group, and of ȮOOH (both starting near ~650 K), and, in the case of tetrahydrofuran, ȮOOH ring-expansion that yields a closed-shell six-membered heterocyclic species + ȮH.

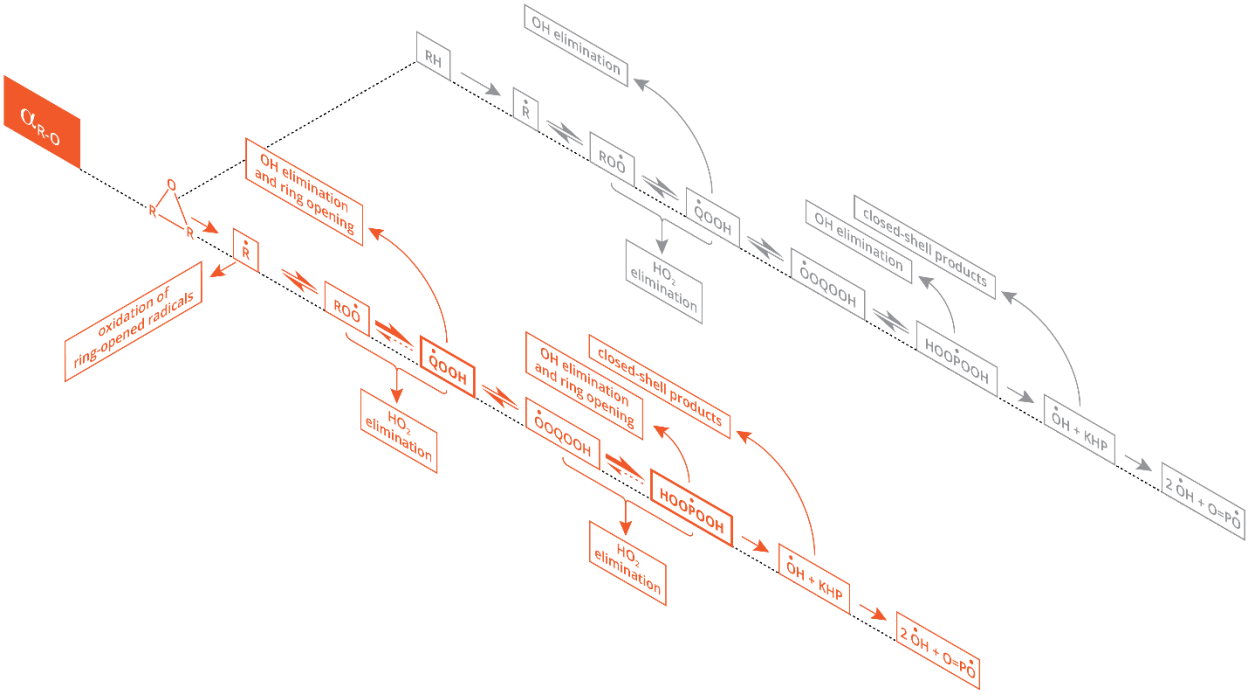

Figure 111. Summary of ether functional group effects on low-temperature chain-branching of cyclic species. The leftward-pointing and downward-pointing arrows indicate a shift in flux away from chain-branching pathways responsible for ignition. Each type of initial radical is depicted in a separate plane, with different colors used to guide the eye. The alkane oxidation mechanism is depicted in the back plane for reference. Pathways that are enhanced by the effects of the functional group are emphasized with bold arrows and labels, and those that are diminished are made lighter or omitted. Hydrogen-abstraction from α carbon (adjacent to the ether group) introduces ring-opening of both Ṙ and ȮOOH radicals, which may undergo unimolecular decomposition or reaction with O_2 and preclude second-O_2-addition reactions that are required for chain-branching. HOO-elimination reactions are enhanced when involving hydrogen α carbon due to low C–H bond energy.

4. Research directions

The sections below identify gaps in the understanding of functional group chemistry in relation to low-temperature combustion and outline research directions for alcohols (*Section 4.1*), esters (*Section 4.2*), ketones (*Section 4.3*), acyclic ethers (*Section 4.4*), and cyclic ethers (*Section 4.5*). The main goal of the highlighted points is to summarize relevant experimental and computational studies necessary for improving the fidelity of chemical kinetics mechanisms for prediction of biofuel oxidation mechanisms and ignition. Among the computational studies, continued utilization of automated transition state and reaction mechanism algorithms, including RMG [400], Genesys [401, 402], and KinBot [421] can facilitate progress and uncover new directions for chemistry, as shown in Grambow et al. [423] for 3-hydroperoxypropanal and in the Welz et al. [301] identification of water-elimination reactions in alcohol oxidation, which was initially suggested from KinBot calculations on *iso*-pentanol oxidation chemistry [1033]. Elliott et al. [422] have recently shown the power of automated methods by applying a suite of automatic first-principles

quantum chemistry and rate coefficient codes (AutoMech [1034]) to generate predictive chemical models for pyrolysis.

Several fundamental chemistry issues are common among all functional groups:

- Only a limited number of experimental rate coefficient measurements exist from ~500 – 900 K for $\dot{O}H + RH \rightarrow H_2O + \dot{R}$ for species of all functional group types.
- Direct experimental measurements of rate coefficients for $HO\dot{O} + RH \rightarrow H_2O_2 + \dot{R}$ do not exist for any biofuel species.
- Uncertainties in branching fraction calculations for initiation reactions with $\dot{O}H$ and $HO\dot{O}$ are non-negligible in most cases, even for cases where total rate coefficients are consistent, and exhibit a dependence on the level of theory utilized, as shown for alcohols (*Section 3.1.1*), esters (*Section 3.2.1*), ketones (*Section 3.3.1*), and ethers (*Sections 3.4.1* and *Section 3.5*). However, the effects of variation in branching fractions on chemical kinetics mechanisms remain unaddressed and is potentially important for accurate predictions of ignition delay times and species profiles predictions.
- The addition of radicals ($\dot{R}$ or $\dot{Q}OOH$) to O_2 is barrierless and difficult to calculate rigorously because of inaccuracies in determining the interaction energies along the reaction path. Goldsmith et al. [1035] have shown that use of multireference methods can produce reliable results and have applied these methods to reactions of hydrocarbon radicals with O_2 [1035, 1036]. Accurate kinetics measurements and high-level calculations of biofuel derived radical additions to O_2 will be valuable for establishing the foundational reactions of low temperature combustion.
- Application of local and global uncertainty and sensitivity analysis [864, 1037-1039], uncertainty propagation and minimization methods [1040], and machine learning [1041-1044] are vital for refining detailed chemical kinetics mechanisms of biofuels given the complexity introduced by functional groups, particularly since rate rules are often relied upon for producing first-generation mechanisms. As an example, Agbro and Tomlin [1045] applied global sensitivity analysis to predictions of low-temperature ignition delay time measurements using a 1-butanol mechanism, which provided clear constraints for branching fractions of $\dot{O}H$ + 1-butanol $\rightarrow H_2O + \dot{R}$.
- The role of accurate thermochemistry for intermediate species related to the formation and decomposition of $\dot{Q}OOH$ and of $\dot{O}OQOOH$ is significant, as shown for alkanes [710] and ethers [1046, 1047]. Given the complexity of most species involved in reactions of the two radicals, and that group additivity principles are only of limited utility, high-level quantum chemical calculations are needed, particularly for those related to oxygenated biofuels given the limited amount of experimental measurements. Moreover, noting the limitations of group additivity and that the majority of the acyclic species contain multiple torsional modes and distinct conformers, accurate thermochemistry requires multi-dimensional torsional scans/partition functions and conformer analyses to properly account for hydrogen bonding and formation of quasi-cyclic species.
- Grambow et al. [423] utilized several state-of-the-art automated transition-state search algorithms and discovered dozens of alternative reaction pathways for unimolecular decomposition of the γ-ketohydroperoxide formed in propane combustion. While some alternative ketohydroperoxide reaction decomposition are proposed based on experiments [898, 961], products from dissociation

pathways competing with O–O bond-scission identified in [423], such as 1,2-H_2O_2 elimination and internally catalyzed enol-oxo tautomerization, remain largely uncharacterized. Speciation measurements of expected products from the proposed pathways are needed to determine the extent to which such reactions are relevant at combustion conditions.

- The detection, and to a larger extent quantification, of multi-functional ȮOOH-mediated species remains a challenge often encountered due to a lack of reference measurements of absorption cross-sections, absolute photoionization cross-sections, and mass spectra [1048]. Examples include pentanedial produced from tetrahydropyran oxidation [522], 2-methyloxetan-3-one produced from butanone oxidation [764], and 2-methyl-4-butoxyoxetane produced from diethyl ether oxidation [901]. Advances in speciation diagnostics and theoretical methods to produce quantitative spectra are needed.
- Speciation experiments are needed to aid in the understanding of the potential effects of functional groups on non-Boltzmann reactions discussed in Burke et al. [1049] and Goldsmith et al. [1050] for species derived from propane oxidation.
- Functional group effects on third-O_2-addition reported for alkanes [1051-1053] remain largely unexplored in biofuel oxidation. Belhadj et al. [900, 966] report species produced from multiple O_2-addition steps during oxidation of tetrahydrofuran [966] and diethyl ether [900], yet quantification remains a challenge.

4.1. alcohols

- Uncertainties in branching fractions for ȮH + ethanol are significant as shown in *Section 3.1.1.1* (Figure 4) and in Olm et al. [460] and Glarborg et al. [464]. In addition to ethanol oxidation, accurate site-specific rate coefficients for α and β carbon are relevant because of the connection to abstraction reactions in other alcohols that are influenced by pre-reaction complex formation. The net effect of branching fraction uncertainty on ignition delay time predictions of ethanol, however, is potentially negligible given the relatively simpler reaction mechanisms compared with other alcohols in that both initial radicals predominantly form acetaldehyde + HOȮ upon reaction with O_2.

- Several quantum chemical studies calculated rate coefficients for ȮH + 1-butanol → H_2O + Ṙ in the high-pressure limit and consistently show that α radicals are favored most, accounting for ~50 – 60% over the range 500 – 1000 K. However, uncertainties in branching fractions of the other radicals, β, γ, and δ, are significant and may reduce accuracy of chemical kinetics modeling of peroxy radical chemistry. Additional studies are necessary to determine branching fractions in the initiation step with ȮH, perhaps examining the potential for dependence on quantum chemical methods. Experimental measurements may also provide experimental boundary conditions for theoretical studies, such as OH-initiated H-abstraction from 1-butanol-1,1-d_2 ($CH_3CH_2CH_2CD_2OH$) or 1-butanol-4,4,4-d_3 ($CD_3CH_2CH_2CH_2OH$). The impact of accurately modeling branching fractions on mechanism fidelity for 1-butanol is potentially significant given the complexity of the reaction mechanisms unfolding across the four Ṙ + O_2 potential energy surfaces.

- No studies exist for abstraction reactions of ȮH or HOȮ with 1-pentanol. Branching fractions for ȮH + 1-butanol calculated by Zhou et al. [433] show that the formation of δ radicals are relevant below 1000 K, owing to the formation of a pre-reaction complex. An open question remains as to the degree of interaction between carbon at the ε position and whether the interaction between the abstracting radical and the –OH group is localized on carbon in the $\alpha - \delta$ range.

- No rate coefficient measurements exist for reactions of ȮH with unsaturated branched alcohols prenol and *iso*-prenol, which are relevant both as biofuel [147, 150, 194, 197, 204, 205] and as primary oxidation intermediates of *iso*-pentanol [295]. Xing et al. [482] reported the lone set of high-pressure limit rate coefficients for ȮH-initiated H-abstraction from *iso*-pentanol.

- Although the most abundant radicals produced in the initiation step, α radicals are not expected to undergo O_2-addition reactions based on quantum chemical calculations for hydroxyethyl + O_2 [497] and 2-methylpropan-1-ol-1-yl + O_2 [501]. However, what remains unclear is the potential for ROȮ stabilization in reactions with radicals from larger alcohols with a larger number of vibrational modes, such as 1-pentanol or *iso*-pentanol, which may render α-Ṙ + O_2 → α-ROȮ (and subsequent α-ROȮ → ȮOOH) an important set of reactions. The methodology of Burke et al. [1049] and Goldsmith et al. [1050] for quantifying non-Boltzmann distribution effects of reactants on product branching fractions may contribute to the understanding of α-Ṙ + O_2 association reactions, as shown for ȮOOH* + O_2 occurring in *n*-propyl oxidation [1049] and for decomposition reactions of 3-hydroperoxypropanal [1050].

- As shown in Welz et al. [296] for 1-butanol oxidation, water-elimination reactions are low-lying pathways on Ṙ + O_2 surfaces for β, γ, and δ radicals. Rate calculations using master equation methods for unimolecular reactions of oxy radicals from water-elimination pathways may improve predictions of low-temperature formation of CO, CH_2O, and other intermediates. Welz et al. [296] calculated barrier heights for unimolecular decomposition of 4-oxybutanal and 2-oxybutanal. Pathways to two product pairs on the 4-oxybutanal surfaces were low-lying: $\dot{C}_2H_5$ + glyoxal and HĊO + propanal. For 2-oxybutanal, C–C β-scission led to propan-1-al-3-yl + CH_2O and to propan-1-ol-3-yl + CO; the latter via an isomerization step wherein aldehydic hydrogen is abstracted by the terminal oxy radical, forming an OH-substituted carbonyl radical. Similar reactions of 3-oxobutanal, via C–C β-scission, lead to vinoxy ($\dot{C}H_2CHO$) + acetaldehyde and to propan-2-ol-3-yl + CO.

- In addition to conventional ȮOOH decomposition pathways, the –OH group in alcohols enables isomerization reactions involving abstraction of α hydrogen from non-terminal oxygen in the –OOH group. As an example, in 1-butanol oxidation, δ-ROȮ isomerization, in which hydrogen from the –OH group is abstracted, leads to a ȮOOH radical HOO–$CH_2CH_2CH_2\dot{C}H$–OH. Decomposition via a low-lying OH-transfer reaction produces 4-hydroxybutanal (HO–$CH_2CH_2CH_2C(H)$=O) + ȮH in a chain-propagating step. Analogous reactions are possible for γ-ROȮ in 1-butanol, which ultimately produces 3-hydroxybutanal + ȮH in a similar sequence of reactions, and for other alcohols. Experimental detection of species from such alternative ȮOOH reactions in alcohols are not reported. In addition, for 1-butanol, neither of the two mechanisms for which peroxy radical chemistry is included (Sarathy et al. [511] and Vranckx et al. [435]) account for alternative ȮOOH

reactions, which may affect global ȮH budgeting and impact the reliability of ignition delay time predictions.

- The Vranckx et al. [435] mechanism for 1-butanol includes only lumped reactions of ȮOOH, leading either directly to chain-branching (producing ȮH + ȮH + carbonyl-oxy radical) or decomposition via Waddington. Only the Sarathy et al. [511] mechanism incorporates unique elementary reactions for ȮOOH → cyclic ether + ȮH. All six cyclic ether species were accounted for. However, the rate parameters were based on rate rule analogies with alkanes and no experimental species profile measurements are reported in the literature for comparison. Quantum chemical calculations of rate coefficients for ȮOOH → cyclic ether + ȮH are required, in addition to direct speciation measurements of cyclic ethers formed in alcohol oxidation.

- Quantum chemical calculations, similar to Sebbar et al. [760-762] conducted for branching fractions for unimolecular reactions of butanone-derived ȮOOH radicals, are not reported for alcohols. The results of such calculations could provide improved chemical kinetics understanding of ȮOOH-mediated reactions from alcohol oxidation, which are potentially more prominent in cases where second-O_2-addition and NTC behavior is less significant since unimolecular reaction becomes the main decomposition channel.

- No speciation measurements are reported for cyclic alcohols, despite numerous synthesis routes for both cyclopentanol [190-193] and cyclohexanol [206-211] and no chemical kinetics mechanism is available for the latter.

- Ignition delay time measurements for alcohols, conducted at the same conditions as analogous alkanes, are lacking. One exception is comparison of ignition delay times of *n*-butane at 15 atm against the four isomers of butanol (*Section 3.1.4.1*). Additional studies similar to Heufer et al. [98] could aid in refining rate coefficients prescribed in chemical kinetics mechanisms for alcohols, which are largely constructed using rate rules from alkanes, and improve predictive capabilities of ignition. Example comparisons could include *iso*-butane/*iso*-butanol, *iso*-pentanol/*iso*-pentane, and *iso*-prenol/*iso*-pentene.

- Ignition delay times of cyclic alcohols are largely unexplored, with the exception of the cyclopentanol shock tube and RCM experiments of Cai et al. [552], which led to the development of a chemical kinetics mechanism [549]. No ignition measurements are reported for cyclohexanol. Several studies exist for alkane analogs, cyclopentane [553, 768, 979] and cyclohexane [987, 988, 1054-1056], which can provide for a direct comparison as to the impact of the –OH functional group on ignition delay times.

4.2. esters

- Theoretical kinetics calculations, focusing on branching fractions for H-abstraction from esters, are needed to determine accurate quantum chemistry and the importance of explicitly treating the hydrogen-bonded reactant complex (i.e., a two-transition-state model). *Section 3.2.1* reviews two cases involving H-abstraction from methyl propanoate by ȮH and by HOȮ, where such dependence may occur.

- Given the importance of C=C bonds to ester reactivity [377], theoretical calculations are needed to quantify ȮH-addition rates with unsaturated esters particularly for polyunsaturated species, where *bis*-allylic hydrogen is present, and enable predictions of the balance between addition and abstraction reactions at combustion-relevant temperatures and pressures. Surrogate molecules, such as 1,4-pentadiene, may provide a means for experimental measurement of such reactions.

- In addition to α' and β' radicals in methyl esters, which are formed on the alkyl group and are favored most in ȮH-initiated and HOȮ-initiated H-abstraction, branching fraction calculations show that radical formation on the methoxy group is also important. An open question remains as to the competition of such radicals, where the unpaired electron resides on the alkoxy portion of the ester, to undergo reaction with O_2 versus unimolecular decomposition via C–C β-scission. The latter reaction yields formaldehyde and a formate radical, the decomposition of which directly yields CO + *n*-alkyl. For example, in methyl butanoate, decomposition of $CH_3(CH_2)_2C(=O)O\dot{C}H_2$ forms CH_2O + $CH_3(CH_2)_2\dot{C}=O$, where the radical species decomposes into CO + *n*-propyl.

- Because chemical kinetics mechanisms most commonly draw analogy with alkanes for rate parameters, theoretical calculations of ROȮ → ȮOOH isomerization rates comparing such reactions in esters to analogous reactions in alkanes are needed to determine the potential impact of additional strain in the transition state when the ester group is included. Glaude et al. [624] estimated the strain energy of cyclic transition states involving the ester group utilizing group additivity methods by considering ring strain equal to the enthalpy of reaction in isodesmic reactions in which the cyclic structure is produced from a linear, unstrained structure. However, no high-level theoretical calculations are reported.

- Direct, isomer-resolved speciation measurements of cyclic ethers produced from ester oxidation, particularly lactone derivatives that involve the ester group in the transition state, are not reported for the majority of methyl esters and are needed as validation targets for chemical kinetics mechanisms. One exception is the experiments of Glaude et al. [624], in which substituted oxolanes were measured from methyl decanoate oxidation.

- Low-temperature oxidation chemistry of alkenyl chains in unsaturated esters, particularly reactions involving *bis*-allylic sites is largely unstudied. Because C=C bonds in practical esters are located several carbons from the ester group, as in methyl oleate, methyl linoleate, and methyl linolenate, examining reaction mechanisms of dienes, such as 3,6-nonadiene, which permit ROȮ ⇌ ȮOOH isomerization that involve the C=C bonds, may provide necessary insight into the role of alkenyl chains in low-temperature oxidation of esters and lead to improved ignition modeling capabilities that account for competing radical-addition reactions and abstraction reactions.

- To examine the potential for alkoxy groups to influence ȮOOH formation and chain-branching in ester oxidation, from the facilitating of reactions across the ester group, ignition delay time measurements for methyl esters and ethyl esters, conducted under the same conditions, are needed. An example may include the comparison between ignition delay times of methyl butanoate versus ethyl butanoate. Peroxy radical formation on the terminal carbon of an ethoxy group in ethyl esters enables a 7-membered transition state for ROȮ → ȮOOH, while the analogous reaction starting from a methoxy group requires a 6-membered transition state. Both involve abstraction of hydrogen from allylic carbon immediately adjacent to the ester group.

- Only a limited number of studies exist on ethyl esters, none of which involve species larger than ethyl propanoate despite synthesis routes for larger ethyl esters [216, 1057, 1058].

4.3. ketones

- Other than the shock tube experiments of Liu et al. [741], the lower limit of which was 900 K, no experimental measurements are reported for rate coefficients of ȮH + cyclic ketones, and theoretical studies on cyclopentanone [79, 724] and cyclohexanone [743] show differences of more than a factor of ~2 compared with the experiments. For ȮH + cyclopentanone, branching fractions towards the two radicals – α and β – are consistent to within 20% between the two studies of Thion et al. [79, 724] and Zhou et al. [79, 724], although the total rate coefficients below ~750 K are within a factor of ~2. Measurements of k(T) for ȮH + cyclopentanone and ȮH + cyclohexanone, complementing the temperature range of Liu et al. [741], could provide experimental benchmarks for additional quantum chemical calculations.

- Rate coefficients are not reported experimentally or computationally for HOȮ + cyclohexanone H_2O_2 + Ṙ. The chemical kinetics mechanism developed in Thion et al. [743] utilizes rate coefficients based on analogy to butanone (for abstraction of α carbon) and to *n*-butane (for β and γ carbon). Because of the importance of the conjugate alkene formation channel in ketone oxidation, via Ṙ + O_2, accurate rate coefficients for abstraction by HOȮ are potentially significant to modeling low-temperature oxidation pathways in cyclohexanone.

- Despite synthetic pathways for the production of 2-methylcyclopentanone [241, 242], low-temperature oxidation experiments and theoretical calculations are largely unexplored. Scheer et al. [757] conducted the single set of experiments, utilizing MPIMS to probe product formation from Ṙ + O_2 reactions. Rate coefficients for abstraction, by ȮH or HOȮ, additional speciation experiments, ignition delay times, and chemical kinetics mechanism development are not reported for 2-methylcyclopentanone.

- With the exception of the series of QRRK calculations of Sebbar et al. [760-762] on the three butanonyl radicals, which focused on branching fractions related to Ṙ + O_2 reactions, no studies exist for reactions of O_2 with other ketonyl radicals at combustion-relevant conditions. Quantum chemical calculations for other species, such as cyclopentanone and cyclohexanone, could contribute to advancing chemical kinetics mechanism development for cyclopentanone and cyclohexanone, particularly since most of the ȮOOH-mediated species from cyclic ketones form bicyclic structures that are difficult to detect experimentally.

- Speciation measurements of ȮOOH-mediated species from butanone oxidation are required in order to confirm several reaction pathways, including (i) the alternative γ-ȮOOH decomposition mechanism postulated in Sebbar et al. [760], leading to 1-hydroxybut-3-en-2-one, (ii) the formation of the cyclic ether 1-(oxiran-2-yl)ethan-1-one 2-butanon-4-peroxy [762], and (iii) 2-methyloxetan-3-one formation derived from 2-butanon-3-peroxy [764], all of which remain unconfirmed because of a lack of isomer-resolved measurements. Similarly, for cyclic ketones, products from ȮOOH-mediated reactions of cyclopentanone and cyclohexanone are not reported in recent experimental studies, and Zhang et al. [767] remarked on the necessity for such speciation measurements for improvement of chemical kinetics modeling of cyclopentanone.

- Speciation measurements are not reported for acyclic ketones in **Table 1** other than butanone, despite synthetic pathways for the production of 2-pentanone [118, 177, 227, 229] and 5-methyl-2-hexanone [162, 212].

- Ignition delay time measurements below 1000 K for ketones in **Table 1** include butanone, 2-pentanone, 3-pentanone, di-*iso*-propyl ketone, and cyclopentanone. No such measurements exist for cyclohexanone. Given the development of a chemical kinetics mechanism for cyclohexanone [743], which incorporates peroxy radical chemistry, ignition delay time measurements are necessary for the purpose of providing validation targets. Moreover, ignition delay time measurements for ketones, conducted at similar conditions as to analogous alkanes, are lacking. Coordinated measurements on ketones and alkanes of similar molecular structure (e.g. methylcyclopentane and 2-methylcyclopentanone) enables improved understanding of ketone oxidation in the context of alkane oxidation upon which most first-generation mechanism development is based.

4.4. acyclic ethers

- Quantum chemical calculations are not reported for HOȮ + diethyl ether → H_2O_2 + Ṙ and are potentially significant in modeling low-temperature oxidation given the abundance of HOȮ formed coincident with ethyl vinyl ether via Ṙ + O_2 reactions.

- In the series of theoretical calculations on dimethyl ether, Andersen and Carter [853] note that VTST calculations, accounting for the intrinsic barrier of the O–O scission reaction, are required to confirm selectivity towards hydroperoxymethyl formate decomposition via O–O scission, leading to chain-branching, over the formic acid + HCȮ + ȮH pathway; Channels III and V, respectively, in **Figure 77**.

- In dimethyl ether oxidation, rate coefficients are needed for several decomposition pathways of the lone ketohydroperoxide, hydroperoxymethyl formate. Specifically, the formic anhydride pathway (Channel II in **Figure 77**) and the performic acid pathway (Channel III in **Figure 77**). Both species were detected experimentally in the JSR experiments of Moshammer et al. [344]. Although the barrier height is the highest among the decomposition channels, the detection of performic acid may arise from acid-catalyzed dehydration given the abundance of formic acid produced from dimethyl ether. Additional rate calculations for the latter reactions are also needed.

- Theoretical calculations of rate coefficients for ketohydroperoxide decomposition channels in diethyl ether are needed, including the proposed acetic acid and acetic anhydride pathways, which were based on rate rules in the chemical kinetics mechanism of Tran et al. [898]. Danilack et al. [943] computed rates for conventional ketohydroperoxide reactions in diethyl ether oxidation using a coupled set of master equations to account for non-Boltzmann effects.

- Isomer-resolved measurements of cyclic ether produced from diethyl ether are not reported and are needed for 2-ethoxyoxirane, 2,4-dimethyl-1,3-dioxetane, and 1,4-dioxane to provide experimental targets for chemical kinetics modeling of the balance between unimolecular decomposition of ȮOOH and second-O_2-addition reactions. Tran et al. [898] quantified 2-methyl-1,3-dioxolane in JSR experiments using GC/MS.

- Neither speciation measurements nor ignition delay times are reported for any of the branched ethers in **Table 1** despite synthetic pathways: ethyl-*tert*-butyl ether [150, 255-257], *tert*-amyl-methyl ether, [150, 255, 258], and di-amyl ether [259].

4.5. cyclic ethers

- No experimental or quantum chemical studies exist for O_2-addition to radicals of cyclic ethers, such as tetrahydrofuran, 2-methyltetrahydrofuran, and tetrahydropyran.

- Because of facile ring-opening of cyclic ether radicals, when an unpaired electron is adjacent to the ether group, master equation calculations are necessary to predict the balance of reactions of both Ṙ and Q̇OOH radicals against reaction with O_2 [522, 951].

- Fenard et al. [959] report the only series of calculations on rates of RO<u>O</u>̇ isomerization, Q̇OOH decomposition for a cyclic ether, which were conducted on tetrahydrofuran using CBS-QB3. Rate calculations at higher levels of theory are needed to improve chemical kinetics mechanisms.

- Quantum chemical calculations are needed for Q̇OOH ring-expansion reactions proposed in Vanhove et al. [965] based on speciation measurements of 1,3-dioxene and 1,4-dioxene during tetrahydrofuran oxidation. Such reactions are potentially important in predicting the balance of reactions in addition to the conventional pathways that Q̇OOH radicals undergo.

- Significant *cis*-/*trans*- isomer dependence of RO<u>O</u>̇ → Q̇OOH isomerization reaction rates were reported for both 2-methyltetrahydrofuran [973] and for 3-methyltetrahydrofuran [976]. However, the impact on ignition delay time predictions is unclear as isomer-specific reactions of RO<u>O</u>̇ radicals are not included in chemical kinetics mechanisms. In addition, branching fractions for Ṙ + O_2 → *cis*-RO<u>O</u>̇ versus Ṙ + O_2 → *trans*-RO<u>O</u>̇ are unknown.

- Speciation measurements of products from low-temperature oxidation of 2-methyltetrahydrofuran, 3-methyltetrahydrofuran, and 2,5-dimethyltetrahydrofuran are not reported, and only two speciation studies on tetrahydropyran exist below 1000 K [522, 951]. Such measurements could provide clarity as to the effect of ring-opening of both Ṙ and Q̇OOH radicals.

- Low-temperature sub-mechanisms are unavailable for tetrahydropyran radicals, despite development of three detailed chemical kinetics mechanisms [984-986].

- Ignition delay times of tetrahydropyran are not reported and, upon comparison with cyclohexane [988, 1056], could provide insight into the effects of Ṙ and Q̇OOH ring-opening on chain-branching.

5. *Conclusions*

The present review provides a historical account and summary of biofuel chemical kinetics relevant to chain-branching reactions in combustion. The presence of oxygenated functional groups in biofuels affects low-temperature oxidation steps that can impact each step in the degeneration chain-branching mechanism, from initiation reactions, reaction rates with O_2, and oxidation mechanisms, all of which are highly coupled and directly control reactivity and ignition. The primary effects include alterations in branching fractions during the initiation step due to reduced C–H bond dissociation energies adjacent to the functional group, competing rates for $\dot{R}$ decomposition versus first-O_2-addition, which impacts $\dot{R} + O_2 \rightleftharpoons RO\dot{O}$ equilibria, the imposing of additional strain in the transition state for $RO\dot{O} \rightleftharpoons \dot{Q}OOH$ isomerization, and complex reaction mechanisms that are unique to a particular functional group. The degree of influence depends on both the type of functional group and the size of the aliphatic component of the biofuel structure.

The review focused on the understanding of fundamental chemical kinetics of biofuels that affects the sequence of reactions leading to chain-branching and ignition delay times in order to develop robust, predictive computational models. The details of each biofuel were contextualized against the corresponding alkane. Concerning validation experiments, because measuring all labile intermediate species, isomers, and conformers, is infeasible both qualitatively and quantitatively, certain types of species are likely to play more pivotal roles in serving as modeling targets for advancing the state of knowledge. As an example, more research is needed to understand the fate of intermediates formed from oxidation reactions of first-O_2-addition reactions, such as cyclic ethers. The balance of the two competing, forward pathways for $\dot{Q}OOH$ (i.e. unimolecular decomposition or second-O_2-addition) ultimately dictates reactivity characteristics of biofuels, which can differ substantially from hydrocarbons. Therefore, unimolecular reactions of $\dot{Q}OOH$ play critical roles in understanding low-temperature oxidation and in developing chemical kinetics mechanisms.

Because of the importance of $\dot{Q}OOH$ chemistry to the development of modeling capabilities for low-temperature combustion, a reasonable expectation is that uncertainty in the balance of reactions involving cyclic ethers, which form predominantly from $\dot{Q}OOH$, contributes directly to uncertainty in predictions of autoignition and species profiles of intermediates. Moreover, as newly identified species and pathways become evident in biofuel combustion, such as alternative reactions of $\dot{Q}OOH$ and ketohydroperoxides, experimental confirmation must rely on quantum chemistry and theoretical chemical kinetics for quantitative predictions. One effective outcome from such work could involve the development of functional-group-specific rate rules, which may benefit further from machine learning approaches.

The combustion chemistry of biofuels remains a highly active area of research, and with the increasing abundance of viable options, the scope of the research continues to broaden. An important aspect of biofuels, as shown in the present review, is the magnitude of impact that functional groups can impose on ignition. As a result, continued integration of liquid biofuels for transportation energy purposes may not require complete displacement of petroleum-derived hydrocarbons and instead may utilize blending in small amounts. One broader objective is the development of modeling capabilities for predicting combustion properties of multi-component biofuels for fundamental understanding of blending effects. Because of the strength of the research and the advances in the theoretical and experimental capabilities, a general and rigorous description of the functional group dependence of autoignition chemistry to achieve such an objective is within reach.

Acknowledgements

The material herein is based upon work supported by the Division of Chemical Sciences, Geosciences and Biosciences, Office of Basic Energy Sciences (BES), U.S. Department of Energy (USDOE). Sandia National Laboratories is a multimission laboratory managed and operated by National Technology and Engineering Solutions of Sandia, LLC., a wholly owned subsidiary of Honeywell International, Inc., for the USDOE National Nuclear Security Administration under contract DE-NA0003525. This paper describes objective technical results and analysis. Any subjective views or opinions that might be expressed in the paper do not necessarily represent the views of the USDOE or the United States Government. BR acknowledges support from the Division of Chemical Sciences, Geosciences and Biosciences, Office of Basic Energy Sciences (BES), U.S. Department of Energy (USDOE) under Award DE-SC0021337.

BR and CAT express sincere appreciation to the reviewers for thorough, constructive, and substanative insight on the content herein.

References

[1] K. Kohse-Hoinghaus, *Proc Combust Inst*, (2020).
[2] K. Kohse-Höinghaus, *Prog. Energy Comb. Sci.*, 65 (2018) 1-5.
[3] F.L. Dryer, *Proc. Combust. Inst.*, 35 (2015) 117-144.
[4] R.D. Reitz, H. Ogawa, R. Payri, T. Fansler, S. Kokjohn, Y. Moriyoshi, A.K. Agarwal, D. Arcoumanis, D. Assanis, C. Bae, K. Boulouchos, M. Canakci, S. Curran, I. Denbratt, M. Gavaises, M. Guenthner, C. Hasse, Z. Huang, T. Ishiyama, B. Johansson, T.V. Johnson, G. Kalghatgi, M. Koike, S.C. Kong, A. Leipertz, P. Miles, R. Novella, A. Onorati, M. Richter, S. Shuai, D. Siebers, W. Su, M. Trujillo, N. Uchida, B.M. Vaglieco, R.M. Wagner, H. Zhao, *International Journal of Engine Research*, (2019) 1468087419877990.
[5] J.R. Serrano, R. Novella, P. Piqueras, *Applied Sciences*, 9 (2019) 4597.
[6] G. Kalghatgi, *Applied Energy*, 225 (2018) 965-974.
[7] G. Kalghatgi, H. Levinsky, M. Colket, *Prog. Energy Comb. Sci.*, 69 (2018) 103-105.
[8] S. Verhelst, T. Wallner, *Prog. Energy Comb. Sci.*, 35 (2009) 490-527.
[9] T. Korakianitis, A.M. Namasivayam, R.J. Crookes, *Prog. Energy Comb. Sci.*, 37 (2011) 89-112.
[10] A. Valera-Medina, H. Xiao, M. Owen-Jones, W.I.F. David, P.J. Bowen, *Prog. Energy Comb. Sci.*, 69 (2018) 63-102.
[11] D. Debnath, M. Khanna, D. Rajagopal, D. Zilberman, *Applied Economic Perspectives and Policy*, 41 (2019) 563-582.
[12] P.J. Meier, K.R. Cronin, E.A. Frost, T.M. Runge, B.E. Dale, D.J. Reinemann, J. Detlor, *Environmental Science & Technology*, 49 (2015) 8277-8286.
[13] L.M. Fulton, L.R. Lynd, A. Körner, N. Greene, L.R. Tonachel, *Biofuels, Bioproducts and Biorefining*, 9 (2015) 476-483.
[14] D.F. Correa, H.L. Beyer, J.E. Fargione, J.D. Hill, H.P. Possingham, S.R. Thomas-Hall, P.M. Schenk, *Renewable and Sustainable Energy Reviews*, 107 (2019) 250-263.
[15] R. Alizadeh, P.D. Lund, L. Soltanisehat, *Renewable and Sustainable Energy Reviews*, 134 (2020) 110326.
[16] C.-Y. Lin, C. Lu, *Renewable and Sustainable Energy Reviews*, 136 (2021) 110445.
[17] MIT Energy Initiative, Insights into Future Mobility, 2019.
[18] M. Unglert, D. Bockey, C. Bofinger, B. Buchholz, G. Fisch, R. Luther, M. Müller, K. Schaper, J. Schmitt, O. Schröder, U. Schümann, H. Tschöke, E. Remmele, R. Wicht, M. Winkler, J. Krahl, *Fuel*, 268 (2020) 117227.

[19] D.A. Rothamer, J.H. Jennings, *Fuel*, 98 (2012) 203-212.
[20] E. Monroe, J. Gladden, K.O. Albrecht, J.T. Bays, R. McCormick, R.W. Davis, A. George, *Fuel*, 239 (2019) 1143-1148.
[21] J.L. Field, T.L. Richard, E.A.H. Smithwick, H. Cai, M.S. Laser, D.S. LeBauer, S.P. Long, K. Paustian, Z. Qin, J.J. Sheehan, P. Smith, M.Q. Wang, L.R. Lynd, *Proceedings of the National Academy of Sciences*, 117 (2020) 21968.
[22] L.R. Lynd, *Nature Biotechnology*, 35 (2017) 912-915.
[23] D. Tilman, R. Socolow, J.A. Foley, J. Hill, E. Larson, L. Lynd, S. Pacala, J. Reilly, T. Searchinger, C. Somerville, R. Williams, *Science*, 325 (2009) 270.
[24] D. Tilman, J. Hill, C. Lehman, *Science*, 314 (2006) 1598-1600.
[25] G.P. Robertson, S.K. Hamilton, B.L. Barham, B.E. Dale, R.C. Izaurralde, R.D. Jackson, D.A. Landis, S.M. Swinton, K.D. Thelen, J.M. Tiedje, *Science*, 356 (2017).
[26] J.C. Abanades, E.S. Rubin, M. Mazzotti, H.J. Herzog, *Energy & Environmental Science*, 10 (2017) 2491-2499.
[27] C.R. Somerville, S.P. Long, National Academy of Engineering, The Future of Biofuel and Food Production in the Context of Climate Change and Emerging Resource Stresses, 2015.
[28] V.H. Dale, E.S. Parish, K.L. Kline, *Biofuels, Bioproducts and Biorefining*, 9 (2015) 177-189.
[29] B.E. Dale, J.E. Anderson, R.C. Brown, S. Csonka, V.H. Dale, G. Herwick, R.D. Jackson, N. Jordan, S. Kaffka, K.L. Kline, L.R. Lynd, C. Malmstrom, R.G. Ong, T.L. Richard, C. Taylor, M.Q. Wang, *Environmental Science & Technology*, 48 (2014) 7200-7203.
[30] S. Kim, X. Zhang, A.D. Reddy, B.E. Dale, K.D. Thelen, C.D. Jones, R.C. Izaurralde, T. Runge, C. Maravelias, *Environmental Science & Technology*, 54 (2020) 10797-10807.
[31] B. Buchspies, M. Kaltschmitt, U. Neuling, *Renewable and Sustainable Energy Reviews*, 134 (2020) 110395.
[32] S.V. Hanssen, V. Daioglou, Z.J.N. Steinmann, J.C. Doelman, D.P. Van Vuuren, M.A.J. Huijbregts, *Nature Climate Change*, 10 (2020) 1023-1029.
[33] L. Reijnders, M.A.J. Huijbregts, Biofuels for road transport : a seed to wheel perspective, Springer, London, 2009.
[34] Fuels Institute, Impact of Transportation-Related Environmental Initiatives, 2020.
[35] United States Department of Energy, https://www.energy.gov/eere/bioenergy/co-optimization-fuels-engines.
[36] J.B. Dunn, E. Newes, H. Cai, Y. Zhang, A. Brooker, L. Ou, N. Mundt, A. Bhatt, S. Peterson, M. Biddy, *Energy & Environmental Science*, (2020).
[37] J.P. Szybist, S. Busch, R.L. McCormick, J.A. Pihl, D.A. Splitter, M.A. Ratcliff, C.P. Kolodziej, J.M.E. Storey, M. Moses-DeBusk, D. Vuilleumier, M. Sjöberg, C.S. Sluder, T. Rockstroh, P. Miles, *Prog. Energy Comb. Sci.*, 82 (2021) 100876.
[38] J.P. Szybist, D.A. Splitter, *Applications in Energy and Combustion Science*, 1-4 (2020) 100003.
[39] A.J. Janssen, F.W. Kremer, J.H. Baron, M. Muether, S. Pischinger, J. Klankermayer, *Energy & Fuels*, 25 (2011) 4734-4744.
[40] M. Dahmen, W. Marquardt, *Energy & Fuels*, 30 (2016) 1109-1134.
[41] M. Pelucchi, L. Cai, W. Pejpichestakul, R. Tripathi, S. Wagnon, K. Zhang, M. Raju, M. Mehl, T. Faravelli, W. Pitz, H. Pitsch, H. Curran, P.K. Senecal, *SAE Technical Paper 2019-24-0020*, (2019).
[42] Joint BioEnergy Institute (JBEI), www.jbei.org/.
[43] Great Lakes Bioenergy Research Center, www.glbrc.org/.
[44] BioEnergy Science Center, www.bioenergycenter.org/besc/.
[45] Center for Advanced Bioenergy and Bioproducts Innovation (CABBI), https://cabbi.bio/.
[46] W. Leitner, J. Klankermayer, S. Pischinger, H. Pitsch, K. Kohse-Höinghaus, *Angewandte Chemie*, 56 (2017) 5412-5452.
[47] J.E. Dec, *Proc. Combust. Inst.*, 32 (2009) 2727-2742.
[48] K. Epping, S. Aceves, R. Bechtold, J.E. Dec, *SAE Technical Paper 2002-01-1923*, (2002) 1-15.
[49] M. Sjöberg, J.E. Dec, *Proc. Combust. Inst.*, 30 (2005) 2719-2726.

[50] J.H. Mack, D. Schuler, R.H. Butt, R.W. Dibble, *Applied Energy*, 165 (2016) 612-626.
[51] R.D. Reitz, G. Duraisamy, *Prog. Energy Comb. Sci.*, 46 (2015) 12-71.
[52] A. Shah, D. Kang, S. Goldsborough, T. Rockstroh, *SAE Technical Paper 2019-01-0957*, (2019) 1-15.
[53] E.A. Ortiz-Soto, G.A. Lavoie, M.S. Wooldridge, D.N. Assanis, *International Journal of Engine Research*, 20 (2018) 304-326.
[54] J. Zádor, C.A. Taatjes, R.X. Fernandes, *Prog. Energy Comb. Sci.*, 37 (2011) 371-421.
[55] A.K. Agarwal, A.P. Singh, R.K. Maurya, *Prog. Energy Comb. Sci.*, 61 (2017) 1-56.
[56] X. Lu, D. Han, Z. Huang, *Prog. Energy Comb. Sci.*, 37 (2011) 741-783.
[57] S. Saxena, I.D. Bedoya, *Prog. Energy Comb. Sci.*, 39 (2013) 457-488.
[58] F. Battin-Leclerc, A. Rodriguez, B. Husson, O. Herbinet, P.A. Glaude, Z. Wang, Z. Cheng, F. Qi, *The journal of physical chemistry. A*, 118 (2014) 673-683.
[59] M. Mehl, W.J. Pitz, C.K. Westbrook, K. Yasunaga, C. Conroy, H.J. Curran, *Proc. Combust. Inst.*, 33 (2011) 201-208.
[60] M. Mehl, G. Vanhove, W.J. Pitz, E. Ranzi, *Combust. Flame*, 155 (2008) 756-772.
[61] X. Meng, A. Rodriguez, O. Herbinet, T. Wang, F. Battin-Leclerc, *Combust. Flame*, 181 (2017) 283-299.
[62] Y. Wu, Y. Liu, C. Tang, Z. Huang, *Combust. Flame*, 197 (2018) 30-40.
[63] S.M. Sarathy, T. Javed, F. Karsenty, A. Heufer, W. Wang, S. Park, A. Elwardany, A. Farooq, C.K. Westbrook, W.J. Pitz, M.A. Oehlschlaeger, G. Dayma, H.J. Curran, P. Dagaut, *Combust. Flame*, 161 (2014) 1444-1459.
[64] B. Rotavera, J. Zador, O. Welz, L. Sheps, A.M. Scheer, J.D. Savee, M. Akbar Ali, T.S. Lee, B.A. Simmons, D.L. Osborn, A. Violi, C.A. Taatjes, *The journal of physical chemistry. A*, 118 (2014) 10188-10200.
[65] T. Turányi, T. Nagy, I.G. Zsély, M. Cserháti, T. Varga, B.T. Szabó, I. Sedyó, P.T. Kiss, A. Zempléni, H.J. Curran, *Int. J. Chem. Kin.*, 44 (2012) 284-302.
[66] Z. Hong, D.F. Davidson, E.A. Barbour, R.K. Hanson, *Proc. Combust. Inst.*, 33 (2011) 309-316.
[67] J.A. Miller, B.C. Garrett, *Int. J. Chem. Kin.*, 29 (1997) 275-287.
[68] A.N. Pirraglia, J.V. Michael, J.W. Sutherland, R.B. Klemm, *The Journal of Physical Chemistry*, 93 (1989) 282-291.
[69] J. Warnatz, *Symposium (International) on Combustion*, 20 (1985) 845-856.
[70] K. Natarajan, P. Roth, *Combust. Flame*, 70 (1987) 267-279.
[71] M.B. Sajid, E. Es-sebbar, T. Javed, C. Fittschen, A. Farooq, *Int. J. Chem. Kin.*, 46 (2014) 275-284.
[72] Z. Hong, D.F. Davidson, K.-Y. Lam, R.K. Hanson, *Combust. Flame*, 159 (2012) 3007-3013.
[73] J. Troe, *Combust. Flame*, 158 (2011) 594-601.
[74] S.R. Sellevåg, Y. Georgievskii, J.A. Miller, *The Journal of Physical Chemistry A*, 113 (2009) 4457-4467.
[75] Q. Zhao, Y. Zhang, W. Sun, F. Deng, F. Yang, Z. Huang, *The Journal of Physical Chemistry A*, (2019).
[76] C.-W. Zhou, J.M. Simmie, H.J. Curran, *Int. J. Chem. Kin.*, 44 (2012) 155-164.
[77] J. Mendes, C.-W. Zhou, H.J. Curran, *The Journal of Physical Chemistry A*, 118 (2014) 1300-1308.
[78] J. Mendes, C.-W. Zhou, H.J. Curran, *The Journal of Physical Chemistry A*, 117 (2013) 4515-4525.
[79] C.-W. Zhou, J.M. Simmie, W.J. Pitz, H.J. Curran, *The Journal of Physical Chemistry A*, (2016).
[80] H.K. Chakravarty, R.X. Fernandes, *The journal of physical chemistry. A*, 117 (2013) 5028-5041.
[81] Z. Hong, K.-Y. Lam, R. Sur, S. Wang, D.F. Davidson, R.K. Hanson, *Proc. Combust. Inst.*, 34 (2013) 565-571.
[82] D.D.Y. Zhou, K. Han, P. Zhang, L.B. Harding, M.J. Davis, R.T. Skodje, *The Journal of Physical Chemistry A*, 116 (2012) 2089-2100.
[83] P.D. Lightfoot, B. Veyret, R. Lesclaux, *Chemical Physics Letters*, 150 (1988) 120-126.
[84] J. Thiébaud, C. Fittschen, *Applied Physics B*, 85 (2006) 383-389.
[85] D. Stone, D.M. Rowley, *Phys Chem Chem Phys*, 7 (2005) 2156-2163.

[86] M.J. Pilling, Low-temperature combustion and autoignition, Elsevier, Amsterdam ; New York, 1997.
[87] J. Zádor, R.X. Fernandes, C.A. Taatjes, *Prog. Energy Comb. Sci.*, 37 (2011) 371-421.
[88] H.J. Curran, *Proc. Combust. Inst.*, 37 (2019) 57-81.
[89] Y. Ju, *Proc. Combust. Inst.*, (2020).
[90] J.D. Savee, E. Papajak, B. Rotavera, H. Huang, A.J. Eskola, O. Welz, L. Sheps, C.A. Taatjes, J. Zádor, D.L. Osborn, *Science*, 347 (2015) 643-646.
[91] L.S. Tran, B. Sirjean, P.-A. Glaude, R. Fournet, F. Battin-Leclerc, *Energy*, 43 (2012) 4-18.
[92] E.J. Hamilton, S. Korcek, L.R. Mahoney, M. Zinbo, *Int. J. Chem. Kin.*, 12 (1980) 577-603.
[93] R.K. Jensen, S. Korcek, L.R. Mahoney, M. Zinbo, *Journal of the American Chemical Society*, 101 (1979) 7574-7584.
[94] R.K. Jensen, S. Korcek, L.R. Mahoney, M. Zinbo, *Journal of the American Chemical Society*, 103 (1981) 1742-1749.
[95] R.K. Jensen, S. Korcek, M. Zinbo, M.D. Johnson, *Int. J. Chem. Kin.*, 22 (1990) 1095-1107.
[96] D. Healy, N.S. Donato, C.J. Aul, E.L. Petersen, C.M. Zinner, G. Bourque, H.J. Curran, *Combust. Flame*, 157 (2010) 1526-1539.
[97] B.W. Weber, K. Kumar, Y. Zhang, C.-J. Sung, *Combust. Flame*, 158 (2011) 809-819.
[98] K.A. Heufer, J. Bugler, H.J. Curran, *Proc. Combust. Inst.*, 34 (2013) 511-518.
[99] F. Battin-Leclerc, *Prog. Energy Comb. Sci.*, 34 (2008) 440-498.
[100] S.M. Sarathy, P. Oßwald, N. Hansen, K. Kohse-Höinghaus, *Prog. Energy Comb. Sci.*, 44 (2014) 40-102.
[101] Z. Wang, O. Herbinet, N. Hansen, F. Battin-Leclerc, *Prog. Energy Comb. Sci.*, 73 (2019) 132-181.
[102] K. Kohse-Hoinghaus, P. Osswald, T.A. Cool, T. Kasper, N. Hansen, F. Qi, C.K. Westbrook, P.R. Westmoreland, *Angew Chem Int Edit*, 49 (2010) 3572-3597.
[103] D. Sandhya, P. Jogam, L.K. Narnoliya, A. Srivastava, J.S. Jadaun, *Biorefinery Production Technologies for Chemicals and Energy*, (2020) 289-312.
[104] E.M. Aro, *Ambio*, 45 (2016) S24-S31.
[105] J.C. Mortimer, *Experimental Biology and Medicine*, 244 (2018) 323-331.
[106] S. Jagadevan, A. Banerjee, C. Banerjee, C. Guria, R. Tiwari, M. Baweja, P. Shukla, *Biotechnology for Biofuels*, 11 (2018) 185.
[107] A. Ghosh, *Current Metabolomics*, 4 (2016) 5-13.
[108] D.R. Georgianna, S.P. Mayfield, *Nature*, 488 (2012) 329-335.
[109] C.A. Rabinovitch-Deere, J.W.K. Oliver, G.M. Rodriguez, S. Atsumi, *Chemical Reviews*, 113 (2013) 4611-4632.
[110] B.G. Harvey, W.W. Merriman, T.A. Koontz, *Energy & Fuels*, (2015).
[111] T.R. Carlson, T.P. Vispute, G.W. Huber, *Chemsuschem*, 1 (2008) 397-400.
[112] C.F. Ryan, C.M. Moore, J.H. Leal, T.A. Semelsberger, J.K. Banh, J. Zhu, C.S. McEnally, L.D. Pfefferle, A.D. Sutton, *Sustainable Energy & Fuels*, (2020).
[113] J. Sun, Y. Wang, *ACS Catalysis*, 4 (2014) 1078-1090.
[114] A. Bohre, S. Dutta, B. Saha, M.M. Abu-Omar, *ACS Sustainable Chemistry & Engineering*, 3 (2015) 1263-1277.
[115] D.M. Alonso, J.Q. Bond, J.A. Dumesic, *Green Chemistry*, 12 (2010) 1493-1513.
[116] G.W. Huber, S. Iborra, A. Corma, *Chemical Reviews*, 106 (2006) 4044-4098.
[117] M.A. Griffin, D.J. Spakowicz, T.A. Gianoulis, S.A. Strobel, *Microbiology*, 156 (2010) 3814-3829.
[118] H.R. Beller, T.S. Lee, L. Katz, *Natural Product Reports*, 32 (2015) 1508-1526.
[119] R.M. Lennen, B.F. Pfleger, *Current Opinion in Biotechnology*, 24 (2013) 1044-1053.
[120] P.P. Peralta-Yahya, J.D. Keasling, *Biotechnology Journal*, 5 (2010) 147-162.
[121] P.P. Peralta-Yahya, M. Ouellet, R. Chan, A. Mukhopadhyay, J.D. Keasling, T.S. Lee, *Nat Commun*, 2 (2011) 483.
[122] P.P. Peralta-Yahya, F. Zhang, S.B. Cardayre, J.D. Keasling, *Nature*, 488 (2012).
[123] M.C. Cuellar, L.A.M. van der Wielen, *Current Opinion in Biotechnology*, 33 (2015) 39-45.
[124] S. Verhelst, J.W.G. Turner, L. Sileghem, J. Vancoillie, *Prog. Energy Comb. Sci.*, 70 (2019) 43-88.

[125] D.A. Ruddy, J.E. Hensley, C.P. Nash, E.C.D. Tan, E. Christensen, C.A. Farberow, F.G. Baddour, K.M. Van Allsburg, J.A. Schaidle, *Nature Catalysis*, 2 (2019) 632-640.
[126] M. Rutkowska, D. Macina, N. Mirocha-Kubień, Z. Piwowarska, L. Chmielarz, *Applied Catalysis B: Environmental*, 174–175 (2015) 336-343.
[127] M. Xu, J.H. Lunsford, D.W. Goodman, A. Bhattacharyya, *Applied Catalysis A: General*, 149 (1997) 289-301.
[128] R.L. Wingad, E.J.E. Bergström, M. Everett, K.J. Pellow, D.F. Wass, *Chemical Communications*, 52 (2016) 5202-5204.
[129] J. Wang, B. Yang, Y. Li, Z. Tian, T. Zhang, F. Qi, K. Nakajima, *International Journal of Mass Spectrometry*, 263 (2007) 30-37.
[130] C. Pera, V. Knop, *Fuel*, 96 (2012) 59-69.
[131] Y. Briker, Z. Ring, A. Iacchelli, N. McLean, P.M. Rahimi, C. Fairbridge, R. Malhotra, M.A. Coggiola, S.E. Young, *Energy & Fuels*, 15 (2001) 23-37.
[132] W.J. Pitz, C.J. Mueller, *Prog. Energy Comb. Sci.*, 37 (2011) 330-350.
[133] Y. Briker, Z. Ring, A. Iacchelli, N. McLean, C. Fairbridge, R. Malhotra, M.A. Coggiola, S.E. Young, *Energy & Fuels*, 15 (2001) 996-1002.
[134] S.M. Paap, T.H. West, D.K. Manley, E.J. Steen, H.R. Beller, J.D. Keasling, D.C. Dibble, S. Chang, B.A. Simmons, *Biomass and Bioenergy*, 49 (2013) 49-62.
[135] H.H. Khoo, *Renewable and Sustainable Energy Reviews*, 46 (2015) 100-119.
[136] J. Littlewood, M. Guo, W. Boerjan, R.J. Murphy, *Biotechnology for Biofuels* 7(2014) 1-12.
[137] J. Clomburg, R. Gonzalez, *Appl Microbiol Biotechnol*, 86 (2010) 419-434.
[138] G. Koçar, N. Civaş, *Renewable and Sustainable Energy Reviews*, 28 (2013) 900-916.
[139] J.N. Chheda, G.W. Huber, J.A. Dumesic, *Angewandte Chemie International Edition*, 46 (2007) 7164-7183.
[140] Y. Sun, J. Cheng, *Bioresource Technology*, 83 (2002) 1-11.
[141] J. Han, J.S. Luterbacher, D.M. Alonso, J.A. Dumesic, C.T. Maravelias, *Bioresource Technology*, 182 (2015) 258-266.
[142] P.V. Harris, F. Xu, N.E. Kreel, C. Kang, S. Fukuyama, *Current Opinion in Chemical Biology*, 19 (2014) 162-170.
[143] C. Louime, H. Uckelmann, *International Journal of Molecular Sciences*, 9 (2008) 838.
[144] L.D. Schmidt, P.J. Dauenhauer, *Nature*, 447 (2007) 914-915.
[145] C.C. Geddes, I.U. Nieves, L.O. Ingram, *Current Opinion in Biotechnology*, 22 (2011) 312-319.
[146] M. Enquist-Newman, A.M.E. Faust, D.D. Bravo, C.N.S. Santos, R.M. Raisner, A. Hanel, P. Sarvabhowman, C. Le, D.D. Regitsky, S.R. Cooper, L. Peereboom, A. Clark, Y. Martinez, J. Goldsmith, M.Y. Cho, P.D. Donohoue, L. Luo, B. Lamberson, P. Tamrakar, E.J. Kim, J.L. Villari, A. Gill, S.A. Tripathi, P. Karamchedu, C.J. Paredes, V. Rajgarhia, H.K. Kotlar, R.B. Bailey, D.J. Miller, N.L. Ohler, C. Swimmer, Y. Yoshikuni, *Nature*, 505 (2014) 239-243.
[147] P. Xu, M.A.G. Koffas, *Biofuels*, 1 (2010) 493-504.
[148] K. Zhang, M.R. Sawaya, D.S. Eisenberg, J.C. Liao, *Proceedings of the National Academy of Sciences*, 105 (2008) 20653-20658.
[149] S. Atsumi, T. Hanai, J.C. Liao, *Nature*, 451 (2008) 86-89.
[150] M.R. Connor, J.C. Liao, *Current Opinion in Biotechnology*, 20 (2009) 307-315.
[151] D. Siebert, V. Wendisch, *Biotechnology for Biofuels*, 8 (2015) 91.
[152] R. Jain, X. Sun, Q. Yuan, Y. Yan, *ACS Synthetic Biology*, 4 (2015) 746-756.
[153] Y. Jun Choi, J. Hwan Park, T. Yong Kim, S. Yup Lee, *Metabolic Engineering*, 14 (2012) 477-486.
[154] D. Sun, S. Sato, W. Ueda, A. Primo, H. Garcia, A. Corma, *Green Chemistry*, 18 (2016) 2579-2597.
[155] J.P. Torella, C.J. Gagliardi, J.S. Chen, D.K. Bediako, B. Colón, J.C. Way, P.A. Silver, D.G. Nocera, *Proceedings of the National Academy of Sciences*, 112 (2015) 2337-2342.
[156] K. Inokuma, J.C. Liao, M. Okamoto, T. Hanai, *Journal of Bioscience and Bioengineering*, 110 (2010) 696-701.

[157] Y. Soma, K. Inokuma, T. Tanaka, C. Ogino, A. Kondo, M. Okamoto, T. Hanai, *Journal of Bioscience and Bioengineering*, 114 (2012) 80-85.
[158] D. Lips, J.M. Schuurmans, F. Branco dos Santos, K.J. Hellingwerf, *Energy & Environmental Science*, 11 (2018) 10-22.
[159] G. Bokinsky, P.P. Peralta-Yahya, A. George, B.M. Holmes, E.J. Steen, J. Dietrich, T. Soon Lee, D. Tullman-Ercek, C.A. Voigt, B.A. Simmons, J.D. Keasling, *Proceedings of the National Academy of Sciences*, 108 (2011) 19949-19954.
[160] L.J. Gallego, A. Escobar, M. Peñuela, J.D. Peña, L.A. Rios, *Fuel*, 143 (2015) 399-403.
[161] C. Jin, M. Yao, H. Liu, C.-f.F. Lee, J. Ji, *Renewable and Sustainable Energy Reviews*, 15 (2011) 4080-4106.
[162] K. Breitkreuz, A. Menne, A. Kraft, *Biofuels, Bioproducts and Biorefining*, 8 (2014) 504-515.
[163] B.G. Harvey, H.A. Meylemans, *Journal of Chemical Technology & Biotechnology*, 86 (2011) 2-9.
[164] K. Melin, M. Hurme, *Cellulose Chemistry and Technology*, 44 (2010) 117-137.
[165] P. Dürre, *Biotechnology Journal*, 2 (2007) 1525-1534.
[166] P. Dürre, *Annals of the New York Academy of Sciences*, 1125 (2008) 353-362.
[167] C.R. Shen, E.I. Lan, Y. Dekishima, A. Baez, K.M. Cho, J.C. Liao, *Applied and Environmental Microbiology*, 77 (2011) 2905-2915.
[168] C.-T. Chen, J.C. Liao, *FEMS Microbiology Letters*, 363 (2016).
[169] P. Jambunathan, K. Zhang, *Current Opinion in Biotechnology*, 29 (2014) 1-7.
[170] N. Qureshi, T.C. Ezeji, *Biofuels, Bioproducts and Biorefining*, 2 (2008) 319-330.
[171] N. Qureshi, B.C. Saha, M.A. Cotta, *Biomass and Bioenergy*, 32 (2008) 176-183.
[172] N. Qureshi, B.C. Saha, R.E. Hector, S.R. Hughes, M.A. Cotta, *Biomass and Bioenergy*, 32 (2008) 168-175.
[173] N. Qureshi, B.C. Saha, R.E. Hector, B. Dien, S. Hughes, S. Liu, L. Iten, M.J. Bowman, G. Sarath, M.A. Cotta, *Biomass and Bioenergy*, 34 (2010) 566-571.
[174] N. Qureshi, B.C. Saha, B. Dien, R.E. Hector, M.A. Cotta, *Biomass and Bioenergy*, 34 (2010) 559-565.
[175] T.C. Ezeji, N. Qureshi, H.P. Blaschek, *Current Opinion in Biotechnology*, 18 (2007) 220-227.
[176] C.R. Fischer, D. Klein-Marcuschamer, G. Stephanopoulos, *Metabolic Engineering*, 10 (2008) 295-304.
[177] K.D. Yang, C.W. Lee, K. Jin, S.W. Im, K.T. Nam, *The Journal of Physical Chemistry Letters*, 8 (2017) 538-545.
[178] C. Xue, X. Zhang, J. Wang, M. Xiao, L. Chen, F. Bai, *Biotechnology for Biofuels*, 10 (2017) 148.
[179] M. Saini, Z.W. Wang, C.-J. Chiang, Y.-P. Chao, *Biotechnology for Biofuels*, 10 (2017) 173.
[180] W. Jiang, J. Zhao, Z. Wang, S.-T. Yang, *Bioresource Technology*, 163 (2014) 172-179.
[181] Z. Chen, Y. Wu, J. Huang, D. Liu, *Bioresource Technology*, 197 (2015) 260-265.
[182] B.-R. Oh, S.-Y. Heo, S.-M. Lee, W.-K. Hong, J.M. Park, Y.R. Jung, D.-H. Kim, J.-H. Sohn, J.-W. Seo, C.H. Kim, *Biotechnol Lett*, 36 (2014) 57-62.
[183] L. Zhang, R. Singh, S. D, Z. Guo, J. Li, F. Chen, Y. He, X. Guan, Y.C. Kang, J.-K. Lee, *Green Chemistry*, 20 (2018) 230-242.
[184] Y. Zhang, D. Liu, Z. Chen, Chapter 12 - Synthetic Biology Approaches for the Production of 2-Butanol, in: S.P. Singh, A. Pandey, G. Du, S. Kumar (Eds.) Current Developments in Biotechnology and Bioengineering, Elsevier, 2019, pp. 295-309.
[185] G. Strobel, *Biotechnol Lett*, (2015) 1-10.
[186] H. Tao, D. Guo, Y. Zhang, Z. Deng, T. Liu, *Biotechnology for Biofuels*, 8 (2015) 92.
[187] A. Baez, K.-M. Cho, J.C. Liao, *Appl Microbiol Biotechnol*, 90 (2011) 1681-1690.
[188] O.K. Lee, D.H. Hur, D.T.N. Nguyen, E.Y. Lee, *Biofuels, Bioproducts and Biorefining*, (2016) n/a-n/a.
[189] S. Sherkhanov, T.P. Korman, S. Chan, S. Faham, H. Liu, M.R. Sawaya, W.-T. Hsu, E. Vikram, T. Cheng, J.U. Bowie, *Nature Communications*, 11 (2020) 4292.

[190] X.-L. Li, J. Deng, J. Shi, T. Pan, C.-G. Yu, H.-J. Xu, Y. Fu, *Green Chemistry*, 17 (2015) 1038-1046.
[191] Y.-F. Ma, H. Wang, G.-Y. Xu, X.-H. Liu, Y. Zhang, Y. Fu, *Chinese Chemical Letters*, 28 (2017) 1153-1158.
[192] Y. Wang, M. Zhou, T. Wang, G. Xiao, *Catalysis Letters*, 145 (2015) 1557-1565.
[193] F. Chen, N. Li, X. Yang, L. Li, G. Li, S. Li, W. Wang, Y. Hu, A. Wang, Y. Cong, X. Wang, T. Zhang, *ACS Sustainable Chemistry & Engineering*, 4 (2016) 6160-6166.
[194] A.F. Cann, J.C. Liao, *Appl Microbiol Biotechnol*, 85 (2010) 893-899.
[195] R.J. Marcheschi, H. Li, K. Zhang, E.L. Noey, S. Kim, A. Chaubey, K.N. Houk, J.C. Liao, *ACS Chemical Biology*, 7 (2012) 689-697.
[196] W. Chanmanee, M.F. Islam, B.H. Dennis, F.M. MacDonnell, *Proceedings of the National Academy of Sciences*, (2016).
[197] K.W. George, M.G. Thompson, A. Kang, E. Baidoo, G. Wang, L.J.G. Chan, P.D. Adams, C.J. Petzold, J.D. Keasling, T. Soon Lee, *Scientific Reports*, 5 (2015) 11128.
[198] M.R. Connor, A.F. Cann, J.C. Liao, *Appl Microbiol Biotechnol*, 86 (2010) 1155-1164.
[199] M.R. Connor, J.C. Liao, *Appl Environ Microbiol*, 74 (2008) 5769-5775.
[200] M.R. Connor, S. Atsumi, *Journal of biomedicine & biotechnology*, 2010 (2010).
[201] C. Dellomonaco, F. Fava, R. Gonzalez, *Microbial Cell Factories*, 9 (2010) 3.
[202] S.K. Lee, H. Chou, T.S. Ham, T.S. Lee, J.D. Keasling, *Current Opinion in Biotechnology*, 19 (2008) 556-563.
[203] C.B. Eiben, T. Tian, M.G. Thompson, D. Mendez-Perez, N. Kaplan, G. Goyal, J. Chiniquy, N.J. Hillson, T.S. Lee, J.D. Keasling, *ACS Synthetic Biology*, (2020).
[204] Y. Zheng, Q. Liu, L. Li, W. Qin, J. Yang, H. Zhang, X. Jiang, T. Cheng, W. Liu, X. Xu, M. Xian, *Biotechnology for Biofuels*, 6 (2013) 57.
[205] Y. Sasaki, T. Eng, R.A. Herbert, J. Trinh, Y. Chen, A. Rodriguez, J. Gladden, B.A. Simmons, C.J. Petzold, A. Mukhopadhyay, *Biotechnology for Biofuels*, 12 (2019) 41.
[206] H. Ben, W. Mu, Y. Deng, A.J. Ragauskas, *Fuel*, 103 (2013) 1148-1153.
[207] D.D. Laskar, B. Yang, H. Wang, J. Lee, *Biofuels, Bioproducts and Biorefining*, 7 (2013) 602-626.
[208] P. Varanasi, P. Singh, M. Auer, P.D. Adams, B.A. Simmons, S. Singh, *Biotechnology for Biofuels*, 6 (2013) 1-9.
[209] K. Ulonska, A. Voll, W. Marquardt, *Energy & Fuels*, 30 (2016) 445-456.
[210] N. Ahmad, F. Abnisa, W.M.A. Wan Daud, *Fuel*, 218 (2018) 227-235.
[211] Y. He, Y. Bie, J. Lehtonen, R. Liu, J. Cai, *Fuel*, 239 (2019) 1015-1027.
[212] J. Donnelly, R. Horton, K. Gopalan, C.D. Bannister, C.J. Chuck, *Energy & Fuels*, 30 (2016) 294-301.
[213] J. Julis, W. Leitner, *Angewandte Chemie International Edition*, 51 (2012) 8615-8619.
[214] Q. Bu, H. Lei, S. Ren, L. Wang, Q. Zhang, J. Tang, R. Ruan, *Bioresource Technology*, 108 (2012) 274-279.
[215] Q. Lu, X.-n. Ye, Z.-b. Zhang, M.-S. Cui, H.-q. Guo, W. Qi, C.-q. Dong, Y.-p. Yang, *Energy & Fuels*, 30 (2016) 10618-10626.
[216] F. Zhang, S. Rodriguez, J.D. Keasling, *Current Opinion in Biotechnology*, 22 (2011) 775-783.
[217] A.I. Ramírez, S.K. Aggarwal, S. Som, T.P. Rutter, D.E. Longman, *Fuel*, 136 (2014) 89-102.
[218] L. Coniglio, J.A.P. Coutinho, J.-Y. Clavier, F. Jolibert, J. Jose, I. Mokbel, D. Pillot, M.-N. Pons, M. Sergent, V. Tschamber, *Prog. Energy Comb. Sci.*, 43 (2014) 1-35.
[219] L. Zhu, *Biofuels, Bioproducts and Biorefining*, 8 (2014) 7-15.
[220] S. Pinzi, D. Leiva, I. López-García, M.D. Redel-Macías, M.P. Dorado, *Biofuels, Bioproducts and Biorefining*, 8 (2014) 126-143.
[221] T. Ito, Y. Sakurai, Y. Kakuta, M. Sugano, K. Hirano, *Fuel Processing Technology*, 94 (2012) 47-52.
[222] S. Vranckx, J. Beeckmann, W.A. Kopp, C. Lee, L. Cai, H.K. Chakravarty, H. Olivier, K. Leonhard, H. Pitsch, R.X. Fernandes, *Combust. Flame*, 160 (2013) 2680-2692.

[223] W.S. Teo, H. Ling, A.-Q. Yu, M.W. Chang, *Biotechnology for Biofuels*, 8 (2015) 1-9.
[224] H. Yoneda, D.J. Tantillo, S. Atsumi, *Chemsuschem*, 7 (2014) 92-95.
[225] Y. Gong, L. Lin, J. Shi, S. Liu, *Molecules*, 15 (2010) 7946.
[226] Y. Gong, L. Lin, *Molecules*, 16 (2011) 2714.
[227] E.R. Sacia, M. Balakrishnan, M.H. Deaner, K.A. Goulas, F.D. Toste, A.T. Bell, *Chemsuschem*, 8 (2015) 1726-1736.
[228] A. Multer, N. McGraw, K. Hohn, P. Vadlani, *Ind. Eng. Chem. Res.*, 52 (2013) 56-60.
[229] P. Anbarasan, Z.C. Baer, S. Sreekumar, E. Gross, J.B. Binder, H.W. Blanch, D.S. Clark, F.D. Toste, *Nature*, 491 (2012) 235-239.
[230] G.A. Strobel, B. Knighton, K. Kluck, Y. Ren, T. Livinghouse, M. Griffin, D. Spakowicz, J. Sears, *Microbiology*, 154 (2008) 3319-3328.
[231] A. Demirbas, *Fuel Processing Technology*, 88 (2007) 591-597.
[232] É. Le Roux, M. Chaouch, P.N. Diouf, T. Stevanovic, *Biomass and Bioenergy*, 81 (2015) 202-209.
[233] M. Hronec, K. Fulajtarová, *Catalysis Communications*, 24 (2012) 100-104.
[234] M. Hronec, K. Fulajtarová, T. Liptaj, *Applied Catalysis A: General*, 437-438 (2012) 104-111.
[235] M. Hronec, K. Fulajtárova, M. Mičušik, *Applied Catalysis A: General*, 468 (2013) 426-431.
[236] M. Hronec, K. Fulajtárová, I. Vávra, T. Soták, E. Dobročka, M. Mičušík, *Applied Catalysis B: Environmental*, 181 (2016) 210-219.
[237] R. Fang, H. Liu, R. Luque, Y. Li, *Green Chemistry*, 17 (2015) 4183-4188.
[238] J. Guo, G. Xu, Z. Han, Y. Zhang, Y. Fu, Q. Guo, *ACS Sustainable Chemistry & Engineering*, 2 (2014) 2259-2266.
[239] G.A. Strobel, B. Knighton, K. Kluck, Y. Ren, T. Livinghouse, M. Griffin, D. Spakowicz, J. Sears, *Microbiology*, 156 (2010) 3830-3833.
[240] Q. Bu, H. Lei, L. Wang, G. Yadavalli, Y. Wei, X. Zhang, L. Zhu, Y. Liu, *Journal of Analytical and Applied Pyrolysis*, 112 (2015) 74-79.
[241] H. Pucher, N. Schwaiger, R. Feiner, L. Ellmaier, P. Pucher, B.S. Chernev, M. Siebenhofer, *Green Chemistry*, 17 (2015) 1291-1298.
[242] J.M. Gladden, C.A. Taatjes, C. Gao, G. O'Bryan, A.J. Powell, A.M. Scheer, K. Turner, W. Wu, E.T. Yu, Sandia National Laboratories, Tailoring Next-Generation Biofuels and their Combustion in Next-Generation Engines, 2013.
[243] H.-Y. Zheng, Y.-L. Zhu, Z.-Q. Bai, L. Huang, H.-W. Xiang, Y.-W. Li, *Green Chemistry*, 8 (2006) 107-109.
[244] D.W. Rackemann, W.O.S. Doherty, *Biofuels, Bioproducts and Biorefining*, 5 (2011) 198-214.
[245] E.-B. Goh, E.E.K. Baidoo, J.D. Keasling, H.R. Beller, *Applied and Environmental Microbiology*, 78 (2012) 70-80.
[246] J. Street, F. Yu, *Biofuels*, 2 (2011) 677-691.
[247] M. Cai, V. Subramanian, V.V. Sushkevich, V.V. Ordomsky, A.Y. Khodakov, *Applied Catalysis A: General*, 502 (2015) 370-379.
[248] Q. Ge, Y. Huang, F. Qiu, S. Li, *Applied Catalysis A: General*, 167 (1998) 23-30.
[249] D.M. Brown, B.L. Bhatt, T.H. Hsiung, J.J. Lewnard, F.J. Waller, *Catalysis Today*, 8 (1991) 279-304.
[250] T. Shikada, Y. Ohno, T. Ogawa, M. Ono, M. Mizuguchi, K. Tomura, K. Fujimoto, Direct Synthesis of Dimethyl Ether form Synthesis Gas, in: D.S.F.F.A.V. A. Parmaliana, F. Arena (Eds.) Studies in Surface Science and Catalysis, Elsevier, 1998, pp. 515-520.
[251] Y. Adachi, M. Komoto, I. Watanabe, Y. Ohno, K. Fujimoto, *Fuel*, 79 (2000) 229-234.
[252] D.F. Carvalho, G.C. Almeida, R.S. Monteiro, C.J.A. Mota, *Energy & Fuels*, 34 (2020) 7269-7274.
[253] T.K. Phung, G. Busca, *Catalysis Communications*, 68 (2015) 110-115.
[254] A. Rahmanian, H.S. Ghaziaskar, *The Journal of Supercritical Fluids*, 78 (2013) 34-41.
[255] Conversion of Biodiesel By-Product Glycerol to Fuel Ethers over Different Solid Acid Catalysts, https://www.degruyter.com/view/j/ijcre.2010.8.1/ijcre.2010.8.1.2149/ijcre.2010.8.1.2149.xml, 2010.

[256] K.F. Yee, A.R. Mohamed, S.H. Tan, *Renewable and Sustainable Energy Reviews*, 22 (2013) 604-620.
[257] Rapid facile biofuel synthesis by microwave irradiation, 2012.
[258] J.F. Izquierdo, M. Montiel, I. Palés, P.R. Outón, M. Galán, L. Jutglar, M. Villarrubia, M. Izquierdo, M.P. Hermo, X. Ariza, *Renewable and Sustainable Energy Reviews*, 16 (2012) 6717-6724.
[259] R. Cataluña, Z. Shah, V. Venturi, N.R. Caetano, B.P. da Silva, C.M.N. Azevedo, R. da Silva, P.A.Z. Suarez, L.P. Oliveira, *Fuel*, 228 (2018) 226-233.
[260] N.A. Huq, X. Huo, G.R. Hafenstine, S.M. Tifft, J. Stunkel, E.D. Christensen, G.M. Fioroni, L. Fouts, R.L. McCormick, P.A. Cherry, C.S. McEnally, L.D. Pfefferle, M.R. Wiatrowski, P.T. Benavides, M.J. Biddy, R.M. Connatser, M.D. Kass, T.L. Alleman, P.C. St. John, S. Kim, D.R. Vardon, *Proceedings of the National Academy of Sciences*, 116 (2019) 26421.
[261] A. Voll, W. Marquardt, *Biofuels, Bioproducts and Biorefining*, 6 (2012) 292-301.
[262] M.J. Climent, A. Corma, S. Iborra, *Green Chemistry*, 16 (2014) 516-547.
[263] G. Li, N. Li, Z. Wang, C. Li, A. Wang, X. Wang, Y. Cong, T. Zhang, *Chemsuschem*, 5 (2012) 1958-1966.
[264] S. Li, N. Li, G. Li, L. Li, A. Wang, Y. Cong, X. Wang, T. Zhang, *Green Chemistry*, 17 (2015) 3644-3652.
[265] Y.-L. Zhu, H.-W. Xiang, Y.-W. Li, H. Jiao, G.-S. Wu, B. Zhong, G.-Q. Guo, *New Journal of Chemistry*, 27 (2003) 208-210.
[266] J. Zhang, L. Lin, S. Liu, *Energy & Fuels*, 26 (2012) 4560-4567.
[267] F. Cherubini, A.H. Strømman, *Biofuels, Bioproducts and Biorefining*, 5 (2011) 548-561.
[268] W. Geng, W. Li, L. Liu, J. Liu, L. Liu, X. Kong, *Fuel*, 259 (2020) 116267.
[269] Y. Roman-Leshkov, C.J. Barrett, Z.Y. Liu, J.A. Dumesic, *Nature*, 447 (2007) 982-985.
[270] M. Chidambaram, A.T. Bell, *Green Chemistry*, 12 (2010) 1253-1262.
[271] J.B. Binder, R.T. Raines, *Journal of the American Chemical Society*, 131 (2009) 1979-1985.
[272] T. Thananatthanachon, T.B. Rauchfuss, *Angewandte Chemie International Edition*, 49 (2010) 6616-6618.
[273] P.P. Upare, D.W. Hwang, Y.K. Hwang, U.H. Lee, D.-Y. Hong, J.-S. Chang, *Green Chemistry*, 17 (2015) 3310-3313.
[274] J. Jae, W. Zheng, A.M. Karim, W. Guo, R.F. Lobo, D.G. Vlachos, *ChemCatChem*, 6 (2014) 848-856.
[275] B.R. Caes, R.E. Teixeira, K.G. Knapp, R.T. Raines, *ACS Sustainable Chemistry & Engineering*, 3 (2015) 2591-2605.
[276] P. Yang, Q. Xia, X. Liu, Y. Wang, *Fuel*, 187 (2017) 159-166.
[277] C. Liu, C. Zhang, K. Liu, Y. Wang, G. Fan, S. Sun, J. Xu, Y. Zhu, Y. Li, *Biomass and Bioenergy*, 72 (2015) 189-199.
[278] Z. Gao, C. Li, G. Fan, L. Yang, F. Li, *Applied Catalysis B: Environmental*, 226 (2018) 523-533.
[279] L.M. Esteves, M.H. Brijaldo, E.G. Oliveira, J.J. Martinez, H. Rojas, A. Caytuero, F.B. Passos, *Fuel*, 270 (2020) 117524.
[280] J.-P. Lange, E. van der Heide, J. van Buijtenen, R. Price, *Chemsuschem*, 5 (2012) 150-166.
[281] W. Yang, A. Sen, *Chemsuschem*, 3 (2010) 597-603.
[282] F.M.A. Geilen, B. Engendahl, A. Harwardt, W. Marquardt, J. Klankermayer, W. Leitner, *Angewandte Chemie International Edition*, 49 (2010) 5510-5514.
[283] X.-L. Du, Q.-Y. Bi, Y.-M. Liu, Y. Cao, H.-Y. He, K.-N. Fan, *Green Chemistry*, 14 (2012) 935-939.
[284] I. Obregón, I. Gandarias, N. Miletić, A. Ocio, P.L. Arias, *Chemsuschem*, 8 (2015) 3483-3488.
[285] F. Dong, Y. Zhu, G. Ding, J. Cui, X. Li, Y. Li, *Chemsuschem*, 8 (2015) 1534-1537.
[286] R.M. West, E.L. Kunkes, D.A. Simonetti, J.A. Dumesic, *Catalysis Today*, 147 (2009) 115-125.
[287] A. Osmont, L. Catoire, P. Escot Bocanegra, I. Gökalp, B. Thollas, J.A. Kozinski, *Combust. Flame*, 157 (2010) 1230-1234.
[288] H. Frauenrath, T. Philipps, *Liebigs Annalen der Chemie*, 1985 (1985) 1951-1961.
[289] H.C. Brown, J.V.N.V. Prasad, S.H. Zee, *The Journal of Organic Chemistry*, 50 (1985) 1582-1589.

[290] Furanics: A Novel Diesel Fuel with Superior Characteristics, http://dx.doi.org/10.4271/2009-01-2767, 2009.
[291] Q. Cao, J. Guan, G. Peng, T. Hou, J. Zhou, X. Mu, *Catalysis Communications*, 58 (2015) 76-79.
[292] W. Xu, Q. Xia, Y. Zhang, Y. Guo, Y. Wang, G. Lu, *Chemsuschem*, 4 (2011) 1758-1761.
[293] A. Tomsheck, G. Strobel, E. Booth, B. Geary, D. Spakowicz, B. Knighton, C. Floerchinger, J. Sears, O. Liarzi, D. Ezra, *Microb Ecol*, 60 (2010) 903-914.
[294] B. Pholjaroen, N. Li, J. Yang, G. Li, W. Wang, A. Wang, Y. Cong, X. Wang, T. Zhang, *Ind. Eng. Chem. Res.*, 53 (2014) 13618-13625.
[295] O. Welz, J. Zador, J.D. Savee, M.Y. Ng, G. Meloni, R.X. Fernandes, L. Sheps, B.A. Simmons, T.S. Lee, D.L. Osborn, C.A. Taatjes, *Phys Chem Chem Phys*, 14 (2012) 3112-3127.
[296] O. Welz, J. Zador, J.D. Savee, L. Sheps, D.L. Osborn, C.A. Taatjes, *The journal of physical chemistry. A*, 117 (2013) 11983-12001.
[297] J. Zador, H. Huang, O. Welz, J. Zetterberg, D.L. Osborn, C.A. Taatjes, *Phys Chem Chem Phys*, 15 (2013) 10753-10760.
[298] A.J. Eskola, O. Welz, J.D. Savee, D.L. Osborn, C.A. Taatjes, *Proc. Combust. Inst.*, 34 (2013) 385-392.
[299] A.M. Scheer, O. Welz, J. Zador, D.L. Osborn, C.A. Taatjes, *Phys Chem Chem Phys*, (2014).
[300] J.D. Savee, O. Welz, C.A. Taatjes, D.L. Osborn, *Phys Chem Chem Phys*, 14 (2012) 10410-10423.
[301] O. Welz, S.J. Klippenstein, L.B. Harding, C.A. Taatjes, J. Zádor, *The Journal of Physical Chemistry Letters*, 4 (2013) 350-354.
[302] A.M. Scheer, O. Welz, D.Y. Sasaki, D.L. Osborn, C.A. Taatjes, *Journal of the American Chemical Society*, 135 (2013) 14256-14265.
[303] A.M. Knepp, G. Meloni, L.E. Jusinski, C.A. Taatjes, C. Cavallotti, S.J. Klippenstein, *Phys Chem Chem Phys*, 9 (2007) 4315-4331.
[304] C.A. Taatjes, *The Journal of Physical Chemistry A*, 110 (2006) 4299-4312.
[305] J.D. DeSain, S.J. Klippenstein, J.A. Miller, C.A. Taatjes, *The Journal of Physical Chemistry A*, 108 (2004) 7127-7128.
[306] J.D. DeSain, S.J. Klippenstein, J.A. Miller, C.A. Taatjes, *The Journal of Physical Chemistry A*, 107 (2003) 4415-4427.
[307] J.D. DeSain, E.P. Clifford, C.A. Taatjes, *The Journal of Physical Chemistry A*, 105 (2001) 3205-3213.
[308] E.P. Clifford, J.T. Farrell, J.D. DeSain, C.A. Taatjes, *The Journal of Physical Chemistry A*, 104 (2000) 11549-11560.
[309] M.W. Chen, B. Rotavera, W. Chao, J. Zador, C.A. Taatjes, *Phys Chem Chem Phys*, 20 (2018) 10815-10825.
[310] D.L. Osborn, P. Zou, H. Johnsen, C.C. Hayden, C.A. Taatjes, V.D. Knyazev, S.W. North, D.S. Peterka, M. Ahmed, S.R. Leone, *Review of Scientific Instruments*, 79 (2008) 104103-104110.
[311] C.A. Taatjes, N. Hansen, D.L. Osborn, K. Kohse-Hoinghaus, T.A. Cool, P.R. Westmoreland, *Phys Chem Chem Phys*, 10 (2008) 20-34.
[312] L. Sheps, I. Antonov, K. Au, *The Journal of Physical Chemistry A*, 123 (2019) 10804-10814.
[313] R.K. Hanson, *Proc. Combust. Inst.*, 33 (2011) 1-40.
[314] D.F. Davidson, R.K. Hanson, *Int. J. Chem. Kin.*, 36 (2004) 510-523.
[315] S.S. Vasu, L.K. Huynh, D.F. Davidson, R.K. Hanson, D.M. Golden, *The Journal of Physical Chemistry A*, 115 (2011) 2549-2556.
[316] I. Stranic, G.A. Pang, R.K. Hanson, D.M. Golden, C.T. Bowman, *The Journal of Physical Chemistry A*, 118 (2014) 822-828.
[317] D.R. Haylett, D.F. Davidson, R.D. Cook, Z. Hong, W. Ren, S.H. Pyun, R.K. Hanson, *Proc. Combust. Inst.*, 34 (2013) 369-376.
[318] D.F. Davidson, Z. Hong, G.L. Pilla, A. Farooq, R.D. Cook, R.K. Hanson, *Combust. Flame*, 157 (2010) 1899-1905.

[319] D.F. Davidson, Z. Hong, G.L. Pilla, A. Farooq, R.D. Cook, R.K. Hanson, *Proc. Combust. Inst.*, 33 (2011) 151-157.
[320] The single pulse shock tube: its Odyssey in chemical kinetics, 2005.
[321] A. Lifshitz, C. Tamburu, *The Journal of Physical Chemistry*, 99 (1995) 10251-10260.
[322] A. Lifshitz, C. Tamburu, *The Journal of Physical Chemistry*, 98 (1994) 1161-1170.
[323] R.S. Tranter, K. Brezinsky, D. Fulle, *Review of Scientific Instruments*, 72 (2001) 3046-3054.
[324] X. Han, J.M. Mehta, K. Brezinsky, *Combust. Flame*, 209 (2019) 1-12.
[325] P. Oßwald, M. Köhler, *Review of Scientific Instruments*, 86 (2015) 105109.
[326] A.M. Ferris, D.F. Davidson, R.K. Hanson, *Combust. Flame*, 195 (2018) 40-49.
[327] A.M. Ferris, J.W. Streicher, A.J. Susa, D.F. Davidson, R.K. Hanson, *Proc. Combust. Inst.*, 37 (2019) 249-257.
[328] K. Yasunaga, R.S. Tranter, Speciation in Shock Tubes, in: F. Battin-Leclerc, J.M. Simmie, E. Blurock (Eds.) Cleaner Combustion: Developing Detailed Chemical Kinetic Models, Springer London, London, 2013, pp. 143-161.
[329] P.T. Lynch, T.P. Troy, M. Ahmed, R.S. Tranter, *Analytical Chemistry*, 87 (2015) 2345-2352.
[330] C.-J. Sung, H.J. Curran, *Prog. Energy Comb. Sci.*, 44 (2014) 1-18.
[331] S.S. Goldsborough, S. Hochgreb, G. Vanhove, M.S. Wooldridge, H.J. Curran, C.-J. Sung, *Prog. Energy Comb. Sci.*, 63 (2017) 1-78.
[332] S. Jahangirian, S. Dooley, F.M. Haas, F.L. Dryer, *Combust. Flame*, 159 (2012) 30-43.
[333] S.L. Fischer, F.L. Dryer, H.J. Curran, *Int. J. Chem. Kin.*, 32 (2000) 713-740.
[334] M.S. Kurman, R.H. Natelson, N.P. Cernansky, D.L. Miller, *Proc. Combust. Inst.*, 33 (2011) 159-166.
[335] C.L. Rasmussen, J. Hansen, P. Marshall, P. Glarborg, *Int. J. Chem. Kin.*, 40 (2008) 454-480.
[336] D. Kaczmarek, B. Atakan, T. Kasper, *Combust. Flame*, 205 (2019) 345-357.
[337] F. Sen, B. Shu, T. Kasper, J. Herzler, O. Welz, M. Fikri, B. Atakan, C. Schulz, *Combust. Flame*, 169 (2016) 307-320.
[338] K. Maruta, T. Kataoka, N.I. Kim, S. Minaev, R. Fursenko, *Proc. Combust. Inst.*, 30 (2005) 2429-2436.
[339] T. Onda, H. Nakamura, T. Tezuka, S. Hasegawa, K. Maruta, *Combust. Flame*, 206 (2019) 292-307.
[340] H. Oshibe, H. Nakamura, T. Tezuka, S. Hasegawa, K. Maruta, *Combust. Flame*, 157 (2010) 1572-1580.
[341] P. Dagaut, M. Cathonnet, J.P. Rouan, R. Foulatier, A. Quilgars, J.-C. Boettner, F. Gaillard, H. James, *Journal of Physics E: Scientific Instruments*, 19 (1986) 207-209.
[342] N. Hansen, K. Moshammer, A.W. Jasper, *The Journal of Physical Chemistry A*, 123 (2019) 8274-8284.
[343] F. Battin-Leclerc, O. Herbinet, P.A. Glaude, R. Fournet, Z. Zhou, L. Deng, H. Guo, M. Xie, F. Qi, *Angew Chem Int Ed Engl*, 49 (2010) 3169-3172.
[344] K. Moshammer, A.W. Jasper, D.M. Popolan-Vaida, A. Lucassen, P. Diévart, H. Selim, A.J. Eskola, C.A. Taatjes, S.R. Leone, S.M. Sarathy, Y. Ju, P. Dagaut, K. Kohse-Höinghaus, N. Hansen, *The Journal of Physical Chemistry A*, 119 (2015) 7361-7374.
[345] F.L. Dryer, F.M. Haas, J. Santner, T.I. Farouk, M. Chaos, *Prog. Energy Comb. Sci.*, 44 (2014) 19-39.
[346] O. Herbinet, F. Battin-Leclerc, *Int. J. Chem. Kin.*, 46 (2014) 619-639.
[347] O. Herbinet, G. Dayma, Jet-Stirred Reactors, in: F. Battin-Leclerc, J.M. Simmie, E. Blurock (Eds.) Cleaner Combustion: Developing Detailed Chemical Kinetic Models, Springer London, London, 2013, pp. 183-210.
[348] E.L. Petersen, R.K. Hanson, *Shock Waves*, 10 (2001) 405-420.
[349] E.L. Petersen, R.K. Hanson, *Shock Waves*, 15 (2006) 333-340.
[350] M. Chaos, F.L. Dryer, *Int. J. Chem. Kin.*, 42 (2010) 143-150.
[351] J.F. Griffiths, P.A. Halford-Maw, D.J. Rose, *Combust. Flame*, 95 (1993) 291-306.

[352] J.F. Griffiths, J.P. MacNamara, C. Mohamed, B.J. Whitaker, J. Pan, C.G.W. Sheppard, *Faraday Discussions*, 119 (2002) 287-303.
[353] A. Kéromnès, Rapid Compression Machines, in: F. Battin-Leclerc, J.M. Simmie, E. Blurock (Eds.) Cleaner Combustion: Developing Detailed Chemical Kinetic Models, Springer London, London, 2013, pp. 163-181.
[354] M. Ihme, *Combust. Flame*, 159 (2012) 1592-1604.
[355] A. Lifshitz, Chapter 16.5 - Chemical and Combustion Kinetics: 16.5 Ignition Delay Times, in: G. Ben-Dor, O. Igra, T. Elperin (Eds.) Handbook of Shock Waves, Academic Press, Burlington, 2001, pp. 211-VII.
[356] A.G. Gaydon, I.R. Hurle, The Shock Tube in High-Temperature Chemical Physics, Reinhold, New York, 1963.
[357] E.F. Greene, J.P. Toennies, Chemical Reactions in Shock Waves, Academic Press, New York, 1964.
[358] E.L. Petersen, M.J.A. Rickard, M.W. Crofton, E.D. Abbey, M.J. Traum, D.M. Kalitan, *Measurement Science and Technology*, 16 (2005) 1716-1729.
[359] R.K. Hanson, D.F. Davidson, *Prog. Energy Comb. Sci.*, 44 (2014) 103-114.
[360] E.L. Petersen, *Comb. Sci. Tech.*, 181 (2009) 1123-1144.
[361] B. Rotavera, P. Dagaut, E.L. Petersen, *Combust. Flame*, 161 (2014) 1146-1163.
[362] A. Amadio, M. Crofton, E. Petersen, *Shock Waves*, 16 (2006) 157-165.
[363] Z. Hong, G. Pang, S. Vasu, D. Davidson, R. Hanson, *Shock Waves*, 19 (2009) 113-123.
[364] D.R. Haylett, D.F. Davidson, R.K. Hanson, *Combust. Flame*, 159 (2012) 552-561.
[365] R.K. Hanson, G.A. Pang, S. Chakraborty, W. Ren, S. Wang, D.F. Davidson, *Combust. Flame*, 160 (2013) 1550-1558.
[366] Y. Zhu, D.F. Davidson, R.K. Hanson, *Combust. Flame*, 161 (2014) 634-643.
[367] M.F. Campbell, D.F. Davidson, R.K. Hanson, C.K. Westbrook, *Proc. Combust. Inst.*, 34 (2013) 419-425.
[368] C.K. Westbrook, H.J. Curran, W.J. Pitz, J.F. Griffiths, C. Mohamed, S.K. Wo, *Twenty-Seventh Symposium (International) on Combustion, Vols 1 and 2*, (1998) 371-378.
[369] J. Würmel, E.J. Silke, H.J. Curran, M.S. Ó Conaire, J.M. Simmie, *Combust. Flame*, 151 (2007) 289-302.
[370] S.S. Goldsborough, G. Mittal, C. Banyon, *Proc. Combust. Inst.*, 34 (2013) 685-693.
[371] D.M.A. Karwat, S.W. Wagnon, M.S. Wooldridge, C.K. Westbrook, *Combust. Flame*, 160 (2013) 2693-2706.
[372] C.L. Barraza-Botet, S.W. Wagnon, M.S. Wooldridge, *The Journal of Physical Chemistry A*, 120 (2016) 7408-7418.
[373] P. Dagaut, M. Cathonnet, *Prog. Energy Comb. Sci.*, 32 (2006) 48-92.
[374] P. Dagaut, S. Gaı¨l, M. Sahasrabudhe, *Proc. Combust. Inst.*, 31 (2007) 2955-2961.
[375] C.K. Westbrook, F.L. Dryer, *Prog. Energy Comb. Sci.*, 10 (1984) 1-57.
[376] C.K. Westbrook, W.J. Pitz, O. Herbinet, H.J. Curran, E.J. Silke, *Combust. Flame*, 156 (2009) 181-199.
[377] C.K. Westbrook, C.V. Naik, O. Herbinet, W.J. Pitz, M. Mehl, S.M. Sarathy, H.J. Curran, *Combust. Flame*, 158 (2011) 742-755.
[378] C.K. Westbrook, Y. Mizobuchi, T.J. Poinsot, P.J. Smith, E. Warnatz, *Proc. Combust. Inst.*, 30 (2005) 125-157.
[379] L.S. Tran, B. Sirjean, P.-A. Glaude, R. Fournet, F. Battin-Leclerc, *Energy*, (2012).
[380] V.W. J. Biet, O. Herbinet, P. A. Glaude, F. Battin-Leclerc, *Proc. Euro. Comb. Meeting*, 4 (2009).
[381] O. Herbinet, J. Biet, M.H. Hakka, V. Warth, P.A. Glaude, A. Nicolle, F. Battin-Leclerc, *Proc. Combust. Inst.*, 33 (2011) 391-398.
[382] F. Buda, P.A. Glaude, F. Battin-Leclerc, R. Porter, K.J. Hughes, J.F. Griffiths, *Journal of Loss Prevention in the Process Industries*, 19 (2006) 227-232.

[383] F. Buda, R. Bounaceur, V. Warth, P.A. Glaude, R. Fournet, F. Battin-Leclerc, *Combust. Flame*, 142 (2005) 170-186.
[384] J.P. Orme, H.J. Curran, J.M. Simmie, *The Journal of Physical Chemistry A*, 110 (2005) 114-131.
[385] H.J. Curran, P. Gaffuri, W.J. Pitz, C.K. Westbrook, *Combust. Flame*, 114 (1998) 149-177.
[386] H.J. Curran, P. Gaffuri, W.J. Pitz, C.K. Westbrook, *Combust. Flame*, 129 (2002) 253-280.
[387] E. Ranzi, A. Frassoldati, S. Granata, T. Faravelli, *Ind. Eng. Chem. Res.*, 44 (2005) 5170-5183.
[388] R. Grana, A. Frassoldati, C. Saggese, T. Faravelli, E. Ranzi, *Combust. Flame*, 159 (2012) 2280-2294.
[389] R. Grana, A. Frassoldati, A. Cuoci, T. Faravelli, E. Ranzi, *Energy*, 43 (2012) 124-139.
[390] T. Lu, C.K. Law, *Prog. Energy Comb. Sci.*, 35 (2009) 192-215.
[391] M.J. McNenly, R.A. Whitesides, D.L. Flowers, *Proc. Combust. Inst.*, 35 (2015) 581-587.
[392] G. Dixon-Lewis, *Proceedings of the Royal Society of London. Series A. Mathematical and Physical Sciences*, 298 (1967) 495-513.
[393] G. Dixon-Lewis, *Proceedings of the Royal Society of London. Series A. Mathematical and Physical Sciences*, 307 (1968) 111-135.
[394] J.A. Miller, R.E. Mitchell, M.D. Smooke, R.J. Kee, *Symposium (International) on Combustion*, 19 (1982) 181-196.
[395] R.J. Kee, G. Dixon-Lewis, J. Warnatz, M.E. Coltrin, J.A. Miller, Sandia National Laboratories SAND86-8246 1986.
[396] R.J. Kee, F.M. Rupley, J.A. Miller, Sandia National Laboratories SAND89-8003, 1989.
[397] J. Warnatz, *Symposium (International) on Combustion*, 24 (1992) 553-579.
[398] J. Troe, *Symposium (International) on Combustion*, 22 (1989) 843-862.
[399] C.K. Westbrook, F.L. Dryer, *Symposium (International) on Combustion*, 18 (1981) 749-767.
[400] C.W. Gao, J.W. Allen, W.H. Green, R.H. West, *Computer Physics Communications*, 203 (2016) 212-225.
[401] N.M. Vandewiele, K.M. Van Geem, M.-F. Reyniers, G.B. Marin, *Chemical Engineering Journal*, 207-208 (2012) 526-538.
[402] N.M. Vandewiele, R. Van De Vijver, H.-H. Carstensen, K.M. Van Geem, M.-F. Reyniers, G.B. Marin, *Int. J. Chem. Kin.*, 48 (2016) 755-769.
[403] E. Ranzi, A. Frassoldati, R. Grana, A. Cuoci, T. Faravelli, A.P. Kelley, C.K. Law, *Prog. Energy Comb. Sci.*, 38 (2012) 468-501.
[404] F. Battin-Leclerc, E. Blurock, R. Bounaceur, R. Fournet, P.-A. Glaude, O. Herbinet, B. Sirjean, V. Warth, *Chemical Society Reviews*, 40 (2011) 4762-4782.
[405] H. Wang, R. Xu, K. Wang, C.T. Bowman, R.K. Hanson, D.F. Davidson, K. Brezinsky, F.N. Egolfopoulos, *Combust. Flame*, 193 (2018) 502-519.
[406] R. Xu, K. Wang, S. Banerjee, J. Shao, T. Parise, Y. Zhu, S. Wang, A. Movaghar, D.J. Lee, R. Zhao, X. Han, Y. Gao, T. Lu, K. Brezinsky, F.N. Egolfopoulos, D.F. Davidson, R.K. Hanson, C.T. Bowman, H. Wang, *Combust. Flame*, 193 (2018) 520-537.
[407] S.M. Villano, H.-H. Carstensen, A.M. Dean, *The Journal of Physical Chemistry A*, 117 (2013) 6458-6473.
[408] S.M. Villano, L.K. Huynh, H.-H. Carstensen, A.M. Dean, *The Journal of Physical Chemistry A*, 116 (2012) 5068-5089.
[409] S.M. Villano, L.K. Huynh, H.-H. Carstensen, A.M. Dean, *The Journal of Physical Chemistry A*, 115 (2011) 13425-13442.
[410] A. Miyoshi, *The Journal of Physical Chemistry A*, 115 (2011) 3301-3325.
[411] L. Cai, H. Pitsch, S.Y. Mohamed, V. Raman, J. Bugler, H. Curran, S.M. Sarathy, *Combust. Flame*, 173 (2016) 468-482.
[412] S.J. Klippenstein, V.S. Pande, D.G. Truhlar, *Journal of the American Chemical Society*, 136 (2013) 528-546.
[413] J. Zádor, S.J. Klippenstein, J.A. Miller, *The Journal of Physical Chemistry A*, 115 (2011) 10218-10225.

[414] J.A. Miller, S.J. Klippenstein, *The Journal of Physical Chemistry A*, 110 (2006) 10528-10544.
[415] S.J. Klippenstein, J.A. Miller, *The Journal of Physical Chemistry A*, 106 (2002) 9267-9277.
[416] S.J. Klippenstein, *Proc. Combust. Inst.*, 36 (2017) 77-111.
[417] J.A. Miller, R. Sivaramakrishnan, Y. Tao, C.F. Goldsmith, M.P. Burke, A.W. Jasper, N. Hansen, N.J. Labbe, P. Glarborg, J. Zádor, *Prog. Energy Comb. Sci.*, 83 (2021) 100886.
[418] C. Cavallotti, M. Pelucchi, Y. Georgievskii, S.J. Klippenstein, *Journal of Chemical Theory and Computation*, 15 (2019) 1122-1145.
[419] A.L. Dewyer, A.J. Argüelles, P.M. Zimmerman, *WIREs Computational Molecular Science*, 8 (2018) e1354.
[420] R. Van de Vijver, K.M. Van Geem, G.B. Marin, *Proceedings of the Combustion Institute*, 37 (2019) 283-290.
[421] R. Van de Vijver, J. Zádor, *Computer Physics Communications*, (2019) 106947.
[422] S.N. Elliott, K.B. Moore, A.V. Copan, M. Keçeli, C. Cavallotti, Y. Georgievskii, H.F. Schaefer, S.J. Klippenstein, *Proceedings of the Combustion Institute*, (2020).
[423] C.A. Grambow, A. Jamal, Y.P. Li, W.H. Green, J. Zador, Y.V. Suleimanov, *Journal of the American Chemical Society*, 140 (2018) 1035-1048.
[424] J.P. Perdew, A. Ruzsinszky, J. Tao, V.N. Staroverov, G.E. Scuseria, G.I. Csonka, *The Journal of Chemical Physics*, 123 (2005) 062201.
[425] N. Mardirossian, M. Head-Gordon, *Molecular Physics*, 115 (2017) 2315-2372.
[426] L. Goerigk, A. Hansen, C. Bauer, S. Ehrlich, A. Najibi, S. Grimme, *Physical Chemistry Chemical Physics*, 19 (2017) 32184-32215.
[427] L. Goerigk, N. Mehta, *Australian Journal of Chemistry*, 72 (2019) 563-573.
[428] B. Rotavera, R.L. Caravan, C.A. Taatjes, Sandia National Laboratories, Subsequent R + O_2 Chemistry of Intermediates Formed in Low-Temperature R + O_2 Reactions: Potential Importance in Modeling Autoignition Behavior, SAND2017-9099, 2017.
[429] A.C. Doner, M.M. Davis, A.L. Koritzke, M.G. Christianson, J.M. Turney, H.F.S. III, L. Sheps, D.L. Osborn, C.A. Taatjes, B. Rotavera, *Int. J. Chem. Kin.*, (2020).
[430] M.G. Christianson, A.C. Doner, M.M. Davis, A.L. Koritzke, J.M. Turney, H.F. Schaefer, L. Sheps, D.L. Osborn, C.A. Taatjes, B. Rotavera, *Int. J. Chem. Kin.*, 53 (2021) 43-59.
[431] V.B. Oyeyemi, J.A. Keith, E.A. Carter, *The Journal of Physical Chemistry A*, 118 (2014) 3039-3050.
[432] G. Black, H.J. Curran, S. Pichon, J.M. Simmie, V. Zhukov, *Combust. Flame*, 157 (2010) 363-373.
[433] C.-W. Zhou, J.M. Simmie, H.J. Curran, *Combust. Flame*, 158 (2011) 726-731.
[434] P. Seal, G. Oyedepo, D.G. Truhlar, *The Journal of Physical Chemistry A*, 117 (2013) 275-282.
[435] S. Vranckx, K.A. Heufer, C. Lee, H. Olivier, L. Schill, W.A. Kopp, K. Leonhard, C.A. Taatjes, R.X. Fernandes, *Combust. Flame*, 158 (2011) 1444-1455.
[436] R. Sivaramakrishnan, M.C. Su, J.V. Michael, S.J. Klippenstein, L.B. Harding, B. Ruscic, *The Journal of Physical Chemistry A*, 114 (2010) 9425-9439.
[437] K.A. Heufer, S.M. Sarathy, H.J. Curran, A.C. Davis, C.K. Westbrook, W.J. Pitz, *Energy & Fuels*, 26 (2012) 6678-6685.
[438] P. Zhang, S.J. Klippenstein, C.K. Law, *The Journal of Physical Chemistry A*, 117 (2013) 1890-1906.
[439] I.M. Alecu, J. Zheng, E. Papajak, T. Yu, D.G. Truhlar, *The Journal of Physical Chemistry A*, 116 (2012) 12206-12213.
[440] J. Moc, J.M. Simmie, *The Journal of Physical Chemistry A*, 114 (2010) 5558-5564.
[441] K. Yasunaga, T. Mikajiri, S.M. Sarathy, T. Koike, F. Gillespie, T. Nagy, J.M. Simmie, H.J. Curran, *Combust. Flame*, 159 (2012) 2009-2027.
[442] U. Meier, H.H. Grotheer, G. Riekert, T. Just, *Chemical Physics Letters*, 133 (1987) 162-164.
[443] S.A. Carr, M.A. Blitz, P.W. Seakins, *The Journal of Physical Chemistry A*, 115 (2011) 3335-3345.
[444] W.P. Hess, F.P. Tully, *Chemical Physics Letters*, 152 (1988) 183-189.
[445] S. Xu, M.C. Lin, *Proc. Combust. Inst.*, 31 (2007) 159-166.

[446] J. Zheng, D.G. Truhlar, *Faraday Discussions*, 157 (2012) 59-88.
[447] G.A. Pang, R.K. Hanson, D.M. Golden, C.T. Bowman, *The Journal of Physical Chemistry A*, 116 (2012) 9607-9613.
[448] G.A. Pang, R.K. Hanson, D.M. Golden, C.T. Bowman, *The Journal of Physical Chemistry A*, 116 (2012) 4720-4725.
[449] M. Yujing, A. Mellouki, *Chemical Physics Letters*, 333 (2001) 63-68.
[450] M.R. McGillen, M. Baasandorj, J.B. Burkholder, *The Journal of Physical Chemistry A*, 117 (2013) 4636-4656.
[451] S.L. Sime, M.A. Blitz, P.W. Seakins, *Int. J. Chem. Kin.*, 52 (2020) 1046-1059.
[452] P. Seal, E. Papajak, D.G. Truhlar, *The Journal of Physical Chemistry Letters*, 3 (2012) 264-271.
[453] G. Black, J.M. Simmie, *Journal of Computational Chemistry*, 31 (2010) 1236-1248.
[454] S.E. Rawadieh, I.S. Altarawneh, M.A. Batiha, L.A. Al-Makhadmeh, M.H. Almatarneh, M. Altarawneh, *Energy & Fuels*, (2019).
[455] Z.F. Xu, J. Park, M.C. Lin, *The Journal of Chemical Physics*, 120 (2004) 6593-6599.
[456] P. Gray, A.A. Herod, *Transactions of the Faraday Society*, 64 (1968) 1568-1576.
[457] D. Katsikadakos, Y. Hardalupas, A.M.K.P. Taylor, P.A. Hunt, *Phys Chem Chem Phys*, 14 (2012) 9615-9629.
[458] D. Katsikadakos, C.W. Zhou, J.M. Simmie, H.J. Curran, P.A. Hunt, Y. Hardalupas, A.M.K.P. Taylor, *Proc. Combust. Inst.*, 34 (2013) 483-491.
[459] W.K. Metcalfe, S.M. Burke, S.S. Ahmed, H.J. Curran, *Int. J. Chem. Kin.*, 45 (2013) 638-675.
[460] C. Olm, T. Varga, É. Valkó, S. Hartl, C. Hasse, T. Turányi, *Int. J. Chem. Kin.*, 48 (2016) 423-441.
[461] N. Leplat, P. Dagaut, C. Togbé, J. Vandooren, *Combust. Flame*, 158 (2011) 705-725.
[462] N.M. Marinov, *Int. J. Chem. Kin.*, 31 (1999) 183-220.
[463] A. Frassoldati, A. Cuoci, T. Faravelli, E. Ranzi, *Comb. Sci. Tech.*, 182 (2010) 653-667.
[464] H. Hashemi, J.M. Christensen, P. Glarborg, *Fuel*, 218 (2018) 247-257.
[465] T.J. Dillon, D. Hölscher, V. Sivakumaran, A. Horowitz, J.N. Crowley, *Phys Chem Chem Phys*, 7 (2005) 349-355.
[466] T.J. Wallington, M.J. Kurylo, *Int. J. Chem. Kin.*, 19 (1987) 1015-1023.
[467] E. Jiménez, M.K. Gilles, A.R. Ravishankara, *Journal of Photochemistry and Photobiology A: Chemistry*, 157 (2003) 237-245.
[468] VariFlex 2.02m, 2010.
[469] A. Galano, J.R. Alvarez-Idaboy, G. Bravo-Perez, M.E. Ruiz-Santoyo, *Phys Chem Chem Phys*, 4 (2002) 4648-4662.
[470] J. Moc, J.M. Simmie, H.J. Curran, *Journal of Molecular Structure*, 928 (2009) 149-157.
[471] G.A. Pang, R.K. Hanson, D.M. Golden, C.T. Bowman, *The Journal of Physical Chemistry A*, 116 (2012) 2475-2483.
[472] F. Cavalli, H. Geiger, I. Barnes, K.H. Becker, *Environmental Science & Technology*, 36 (2002) 1263-1270.
[473] M.D. Hurley, T.J. Wallington, L. Laursen, M.S. Javadi, O.J. Nielsen, T. Yamanaka, M. Kawasaki, *The Journal of Physical Chemistry A*, 113 (2009) 7011-7020.
[474] J. Zheng, G.A. Oyedepo, D.G. Truhlar, *The Journal of Physical Chemistry A*, 119 (2015) 12182-12192.
[475] A. Mellouki, F. Oussar, X. Lun, A. Chakir, *Phys Chem Chem Phys*, 6 (2004) 2951-2955.
[476] M.R. McGillen, G.S. Tyndall, J.J. Orlando, A.S. Pimentel, D.J. Medeiros, J.B. Burkholder, *The Journal of Physical Chemistry A*, 120 (2016) 9968-9981.
[477] S.S. Vasu, D.F. Davidson, R.K. Hanson, D.M. Golden, *Chemical Physics Letters*, 497 (2010) 26-29.
[478] J. Zheng, R. Meana-Pañeda, D.G. Truhlar, *Journal of the American Chemical Society*, 136 (2014) 5150-5160.
[479] V.F. Andersen, T.J. Wallington, O.J. Nielsen, *The Journal of Physical Chemistry A*, 114 (2010) 12462-12469.

[480] J.S. Baxley, J.R. Wells, *Int. J. Chem. Kin.*, 30 (1998) 745-752.
[481] A.A. Chew, R. Atkinson, *Journal of Geophysical Research: Atmospheres*, 101 (1996) 28649-28653.
[482] L. Xing, Z. Wang, D.G. Truhlar, *Journal of the American Chemical Society*, (2019).
[483] S.M. Sarathy, S. Park, B.W. Weber, W. Wang, P.S. Veloo, A.C. Davis, C. Togbe, C.K. Westbrook, O. Park, G. Dayma, Z. Luo, M.A. Oehlschlaeger, F.N. Egolfopoulos, T. Lu, W.J. Pitz, C.-J. Sung, P. Dagaut, *Combust. Flame*, 160 (2013) 2712-2728.
[484] T. Tsujimura, W.J. Pitz, F. Gillespie, H.J. Curran, B.W. Weber, Y. Zhang, C.-J. Sung, *Energy & Fuels*, 26 (2012) 4871-4886.
[485] Y. Zhang, H. El-Merhubi, B. Lefort, L. Le Moyne, H.J. Curran, A. Kéromnès, *Combust. Flame*, 190 (2018) 74-86.
[486] H. Jin, J. Pieper, C. Hemken, E. Bräuer, L. Ruwe, K. Kohse-Höinghaus, *Combust. Flame*, 193 (2018) 36-53.
[487] C. Lefebvre, G. Rubez, H. Khartabil, J.-C. Boisson, J. Contreras-García, E. Hénon, *Phys Chem Chem Phys*, 19 (2017) 17928-17936.
[488] F.M. Bickelhaupt, K.N. Houk, *Angewandte Chemie International Edition*, 56 (2017) 10070-10086.
[489] L.R. Cancino, M. Fikri, A.A.M. Oliveira, C. Schulz, *Energy & Fuels*, 24 (2010) 2830-2840.
[490] C. Lee, S. Vranckx, K.A. Heufer, S.V. Khomik, Y. Uygun, H. Olivier, R.X. Fernandez, *Zeitschrift für Physikalische Chemie*, 226 (2012) 1-28.
[491] J.L. Bao, R. Meana-Paneda, D.G. Truhlar, *Chemical Science*, 6 (2015) 5866-5881.
[492] C. Chen, W.Z. Li, Y.C. Song, J. Yang, *Journal of Molecular Liquids*, 146 (2009) 23-28.
[493] P.R. Parab, K.A. Heufer, R.X. Fernandes, *Phys Chem Chem Phys*, (2018).
[494] O. Welz, J.D. Savee, A.J. Eskola, L. Sheps, D.L. Osborn, C.A. Taatjes, *Proc. Combust. Inst.*, 34 (2013) 493-500.
[495] C. Togbé, F. Halter, F. Foucher, C. Mounaim-Rousselle, P. Dagaut, *Proc. Combust. Inst.*, 33 (2011) 367-374.
[496] T.S. Norton, F.L. Dryer, *Symposium (International) on Combustion*, 23 (1991) 179-185.
[497] J. Zádor, R.X. Fernandes, Y. Georgievskii, G. Meloni, C.A. Taatjes, J.A. Miller, *Proc. Combust. Inst.*, 32 (2009) 271-277.
[498] G. da Silva, J.W. Bozzelli, L. Liang, J.T. Farrell, *The Journal of Physical Chemistry A*, 113 (2009) 8923-8933.
[499] T.S. Dibble, *Chemical Physics Letters*, 355 (2002) 193-200.
[500] A. Schocker, M. Uetake, N. Kanno, M. Koshi, K. Tonokura, *The Journal of Physical Chemistry A*, 111 (2007) 6622-6627.
[501] M.J. Goldman, N.W. Yee, J.H. Kroll, W.H. Green, *Phys Chem Chem Phys*, 22 (2020) 19802-19815.
[502] S.J. Klippenstein, L.B. Harding, M.J. Davis, A.S. Tomlin, R.T. Skodje, *Proc. Combust. Inst.*, 33 (2011) 351-357.
[503] K.A. Heufer, R.X. Fernandes, H. Olivier, J. Beeckmann, O. Röhl, N. Peters, *Proc. Combust. Inst.*, 33 (2011) 359-366.
[504] G. Mittal, S.M. Burke, V.A. Davies, B. Parajuli, W.K. Metcalfe, H.J. Curran, *Combust. Flame*, 161 (2014) 1164-1171.
[505] Y. Duan, M. Monge-Palacios, E. Grajales-Gonzalez, D. Han, K.H. Møller, H.G. Kjaergaard, S.M. Sarathy, *Combust. Flame*, 219 (2020) 20-32.
[506] O. Welz, J.D. Savee, D.L. Osborn, C.A. Taatjes, *Proc. Combust. Inst.*, 35 (2015) 401-408.
[507] D.J.M. Ray, A. Redfearn, D.J. Waddington, *Journal of the Chemical Society, Perkin Transactions 2*, (1973) 540-543.
[508] D.J.M. Ray, D.J. Waddington, *Combust. Flame*, 20 (1973) 327-334.
[509] Y. Li, Q. Zhao, Y. Zhang, Z. Huang, S.M. Sarathy, *The Journal of Physical Chemistry A*, (2020).
[510] J. Cai, W. Yuan, L. Ye, Z. Cheng, Y. Wang, L. Zhang, F. Zhang, Y. Li, F. Qi, *Combust. Flame*, 160 (2013) 1939-1957.

[511] S.M. Sarathy, S. Vranckx, K. Yasunaga, M. Mehl, P. Osswald, W.K. Metcalfe, C.K. Westbrook, W.J. Pitz, K. Kohse-Hoinghaus, R.X. Fernandes, H.J. Curran, *Combust. Flame*, 159 (2012) 2028-2055.
[512] C. Togbé, A. Mzé-Ahmed, P. Dagaut, *Energy & Fuels*, 24 (2010) 5244-5256.
[513] P. Oßwald, H. Güldenberg, K. Kohse-Höinghaus, B. Yang, T. Yuan, F. Qi, *Combust. Flame*, 158 (2011) 2-15.
[514] R. Grana, A. Frassoldati, T. Faravelli, U. Niemann, E. Ranzi, R. Seiser, R. Cattolica, K. Seshadri, *Combust. Flame*, 157 (2010) 2137-2154.
[515] K.M. Van Geem, S.P. Pyl, G.B. Marin, M.R. Harper, W.H. Green, *Ind. Eng. Chem. Res.*, 49 (2010) 10399-10420.
[516] Q. Li, C. Tang, Y. Cheng, L. Guan, Z. Huang, *Energy & Fuels*, (2015).
[517] J.A. Montgomery, M.J. Frisch, J.W. Ochterski, G.A. Petersson, *The Journal of Chemical Physics*, 110 (1999) 2822-2827.
[518] J. Bugler, J. Power, H.J. Curran, *Proc. Combust. Inst.*, 36 (2017) 161-167.
[519] H. Sun, J.W. Bozzelli, C.K. Law, *The Journal of Physical Chemistry A*, 111 (2007) 4974-4986.
[520] R.W. Walker, C. Morley, Chapter 1 - Basic Chemistry of Combustion, in: M.J. Pilling (Ed.) Comprehensive Chemical Kinetics, Elsevier, 1997, pp. 1-124.
[521] J.C. Lizardo-Huerta, B. Sirjean, R. Bounaceur, R. Fournet, *Phys Chem Chem Phys*, 18 (2016) 12231-12251.
[522] J.C. Davis, A.L. Koritzke, R.L. Caravan, I.O. Antonov, M.G. Christianson, A.C. Doner, D.L. Osborn, L. Sheps, C.A. Taatjes, B. Rotavera, *J. Phys. Chem. A*, 123 (2019) 3634-3646.
[523] C. Fittschen, H. Hippler, B. Viskolcz, *Phys Chem Chem Phys*, 2 (2000) 1677-1683.
[524] F.M. Haas, M. Chaos, F.L. Dryer, *Combust. Flame*, 156 (2009) 2346-2350.
[525] P. Dagaut, S.M. Sarathy, M.J. Thomson, *Proc. Combust. Inst.*, 32 (2009) 229-237.
[526] M. Pelucchi, S. Namysl, E. Ranzi, A. Rodriguez, C. Rizzo, K.P. Somers, Y. Zhang, O. Herbinet, H.J. Curran, F. Battin-Leclerc, T. Faravelli, *Energy & Fuels*, 34 (2020) 14708-14725.
[527] M. Carbonnier, Z. Serinyel, A. Kéromnès, G. Dayma, B. Lefort, L. Le Moyne, P. Dagaut, *Proc. Combust. Inst.*, 37 (2019) 477-484.
[528] Z. Serinyel, C. Togbé, G. Dayma, P. Dagaut, *Combust. Flame*, 161 (2014) 3003-3013.
[529] G. Dayma, C. Togbé, P. Dagaut, *Energy & Fuels*, 25 (2011) 4986-4998.
[530] R. De Bruycker, O. Herbinet, H.-H. Carstensen, F. Battin-Leclerc, K.M. Van Geem, *Combust. Flame*, 171 (2016) 237-251.
[531] K.A. Heufer, H. Olivier, *Shock Waves*, 20 (2010) 307-316.
[532] L.R. Cancino, M. Fikri, A.A.M. Oliveira, C. Schulz, *Fuel*, 90 (2011) 1238-1244.
[533] S.M. Gallagher, H.J. Curran, W.K. Metcalfe, D. Healy, J.M. Simmie, G. Bourque, *Combust. Flame*, 153 (2008) 316-333.
[534] C.F. Goldsmith, W.H. Green, S.J. Klippenstein, *The Journal of Physical Chemistry A*, 116 (2012) 3325-3346.
[535] M.P. Burke, C.F. Goldsmith, S.J. Klippenstein, O. Welz, H. Huang, I.O. Antonov, J.D. Savee, D.L. Osborn, J. Zádor, C.A. Taatjes, L. Sheps, *The Journal of Physical Chemistry A*, 119 (2015) 7095-7115.
[536] O. Welz, M.P. Burke, I.O. Antonov, C.F. Goldsmith, J.D. Savee, D.L. Osborn, C.A. Taatjes, S.J. Klippenstein, L. Sheps, *The Journal of Physical Chemistry A*, 119 (2015) 7116-7129.
[537] S.S. Merchant, C.F. Goldsmith, A.G. Vandeputte, M.P. Burke, S.J. Klippenstein, W.H. Green, *Combust. Flame*, 162 (2015) 3658-3673.
[538] K. Yang, C. Zhan, X. Man, L. Guan, Z. Huang, C. Tang, *Energy & Fuels*, 30 (2016) 717-724.
[539] K. Kumar, C.-J. Sung, *Int. J. Chem. Kin.*, 43 (2011) 175-184.
[540] K. Fieweger, R. Blumenthal, G. Adomeit, *Combust. Flame*, 109 (1997) 599-619.
[541] M.P. Dunphy, J.M. Simmie, *Journal of the Chemical Society, Faraday Transactions*, 87 (1991) 1691.
[542] K.E. Noorani, B. Akih-Kumgeh, J.M. Bergthorson, *Energy & Fuels*, 24 (2010) 5834-5843.
[543] X. Man, C. Tang, J. Zhang, Y. Zhang, L. Pan, Z. Huang, C.K. Law, *Combust. Flame*, 161 (2014) 644-656.

[544] D.M.A. Karwat, S.W. Wagnon, M.S. Wooldridge, C.K. Westbrook, *The Journal of Physical Chemistry A*, 116 (2012) 12406-12421.
[545] B.W. Weber, C.-J. Sung, *Energy & Fuels*, 27 (2013) 1688-1698.
[546] L. Pan, Y. Zhang, Z. Tian, F. Yang, Z. Huang, *Energy & Fuels*, 28 (2014) 2160-2169.
[547] E. Ninnemann, G. Kim, A. Laich, B. Almansour, A.C. Terracciano, S. Park, K. Thurmond, S. Neupane, S. Wagnon, W.J. Pitz, S.S. Vasu, *Fuel*, 254 (2019) 115630.
[548] L. Cai, Y. Uygun, C. Togbé, H. Pitsch, H. Olivier, P. Dagaut, S.M. Sarathy, *Proc. Combust. Inst.*, 35 (2015) 419-427.
[549] L. Cai, L. Kröger, M. Döntgen, K. Leonhard, K. Narayanaswamy, S.M. Sarathy, K.A. Heufer, H. Pitsch, *Combust. Flame*, (2019).
[550] C. Wadkar, P. Chinnathambi, E. Toulson, *Fuel*, 264 (2020) 116546.
[551] S. Gersen, A.V. Mokhov, J.H. Darmeveil, H.B. Levinsky, *Combust. Flame*, 157 (2010) 240-245.
[552] L. Cai, H. Minwegen, S. Kruse, R. Daniel Büttgen, R. Hesse, A. Ramalingam, J. Beeckmann, K. Leonhard, K.A. Heufer, H. Pitsch, *Combust. Flame*, 210 (2019) 134-144.
[553] M.J. Al Rashidi, J.C. Mármol, C. Banyon, M.B. Sajid, M. Mehl, W.J. Pitz, S. Mohamed, A. Alfazazi, T. Lu, H.J. Curran, A. Farooq, S.M. Sarathy, *Combust. Flame*, 183 (2017) 372-385.
[554] J. Bugler, B. Marks, O. Mathieu, R. Archuleta, A. Camou, C. Grégoire, K.A. Heufer, E.L. Petersen, H.J. Curran, *Combust. Flame*, 163 (2016) 138-156.
[555] S. Park, O. Mannaa, F. Khaled, R. Bougacha, M.S. Mansour, A. Farooq, S.H. Chung, S.M. Sarathy, *Combust. Flame*.
[556] C.K. Westbrook, F.L. Dryer, *Comb. Sci. Tech.*, 20 (1979) 125-140.
[557] F.N. Egolfopoulos, D.X. Du, C.K. Law, *Comb. Sci. Tech.*, 83 (1992) 33-75.
[558] T.J. Held, F.L. Dryer, *Int. J. Chem. Kin.*, 30 (1998) 805-830.
[559] W.-C. Ing, C.Y. Sheng, J.W. Bozzelli, *Fuel Processing Technology*, 83 (2003) 111-145.
[560] J. Li, Z. Zhao, A. Kazakov, M. Chaos, F.L. Dryer, J.J. Scire, *Int. J. Chem. Kin.*, 39 (2007) 109-136.
[561] V. Aranda, J.M. Christensen, M.U. Alzueta, P. Glarborg, S. Gersen, Y. Gao, P. Marshall, *Int. J. Chem. Kin.*, 45 (2013) 283-294.
[562] U. Burke, W.K. Metcalfe, S.M. Burke, K.A. Heufer, P. Dagaut, H.J. Curran, *Combust. Flame*, 165 (2016) 125-136.
[563] K. Natarajan, K.A. Bhaskaran, *Combust. Flame*, 43 (1981) 35-49.
[564] F.N. Egolfopoulos, D.X. Du, C.K. Law, *Symposium (International) on Combustion*, 24 (1992) 833-841.
[565] A. Zyada, O. Samimi-Abianeh, *Energy & Fuels*, 33 (2019) 7791-7804.
[566] A. Frassoldati, A. Cuoci, T. Faravelli, U. Niemann, E. Ranzi, R. Seiser, K. Seshadri, *Combust. Flame*, 157 (2010) 2-16.
[567] C. Togbé, P. Dagaut, F. Halter, F. Foucher, *Energy & Fuels*, 25 (2011) 676-683.
[568] M.V. Johnson, S.S. Goldsborough, Z. Serinyel, P. O'Toole, E. Larkin, G. O'Malley, H.J. Curran, *Energy & Fuels*, 23 (2009) 5886-5898.
[569] P. Dagaut, C. Togbé, *Fuel*, 87 (2008) 3313-3321.
[570] J.T. Moss, A.M. Berkowitz, M.A. Oehlschlaeger, J. Biet, V. Warth, P.-A. Glaude, F. Battin-Leclerc, *The Journal of Physical Chemistry A*, 112 (2008) 10843-10855.
[571] S.M. Sarathy, M.J. Thomson, C. Togbé, P. Dagaut, F. Halter, C. Mounaim-Rousselle, *Combust. Flame*, 156 (2009) 852-864.
[572] N. Hansen, M.R. Harper, W.H. Green, *Phys Chem Chem Phys*, 13 (2011) 20262-20274.
[573] M.R. Harper, K.M. Van Geem, S.P. Pyl, G.B. Marin, W.H. Green, *Combust. Flame*, 158 (2011) 16-41.
[574] S.S. Merchant, E.F. Zanoelo, R.L. Speth, M.R. Harper, K.M. Van Geem, W.H. Green, *Combust. Flame*, 160 (2013) 1907-1929.
[575] N. Hansen, S.S. Merchant, M.R. Harper, W.H. Green, *Combust. Flame*, 160 (2013) 2343-2351.
[576] M. Pelucchi, S. Namysl, E. Ranzi, A. Rodriguez, C. Rizzo, K.P. Somers, Y. Zhang, O. Herbinet, H.J. Curran, F. Battin-Leclerc, T. Faravelli, *Energy & Fuels*, 34 (2020) 14688-14707.

[577] C. Togbé, P. Dagaut, A. Mzé-Ahmed, P. Diévart, F. Halter, F. Foucher, *Energy & Fuels*, 24 (2010) 5859-5875.
[578] U. Burke, K.P. Somers, P. O'Toole, C.M. Zinner, N. Marquet, G. Bourque, E.L. Petersen, W.K. Metcalfe, Z. Serinyel, H.J. Curran, *Combust. Flame*, 162 (2015) 315-330.
[579] A. Kéromnès, W.K. Metcalfe, K.A. Heufer, N. Donohoe, A.K. Das, C.-J. Sung, J. Herzler, C. Naumann, P. Griebel, O. Mathieu, M.C. Krejci, E.L. Petersen, W.J. Pitz, H.J. Curran, *Combust. Flame*, 160 (2013) 995-1011.
[580] S.M. Burke, W. Metcalfe, O. Herbinet, F. Battin-Leclerc, F.M. Haas, J. Santner, F.L. Dryer, H.J. Curran, *Combust. Flame*, 161 (2014) 2765-2784.
[581] A.W. Jasper, S.J. Klippenstein, L.B. Harding, B. Ruscic, *The Journal of Physical Chemistry A*, 111 (2007) 3932-3950.
[582] M. Altarawneh, A.A.H. Al-Muhtaseb, B.Z. Dlugogorski, E.M. Kennedy, J.C. Mackie, *Journal of Computational Chemistry*, 32 (2011) 1725-1733.
[583] I.M. Alecu, D.G. Truhlar, *The Journal of Physical Chemistry A*, 115 (2011) 14599-14611.
[584] T. Varga, T. Nagy, C. Olm, I.G. Zsély, R. Pálvölgyi, É. Valkó, G. Vincze, M. Cserháti, H.J. Curran, T. Turányi, *Proc. Combust. Inst.*, 35 (2015) 589-596.
[585] P. Saxena, F.A. Williams, *Proc. Combust. Inst.*, 31 (2007) 1149-1156.
[586] H. Hashemi, J.M. Christensen, S. Gersen, P. Glarborg, *Proc. Combust. Inst.*, 35 (2015) 553-560.
[587] H. Hashemi, J.M. Christensen, S. Gersen, H. Levinsky, S.J. Klippenstein, P. Glarborg, *Combust. Flame*, 172 (2016) 349-364.
[588] J. Gimenez-Lopez, C.T. Rasmussen, H. Hashemi, M.U. Alzueta, Y. Gao, P. Marshall, C.F. Goldsmith, P. Glarborg, *Int. J. Chem. Kin.*, 48 (2016) 724-738.
[589] J. Gimenez-Lopez, C.L. Rasmussen, M.U. Alzueta, Y. Gao, P. Marshall, P. Glarborg, *Proc. Combust. Inst.*, 32 (2009) 367-375.
[590] H. Hashemi, J.G. Jacobsen, C.T. Rasmussen, J.M. Christensen, P. Glarborg, S. Gersen, M. van Essen, H.B. Levinsky, S.J. Klippenstein, *Combust. Flame*, 182 (2017) 150-166.
[591] T.M. Lenhardt, C.E. McDade, K.D. Bayes, *The Journal of Chemical Physics*, 72 (1980) 304-310.
[592] R.R. Baker, R.R. Baldwin, R.W. Walker, *Journal of the Chemical Society, Faraday Transactions 1: Physical Chemistry in Condensed Phases*, 71 (1975) 756-779.
[593] R. Minetti, M. Ribaucour, M. Carlier, C. Fittschen, L.R. Sochet, *Combust. Flame*, 96 (1994) 201-211.
[594] O. Herbinet, F. Battin-Leclerc, S. Bax, H.L. Gall, P.-A. Glaude, R. Fournet, Z. Zhou, L. Deng, H. Guo, M. Xie, F. Qi, *Phys Chem Chem Phys*, 13 (2011) 296-308.
[595] A.J. Eskola, O. Welz, J.D. Savee, D.L. Osborn, C.A. Taatjes, *The Journal of Physical Chemistry A*, 117 (2013) 12216-12235.
[596] G. Knothe, *Fuel Process Technol*, 86 (2005).
[597] G. Knothe, *Prog. Energy Comb. Sci.*, 36 (2010) 364-373.
[598] G. Knothe, L.F. Razon, *Prog. Energy Comb. Sci.*, 58 (2017) 36-59.
[599] M.S. Graboski, R.L. McCormick, *Prog. Energy Comb. Sci.*, 24 (1998) 125-164.
[600] S.K. Hoekman, A. Broch, C. Robbins, E. Ceniceros, M. Natarajan, *Renewable and Sustainable Energy Reviews*, 16 (2012) 143-169.
[601] A. Srivastava, R. Prasad, *Renewable and Sustainable Energy Reviews*, 4 (2000) 111-133.
[602] C.J. Hayes, D.R. Burgess Jr, *Proc. Combust. Inst.*, 32 (2009) 263-270.
[603] H. Tao, K.C. Lin, *Combust. Flame*, 161 (2014) 2270-2287.
[604] Y. Jiao, F. Zhang, T.S. Dibble, *The Journal of Physical Chemistry A*, (2015).
[605] G. Muller, A. Scheer, D.L. Osborn, C.A. Taatjes, G. Meloni, *The Journal of Physical Chemistry A*, 120 (2016) 1677-1690.
[606] J. Czekner, C.A. Taatjes, D.L. Osborn, G. Meloni, *Phys Chem Chem Phys*, (2018).
[607] S.M. Sarathy, S. Gaïl, S.A. Syed, M.J. Thomson, P. Dagaut, *Proc. Combust. Inst.*, 31 (2007) 1015-1022.

[608] S. Gaïl, M.J. Thomson, S.M. Sarathy, S.A. Syed, P. Dagaut, P. Diévart, A.J. Marchese, F.L. Dryer, *Proc. Combust. Inst.*, 31 (2007) 305-311.
[609] S. Gaïl, S.M. Sarathy, M.J. Thomson, P. Diévart, P. Dagaut, *Combust. Flame*, 155 (2008) 635-650.
[610] S.M. Walton, D.M. Karwat, P.D. Teini, A.M. Gorny, M.S. Wooldridge, *Fuel*, 90 (2011) 1796-1804.
[611] M.H. Hakka, H. Bennadji, J. Biet, M. Yahyaoui, B. Sirjean, V. Warth, L. Coniglio, O. Herbinet, P.A. Glaude, F. Billaud, F. Battin-Leclerc, *Int. J. Chem. Kin.*, 42 (2010) 226-252.
[612] K. HadjAli, M. Crochet, G. Vanhove, M. Ribaucour, R. Minetti, *Proc. Combust. Inst.*, 32 (2009) 239-246.
[613] W.K. Metcalfe, S. Dooley, H.J. Curran, J.M. Simmie, A.M. El-Nahas, M.V. Navarro, *The Journal of Physical Chemistry A*, 111 (2007) 4001-4014.
[614] S. Dooley, H.J. Curran, J.M. Simmie, *Combust. Flame*, 153 (2008) 2-32.
[615] S.M. Walton, M.S. Wooldridge, C.K. Westbrook, *Proc. Combust. Inst.*, 32 (2009) 255-262.
[616] B. Akih-Kumgeh, J.M. Bergthorson, *Combust. Flame*, 158 (2011) 1037-1048.
[617] K. Kumar, C.-J. Sung, *Combust. Flame*, 171 (2016) 1-14.
[618] A. Rodriguez, O. Herbinet, F. Battin-Leclerc, A. Frassoldati, T. Faravelli, E. Ranzi, *Combust. Flame*, 164 (2016) 346-362.
[619] K. Zhang, C. Togbé, G. Dayma, P. Dagaut, *Combust. Flame*, 161 (2014) 818-825.
[620] J. Mendes, C.-W. Zhou, H.J. Curran, *The Journal of Physical Chemistry A*, 118 (2014) 4889-4899.
[621] J. Mendes, C.-W. Zhou, H.J. Curran, *The Journal of Physical Chemistry A*, 117 (2013) 14006-14018.
[622] G. Dayma, F. Halter, F. Foucher, C. Togbé, C. Mounaim-Rousselle, P. Dagaut, *Energy & Fuels*, 26 (2012) 4735-4748.
[623] G. Dayma, C. Togbé, P. Dagaut, *Energy & Fuels*, 23 (2009) 4254-4268.
[624] P.A. Glaude, O. Herbinet, S. Bax, J. Biet, V. Warth, F. Battin-Leclerc, *Combust. Flame*, 157 (2010) 2035-2050.
[625] S. Bax, M.H. Hakka, P.A. Glaude, O. Herbinet, F. Battin-Leclerc, *Combust. Flame*, 157 (2010) 1220-1229.
[626] C.K. Westbrook, W.J. Pitz, S.M. Sarathy, M. Mehl, *Proc. Combust. Inst.*, 34 (2013) 3049-3056.
[627] Q.-D. Wang, Z.-H. Ni, *Chemical Physics Letters*, 650 (2016) 119-125.
[628] A. Osmont, L. Catoire, I. Gökalp, *Int. J. Chem. Kin.*, 39 (2007) 481-491.
[629] A. Osmont, M. Yahyaoui, L. Catoire, I. Gökalp, M.T. Swihart, *Combust. Flame*, 155 (2008) 334-342.
[630] A. Osmont, L. Catoire, P. Dagaut, *The Journal of Physical Chemistry A*, 114 (2010) 3788-3795.
[631] A.M. El-Nahas, M.V. Navarro, J.M. Simmie, J.W. Bozzelli, H.J. Curran, S. Dooley, W. Metcalfe, *The Journal of Physical Chemistry A*, 111 (2007) 3727-3739.
[632] V.B. Oyeyemi, J.A. Keith, E.A. Carter, *The Journal of Physical Chemistry A*, 118 (2014) 7392-7403.
[633] V.B. Oyeyemi, J.M. Dieterich, D.B. Krisiloff, T. Tan, E.A. Carter, *The Journal of Physical Chemistry A*, 119 (2015) 3429-3439.
[634] X. Li, X. Xu, X. You, D.G. Truhlar, *The Journal of Physical Chemistry A*, 120 (2016) 4025-4036.
[635] A. Osmont, L. Catoire, I. Gökalp, M.T. Swihart, *Energy & Fuels*, 21 (2007) 2027-2032.
[636] M. Lapuerta, J. Rodríguez-Fernández, F. Oliva, *Chemistry and Physics of Lipids*, 163 (2010) 172-181.
[637] V.M.L. dos Santos, J.A.B. da Silva, L. Stragevitch, R.L. Longo, *Fuel*, 90 (2011) 811-817.
[638] A.M. El-Nahas, L.A. Heikal, A.H. Mangood, E.-S.E. El-Shereefy, *The Journal of Physical Chemistry A*, 114 (2010) 7996-8002.
[639] T.T. Mai, X. Le, L. Huynh, *Struct Chem*, 26 (2015) 431-444.
[640] N. Cohen, S.W. Benson, *Chemical Reviews*, 93 (1993) 2419-2438.
[641] S. Dooley, M.P. Burke, M. Chaos, Y. Stein, F.L. Dryer, V.P. Zhukov, O. Finch, J.M. Simmie, H.J. Curran, *Int. J. Chem. Kin.*, 42 (2010) 527-549.
[642] V.B. Oyeyemi, M. Pavone, E.A. Carter, *ChemPhysChem*, 12 (2011) 3354-3364.

[643] W. Kohn, L.J. Sham, *Physical Review*, 140 (1965) A1133-A1138.
[644] T.J. Wallington, P. Dagaut, R. Liu, M.J. Kurylo, *Int. J. Chem. Kin.*, 20 (1988) 177-186.
[645] T. Tan, M. Pavone, D.B. Krisiloff, E.A. Carter, *The Journal of Physical Chemistry A*, 116 (2012) 8431-8443.
[646] T. Tan, X. Yang, Y. Ju, E.A. Carter, *Phys Chem Chem Phys*, 18 (2016) 4594-4607.
[647] K.-Y. Lam, D.F. Davidson, R.K. Hanson, *The Journal of Physical Chemistry A*, 116 (2012) 12229-12241.
[648] T. Tan, X. Yang, C.M. Krauter, Y. Ju, E.A. Carter, *The Journal of Physical Chemistry A*, 119 (2015) 6377-6390.
[649] A. El Boudali, S. Le Calvé, G. Le Bras, A. Mellouki, *The Journal of Physical Chemistry*, 100 (1996) 12364-12368.
[650] S. Le Calvé, G. Le Bras, A. Mellouki, *The Journal of Physical Chemistry A*, 101 (1997) 5489-5493.
[651] S. Jørgensen, V.F. Andersen, E.J.K. Nilsson, O.J. Nielsen, M.S. Johnson, *Chemical Physics Letters*, 490 (2010) 116-122.
[652] S. Le Calvé, G. Le Bras, A. Mellouki, *The Journal of Physical Chemistry A*, 101 (1997) 9137-9141.
[653] D. Hartmann, A. Gedra, D. Rhäsa, R. Zellner, *Proceedings of the 4th European Symposium on the Physico-Chemical Behavior of Atmospheric Pollutants*, (1987) 225-235.
[654] Y. Shang, H. Ning, J. Shi, H. Wang, S.-N. Luo, *Phys Chem Chem Phys*, 21 (2019) 20857-20867.
[655] W.A. Kopp, R.T. Langer, M. Döntgen, K. Leonhard, *The Journal of Physical Chemistry A*, 117 (2013) 6757-6770.
[656] S. Cagnina, A. Nicolle, T. de Bruin, Y. Georgievskii, S.J. Klippenstein, *The Journal of Physical Chemistry A*, 121 (2017) 1909-1915.
[657] Q. Meng, L. Zhang, Q. Chen, Y. Chi, P. Zhang, *The Journal of Physical Chemistry A*, 124 (2020) 8643-8652.
[658] N. Arthur, P. Newitt, *Australian Journal of Chemistry*, 32 (1979) 1697-1708.
[659] K.C. Ferguson, J.T. Pearson, *Transactions of the Faraday Society*, 66 (1970) 910.
[660] Q.-D. Wang, X.-J. Wang, G.-J. Kang, *Computational and Theoretical Chemistry*, 1027 (2014) 103-111.
[661] Q.-D. Wang, W. Zhang, *RSC Advances*, 5 (2015) 68314-68325.
[662] T.J. Wallington, M.J. Kurylo, *The Journal of Physical Chemistry*, 91 (1987) 5050-5054.
[663] Y. Georgievskii, S.J. Klippenstein, *The Journal of Physical Chemistry A*, 111 (2007) 3802-3811.
[664] J. Zheng, D.G. Truhlar, *Journal of Chemical Theory and Computation*, 9 (2013) 1356-1367.
[665] J. Zheng, T. Yu, E. Papajak, I.M. Alecu, S.L. Mielke, D.G. Truhlar, *Phys Chem Chem Phys*, 13 (2011) 10885-10907.
[666] X.T. Le, T.V.T. Mai, A. Ratkiewicz, L.K. Huynh, *The Journal of Physical Chemistry A*, 119 (2015) 3689-3703.
[667] S.P. Joshi, P. Seal, T.T. Pekkanen, R.S. Timonen, A.J. Eskola, *Zeitschrift für Physikalische Chemie*, 0 (2020).
[668] H. Tao, K.C. Lin, *Combust. Flame*, 180 (2017) 148-157.
[669] E.M. Fisher, W.J. Pitz, H.J. Curran, C.K. Westbrook, *Proc. Combust. Inst.*, 28 (2000) 1579-1586.
[670] O. Herbinet, W.J. Pitz, C.K. Westbrook, *Combust. Flame*, 154 (2008) 507-528.
[671] C. Togbé, J.B. May-Carle, G. Dayma, P. Dagaut, *J. Phys. Chem. A*, 114 (2010) 3896-3908.
[672] D.R. Glowacki, C.-H. Liang, C. Morley, M.J. Pilling, S.H. Robertson, *The Journal of Physical Chemistry A*, 116 (2012) 9545-9560.
[673] P. Dagaut, N. Smoucovit, M. Cathonnet, *Comb. Sci. Tech.*, 127 (1997) 275-291.
[674] G. Dayma, S. Gaïl, P. Dagaut, *Energy & Fuels*, 22 (2008) 1469-1479.
[675] S.W. Wagnon, D.M.A. Karwat, M.S. Wooldridge, C.K. Westbrook, *Energy & Fuels*, 28 (2014) 7227-7234.
[676] S. Garner, K. Brezinsky, *Combust. Flame*, 158 (2011) 2289-2301.
[677] S. Garner, T. Dubois, C. Togbé, N. Chaumeix, P. Dagaut, K. Brezinsky, *Combust. Flame*, 158 (2011) 2302-2313.

[678] A. Li, W. Ji, Z. Huang, L. Zhu, *Fuel*, 251 (2019) 162-174.
[679] H. Bennadji, P.A. Glaude, L. Coniglio, F. Billaud, *Fuel*, 90 (2011) 3237-3253.
[680] G. Dayma, S. Thion, M. Lailliau, Z. Serinyel, P. Dagaut, B. Sirjean, R. Fournet, *Proc. Combust. Inst.*, 37 (2019) 429-436.
[681] H.P. Ramirez, K. Hadj-Ali, P. Dievart, G. Dayma, C. Togbé, G. Moreac, P. Dagaut, *Proc. Combust. Inst.*, 33 (2011) 375-382.
[682] C. Togbé, G. Dayma, A. Mze-Ahmed, P. Dagaut, *Energy & Fuels*, 24 (2010) 3906-3916.
[683] M.H. Hakka, P.A. Glaude, O. Herbinet, F. Battin-Leclerc, *Combust. Flame*, 156 (2009) 2129-2144.
[684] T. Tan, X. Yang, Y. Ju, E.A. Carter, *Phys Chem Chem Phys*, 17 (2015) 31061-31072.
[685] Q. Meng, Y. Chi, L. Zhang, P. Zhang, L. Sheng, *Phys Chem Chem Phys*, 21 (2019) 5232-5242.
[686] F. Battin-Leclerc, A. Rodriguez, B. Husson, O. Herbinet, P.-A. Glaude, Z. Wang, Z. Cheng, F. Qi, *The Journal of Physical Chemistry A*, 118 (2014) 673-683.
[687] R. Bounaceur, V. Warth, B. Sirjean, P.A. Glaude, R. Fournet, F. Battin-Leclerc, *Proc. Combust. Inst.*, 32 (2009) 387-394.
[688] S. Touchard, R. Fournet, P.A. Glaude, V. Warth, F. Battin-Leclerc, G. Vanhove, M. Ribaucour, R. Minetti, *Proc. Combust. Inst.*, 30 (2005) 1073-1081.
[689] G. Vanhove, M. Ribaucour, R. Minetti, *Proc. Combust. Inst.*, 30 (2005) 1065-1072.
[690] N.D. Stothard, R.W. Walker, *Journal of the Chemical Society, Faraday Transactions*, 86 (1990) 2115-2119.
[691] W.K. Metcalfe, C. Togbé, P. Dagaut, H.J. Curran, J.M. Simmie, *Combust Flame*, 156 (2009) 250-260.
[692] B.I. Parsons, *Journal of the Chemical Society (Resumed)*, (1956) 1804-1809.
[693] B.I. Parsons, C.J. Danby, *Journal of the Chemical Society (Resumed)*, (1956) 1795-1798.
[694] B.I. Parsons, C. Hinshelwood, *Journal of the Chemical Society (Resumed)*, (1956) 1799-1803.
[695] D.E. Hoare, T.-M. Li, A.D. Walsh, *Symposium (International) on Combustion*, 11 (1967) 879-887.
[696] L. Coniglio, H. Bennadji, P.A. Glaude, O. Herbinet, F. Billaud, *Prog. Energy Comb. Sci.*, 39 (2013) 340-382.
[697] C.K. Westbrook, *Annual Review of Physical Chemistry*, 64 (2013) 201-219.
[698] J.Y.W. Lai, K.C. Lin, A. Violi, *Prog. Energy Comb. Sci.*, 37 (2011) 1-14.
[699] Z. Zhang, E. Hu, L. Pan, Y. Chen, J. Gong, Z. Huang, *Energy & Fuels*, 28 (2014) 7194-7202.
[700] K. Kumar, C.-J. Sung, B.W. Weber, J.A. Bunnell, *Combust. Flame*, 188 (2018) 116-128.
[701] H. Bennadji, L. Coniglio, F. Billaud, R. Bounaceur, V. Warth, P.A. Glaude, F. Battin-Leclerc, *Int. J. Chem. Kin.*, 43 (2011) 204-218.
[702] B.W. Weber, J.A. Bunnell, K. Kumar, C.-J. Sung, *Fuel*, 212 (2018) 479-486.
[703] I.E. Gerasimov, D.A. Knyazkov, T.A. Bolshova, A.G. Shmakov, O.P. Korobeinichev, M. Carbonnier, B. Lefort, A. Kéromnès, L. Le Moyne, M. Lubrano Lavadera, A.A. Konnov, C.-W. Zhou, Z. Serinyel, G. Dayma, P. Dagaut, *Combust. Flame*, 222 (2020) 170-180.
[704] B. Rotavera, E.L. Petersen, *Proc. Combust. Inst.*, 34 (2013) 435-442.
[705] M.F. Campbell, D.F. Davidson, R.K. Hanson, *Fuel*, 126 (2014) 271-281.
[706] Z. Li, W. Wang, Z. Huang, M.A. Oehlschlaeger, *Energy & Fuels*, 26 (2012) 4887-4895.
[707] W. Wang, M.A. Oehlschlaeger, *Combust. Flame*, 159 (2012) 476-481.
[708] W. Wang, S. Gowdagiri, M.A. Oehlschlaeger, *Energy & Fuels*, 27 (2013) 5527-5532.
[709] B. Akih-Kumgeh, J.M. Bergthorson, *Energy & Fuels*, 25 (2011) 4345-4356.
[710] J. Bugler, K.P. Somers, E.J. Silke, H.J. Curran, *J. Phys. Chem. A*, 119 (2015) 7510-7527.
[711] M. Ribaucour, R. Minetti, L.R. Sochet, *Symposium (International) on Combustion*, 27 (1998) 345-351.
[712] D. Felsmann, H. Zhao, Q. Wang, I. Graf, T. Tan, X. Yang, E.A. Carter, Y. Ju, K. Kohse-Höinghaus, *Proc. Combust. Inst.*, 36 (2017) 543-551.
[713] X. Yang, D. Felsmann, N. Kurimoto, J. Krüger, T. Wada, T. Tan, E.A. Carter, K. Kohse-Höinghaus, Y. Ju, *Proc. Combust. Inst.*, 35 (2015) 491-498.

[714] A. Ahmed, W.J. Pitz, C. Cavallotti, M. Mehl, N. Lokachari, E.J.K. Nilsson, J.-Y. Wang, A.A. Konnov, S.W. Wagnon, B. Chen, Z. Wang, S. Kim, H.J. Curran, S.J. Klippenstein, W.L. Roberts, S.M. Sarathy, *Proc. Combust. Inst.*, 37 (2019) 419-428.
[715] L.K. Huynh, K.C. Lin, A. Violi, *The Journal of Physical Chemistry A*, 112 (2008) 13470-13480.
[716] G. Dayma, S.M. Sarathy, C. Togbé, C. Yeung, M.J. Thomson, P. Dagaut, *Proc. Combust. Inst.*, 33 (2011) 1037-1043.
[717] S.M. Sarathy, M.J. Thomson, W.J. Pitz, T. Lu, *Proc. Combust. Inst.*, 33 (2011) 399-405.
[718] P. Diévart, S.H. Won, S. Dooley, F.L. Dryer, Y. Ju, *Combust. Flame*, 159 (2012) 1793-1805.
[719] C.V. Naik, C.K. Westbrook, O. Herbinet, W.J. Pitz, M. Mehl, *Proc. Combust. Inst.*, 33 (2011) 383-389.
[720] P. Diévart, S.H. Won, J. Gong, S. Dooley, Y. Ju, *Proc. Combust. Inst.*, 34 (2013) 821-829.
[721] A. Farooq, D.F. Davidson, R.K. Hanson, C.K. Westbrook, *Fuel*, 134 (2014) 26-38.
[722] O. Herbinet, W.J. Pitz, C.K. Westbrook, *Combust. Flame*, 157 (2010) 893-908.
[723] J.M. Hudzik, J.W. Bozzelli, *The Journal of Physical Chemistry A*, 116 (2012) 5707-5722.
[724] S. Thion, C. Togbé, G. Dayma, Z. Serinyel, P. Dagaut, *Energy & Fuels*, 31 (2016) 2144-2155.
[725] A. Klamt, *Chemosphere*, 32 (1996) 717-726.
[726] I. Frank, M. Parrinello, A. Klamt, *The Journal of Physical Chemistry A*, 102 (1998) 3614-3617.
[727] M.D. Boot, M. Tian, E.J.M. Hensen, S. Mani Sarathy, *Prog Energ Combust*, 60 (2017) 1-25.
[728] K.-Y. Lam, D.F. Davidson, R.K. Hanson, *The Journal of Physical Chemistry A*, 116 (2012) 5549-5559.
[729] J. Badra, A.E. Elwardany, A. Farooq, *Phys Chem Chem Phys*, 16 (2014) 12183-12193.
[730] P. Dagaut, T.J. Wallington, R. Liu, M.J. Kurylo, *The Journal of Physical Chemistry*, 92 (1988) 4375-4377.
[731] E. Jiménez, B. Ballesteros, E. Martínez, J. Albaladejo, *Environmental Science & Technology*, 39 (2005) 814-820.
[732] S. Le Calvé, D. Hitier, G. Le Bras, A. Mellouki, *The Journal of Physical Chemistry A*, 102 (1998) 4579-4584.
[733] J.R. Alvarez-Idaboy, A. Cruz-Torres, A. Galano, M.E. Ruiz-Santoyo, *The Journal of Physical Chemistry A*, 108 (2004) 2740-2749.
[734] C.-W. Zhou, J.M. Simmie, H.J. Curran, *Phys Chem Chem Phys*, 13 (2011) 11175-11192.
[735] R. Atkinson, S.M. Aschmann, W.P.L. Carter, J.N. Pitts, *Int. J. Chem. Kin.*, 14 (1982) 839-847.
[736] R.S. Tranter, R.W. Walker, *Phys Chem Chem Phys*, 3 (2001) 1262-1270.
[737] S.A. Carr, M.T. Baeza-Romero, M.A. Blitz, B.J.S. Price, P.W. Seakins, *Int. J. Chem. Kin.*, 40 (2008) 504-514.
[738] C.-W. Zhou, J. Mendes, H.J. Curran, *The Journal of Physical Chemistry A*, 117 (2013) 4526-4533.
[739] W.A. Kopp, U. Burke, M. Döntgen, L.C. Kröger, H. Minwegen, K.A. Heufer, K. Leonhard, *Proc. Combust. Inst.*, 36 (2017) 203-210.
[740] J. Badra, A.E. Elwardany, F. Khaled, S.S. Vasu, A. Farooq, *Combust. Flame*, 161 (2014) 725-734.
[741] D. Liu, B.R. Giri, A. Farooq, *The Journal of Physical Chemistry A*, 123 (2019) 4325-4332.
[742] C.-W. Zhou, J.M. Simmie, W.J. Pitz, H.J. Curran, *The Journal of Physical Chemistry A*, 120 (2016) 7037-7044.
[743] S. Thion, Z. Serinyel, G. Dayma, P. Dagaut, *Fuel*, 220 (2018) 908-915.
[744] Z. Serinyel, C. Togbé, A. Zaras, G. Dayma, P. Dagaut, *Proc. Combust. Inst.*, 35 (2015) 507-514.
[745] S. Pichon, G. Black, N. Chaumeix, M. Yahyaoui, J. Simmie, H. Curran, R. Donohue, *Combust. Flame*, 156 (2009) 494-504.
[746] R. Sivaramakrishnan, J.V. Michael, *Combust. Flame*, 156 (2009) 1126-1134.
[747] A.T. Droege, F.P. Tully, *J Phys Chem-Us*, 91 (1987) 1222-1225.
[748] G.S. Jolly, G. Paraskevopoulos, D.L. Singleton, *Int. J. Chem. Kin.*, 17 (1985) 1-10.
[749] J. Bott, N. Cohen, *Int. J. Chem. Kin.*, 21 (1989) 485-498.
[750] W.B. DeMore, K.D. Bayes, *The Journal of Physical Chemistry A*, 103 (1999) 2649-2654.

[751] S.M. Handford-Styring, R.W. Walker, *Journal of the Chemical Society, Faraday Transactions*, 91 (1995) 1431-1438.
[752] F. Kramp, S.E. Paulson, *The Journal of Physical Chemistry A*, 102 (1998) 2685-2690.
[753] N.M. Donahue, J.G. Anderson, K.L. Demerjian, *The Journal of Physical Chemistry A*, 102 (1998) 3121-3126.
[754] R. Atkinson, S. Aschmann, W. Carter, A. Winer, J. Pitts Jr, *Int. J. Chem. Kin.*, 14 (1982) 781-788.
[755] E.W. Wilson, W.A. Hamilton, H.R. Kennington, B. Evans, N.W. Scott, W.B. DeMore, *The Journal of Physical Chemistry A*, 110 (2006) 3593-3604.
[756] R.S. Anderson, L. Huang, R. Iannone, A.E. Thompson, J. Rudolph, *The Journal of Physical Chemistry A*, 108 (2004) 11537-11544.
[757] A.M. Scheer, O. Welz, S.S. Vasu, D.L. Osborn, C.A. Taatjes, *Phys Chem Chem Phys*, 17 (2015) 12124-12134
[758] A.M. Scheer, A.J. Eskola, D.L. Osborn, L. Sheps, C.A. Taatjes, *The Journal of Physical Chemistry A*, 120 (2016) 8625-8636.
[759] B. Rotavera, A.M. Scheer, H. Huang, D.L. Osborn, C.A. Taatjes, *Proc. Combust. Inst.*, 35 (2015) 543-552.
[760] N. Sebbar, J.W. Bozzelli, H. Bockhorn, *The Journal of Physical Chemistry A*, 118 (2014) 21-37.
[761] N. Sebbar, J.W. Bozzelli, H. Bockhorn, *Zeitschrift für Physikalische Chemie*, 225 (2011) 993-1018.
[762] N. Sebbar, J.W. Bozzelli, D. Trimis, H. Bockhorn, *Int. J. Chem. Kin.*, 0 (2019).
[763] S. Kuzhanthaivelan, B. Rajakumar, *The Journal of Physical Chemistry A*, 122 (2018) 6134-6146.
[764] C. Hemken, U. Burke, K.-Y. Lam, D.F. Davidson, R.K. Hanson, K.A. Heufer, K. Kohse-Höinghaus, *Combust. Flame*, 184 (2017) 195-207.
[765] S. Khanniche, W.H. Green, *The Journal of Physical Chemistry A*, 123 (2019) 9644-9657.
[766] J. Allen, W. Green, *Included in: Reaction Mechanism Generator, v2. 0.0*, (2016).
[767] K. Zhang, N. Lokachari, E. Ninnemann, S. Khanniche, W.H. Green, H.J. Curran, S.S. Vasu, W.J. Pitz, *Proc. Combust. Inst.*, 37 (2019) 657-665.
[768] M.J. Al Rashidi, M. Mehl, W.J. Pitz, S. Mohamed, S.M. Sarathy, *Combust. Flame*, 183 (2017) 358-371.
[769] S. Yommee, J.W. Bozzelli, *The Journal of Physical Chemistry A*, 120 (2016) 433-451.
[770] H. Wang, K. Brezinsky, *The Journal of Physical Chemistry A*, 102 (1998) 1530-1541.
[771] S. Kuzhanthaivelan, R. B, *Combust. Flame*, 219 (2020) 147-160.
[772] J. Bardwell, *Proceedings of the Royal Society of London A: Mathematical, Physical and Engineering Sciences*, 207 (1951) 470-482.
[773] J. Bardwell, C. Hinshelwood, *Proceedings of the Royal Society of London A: Mathematical, Physical and Engineering Sciences*, 205 (1951) 375-390.
[774] J. Bardwell, C. Hinshelwood, *Proceedings of the Royal Society of London A: Mathematical, Physical and Engineering Sciences*, 207 (1951) 461-470.
[775] J. Bardwell, C. Hinshelwood, *Proceedings of the Royal Society of London A: Mathematical, Physical and Engineering Sciences*, 201 (1950) 26-39.
[776] S. Thion, P. Diévart, P. Van Cauwenberghe, G. Dayma, Z. Serinyel, P. Dagaut, *Proc. Combust. Inst.*, 36 (2017) 459-467.
[777] Y. Fenard, J. Pieper, C. Hemken, H. Minwegen, R.D. Büttgen, K. Kohse-Höinghaus, K.A. Heufer, *Combust. Flame*, 216 (2020) 29-44.
[778] M. Schenk, L. Leon, K. Moshammer, P. Oßwald, T. Zeuch, L. Seidel, F. Mauss, K. Kohse-Höinghaus, *Combust. Flame*, 160 (2013) 487-503.
[779] F. Hoppe, U. Burke, M. Thewes, A. Heufer, F. Kremer, S. Pischinger, *Fuel*, 167 (2016) 106-117.
[780] U. Burke, J. Beeckmann, W.A. Kopp, Y. Uygun, H. Olivier, K. Leonhard, H. Pitsch, K.A. Heufer, *Combust. Flame*, 168 (2016) 296-309.
[781] J.W. Allen, A.M. Scheer, C.W. Gao, S.S. Merchant, S.S. Vasu, O. Welz, J.D. Savee, D.L. Osborn, C. Lee, S. Vranckx, Z. Wang, F. Qi, R.X. Fernandes, W.H. Green, M.Z. Hadi, C.A. Taatjes, *Combust. Flame*, 161 (2014) 711-724.

[782] M. Fikri, L.R. Cancino, M. Hartmann, C. Schulz, *Proc. Combust. Inst.*, 34 (2013) 393-400.
[783] H. Minwegen, U. Burke, K.A. Heufer, *Proc. Combust. Inst.*, 36 (2017) 561-568.
[784] Z. Serinyel, G. Black, H.J. Curran, J.M. Simmie, *Comb. Sci. Tech.*, 182 (2010) 574-587.
[785] Z. Serinyel, N. Chaumeix, G. Black, J.M. Simmie, H.J. Curran, *The Journal of Physical Chemistry A*, 114 (2010) 12176-12186.
[786] J. He, Y. Gou, P. Lu, C. Zhang, P. Li, X. Li, *Combust. Flame*, 192 (2018) 358-368.
[787] G. Barari, S.M. Sarathy, S.S. Vasu, *Fuel*, 164 (2016) 141-150.
[788] F. Battin-Leclerc, O. Herbinet, P.-A. Glaude, R. Fournet, Z. Zhou, L. Deng, H. Guo, M. Xie, F. Qi, *Proc. Combust. Inst.*, 33 (2011) 325-331.
[789] A.J. Eskola, O. Welz, J. Zádor, I.O. Antonov, L. Sheps, J.D. Savee, D.L. Osborn, C.A. Taatjes, *Proc. Combust. Inst.*, 35 (2015) 291-298.
[790] Y. Fenard, P. Dagaut, G. Dayma, F. Halter, F. Foucher, *Proc. Combust. Inst.*, 35 (2015) 317-324.
[791] Y. Fenard, G. Dayma, F. Halter, F. Foucher, Z. Serinyel, P. Dagaut, *Energy & Fuels*, 29 (2015) 1107-1118.
[792] K. Zhang, C. Banyon, J. Bugler, H.J. Curran, A. Rodriguez, O. Herbinet, F. Battin-Leclerc, C. B'Chir, K.A. Heufer, *Combust. Flame*, 172 (2016) 116-135.
[793] M.J. Al Rashidi, S. Thion, C. Togbé, G. Dayma, M. Mehl, P. Dagaut, W.J. Pitz, J. Zádor, S.M. Sarathy, *Proc. Combust. Inst.*, 36 (2017) 469-477.
[794] B. Heyberger, F. Battin-Leclerc, V. Warth, R. Fournet, G.M. Côme, G. Scacchi, *Combust. Flame*, 126 (2001) 1780-1802.
[795] Z. Serinyel, O. Herbinet, O. Frottier, P. Dirrenberger, V. Warth, P.A. Glaude, F. Battin-Leclerc, *Combust. Flame*, 160 (2013) 2319-2332.
[796] A.L. Koritzke, J.C. Davis, R.L. Caravan, M.G. Christianson, D.L. Osborn, C.A. Taatjes, B. Rotavera, *Proc. Combust. Inst.*, 37 (2019) 323-335.
[797] L. Cai, A. Sudholt, D.J. Lee, F.N. Egolfopoulos, H. Pitsch, C.K. Westbrook, S.M. Sarathy, *Combust. Flame*, 161 (2014) 798-809.
[798] S. Thion, C. Togbé, Z. Serinyel, G. Dayma, P. Dagaut, *Combust. Flame*, 185 (2017) 4-15.
[799] A. García, J. Monsalve-Serrano, D. Villalta, M. Guzmán-Mendoza, *Fuel*, 287 (2021) 119548.
[800] L. Cai, S. Jacobs, R. Langer, F. vom Lehn, K.A. Heufer, H. Pitsch, *Fuel*, 264 (2020) 116711.
[801] A. Omari, B. Heuser, S. Pischinger, C. Rüdinger, *Applied Energy*, 239 (2019) 1242-1249.
[802] Z. Gao, E. Hu, Z. Xu, G. Yin, Z. Huang, *Combust. Flame*, 207 (2019) 20-35.
[803] C. Bänsch, M. Olzmann, *Chemical Physics Letters*, 720 (2019) 19-24.
[804] S. Jacobs, M. Döntgen, A.B.S. Alquaity, W.A. Kopp, L.C. Kröger, U. Burke, H. Pitsch, K. Leonhard, H.J. Curran, K.A. Heufer, *Combust. Flame*, 205 (2019) 522-533.
[805] W.A. Kopp, L.C. Kröger, M. Döntgen, S. Jacobs, U. Burke, H.J. Curran, K. Alexander Heufer, K. Leonhard, *Combust. Flame*, 189 (2018) 433-442.
[806] C.A. Daly, J.M. Simmie, P. Dagaut, M. Cathonnet, *Combustion and Flame*, 125 (2001) 1106-1117.
[807] S. Jacobs, M. Dontgen, A.B.S. Alquaity, W.A. Kopp, L.C. Kroger, U. Burke, H. Pitsch, K. Leonhard, H.J. Curran, K.A. Heufer, *Combustion and Flame*, 205 (2019) 522-533.
[808] W.A. Kopp, L.C. Kroger, M. Dontgen, S. Jacobs, U. Burke, H.J. Curran, K.A. Heufer, K. Leonhard, *Combustion and Flame*, 189 (2018) 433-442.
[809] W.Y. Sun, T. Tao, M. Lailliau, N. Hansen, B. Yang, P. Dagaut, *Combustion and Flame*, 193 (2018) 491-501.
[810] F.H. Vermeire, H.-H. Carstensen, O. Herbinet, F. Battin-Leclerc, G.B. Marin, K.M. Van Geem, *Combust. Flame*, 190 (2018) 270-283.
[811] R.A. Perry, R. Atkinson, J.N. Pitts, *The Journal of Chemical Physics*, 67 (1977) 611-614.
[812] F.P. Tully, A.T. Droege, *Int. J. Chem. Kin.*, 19 (1987) 251-259.
[813] A. Mellouki, S. Teton, G. Le Bras, *Int. J. Chem. Kin.*, 27 (1995) 791-805.
[814] M. Arif, B. Dellinger, P.H. Taylor, *The Journal of Physical Chemistry A*, 101 (1997) 2436-2441.
[815] R.S. Tranter, R.W. Walker, *Phys Chem Chem Phys*, 3 (2001) 4722-4732.

[816] A. Bottoni, P.D. Casa, G. Poggi, *Journal of Molecular Structure: THEOCHEM*, 542 (2001) 123-137.
[817] F. Atadinc, C. Selcuki, L. Sari, V. Aviyente, *Phys Chem Chem Phys*, 4 (2002) 1797-1806.
[818] A. Bonard, V. Daële, J.-L. Delfau, C. Vovelle, *The Journal of Physical Chemistry A*, 106 (2002) 4384-4389.
[819] J.-y. Wu, J.-y. Liu, Z.-s. Li, C.-c. Sun, *The Journal of Chemical Physics*, 118 (2003) 10986-10995.
[820] A.M. El-Nahas, T. Uchimaru, M. Sugie, K. Tokuhashi, A. Sekiya, *Journal of Molecular Structure: THEOCHEM*, 722 (2005) 9-19.
[821] T. Ogura, A. Miyoshi, M. Koshi, *Phys Chem Chem Phys*, 9 (2007) 5133-5142.
[822] C. Zavala-Oseguera, J.R. Alvarez-Idaboy, G. Merino, A. Galano, *The Journal of Physical Chemistry A*, 113 (2009) 13913-13920.
[823] C.-W. Zhou, J.M. Simmie, H.J. Curran, *Phys Chem Chem Phys*, 12 (2010) 7221-7233.
[824] S.A. Carr, T.J. Still, M.A. Blitz, A.J. Eskola, M.J. Pilling, P.W. Seakins, R.J. Shannon, B. Wang, S.H. Robertson, *The Journal of Physical Chemistry A*, 117 (2013) 11142-11154.
[825] C. Bänsch, J. Kiecherer, M. Szöri, M. Olzmann, *The Journal of Physical Chemistry A*, 117 (2013) 8343-8351.
[826] T.J. Wallington, R. Liu, P. Dagaut, M.J. Kurylo, *Int. J. Chem. Kin.*, 20 (1988) 41-49.
[827] P.J. Bennett, J.A. Kerr, *Journal of Atmospheric Chemistry*, 10 (1990) 27-38.
[828] M. Semadeni, D.W. Stocker, J.A. Kerr, *Journal of Atmospheric Chemistry*, 16 (1993) 79-93.
[829] S. Teton, A. Mellouki, G. Le Bras, H. Sidebottom, *Int. J. Chem. Kin.*, 28 (1996) 291-297.
[830] D.P. Starkey, K.A. Holbrook, G.A. Oldershaw, R.W. Walker, *Int. J. Chem. Kin.*, 29 (1997) 231-236.
[831] L. Yang, J.-Y. Liu, L. Wang, H.-Q. He, Y. Wang, Z.-S. Li, *Journal of Computational Chemistry*, 29 (2008) 550-561.
[832] T.J. Wallington, M.D. Hurley, J.C. Ball, A.M. Straccia, J. Platz, L.K. Christensen, J. Sehested, O.J. Nielsen, *Journal of Physical Chemistry A*, 101 (1997) 5302-5308.
[833] C. Vovelle, A. Bonard, V. Daele, J.L. Delfau, *Physical Chemistry Chemical Physics*, 3 (2001) 4939-4945.
[834] W.-P. Hu, I. Rossi, J.C. Corchado, D.G. Truhlar, *The Journal of Physical Chemistry A*, 101 (1997) 6911-6921.
[835] L. Nelson, O. Rattigan, R. Neavyn, H. Sidebottom, J. Treacy, O.J. Nielsen, *Int. J. Chem. Kin.*, 22 (1990) 1111-1126.
[836] T.J. Wallington, J.M. Andino, L.M. Skewes, W.O. Siegl, S.M. Japar, *Int. J. Chem. Kin.*, 21 (1989) 993-1001.
[837] R.D. Cook, D.F. Davidson, R.K. Hanson, *The Journal of Physical Chemistry A*, 113 (2009) 9974-9980.
[838] E. Porter, J. Wenger, J. Treacy, H. Sidebottom, A. Mellouki, S. Teton, G. LeBras, *Journal of Physical Chemistry A*, 101 (1997) 5770-5775.
[839] T.J. He, Z. Wang, X.Q. You, H.Y. Liu, Y.D. Wang, X.Y. Li, X. He, *Fuel*, 212 (2018) 223-235.
[840] P. Sela, Y. Sakai, H.S. Choi, J. Herzler, M. Fikri, C. Schulz, S. Peukert, *The Journal of Physical Chemistry A*, 123 (2019) 6813-6827.
[841] R. Sivaramakrishnan, J.V. Michael, *The Journal of Physical Chemistry A*, 113 (2009) 5047-5060.
[842] D.G. Potter, S. Wiseman, M.A. Blitz, P.W. Seakins, *The Journal of Physical Chemistry A*, 122 (2018) 9701-9711.
[843] R.S. Tranter, P.T. Lynch, C.J. Annesley, *The Journal of Physical Chemistry A*, 116 (2012) 7287-7292.
[844] J. Long, G. Skirrow, *Transactions of the Faraday Society*, 58 (1962) 1403-1408.
[845] P.D. Pacey, *Canadian Journal of Chemistry*, 53 (1975) 2742-2747.
[846] Y. Hidaka, K. Sato, M. Yamane, *Combust. Flame*, 123 (2000) 1-22.
[847] A.M. Held, K.C. Manthorne, P.D. Pacey, H.P. Reinholdt, *Canadian Journal of Chemistry*, 55 (1977) 4128-4134.

[848] H.J. Curran, S.L. Fischer, F.L. Dryer, *Int. J. Chem. Kin.*, 32 (2000) 741-759.
[849] V. Saheb, *Journal of Physical Chemistry A*, 119 (2015) 4711-4717.
[850] Y.L. Guan, Y. Li, L.D. Zhao, H.X. Ma, J.R. Song, *Comput. Theor. Chem.*, 1096 (2016) 7-16.
[851] S. Wang, L. Wang, *Phys Chem Chem Phys*, 18 (2016) 7707-7714.
[852] K. Moshammer, A.W. Jasper, D.M. Popolan-Vaida, Z. Wang, V.S. Bhavani Shankar, L. Ruwe, C.A. Taatjes, P. Dagaut, N. Hansen, *The Journal of Physical Chemistry A*, 120 (2016) 7890-7901.
[853] A. Andersen, E.A. Carter, *The Journal of Physical Chemistry A*, 107 (2003) 9463-9478.
[854] K. Suzaki, N. Kanno, K. Tonokura, M. Koshi, K. Tsuchiya, A. Tezaki, *Chemical Physics Letters*, 425 (2006) 179-184.
[855] T.J. Wallington, M.D. Hurley, J.C. Ball, M.E. Jenkin, *Chemical Physics Letters*, 211 (1993) 41-47.
[856] M.E. Jenkin, G.D. Hayman, T.J. Wallington, M.D. Hurley, J.C. Ball, O.J. Nielsen, T. Ellermann, *The Journal of Physical Chemistry*, 97 (1993) 11712-11723.
[857] M.M. Maricq, J.J. Szente, J.D. Hybl, *The Journal of Physical Chemistry A*, 101 (1997) 5155-5167.
[858] C.M. Rosado-Reyes, J.S. Francisco, J.J. Szente, M.M. Maricq, L. Frøsig Østergaard, *The Journal of Physical Chemistry A*, 109 (2005) 10940-10953.
[859] J. Sehested, K. Sehested, J. Platz, H. Egsgaard, O.J. Nielsen, *Int. J. Chem. Kin.*, 29 (1997) 627-636.
[860] K. Hoyermann, F. Nacke, *Symposium (International) on Combustion*, 26 (1996) 505-512.
[861] A. Masaki, S. Tsunashima, N. Washida, *The Journal of Physical Chemistry*, 99 (1995) 13126-13131.
[862] T. Yamada, J.W. Bozzelli, T.H. Lay, *Int. J. Chem. Kin.*, 32 (2000) 435-452.
[863] A.J. Eskola, S.A. Carr, R.J. Shannon, B. Wang, M.A. Blitz, M.J. Pilling, P.W. Seakins, S.H. Robertson, *The Journal of Physical Chemistry A*, 118 (2014) 6773-6788.
[864] R.J. Shannon, A.S. Tomlin, S.H. Robertson, M.A. Blitz, M.J. Pilling, P.W. Seakins, *The Journal of Physical Chemistry A*, 119 (2015) 7430-7438.
[865] D.G. Potter, M.A. Blitz, P.W. Seakins, *Chemical Physics Letters*, 730 (2019) 213-219.
[866] A. Andersen, E.A. Carter, *Molecular Physics*, 106 (2008) 367-396.
[867] H.J. Curran, W.J. Pitz, C.K. Westbrook, P. Dagaut, J.C. Boettner, M. Cathonnet, *Int. J. Chem. Kin.*, 30 (1998) 229-241.
[868] R.P. Ruiz, K.D. Bayes, *The Journal of Physical Chemistry*, 88 (1984) 2592-2595.
[869] K. Suzaki, K. Tsuchiya, M. Koshi, A. Tezaki, *The Journal of Physical Chemistry A*, 111 (2007) 3776-3788.
[870] A. Andersen, E.A. Carter, *Israel Journal of Chemistry*, 42 (2002) 245-260.
[871] A. Andersen, E.A. Carter, *The Journal of Physical Chemistry A*, 110 (2006) 1393-1407.
[872] A. Rodriguez, O. Frottier, O. Herbinet, R. Fournet, R. Bounaceur, C. Fittschen, F. Battin-Leclerc, *The Journal of Physical Chemistry A*, 119 (2015) 7905-7923.
[873] J. Sehested, T. Møgelberg, T.J. Wallington, E.W. Kaiser, O.J. Nielsen, *The Journal of Physical Chemistry*, 100 (1996) 17218-17225.
[874] I. Liu, N.W. Cant, J.H. Bromly, F.J. Barnes, P.F. Nelson, B.S. Haynes, *Chemosphere*, 42 (2001) 583-589.
[875] J. Thamm, S. Wolff, W.V. Turner, S. Gäb, W. Thomas, F. Zabel, E.H. Fink, K.H. Becker, *Chemical Physics Letters*, 258 (1996) 155-158.
[876] M. Dontgen, W.A. Kopp, F. vom Lehn, L.C. Kroger, H. Pitsch, K. Leonhard, K.A. Heufer, *International Journal of Chemical Kinetics*.
[877] S. Di Tommaso, P. Rotureau, O. Crescenzi, C. Adamo, *Phys Chem Chem Phys*, 13 (2011) 14636-14645.
[878] S. Di Tommaso, P. Rotureau, C. Adamo, *The Journal of Physical Chemistry A*, 116 (2012) 9010-9019.
[879] Y. Sakai, H. Ando, H.K. Chakravarty, H. Pitsch, R.X. Fernandes, *Proc. Combust. Inst.*, 35 (2015) 161-169.
[880] Y. Sakai, J. Herzler, M. Werler, C. Schulz, M. Fikri, *Proc. Combust. Inst.*, 36 (2017) 195-202.
[881] J.J. Orlando, *Phys Chem Chem Phys*, 9 (2007) 4189-4199.

[882] M. Demireva, K. Au, L. Sheps, *Phys Chem Chem Phys*, 22 (2020) 24649-24661.
[883] M. Winfough, R. Yao, M. Ng, K. Catani, G. Meloni, *The Journal of Physical Chemistry A*, (2017).
[884] A. Giustini, G. Meloni, *ChemPhysChem*, 21 (2020) 927-937.
[885] M.U. Alzueta, J. Muro, R. Bilbao, P. Glarborg, *Israel Journal of Chemistry*, 39 (1999) 73-86.
[886] P. Dagaut, C. Daly, J.M. Simmie, M. Cathonnet, *Symposium (International) on Combustion*, 27 (1998) 361-369.
[887] P. Dagaut, J.-C. Boettner, M. Cathonnet, *Symposium (International) on Combustion*, 26 (1996) 627-632.
[888] F. Herrmann, P. Oßwald, K. Kohse-Höinghaus, *Proc. Combust. Inst.*, 34 (2013) 771-778.
[889] F. Herrmann, B. Jochim, P. Oßwald, L. Cai, H. Pitsch, K. Kohse-Höinghaus, *Combust. Flame*, 161 (2014) 384-397.
[890] Z. Wang, X. Zhang, L. Xing, L. Zhang, F. Herrmann, K. Moshammer, F. Qi, K. Kohse-Höinghaus, *Combust. Flame*, 162 (2015) 1113-1125.
[891] K.-D. Stoehr, N. Peters, J. Beeckmann, *Proc. Combust. Inst.*, 35 (2015) 3601-3607.
[892] P. Dagaut, J. Luche, M. Cathonnet, *Comb. Sci. Tech.*, 165 (2001) 61-84.
[893] A. Sudholt, L. Cai, H. Pitsch, *Combust. Flame*, 202 (2019) 347-361.
[894] H. Hashemi, J.M. Christensen, P. Glarborg, *Combust. Flame*, 205 (2019) 80-92.
[895] D.J. Waddington, *Proceedings of the Royal Society of London A: Mathematical, Physical and Engineering Sciences*, 252 (1959) 260-272.
[896] J.F. Griffiths, T. Inomata, *Journal of the Chemical Society, Faraday Transactions*, 88 (1992) 3153-3158.
[897] Z. Serinyel, M. Lailliau, S. Thion, G. Dayma, P. Dagaut, *Combust. Flame*, 193 (2018) 453-462.
[898] L.-S. Tran, O. Herbinet, Y. Li, J. Wullenkord, M. Zeng, E. Bräuer, F. Qi, K. Kohse-Höinghaus, F. Battin-Leclerc, *Proc. Combust. Inst.*, 37 (2019) 511-519.
[899] L.-S. Tran, Y. Li, M. Zeng, J. Pieper, F. Qi, F. Battin-Leclerc, K. Kohse-Höinghaus, O. Herbinet, *Zeitschrift für Physikalische Chemie*, 0 (2020).
[900] N. Belhadj, R. Benoit, M. Lailliau, V. Glasziou, P. Dagaut, *Combust. Flame*, 228 (2021) 340-350.
[901] L.-S. Tran, J. Wullenkord, Y. Li, O. Herbinet, M. Zeng, F. Qi, K. Kohse-Höinghaus, F. Battin-Leclerc, *Combust. Flame*, 210 (2019) 9-24.
[902] N. Belhadj, R. Benoit, P. Dagaut, M. Lailliau, Z. Serinyel, G. Dayma, F. Khaled, B. Moreau, F. Foucher, *Combust. Flame*, 222 (2020) 133-144.
[903] B. Brumfield, W. Sun, Y. Ju, G. Wysocki, *The Journal of Physical Chemistry Letters*, 4 (2013) 872-876.
[904] Z. Zhao, M. Chaos, A. Kazakov, F.L. Dryer, *Int. J. Chem. Kin.*, 40 (2008) 1-18.
[905] H. Guo, W. Sun, F.M. Haas, T. Farouk, F.L. Dryer, Y. Ju, *Proc. Combust. Inst.*, 34 (2013) 573-581.
[906] K. Yasunaga, F. Gillespie, J.M. Simmie, H.J. Curran, Y. Kuraguchi, H. Hoshikawa, M. Yamane, Y. Hidaka, *The Journal of Physical Chemistry A*, 114 (2010) 9098-9109.
[907] N. Kurimoto, B. Brumfield, X. Yang, T. Wada, P. Diévart, G. Wysocki, Y. Ju, *Proc. Combust. Inst.*, 35 (2015) 457-464.
[908] D. Liu, J. Santner, C. Togbé, D. Felsmann, J. Koppmann, A. Lackner, X. Yang, X. Shen, Y. Ju, K. Kohse-Höinghaus, *Combust. Flame*, 160 (2013) 2654-2668.
[909] L.J. Stief, D.F. Nava, W.A. Payne, J.V. Michael, *The Journal of Chemical Physics*, 73 (1980) 2254-2258.
[910] J. Gao, Y. Nakamura, *Combust. Flame*, 165 (2016) 68-82.
[911] L.B. Harding, S.J. Klippenstein, A.W. Jasper, *Phys Chem Chem Phys*, 9 (2007) 4055-4070.
[912] J.M.L. Martin, O. Uzan, *Chemical Physics Letters*, 282 (1998) 16-24.
[913] A. Jalan, I.M. Alecu, R. Meana-Pañeda, J. Aguilera-Iparraguirre, K.R. Yang, S.S. Merchant, D.G. Truhlar, W.H. Green, *Journal of the American Chemical Society*, 135 (2013) 11100-11114.
[914] J.C. Brocard, F. Baronnet, H.E. O'Neal, *Combust. Flame*, 52 (1983) 25-35.
[915] A. Goldaniga, T. Faravelli, E. Ranzi, P. Dagaut, M. Cathonnet, *Symposium (International) on Combustion*, 27 (1998) 353-360.

[916] P.A. Glaude, F. Battin-Leclerc, B. Judenherc, V. Warth, R. Fournet, G.M. Côme, G. Scacchi, P. Dagaut, M. Cathonnet, *Combust. Flame*, 121 (2000) 345-355.
[917] B. Kerschgens, L. Cai, H. Pitsch, B. Heuser, S. Pischinger, *Combust. Flame*, 163 (2016) 66-78.
[918] D.C. Rakopoulos, C.D. Rakopoulos, E.G. Giakoumis, A.M. Dimaratos, *Fuel*, 109 (2013) 325-335.
[919] M.P. Ashok, C.G. Saravanan, *Energy & Fuels*, 21 (2007) 1878-1882.
[920] H. Yamada, K. Suzaki, H. Sakanashi, N. Choi, A. Tezaki, *Combust. Flame*, 140 (2005) 24-33.
[921] P.Q.E. Clothier, A. Moise, H.O. Pritchard, *Combust. Flame*, 81 (1990) 242-250.
[922] C. Arcoumanis, C. Bae, R. Crookes, E. Kinoshita, *Fuel*, 87 (2008) 1014-1030.
[923] K.E. Marrouni, H. Abou-Rachid, S. Kaliaguine, *International Journal of Quantum Chemistry*, 108 (2008) 40-50.
[924] G. Mittal, M. Chaos, C.-J. Sung, F.L. Dryer, *Fuel Processing Technology*, 89 (2008) 1244-1254.
[925] Z. Li, W. Wang, Z. Huang, M.A. Oehlschlaeger, *Energy & Fuels*, 27 (2013) 2811-2817.
[926] U. Pfahl, K. Fieweger, G. Adomeit, *Symposium (International) on Combustion*, 26 (1996) 781-789.
[927] N. Djordjevic, M. Rekus, J. Vinkeloe, L. Zander, *Energy & Fuels*, 33 (2019) 10197-10208.
[928] M. Werler, L.R. Cancino, R. Schiessl, U. Maas, C. Schulz, M. Fikri, *Proc. Combust. Inst.*, 35 (2015) 259-266.
[929] T. Inomata, J.F. Griffiths, A.J. Pappin, *Symposium (International) on Combustion*, 23 (1991) 1759-1766.
[930] Y. Uygun, *Combust. Flame*, 194 (2018) 396-409.
[931] K. Hakimov, F. Arafin, K. Aljohani, K. Djebbi, E. Ninnemann, S.S. Vasu, A. Farooq, *Combust. Flame*, 223 (2021) 98-109.
[932] H.K. Ciezki, G. Adomeit, *Combust. Flame*, 93 (1993) 421-433.
[933] B.M. Gauthier, D.F. Davidson, R.K. Hanson, *Combust. Flame*, 139 (2004) 300-311.
[934] A. Vandersickel, M. Hartmann, K. Vogel, Y.M. Wright, M. Fikri, R. Starke, C. Schulz, K. Boulouchos, *Fuel*, 93 (2012) 492-501.
[935] E. Toulson, C.M. Allen, D.J. Miller, H.J. Schock, T. Lee, *Energy & Fuels*, 24 (2010) 3510-3516.
[936] M.P. Halstead, L.J. Kirsch, C.P. Quinn, *Combust. Flame*, 30 (1977) 45-60.
[937] S. Di Tommaso, P. Rotureau, B. Sirjean, R. Fournet, W. Benaissa, P. Gruez, C. Adamo, *Process Safety Progress*, 33 (2014) 64-69.
[938] J. Eble, J. Kiecherer, M. Olzmann, *Zeitschrift für Physikalische Chemie*, 231 (2017) 1603-1623.
[939] Z. Tang, L. Zhang, X. Chen, G. Tang, *Energy & Fuels*, 31 (2017) 2803-2813.
[940] E. Hu, Y. Chen, Z. Zhang, J.-Y. Chen, Z. Huang, *Fuel*, 209 (2017) 509-520.
[941] J.P. Orme, H.J. Curran, J.M. Simmie, *J. Phys. Chem. A*, 110 (2006) 114-131.
[942] A. Rodriguez, O. Herbinet, Z. Wang, F. Qi, C. Fittschen, P.R. Westmoreland, F. Battin-Leclerc, *Proc. Combust. Inst.*, 36 (2017) 333-342.
[943] A.D. Danilack, S.J. Klippenstein, Y. Georgievskii, C.F. Goldsmith, *Proc. Combust. Inst.*, (2020).
[944] M.J. Al Rashidi, A.C. Davis, S.M. Sarathy, *Proc. Combust. Inst.*, 35 (2015) 385-392.
[945] K. Yasunaga, J.M. Simmie, H.J. Curran, T. Koike, O. Takahashi, Y. Kuraguchi, Y. Hidaka, *Combust. Flame*, 158 (2011) 1032-1036.
[946] B. Rotavera, R.L. Caravan, C.A. Taatjes, Sandia National Laboratories, Subsequent R + O_2 Chemistry of Intermediates Formed in Low-Temperature R + O_2 Reactions: Potential Importance in Modeling Autoignition Behavior, Sandia National Laboratories Report SAND2017-9099, 2017.
[947] A.C. Doner, M.M. Davis, A.L. Koritzke, M.G. Christianson, J.M. Turney, H.F. Schaefer Iii, L. Sheps, D.L. Osborn, C.A. Taatjes, B. Rotavera, *Int. J. Chem. Kin.*, 53 (2021) 127-145.
[948] Z. Wang, O. Herbinet, Z. Cheng, B. Husson, R. Fournet, F. Qi, F. Battin-Leclerc, *The Journal of Physical Chemistry A*, 118 (2014) 5573-5594.
[949] F. Battin-Leclerc, J.M. Simmie, E. Blurock, Cleaner Combustion: Developing Detailed Chemical Kinetic Models, Springer-Verlag, 2013
[950] J.M. Simmie, *J. Phys. Chem. A.*, 116 (2012) 4528-4538.
[951] B. Rotavera, J.D. Savee, I.O. Antonov, R.L. Caravan, L. Sheps, D.L. Osborn, J. Zádor, C.A. Taatjes, *Proc. Combust. Inst.*, 36 (2017) 597-606.

[952] A. Sudholt, C. Lee, J. Klankermayer, R.X. Fernandes, H. Pitsch, *Combust. Flame*, 171 (2016) 133-136.
[953] A. Sudholt, L. Cai, J. Heyne, F.M. Haas, H. Pitsch, F.L. Dryer, *Proc. Combust. Inst.*, 35 (2015) 2957-2965.
[954] R. Tripathi, C. Lee, R.X. Fernandes, H. Olivier, H.J. Curran, S. Mani Sarathy, H. Pitsch, *Proc. Combust. Inst.*, 36 (2017) 587-595.
[955] B.R. Giri, F. Khaled, M. Szőri, B. Viskolcz, A. Farooq, *Proc. Combust. Inst.*, 36 (2017) 143-150.
[956] J. Moriarty, H. Sidebottom, J. Wenger, A. Mellouki, G. Le Bras, *The Journal of Physical Chemistry A*, 107 (2003) 1499-1505.
[957] A.M. Winer, A.C. Lloyd, K.R. Darnall, J.N. Pitts, *The Journal of Physical Chemistry*, 80 (1976) 1635-1639.
[958] A.R. Ravishankara, D.D. Davis, *The Journal of Physical Chemistry*, 82 (1978) 2852-2853.
[959] Y. Fenard, A. Gil, G. Vanhove, H.-H. Carstensen, K.M. Van Geem, P.R. Westmoreland, O. Herbinet, F. Battin-Leclerc, *Combust. Flame*, 191 (2018) 252-269.
[960] S.M. Sarathy, C.K. Westbrook, M. Mehl, W.J. Pitz, C. Togbe, P. Dagaut, H. Wang, M.A. Oehlschlaeger, U. Niemann, K. Seshadri, P.S. Veloo, C. Ji, F.N. Egolfopoulos, T. Lu, *Combust. Flame*, 158 (2011) 2338-2357.
[961] I.O. Antonov, J. Zádor, B. Rotavera, E. Papajak, D.L. Osborn, C.A. Taatjes, L. Sheps, *The Journal of Physical Chemistry A*, 120 (2016) 6582-6595.
[962] Y. Georgievskii, J.A. Miller, M.P. Burke, S.J. Klippenstein, *The Journal of Physical Chemistry A*, 117 (2013) 12146-12154.
[963] M.J. Molera, A. Couto, J.A. Garcia-Dominguez, *Int. J. Chem. Kin.*, 20 (1988) 673-685.
[964] P. Dagaut, M. McGuinness, J.M. Simmie, M. Cathonnet, *Comb. Sci. Tech.*, 135 (1998) 3-29.
[965] G. Vanhove, Y. Yu, M.A. Boumehdi, O. Frottier, O. Herbinet, P.-A. Glaude, F. Battin-Leclerc, *Energy & Fuels*, (2015).
[966] N. Belhadj, R. Benoit, P. Dagaut, M. Lailliau, *Energy & Fuels*, (2020).
[967] L.S. Tran, M. Verdicchio, F. Monge, R.C. Martin, R. Bounaceeur, B. Sirjean, P.A. Glaude, M.U. Alzueta, F. Battin-Leclerc, *Combust. Flame*, 162 (2015) 1899-1918.
[968] L. Cai, H. Minwegen, J. Beeckmann, U. Burke, R. Tripathi, A. Ramalingam, L.C. Kröger, A. Sudholt, K. Leonhard, J. Klankermayer, K.A. Heufer, H. Pitsch, *Combust. Flame*, 178 (2017) 257-267.
[969] Y. Wu, N. Xu, M. Yang, Y. Liu, C. Tang, Z. Huang, *Combust. Flame*, 213 (2020) 226-236.
[970] L.-S. Tran, Z. Wang, H.-H. Carstensen, C. Hemken, F. Battin-Leclerc, K. Kohse-Höinghaus, *Combust. Flame*, 181 (2017) 251-269.
[971] X. Fan, X. Wang, J. Wang, K. Yang, *Energy & Fuels*, 30 (2016) 8727-8736.
[972] Y. Uygun, S. Ishihara, H. Olivier, *Combust. Flame*, 161 (2014) 2519-2530.
[973] P.R. Parab, N. Sakade, Y. Sakai, R. Fernandes, K.A. Heufer, *Int. J. Chem. Kin.*, (2017) n/a-n/a.
[974] Y. Fenard, M.A. Boumehdi, G. Vanhove, *Combust. Flame*, 178 (2017) 168-181.
[975] R. De Bruycker, L.-S. Tran, H.-H. Carstensen, P.-A. Glaude, F. Monge, M.U. Alzueta, F. Battin-Leclerc, K.M. Van Geem, *Combust. Flame*, 176 (2017) 409-428.
[976] P.R. Parab, N. Sakade, Y. Sakai, R. Fernandes, K.A. Heufer, *The Journal of Physical Chemistry A*, 119 (2015) 10917-10928.
[977] R. Tripathi, A.K. Ramalingam, H. Minwegen, A.B.S. Alquaity, K.A. Heufer, H. Pitsch, *Proc. Combust. Inst.*, 37 (2019) 221-230.
[978] J. Wang, X. Wang, X. Fan, K. Yang, 1 (2015).
[979] A. Fridlyand, S.S. Goldsborough, M. Al Rashidi, S.M. Sarathy, M. Mehl, W.J. Pitz, *Combust. Flame*, 200 (2019) 387-404.
[980] G. Blanquart, P. Pepiot-Desjardins, H. Pitsch, *Combust. Flame*, 156 (2009) 588-607.
[981] K. Moshammer, S. Vranckx, H.K. Chakravarty, P. Parab, R.X. Fernandes, K. Kohse-Höinghaus, *Combust. Flame*, 160 (2013) 2729-2743.
[982] H.S. Johnston, J. Heicklen, *The Journal of Physical Chemistry*, 66 (1962) 532-533.

[983] Y. Fenard, H. Song, H. Minwegen, P. Parab, C. Sampaio Mergulhão, G. Vanhove, K.-A. Heufer, *Combust. Flame*, 203 (2019) 341-351.
[984] P. Dagaut, M. McGuinness, J.M. Simmie, M. Cathonnet, *Comb. Sci. Tech.*, 129 (1997) 1-16.
[985] N.J. Labbe, V. Seshadri, T. Kasper, N. Hansen, P. Oßwald, P.R. Westmoreland, *Proc. Combust. Inst.*, 34 (2013) 259-267.
[986] L.-S. Tran, R. De Bruycker, H.-H. Carstensen, P.-A. Glaude, F. Monge, M.U. Alzueta, R.C. Martin, F. Battin-Leclerc, K.M. Van Geem, G.B. Marin, *Combust. Flame*, 162 (2015) 4283-4303.
[987] S.M. Daley, A.M. Berkowitz, M.A. Oehlschlaeger, *Int. J. Chem. Kin.*, 40 (2008) 624-634.
[988] O. Lemaire, M. Ribaucour, M. Carlier, R. Minetti, *Combust. Flame*, 127 (2001) 1971-1980.
[989] J.M. Simmie, H.J. Curran, *The Journal of Physical Chemistry A*, 113 (2009) 5128-5137.
[990] D. Feller, J.M. Simmie, *The Journal of Physical Chemistry A*, 116 (2012) 11768-11775.
[991] D.A. Dixon, D. Feller, K.A. Peterson, Chapter One - A Practical Guide to Reliable First Principles Computational Thermochemistry Predictions Across the Periodic Table, in: R.A. Wheeler (Ed.) Annual Reports in Computational Chemistry, Elsevier, 2012, pp. 1-28.
[992] M. Thewes, M. Muether, S. Pischinger, M. Budde, A. Brunn, A. Sehr, P. Adomeit, J. Klankermayer, *Energy & Fuels*, 25 (2011) 5549-5561.
[993] Z. Cheng, L. Xing, M. Zeng, W. Dong, F. Zhang, F. Qi, Y. Li, *Combust. Flame*, 161 (2014) 2496-2511.
[994] B. Sirjean, R. Fournet, *The Journal of Physical Chemistry A*, 116 (2012) 6675-6684.
[995] K.N. Urness, Q. Guan, A. Golan, J.W. Daily, M.R. Nimlos, J.F. Stanton, M. Ahmed, G.B. Ellison, *The Journal of Chemical Physics*, 139 (2013) 124305.
[996] P.P. Organ, J.C. Mackie, *Journal of the Chemical Society, Faraday Transactions*, 87 (1991) 815-823.
[997] R.S. Tranter, P.T. Lynch, J.B. Randazzo, J.P.A. Lockhart, X. Chen, C.F. Goldsmith, *Phys Chem Chem Phys*, (2018).
[998] X. Wu, Z. Huang, T. Yuan, K. Zhang, L. Wei, *Combust. Flame*, 156 (2009) 1365-1376.
[999] Z. Tian, T. Yuan, R. Fournet, P.-A. Glaude, B. Sirjean, F. Battin-Leclerc, K. Zhang, F. Qi, *Combust. Flame*, 158 (2011) 756-773.
[1000] D. Liu, C. Togbé, L.-S. Tran, D. Felsmann, P. Oßwald, P. Nau, J. Koppmann, A. Lackner, P.-A. Glaude, B. Sirjean, R. Fournet, F. Battin-Leclerc, K. Kohse-Höinghaus, *Combust. Flame*, 161 (2014) 748-765.
[1001] C. Togbé, L.-S. Tran, D. Liu, D. Felsmann, P. Oßwald, P.-A. Glaude, B. Sirjean, R. Fournet, F. Battin-Leclerc, K. Kohse-Höinghaus, *Combust. Flame*, 161 (2014) 780-797.
[1002] L.-S. Tran, C. Togbé, D. Liu, D. Felsmann, P. Oßwald, P.-A. Glaude, R. Fournet, B. Sirjean, F. Battin-Leclerc, K. Kohse-Höinghaus, *Combust. Flame*, 161 (2014) 766-779.
[1003] M.A. Eldeeb, B. Akih-Kumgeh, *Energy & Fuels*, 28 (2014) 6618-6626.
[1004] L. Wei, C. Tang, X. Man, X. Jiang, Z. Huang, *Energy & Fuels*, 26 (2012) 2075-2081.
[1005] N. Xu, C. Tang, X. Meng, X. Fan, Z. Tian, Z. Huang, *Energy & Fuels*, 29 (2015) 5372-5381.
[1006] N. Xu, Y. Wu, C. Tang, P. Zhang, X. He, Z. Wang, Z. Huang, *Combust. Flame*, 168 (2016) 216-227.
[1007] K.P. Somers, J.M. Simmie, F. Gillespie, C. Conroy, G. Black, W.K. Metcalfe, F. Battin-Leclerc, P. Dirrenberger, O. Herbinet, P.-A. Glaude, P. Dagaut, C. Togbé, K. Yasunaga, R.X. Fernandes, C. Lee, R. Tripathi, H.J. Curran, *Combust. Flame*, 160 (2013) 2291-2318.
[1008] M.A. Eldeeb, B. Akih-Kumgeh, *Combust. Flame*, 162 (2015) 2454-2465.
[1009] B. Sirjean, R. Fournet, P.-A. Glaude, F. Battin-Leclerc, W. Wang, M.A. Oehlschlaeger, *The Journal of Physical Chemistry A*, 117 (2013) 1371-1392.
[1010] Y. Qian, L. Zhu, Y. Wang, X. Lu, *Renewable and Sustainable Energy Reviews*, 41 (2015) 633-646.
[1011] C. Whelan, J. Eble, Z. Mir, M. Blitz, P. Seakins, M. Olzmann, D. Stone, *J. Phys. Chem. A*, (2020).
[1012] A. Elwardany, E. Es-sebbar, F. Khaled, A. Farooq, *Fuel*, 166 (2016) 245-252.
[1013] P.H. Wine, R.J. Thompson, *Int. J. Chem. Kin.*, 16 (1984) 867-878.

[1014] D. Kim, I. El Gharamti, M. Hantouche, A.E. Elwardany, A. Farooq, F. Bisetti, O. Knio, *Combust. Flame*, 184 (2017) 55-67.
[1015] P. Friese, J.M. Simmie, M. Olzmann, *Proc. Combust. Inst.*, 34 (2013) 233-239.
[1016] M.M. Thorton, P.C. Malte, A.L. Crittenden, *Symposium (International) on Combustion*, 21 (1988) 979-989.
[1017] A. Bierbach, I. Barnes, K.H. Becker, *Atmospheric Environment*, 29 (1995) 2651-2660.
[1018] K. Alexandrino, Á. Millera, R. Bilbao, M.U. Alzueta, *Proc. Combust. Inst.*, 35 (2015) 1717-1725.
[1019] Y. Fathi, G. Meloni, *The Journal of Physical Chemistry A*, (2017).
[1020] N. Balucani, F. Leonori, P. Casavecchia, *Energy*, 43 (2012) 47-54.
[1021] B. Fu, Y.-C. Han, J.M. Bowman, L. Angelucci, N. Balucani, F. Leonori, P. Casavecchia, *Proceedings of the National Academy of Sciences*, 109 (2012) 9733.
[1022] F. Leonori, A. Occhiogrosso, N. Balucani, A. Bucci, R. Petrucci, P. Casavecchia, *The Journal of Physical Chemistry Letters*, 3 (2012) 75-80.
[1023] E. Christensen, G.M. Fioroni, S. Kim, L. Fouts, E. Gjersing, R.S. Paton, R.L. McCormick, *Fuel*, 212 (2018) 576-585.
[1024] S.H. Mousavipour, S. Ramazani, Z. Shahkolahi, *The Journal of Physical Chemistry A*, 113 (2009) 2838-2846.
[1025] J.M. Anglada, *The Open Chemical Physics Journal*, 1 (2008) 80-93.
[1026] Y. Yuan, X. Zhao, S. Wang, L. Wang, *The Journal of Physical Chemistry A*, 121 (2017) 9306-9319.
[1027] A.C. Davis, S.M. Sarathy, *The Journal of Physical Chemistry A*, 117 (2013) 7670-7685.
[1028] J.M. Hudzik, J.W. Bozzelli, *The Journal of Physical Chemistry A*, 121 (2017) 7309-7323.
[1029] Y. Li, Z. Cao, *Phys Chem Chem Phys*, 22 (2020) 3290-3303.
[1030] W. Zhang, B. Du, L. Mu, C. Feng, *Journal of Molecular Structure: THEOCHEM*, 851 (2008) 353-357.
[1031] W. Zhang, B. Du, L. Mu, C. Feng, *International Journal of Quantum Chemistry*, 108 (2008) 1232-1238.
[1032] W. Zhang, C. Feng, B. Du, L. Mu, *Struct Chem*, 20 (2009) 525-532.
[1033] personal communication, 2021.
[1034] K.B. Moore III, A.V. Copan, S.N. Elliott, Y. Georgievskii, C. Cavallotti, M. Keceli, S.J. Klippenstein, AutoMech, 2020.
[1035] C.F. Goldsmith, L.B. Harding, Y. Georgievskii, J.A. Miller, S.J. Klippenstein, *The Journal of Physical Chemistry A*, 119 (2015) 7766-7779.
[1036] A.J. Eskola, T.T. Pekkanen, S.P. Joshi, R.S. Timonen, S.J. Klippenstein, *Proceedings of the Combustion Institute*, 37 (2019) 291-298.
[1037] T. Turányi, A.S. Tomlin, Analysis of Kinetic Reaction Mechanisms, Springer, 2014.
[1038] A.S. Tomlin, *Proc. Combust. Inst.*, 34 (2013) 159-176.
[1039] M.J. Davis, R.T. Skodje, A.S. Tomlin, *The Journal of Physical Chemistry A*, 115 (2011) 1556-1578.
[1040] H. Wang, D.A. Sheen, *Prog. Energy Comb. Sci.*, 47 (2015) 1-31.
[1041] T. Kessler, E.R. Sacia, A.T. Bell, J.H. Mack, *Fuel*, 206 (2017) 171-179.
[1042] B. Yang, *Proc. Combust. Inst.*, (2020).
[1043] L. Pattanaik, J.B. Ingraham, C.A. Grambow, W.H. Green, *Phys Chem Chem Phys*, 22 (2020) 23618-23626.
[1044] S. Li, B. Yang, F. Qi, *Combust. Flame*, 168 (2016) 53-64.
[1045] E. Agbro, A.S. Tomlin, *Fuel*, 207 (2017) 776-789.
[1046] F. vom Lehn, L. Cai, H. Pitsch, *Combust. Flame*, 210 (2019) 454-466.
[1047] F. vom Lehn, L. Cai, H. Pitsch, *Proc. Combust. Inst.*, 37 (2019) 771-779.
[1048] A.L. Koritzke, K.M. Frandsen, M.G. Christianson, J.C. Davis, A.C. Doner, A. Larsson, J. Breda-Nixon, B. Rotavera, *International Journal of Mass Spectrometry*, 454 (2020) 116342.

[1049] M.P. Burke, C.F. Goldsmith, Y. Georgievskii, S.J. Klippenstein, *Proc. Combust. Inst.*, 35 (2015) 205-213.
[1050] C.F. Goldsmith, M.P. Burke, Y. Georgievskii, S.J. Klippenstein, *Proc. Combust. Inst.*, 35 (2015) 283-290.
[1051] Z. Wang, S.M. Sarathy, *Combust. Flame*, 165 (2016) 364-372.
[1052] Z. Wang, L. Zhang, K. Moshammer, D.M. Popolan-Vaida, V.S.B. Shankar, A. Lucassen, C. Hemken, C.A. Taatjes, S.R. Leone, K. Kohse-Höinghaus, N. Hansen, P. Dagaut, S.M. Sarathy, *Combust. Flame*, 164 (2016) 386-396.
[1053] Z. Wang, D.M. Popolan-Vaida, B. Chen, K. Moshammer, S.Y. Mohamed, H. Wang, S. Sioud, M.A. Raji, K. Kohse-Höinghaus, N. Hansen, P. Dagaut, S.R. Leone, S.M. Sarathy, *Proceedings of the National Academy of Sciences*, 114 (2017) 13102.
[1054] E.J. Silke, W.J. Pitz, C.K. Westbrook, M. Ribaucour, *The Journal of Physical Chemistry A*, 111 (2007) 3761-3775.
[1055] Z. Tian, Y. Zhang, F. Yang, L. Pan, X. Jiang, Z. Huang, *Energy & Fuels*, 28 (2014) 7159-7167.
[1056] S. Vranckx, C. Lee, H.K. Chakravarty, R.X. Fernandes, *Proc. Combust. Inst.*, 34 (2013) 377-384.
[1057] J.O. Valle-Rodríguez, S. Shi, V. Siewers, J. Nielsen, *Appl Energy*, 115 (2014).
[1058] Y.J. Zhou, N.A. Buijs, V. Siewers, J. Nielsen, *Frontiers in Bioengineering and Biotechnology*, 2 (2014).